Two-dimensional phononic crystals: Examples and applications

Yan Pennec [a], Jérôme O. Vasseur [a], Bahram Djafari-Rouhani [a], Leonard Dobrzyński [a,*], Pierre A. Deymier [b]

[a] Equipe de Physique, des Ondes, des Nanostructures et des Interfaces, Groupe de Physique, Institut d'Electronique, de Microélectronique et de Nanotechnologie, Université des Sciences et Technologies de Lille, Centre National de la Recherche Scientifique (UMR 8520), F-59655 Villeneuve d'Ascq Cédex, France

[b] Department of Materials Science and Engineering, University of Arizona, Tucson, AZ 85721, USA

ARTICLE INFO

editor: L. Dobrzynski

ABSTRACT

Phononic crystals are composite materials made of periodic distributions of inclusions embedded in a matrix. Due to their periodic structure, these materials may exhibit under certain conditions, absolute acoustic band gaps i.e. forbidden bands that are independent of the direction of propagation of the incident elastic wave. In the first part of this review paper, we present some examples of two-dimensional bulk phononic crystals i.e. two-dimensional arrays of inclusions assumed of infinite extent along the three spatial directions. We show that the bandwidth of the forbidden band depends strongly on the nature of the constituent materials (solid or fluid), as well as the contrast between the physical characteristics (density and elastic moduli) of the inclusions and of the matrix, the geometry of the array of inclusions, the inclusion shape and the filling factor of inclusions. The second part of this review paper is devoted to some possible applications of these composite materials. In particular, we show that defect modes (cavities, waveguides, stubs, etc.) inserted inside the two-dimensional periodic structure may lead to very selective frequency filters and efficient devices for the wavelength demultiplexing. We present also the possibility of sonic insulators for frequencies of the order of kHz with relatively small thicknesses of phononic crystal samples. Finally we report on the vibration modes of a two-dimensional phononic crystal plate i.e. a phononic crystal of finite thickness along the axis of the inclusions. We discuss guided modes which may occur in the band structure of the plate. Surface acoustic waves propagating in two-dimensional phononic crystals should open new perspectives in high-frequency radio-frequency devices. Throughout the paper, the methods of calculation are presented with some details and some experimental results complete the numerical predictions.

Contents

* Corresponding author.
  E-mail addresses: Yan.Pennec@univ-lille1.fr (Y. Pennec), jerome.vasseur@univ-lille1.fr (J.O. Vasseur), Leonard.Dobrzynski@Univ-Lille1.Fr (L. Dobrzyński).

1. Introduction

Optical properties of heterogeneous materials with a periodic structure have received a great deal of attention during the past two decades. Much effort has focused on the search for large band gaps in the optical band structure of periodic inhomogeneous dielectric materials. Several geometries of these so-called "photonic" crystals have been proposed: one-dimensional systems in the form of Bragg lattices [1,2] or comb-like structures [3,4], two-dimensional systems such as arrays of parallel cylinders embedded in a matrix and three-dimensional crystals with various distributions of spherical inclusions suspended in a host matrix [5–8].

The mathematical analogy between Maxwell's equations and the equations of linear elasticity has spurred a renewed interest in "phononic" crystals, that is periodic inhomogeneous elastic media exhibiting forbidden bands in their acoustic transmission spectrum. A comparison between phononic and photonic lattices is in particular presented in Ref. [9]. In these materials, the density as well as the elastic constants are periodic functions of the position. Although the propagation of elastic waves in periodic composite materials is an old topic in condensed matter physics and/or acoustics [10–12], the search for acoustic band gaps in heterogeneous materials gave rise, in recent years, to numerous theoretical and experimental investigations [13–18].

The so-called elastic band gap materials are inhomogeneous elastic media composed of one [19–25], two [11,26,9,27–33] or three [34–36] dimensional periodic arrays of inclusions embedded in a matrix. These composite media typically exhibit stop bands in their transmission spectra where the propagation of sound and vibrations is strictly forbidden. Several classes of phononic materials differing in the physical nature of the inclusions and the matrix have been studied. Among them one finds solid–solid, fluid–fluid and mixed solid–fluid composite systems.

The existence of absolute band gaps in two-dimensional phononic crystals was predicted theoretically [26,9] prior to being demonstrated experimentally in various phononic crystals constituted of solid components [32] or mixed solid/fluid components [33]. In two-dimensional solid–solid phononic materials composed of periodic arrays of cylindrical inclusions, under the assumption of wave propagation in the plane perpendicular to the cylinders, the vibrational modes decouple in the mixed-polarization modes with the elastic displacement **u** perpendicular to the cylinders and in the purely transverse modes with **u** parallel to the inclusions. In contrast only longitudinal modes are allowed in fluid/fluid composites [37]. The opening of wide acoustic band gaps requires: (i) a large contrast in physical properties such as density and speeds of sound, between the inclusions and the matrix, and (ii) a sufficient filling factor of inclusions [37]. In mixed solid–fluid media, the first condition is often satisfied, particularly in the case of solid/gas combinations. The mixed systems present complex vibrational modes ranging from longitudinal modes in the fluid to mixed-polarization modes and transverse vibrations in the solid. In mixed composites, the fluid can be either a condensed liquid (water [38,39], Hg [33]) or a gas (air [35,40–47]). The frequency domain where the band gap occurs scales as the ratio of an effective sound velocity in the composite material to a measure of the periodicity of the array of inclusions. For solid/air systems, the effective sound velocity is significantly lower than that of solid/solid or fluid/fluid composites allowing for the design of acoustic band gaps in the audible frequency domain without excessively large periods and inclusions sizes. In light of this observation, the mixed solid/air phononic materials show the necessary physical characteristics for use as practical sound insulators.

Theoretical models of two-dimensional [48,26,9,31] and three-dimensional [34,35] phononic crystals based on the plane wave expansion method have shown that the width of the acoustic band gaps strongly depends on the composition and the geometry as well as on the nature of the constituent materials. A large contrast in physical properties between the inclusions and the host material is required to obtain large acoustic band gaps [37]. Sigalas et al. [49,50] applied the finite difference time domain method [51], well known in the field of photonic crystals [52,53], to the study of two and three-dimensional elastic band gap materials. In contrast to the plane wave expansion method, the finite difference time domain method enables the calculation of the acoustic transmission coefficient of a finite composite sample that can be measured routinely in experiments. Moreover, the finite difference time domain method can be applied to mixed (solid–fluid) composites where the plane wave expansion fails to work [54] due to the vanishing of the shear modulus in the fluid component. In the finite difference time domain method, the elastic wave equations are discretized in both the spatial and time domains with appropriate boundary conditions. The evolution of the elastic displacement field is calculated in the time and space domain.

Fourier transformed results give the acoustic transmission spectrum. The agreement between the finite difference time domain and the plane wave expansion methods seems to be excellent in locating the forbidden bands [49]. As other reviews on two-dimensional phononic crystals have appeared already [13,15–18], we will give in Section 2 only a few examples of respectively solid–solid, fluid–fluid and solid–fluid two-dimensional phononic crystals. In the next sections, we will focus on applications of these new materials, dealing with filtering, demultiplexing of acoustic waves, phononic crystal plates and high-frequency radio-frequency devices and sonic insulators. This review ends with some general conclusions and prospects.

2. Examples of two-dimensional phononic crystals

2.1. Solid–solid phononic crystals

2.1.1. Examples of dispersion curves

The elastic band structure of two-dimensional composite materials, formed from periodic arrays of parallel solid cylinders embedded in a solid background material, have been treated independently in a few works by Sigalas and Economou [55,56,46,57], and Kushwaha et al. [9,27]. These last authors [9] considered only the transverse polarization mode of vibration, with elastic displacement parallel to the cylinders and perpendicular to the wave vectors. The dispersion curves for Ni (Al) cylinders in an Al (Ni) background were presented. Phononic band gaps, extending throughout the first Brillouin zone, were found in both cases. On the other hand, the dependence of the band gap on the composition of the material and on the physical parameters of the constituents involved in the composite system was investigated [27]. In addition to the above polarization, Sigalas and Economou [46] also studied the coupled longitudinal–transverse polarization mode of vibration for which the elastic displacement as well as the Bloch wave vector are perpendicular to the cylinders' axis. They found that Au cylinders in a Be background exhibit a very narrow, however complete gap, shared by both polarizations. They proposed [55] that the cermet topology, in which the cylinders are made of a low-velocity material surrounded by a high-velocity host material, is the more favorable periodic binary composite structure for the appearance of acoustic gaps.

In what follows, we present results [31] of elastic band structure for composite materials commercially available like epoxy reinforced carbon or glass fibers. The dispersion curves for combinations of two metals like W and Al taken as isotropic were also calculated. We emphasize the existence of several large complete band gaps in the epoxy reinforced carbon cylinders composite while one single narrow low frequency gap was found previously in previous work on elastic composites [46]. We also point out the possibility of very flat bands. The calculation of the band structure is performed for different shapes of the cylinders' cross section, when the array of rods forms a square lattice. A general requirement for the existence of complete band gaps (which is fulfilled in our examples) is a large contrast between the parameters of the constituents. However, these gaps were obtained for carbon cylinders in an epoxy matrix or W inclusions in an Al matrix and not in the reverse situations. In both cases, the elastic constants are higher in the inclusions than in the background material; however carbon and epoxy have similar mass densities and very different elastic constants, whereas in W and Al both elastic constants and mass densities are rather different, the velocities of sound being almost similar. Therefore, these results show that a statement about the relative velocities of sound in the constituents cannot give a general rule for the existence of complete band gaps [55]; rather, the contrast between elastic constants as well as mass densities should be taken into account. The method of calculation is first briefly presented and followed by the numerical results and the main conclusions one can draw from this example.

2.1.1.1. Calculation method. These periodic systems are modeled as arrays of infinite cylinders of arbitrary cross section made of an isotropic material A embedded in an infinite isotropic elastic matrix B (see Fig. 1). The lattice constant is a and the filling fractions are f and $(1 - f)$ for the materials A and B respectively. The elastic parameters are periodic functions of the position. The mass density ρ and the elastic constants C_{ij} are ρ^A and C_{ij}^A inside the cylinders and ρ^B and C_{ij}^B in the background. It means that ρ and C_{ij} are functions of the coordinates x and y where the z axis defines the direction of the cylinders. Considering the double periodicity in the xOy plane, we can write ρ and C_{ij} as Fourier series

$$\rho(\mathbf{r}) = \rho(x, y) = \sum_{\mathbf{G}} \rho(\mathbf{G}) \exp(i\mathbf{Gr}) \tag{1}$$

and

$$C_{ij}(\mathbf{r}) = C_{ij}(x, y) = \sum_{\mathbf{G}} C_{ij}(\mathbf{G}) \exp(i\mathbf{Gr}) \tag{2}$$

where $\mathbf{r}$ is the position vector of components x and y and $\mathbf{G}$ are the reciprocal lattice vectors in the xOy plane. The Fourier coefficients in Eq. (1) take the form

$$\rho(\mathbf{G}) = \frac{1}{A} \int \int d^2\mathbf{r} \rho(\mathbf{r}) \exp(-i\mathbf{Gr}), \tag{3}$$

where the integration is performed over the unit cell of area $A = a^2$. For $\mathbf{G} = 0$, Eq. (3) gives the average density

$$\rho(\mathbf{G} = \mathbf{0}) = \overline{\rho} = \rho^A f + \rho^B(1 - f). \tag{4}$$

For $\mathbf{G} \neq \mathbf{0}$, Eq. (3) may be written as

$$\rho(\mathbf{G} \neq \mathbf{0}) = (\rho^A - \rho^B)F(\mathbf{G}) = (\Delta\rho)F(\mathbf{G}), \tag{5}$$

where $F(\mathbf{G})$ is the structure factor given by

$$F(\mathbf{G}) = \frac{1}{A} \int \int_A d^2\mathbf{r} \exp(-i\mathbf{Gr}). \tag{6}$$

In Eq. (6), the integration is only performed on material A. In an entirely similar way, Eq. (2) gives

$$C_{ij}(\mathbf{G} = \mathbf{0}) = \overline{C_{ij}} = C_{ij}^A f + C_{ij}^B(1 - f) \tag{7}$$

and

$$C_{ij}(\mathbf{G} \neq \mathbf{0}) = (C_{ij}^A - C_{ij}^B)F(\mathbf{G}) = (\Delta C_{ij})F(\mathbf{G}), \tag{8}$$

with $ij = 11, 44$ or 12. Let us now give the equations of motion in the composite material remembering that the elastic constants and the mass density are position dependent

$$\rho(\mathbf{r})\frac{\partial^2 u_i}{\partial t^2} = \nabla.[C_{44}(\mathbf{r})\nabla u_i] + \nabla.\left[C_{44}(\mathbf{r})\frac{\partial \mathbf{u}}{\partial x_i}\right]$$
$$+ \left(\frac{\partial}{\partial x_i}\right)[(C_{11}(\mathbf{r}) - 2C_{44}(\mathbf{r}))\nabla.\mathbf{u}], \tag{9}$$

where $\mathbf{u}$ represents the position and time dependent displacement vector $\mathbf{u}(\mathbf{r}, t)$. For wave propagation in the xOy plane, one can introduce a wave vector $\mathbf{K}(K_x, K_y)$ (which means $K_z = 0$) and use the Bloch theorem to write the displacement field

$$\mathbf{u}(\mathbf{r}, t) = \exp i(\mathbf{K}.\mathbf{r} - \omega t) \sum_{\mathbf{G}} \mathbf{u}_{\mathbf{K}}(\mathbf{G}) \exp i\mathbf{G}.\mathbf{r}, \tag{10}$$

where ω is the wave circular frequency. In this case the vibrations polarized parallel to the z axis become decoupled from those in the xOy plane. The equations of motion for the former modes are written in dyadic notation as

$$[\overline{C_{44}}(\mathbf{K} + \mathbf{G})^2 - \rho\omega^2]u^z_{\mathbf{K}}(\mathbf{G}) + \sum_{\mathbf{G}' \neq \mathbf{G}}[(\Delta C_{44})(\mathbf{K} + \mathbf{G}).(\mathbf{K} + \mathbf{G}')$$
$$- (\Delta\rho)\omega^2]F(\mathbf{G} - \mathbf{G}')u^z_{\mathbf{K}}(\mathbf{G}') = 0, \tag{11}$$

Table 1
Mass density ρ and elastic constants C_{11} and C_{44} of carbon [58], epoxy resin [58], W and Al [59]. c_l and c_t represent respectively the longitudinal and the transverse speed of sound.

Material	ρ (g cm^{-3})	C_{11} (10^{11} dyn cm^{-2})	C_{44} (10^{11} dyn cm^{-2})	$c_l = \sqrt{\frac{C_{11}}{\rho}}$ (m s^{-1})	$c_t = \sqrt{C_{44}\rho}$ (m s^{-1})
C	1.75	30.96	8.846	13310	7110
Epoxy	1.2	0.964	0.161	2830	1160
W	19.3	50.1	15.14	5090	2800
Al	2.692	11.2	2.79	6450	3220
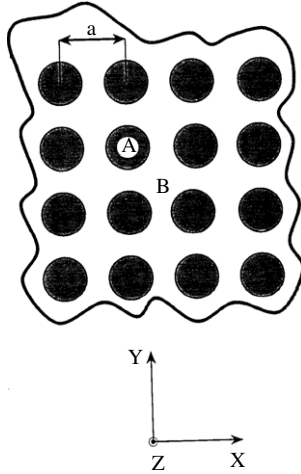
Fig. 1. Transverse cross section of the binary composite system: a square array of infinite cylinders (A) periodically distributed in an infinite matrix (B).

whereas the latter modes are governed by the equation

$$[\overline{C_{44}}(\mathbf{K} + \mathbf{G})^2 - \rho\omega^2].\mathbf{u}_{\mathbf{K}}^{\mathbf{T}}(\mathbf{G}) + (\overline{C_{11}} - \overline{C_{44}})(\mathbf{K} + \mathbf{G})(\mathbf{K} + \mathbf{G}')$$
$$\times \mathbf{u}_{\mathbf{K}}^{\mathbf{T}}(\mathbf{G}) \quad + \sum_{\mathbf{G}' \neq \mathbf{G}} F(\mathbf{G} - \mathbf{G}')\{(\Delta C_{44})[(\mathbf{K} + \mathbf{G}).(\mathbf{K} + \mathbf{G}').\mathbf{u}_{\mathbf{K}}^{\mathbf{T}}(\mathbf{G}')$$
$$+ (\mathbf{K} + \mathbf{G}')(\mathbf{K} + \mathbf{G}).\mathbf{u}_{\mathbf{K}}^{\mathbf{T}}(\mathbf{G}') - 2(\mathbf{K} + \mathbf{G})(\mathbf{K} + \mathbf{G}').\mathbf{u}_{\mathbf{K}}^{\mathbf{T}}(\mathbf{G}')]$$
$$+ (\Delta C_{11})(\mathbf{K} + \mathbf{G})(\mathbf{K} + \mathbf{G}')\mathbf{u}_{\mathbf{K}}^{\mathbf{T}}(\mathbf{G}') - (\Delta\rho)\omega^2\mathbf{u}_{\mathbf{K}}^{\mathbf{T}}(\mathbf{G}')\} = 0, \quad (12)$$

where $\mathbf{u}^{\mathbf{T}} = u_x\mathbf{e_x} + u_y\mathbf{e_y}$, $\mathbf{e_x}$ and $\mathbf{e_y}$ being the unit vectors along the x and y axes. Eqs. (11) and (12) are two infinite sets of linear equations where the unknowns are the Fourier components of the displacement field. In practice, only a finite number of $\mathbf{G}$ vectors are, of course, taken into account. The determinants of these systems of equations must vanish, which conditions yield the band structure $\omega_n(\mathbf{K})$. The eigenmodes of Eq. (11) correspond to transverse vibrations ($\mathbf{u} = u^z\mathbf{e_z} \perp \mathbf{K}$) ($\mathbf{e_z}$ being the unit vector along the z axis) and will be called Z modes or bands. On the other hand, the eigenvalues of Eq. (12) describe coupled longitudinal–transverse vibrations, to be denoted XY modes or bands.

2.1.1.2. Numerical results for a square lattice. We first consider composite systems of technological interest, namely the carbon fiber reinforced epoxy composites which are used, for example, in aeronautics and car manufacture [58]. The dispersion curves for different filling fractions and various cross sections of the cylinders were calculated. Epoxy and carbon are polycrystalline materials, which may be considered as isotropic at a macroscopic scale. Their physical parameters are listed in Table 1.

It is assumed that the array of cylinders forms a square lattice of period a. Then the reciprocal lattice vectors are given by

$$\mathbf{G} = \frac{2\pi}{a}(n_x\mathbf{e_x} + n_y\mathbf{e_y}) \quad (13)$$

where n_x and n_y are two integers. In the course of the numerical calculations, these integers are limited to the interval $-N \leq n_x$,

$n_y \leq +N$. For the sake of consistency, all the results sketched below are obtained with $N = 6$. However, some of the dispersion curves were also calculated with $N = 10$ and confirmed the good accuracy of the results for $N = 6$. The different shapes of the cylinders' cross sections are the following:

(i) circular section of radius r_o,
(ii) square section of width 2ℓ and
(iii) rotated square section of width 2ℓ with a 45° angle of rotation with respect to the x, y axes.

The structure factors $F(\mathbf{G})$ associated with these shapes are respectively
(i)

$$F(\mathbf{G}) = \frac{2fJ_1(Gr_0)}{Gr_0} \quad (14)$$

with

$$f = \frac{\pi r_0^2}{a^2}, \quad 0 \leq f \leq \frac{\pi}{4},$$

where J_1 is the Bessel function of the first kind,
(ii)

$$F(\mathbf{G}) = f\left(\frac{\sin(G_x\ell)}{G_x\ell}\right)\left(\frac{\sin(G_y\ell)}{G_y\ell}\right) \quad (15)$$

with

$$f = \frac{4\ell^2}{a^2}, \quad 0 \leq f \leq 1,$$

and
(iii)

$$F(\mathbf{G}) = f\left(\frac{\sin[\frac{\ell}{\sqrt{2}}(G_x + G_y)]}{\frac{\ell}{\sqrt{2}}(G_x + G_y)}\right)\left(\frac{\sin[\frac{\ell}{\sqrt{2}}(-G_x + G_y)]}{\frac{\ell}{\sqrt{2}}(-G_x + G_y)}\right), \quad (16)$$

with

$$f = \frac{4\ell^2}{a^2} \quad \text{and} \quad 0 \leq f \leq \frac{1}{2}.$$

In each case, the maximum value of the filling fraction f corresponds to the close packing of the cylinders.

The left part of Fig. 2(a) shows the first few Z and XY phononic bands for the square array of carbon cylinders of circular cross section in an epoxy matrix, the filling fraction f being equal to 0.55. The band structure for the Z and XY modes in the three principal symmetry directions of the Brillouin zone was plotted, see the inset in Fig. 2(a). The plots are given in terms of the reduced frequency $\Omega = \frac{\omega a}{2\pi c_0}$ (where c_0 is equal to $\sqrt{\frac{C_{44}}{\rho}}$) versus the reduced Bloch wave vector $\mathbf{k} = \frac{\mathbf{K}a}{2}\pi$.

In the range of frequency of Fig. 2(a), three complete band gaps were found between the XY and the Z mode bands. These gaps are defined by the high symmetry points Γ, X, M of the first Brillouin zone except for the bottom of the first gap. One can also notice that the higher dispersion curves in Fig. 2(a) are rather narrow and we especially mention the presence of a nearly flat Z band between the second and third forbidden bands. These behaviors may indicate
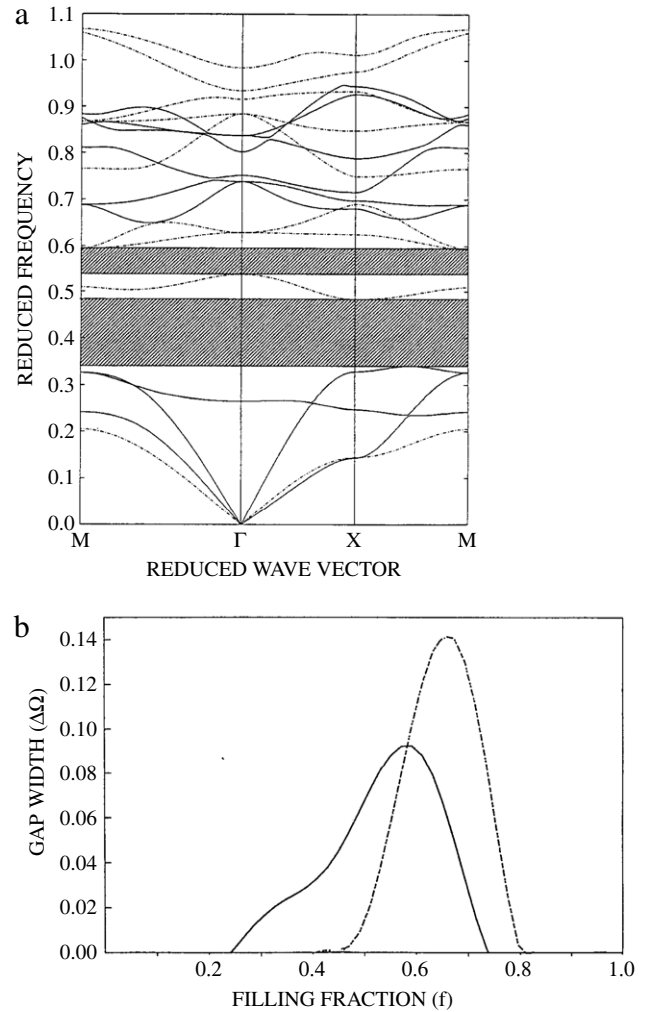
a

DENSITY OF STATES

a

b
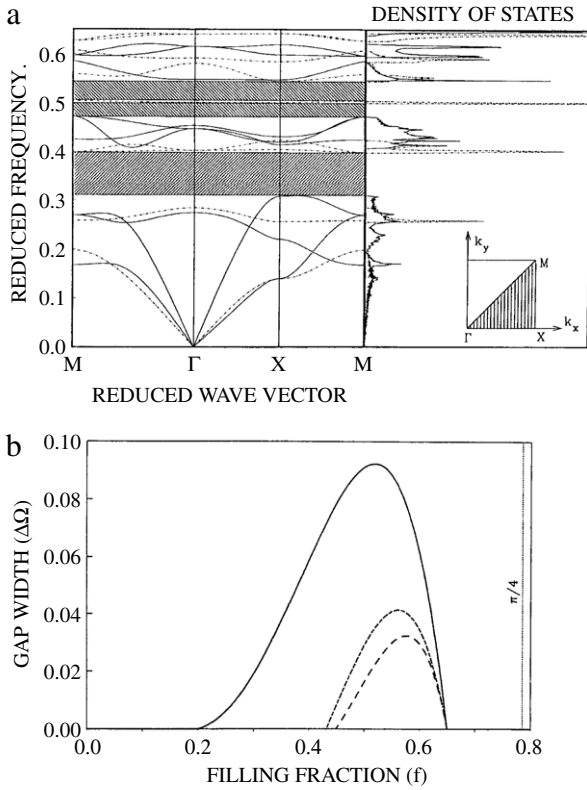
Fig. 2. (a) Elastic plane wave expansion band structure and density of states for carbon cylinders of circular cross section in an epoxy resin matrix, for $f = 0.55$. In the left panel of the figure, the band structure is plotted for Z (dashed lines) and for XY (solid lines) modes of vibrations, in the three high symmetry directions ΓXM of the first Brillouin zone (see inset). One can notice three complete band gaps (a fourth one of lower width exists between the ninth XY band and the eighth Z band) as well as the existence of nearly flat bands as the fifth Z band. The right panel of the figure shows the density of states for Z (dashed lines) and XY (solid lines) modes of vibrations. The phononic complete band gaps in the elastic band structure appear in this figure as regions of null densities of states. (b) Width of the first three complete band gaps as a function of the filling fraction: solid line, first gap; dash-dotted line, second gap; dashed line, third gap.

the existence of localized states in this structure, even though no search for the eigenvectors was done in this computation.

The right panel of Fig. 2(a) presents the variations of the densities of states of XY and Z modes, scanning the interior of the irreducible triangle ΓXM of the Brillouin zone at 1275 points. The phononic gaps in the band structure coincide exactly with regions of null density of states. This leads us to confirm that the existing band gaps extend throughout the Brillouin zone and not only on its periphery. One can also notice that for the nearly flat Z band, the density of states resembles a Dirac δ function.

The band structure in Fig. 2(a) is computed for a filling fraction of 0.55 because this is the value of f which leads to the largest complete gaps. Indeed, in Fig. 2(b), the widths of these three gaps are presented as a function of the filling fraction f. We note the opening of complete band gaps over a large range of the filling fraction, namely, $0.2 < f < 0.65$. One can also notice that the most usual carbon fiber reinforced epoxy composite commercially available corresponds to a filling fraction equal to 0.6 [58].

In Fig. 3(a), the Z and XY band structure for the square array of carbon cylinders of square cross section in an epoxy matrix are drawn for $f = 0.65$. Two complete gaps appear in the range of energy considered, as well as a few rather narrow bands. The value of the largest gap width is now $\Delta \Omega = 0.14$ as compared to a value of $\Delta \Omega = 0.09$ in Fig. 2(a). It is noteworthy, for this cylinder geometry, that there exists a very large gap between the second and the third XY bands, which explains the presence of a very large
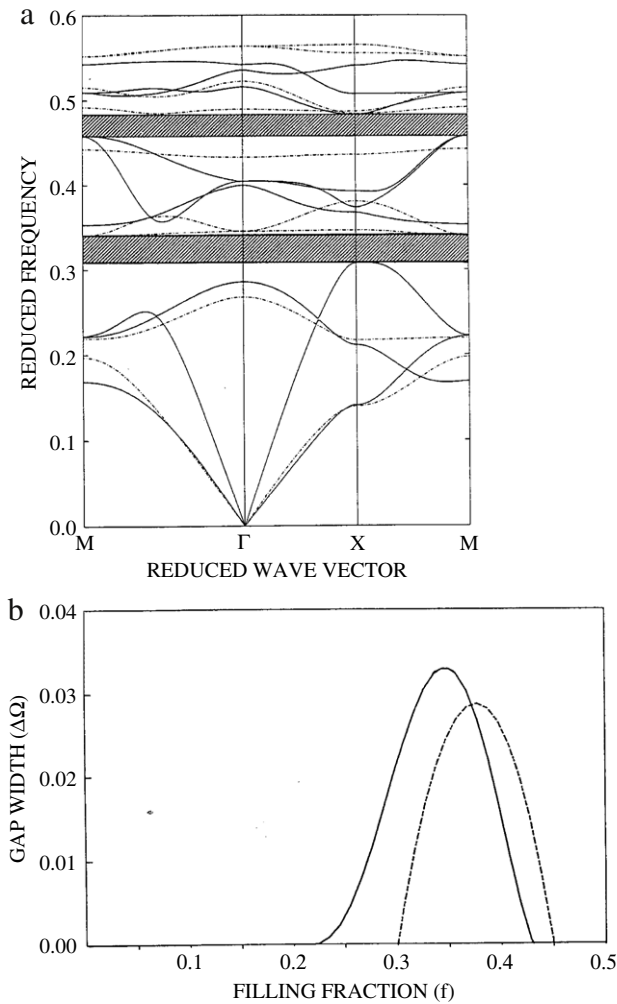
Fig. 3. (a) Elastic plane wave expansion band structures for carbon cylinders of square section in an epoxy matrix, for $f = 0.65$. (b) Width of the first two complete band gaps as a function of the filling fraction: solid line, first gap; dash-dotted line, second gap. It is noteworthy that the second complete band gap which appears for higher filling fraction is larger than the first one.

complete gap. As a function of the filling fraction, complete band gaps open up for $0.25 < f < 0.8$ with a maximum of their width around $f = 0.65$ (Fig. 3(b)). The gap widths are greater than those calculated for the cylinders of circular cross section.

The case of square cylinders rotated 45° with respect to x, y axes was also investigated. In Fig. 4(a), the band structure for $f = 0.35$ displays two complete band gaps. The third, the fifth and the sixth Z bands are quite flat. The largest gap width is $\Delta \Omega = 0.033$ in this case.

Fig. 4(b) shows that the domain of existence of complete band gaps in this structure corresponds to filling fractions in the range $0.225 < f < 0.4$. In this composite system, the gap widths are much lower than those obtained in the two preceding geometries. Let us notice that for the three geometries, the maximum gap width is obtained for $\frac{f}{f_{\max}} \simeq 0.6$ where $f_{\max}$ corresponds to the close-packing value of f.

The acoustic band structures of the carbon fiber reinforced epoxy composites are very sensitive to the cylinders' cross section as well as to the filling fraction. The existence of rather large gaps is here associated with the very large contrast between the elastic constants of the cylinders and the background, while the mass densities of these materials are of the same order of magnitude (see
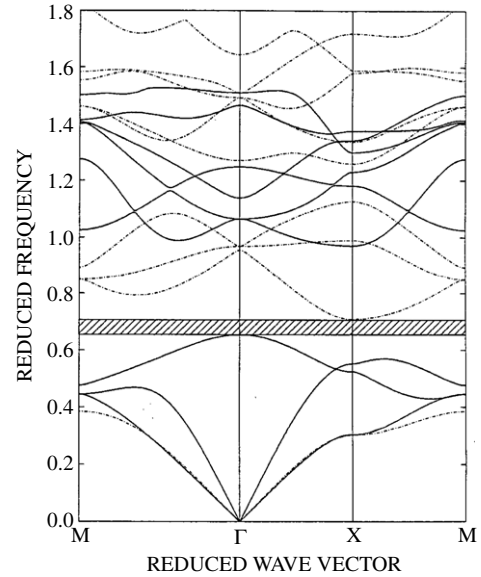
Fig. 5. Elastic plane wave expansion band structures for W cylinders in an Al matrix for $f = 0.30$. One phononic band gap appears between the third XY band and the second Z band.

Fig. 4. (a) Elastic plane wave expansion band structures for carbon cylinders of square cross section 45° rotated around the z axis, in an epoxy matrix for $f = 0.35$. (b) Width of the first two complete band gaps as a function of the filling fraction: solid line, first gap; dash-dotted line, second gap.

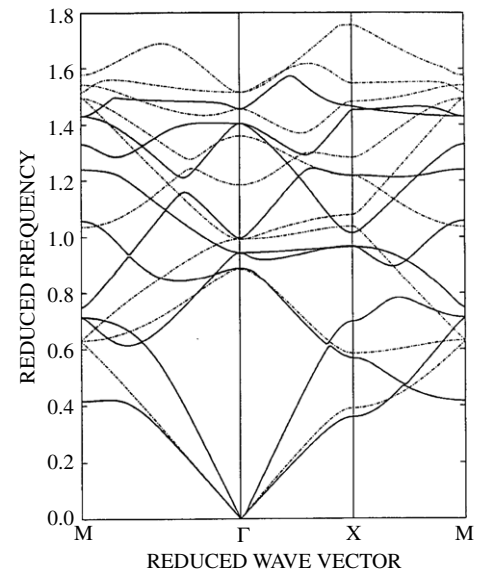**Fig. 6.** Same as in Fig. 5 for Al cylinders in a W matrix for $f = 0.30$. There is no band gap in this case.

Table 1). Notice that for these usual composite systems presenting very large complete acoustic gaps, the cylinders are made of the high velocity material.

Another composite of technological interest was also studied in the same paper [31], namely a glass fiber reinforced epoxy matrix, using a filling fraction of 0.6. Only one complete gap was found in this case, having a width smaller than that of the first gap in the carbon–epoxy composite. The glass fibers' elastic constants being approximately three times lower than those of the carbon fibers [58], the contrast between the elastic constants of the matrix and the background is in this case less important than in the carbon–epoxy system.

Finally, the case of metallic composites was also considered as a matter of comparison, where there is a contrast between both elastic constants and mass densities of the constituents whereas their velocities of sound have the same order of magnitude. W and Al are two quasi-isotropic metals presenting a large ratio between the parameters although the contrast is far from being comparable to the carbon–epoxy case (see Table 1). With a filling fraction of $f = 0.30$, Figs. 5 and 6 give the dispersion curves of W (Al) cylinders in an Al (W) background. Only one complete gap of width, $\Delta\Omega = 0.05$, was found in the first case while there is no such gap in the second case. Qualitatively similar results are also obtained for $f = 0.15$, with a smaller width of the gap than at $f = 0.30$.

These behaviors are similar to those found in Ref. [46] for the Au–Be system. We can notice that W is here the low velocity material.

2.1.2. Examples of transmission spectra

The transmission of elastic waves in two-dimensional solid composite media composed of square and centered rectangular arrays of Duralumin cylindrical inclusions in an epoxy resin matrix were investigated experimentally [32]. In these cases, the measured transmission drops to noise level throughout the frequency intervals in reasonable agreement with the forbidden frequency bands calculated with the plane wave expansion method. In parallel, other groups have studied acoustic band gaps in mixed binary two-dimensional composite materials such as Hg, oil or air cylinders in an Al matrix [50,33] or metallic rods in air [47,44,43].

As an example, we review here [60] a combined theoretical and experimental study of a triangular two-dimensional solid–solid phononic crystal that demonstrates unambiguously the existence

of absolute acoustic band gaps. The band structure for elastic waves propagating in the plane perpendicular to the cylinders and the acoustic transmission spectrum for longitudinal waves were computed with the plane wave expansion method and the finite difference time domain scheme respectively. The numerical results are compared with transmissions measured experimentally with two finite size composite samples oriented along two different directions of propagation.

We are dealing with a triangular array of steel cylinders embedded in an epoxy resin matrix. The choice of these materials is based on the strong contrast in their densities and elastic constants. The densities and the speeds of sound of steel and epoxy were measured in a short cylinder of hard resin and in a small piece of steel. The densities are $\rho^{steel} = 7780$ kg m^{-3} and $\rho^{epoxy} = 1142$ kg m^{-3}. The measured values of the speeds of sound lead to the following elastic constants (in units of 10^{10} N m^{-2}), $C_{11}^{steel} = 26.4$ and $C_{44}^{steel} = 8.1$, $C_{11}^{epoxy} = 0.754$ and $C_{44}^{epoxy} = 0.148$. Two samples of the same physical dimensions, 85 mm × 85 mm × 29 mm were manufactured. The steel cylinders have a diameter $d = 4$ mm. The periodicity of the triangular lattice is $a = 6.023$ mm. This results in a filling fraction $f = \pi d^2/2a^2\sqrt{3} = 0.4$. In order to analyze the effect of the direction of propagation on the band gaps, the first sample contains 60 scatterers arranged in such a manner that its thickness is parallel to the ΓJ direction of the triangular Brillouin zone. A second sample consists of 67 cylinders with the sample thickness along the ΓX direction. We have illustrated in Fig. 7(a) and (b) the two-dimensional cross sections of these samples. The experimental setup is based on the well known ultrasonic transmission technique which uses a couple of ultrasonic broad-band transmitter/receiver transducers with a central frequency of the order of 1 MHz and a diameter of 25 mm (Panametrics contact transducer type Videoscan $N^o V 102$). A pulser/receiver generator (Panametrics model 5052 PR) produces a short duration (about 100 ns) large amplitude (200–380 V) pulse which is applied to the transmitting transducer launching the probing longitudinal waves. The signal acquired by the receiver is post-amplified and then digitized with a maximum sampling rate of 100 MHz (or 10 ns/point) by a Lecroy digital oscilloscope. To reduce the random errors, each measurement is averaged over a sample size of 200 with the oscilloscope which performs a fast Fourier transform on the acquired signals. Both emitter and receiver are coupled to the transversal walls of the specimen using a coupling gel. The acoustic transmission spectra of Fig. 8 clearly show two forbidden bands. The first band gap appears between 120 and 270 kHz for the two directions considered. At higher frequencies, the transmission drops to noise level between 350 and 510 kHz in the direction ΓJ and 430–560 kHz in the direction ΓX. The intersection frequency domain 430–510 kHz is therefore independent of the direction of propagation. One should stress that because of the strong attenuation of the transmitted power at these high frequencies, it is quite difficult to define precisely the edges of the region with noise level transmission.

The band structure of an infinite periodic triangular lattice with the same lattice parameter and physical characteristics as the experimental samples were calculated with the plane wave expansion method depicted previously. The band structure for the *XY* modes (Fig. 9) was calculated with 1381 **G** wavevectors. This number of **G** vectors insures sufficient convergence of the Fourier series. Fig. 9 indicates the existence of two absolute band gaps extending throughout the two-dimensional triangular Brillouin zone. The first gap extends from a frequency of 124 kHz up to 276 kHz and is in very good agreement with the experiment. The second absolute gap occurs between 441 and 483 kHz and falls also in the experimental range although, for both ΓJ and ΓX directions, the transmission drops to the noise level throughout a wider range than the one predicted by the band structure. This
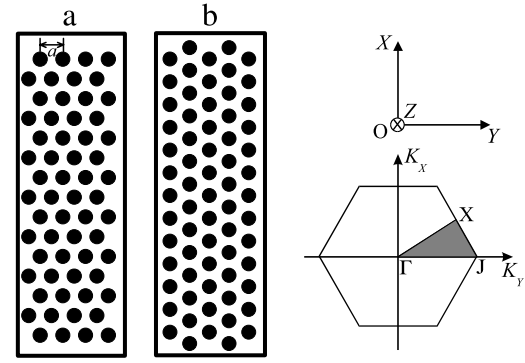

Fig. 7. Two-dimensional cross sections of the triangular array of steel cylinders embedded in an epoxy matrix. (a) The "ΓJ" sample. (b) The "ΓX" sample. The steel cylinders, of circular cross-section, are parallel to the x axis of the Cartesian coordinate system $(0, x, y, z)$. The lattice parameter a is defined as the distance between two nearest neighboring cylinders. The inset shows the irreducible Brillouin zone of the triangular array.
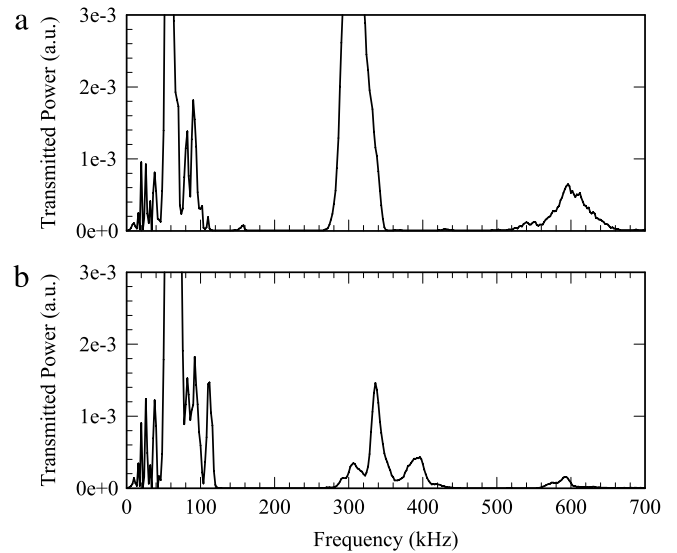
Fig. 8. Transmission power spectrum measured perpendicular to the vertical faces of the (a) "ΓJ" sample and (b) "ΓX" sample. The transmitted power is given in arbitrary units. The probing signal is a longitudinal wave.

difference can be attributed to the low level of transmission in this range of frequencies, but more especially to the fact that some eigenfrequencies of the structure may not contribute very significantly to the transmission.

To gain a better insight into these effects, and also to investigate the qualitative behavior of the transmission inside the pass bands, the finite difference time domain method was applied to calculate the transmission through two finite size samples oriented respectively along the ΓJ and ΓX directions. The calculations were limited to a strictly two-dimensional finite difference time domain scheme. The samples are composed of three adjacent regions. The probing signal corresponding to a longitudinal wave that propagates along the y direction (see Fig. 7), is launched from the first region and detected in the third one. This signal is the superposition of 5 sinusoïdal waves of frequencies 100, 250, 400, 550 and 700 kHz weighed by a Gaussian profile of full width at half maximum of 13.5 mm. Transmission of this signal through a homogeneous epoxy medium produces a broad band spectrum whose envelope resembles the experimental one. The central region contains the phononic crystal. To probe the ΓX direction, the central region with a thickness (along the y direction) of $3a\sqrt{3}$ and a width (along the x direction) of a contains
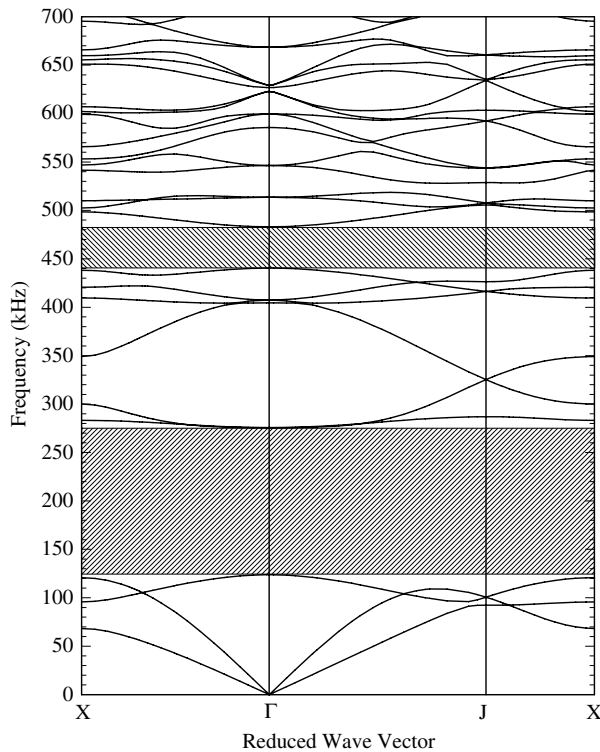
Fig. 9. Plane wave expansion results for the band structure of the two-dimensional XY modes of vibration in the periodic triangular array of steel cylinders in an epoxy resin matrix for a filling fraction $f = 0.4$. The reduced wave vector $\mathbf{k}(k_x, k_y)$ is defined as $\frac{Ka}{2\pi}$ where $\mathbf{K}$ is a two-dimensional wave vector. The points Γ, J and X are defined in the inset of Fig. 7. Absolute band gaps are represented as hatched areas.

Fig. 10. Transmission spectrum computed with the finite difference time domain method along the ΓJ direction (a) and along the ΓX direction (b) of propagation. The longitudinal component u_y of the output displacement field is given in arbitrary units.

9 cylinders. The ΓJ direction is modeled with a rectangular central region containing 8 cylinders, of thickness, $4a$, and width, $a\sqrt{3}$. Periodic boundary conditions are applied in the y direction perpendicular to the direction of propagation. Absorbing boundary conditions are imposed on the external surfaces of the first and third regions. Space and time are discretized with fine enough intervals to achieve convergence of the algorithm. Three output signals (longitudinal vibrations) are detected at different locations. The transmission spectra are calculated as the averages of their Fourier transforms.

The finite difference time domain computed spectrum in the ΓJ direction is shown in Fig. 10(a) where the longitudinal component, u_y, of the displacement field is given in arbitrary units as a function of frequency. One observes an overall agreement with the experiment. The width of the first gap is well reproduced. The shape of the second pass band as well as its width are in better accord compared to the band structure. Moreover one can notice a maximum of the transmission coefficient in the middle of the lowest pass band as well as a qualitative similarity of the theoretical and experimental transmissions at higher frequencies.

Fig. 10(b) contains the finite difference time domain results in the ΓX direction. Again, the width of the first gap and the occurrence of a maximum of transmission in the middle of the lowest pass band are in good agreement with the experiment. However some discrepancies remain when considering the location and shape of the second pass band. The finite difference time domain spectrum presents, between 260 and 400 kHz, two peaks separated by a narrow stop-band centered around 320 kHz, in accordance with the local gap in the band structure of Fig. 9. In contrast the experimental spectrum exhibits three distinct peaks, the second of maximal amplitude centered on 340 kHz. Also the second gap (430–560 kHz in Fig. 8) is located nearly 40 kHz higher
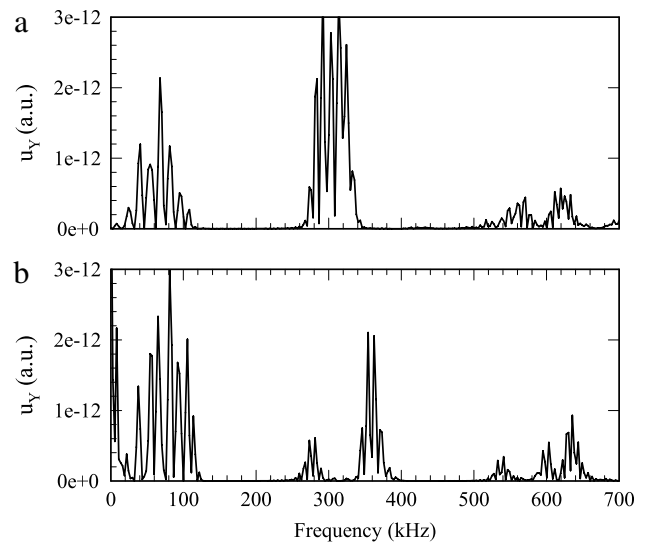
than predicted by the finite difference time domain method. At this point, it is worthwhile to notice that the measurement of sound velocities in epoxy is subject to important uncertainties (since these velocities are quite dependent on the conditions of sample preparation), and in turn the location of the higher bands in the theoretical calculations may be affected by a few tens of kHz. Therefore a detailed interpretation of the measured spectrum above 280 kHz, with a one to one correspondence between experiment and theory, does not seem possible although one may infer that there is a good correspondence between the major peak (around 340 kHz) in the measured and calculated spectra. Another point that deserves further attention concerns the divergence of the emitted acoustic signal, i.e. the fact that the input signal is not a plane wave but is composed of a set of wave vectors inside a cone around the incident direction. Therefore other modes than those considered till now in the plane wave expansion and finite difference time domain calculations can be excited, which in turn may affect the final transmission.

2.2. Fluid–fluid phononic crystals

2.2.1. An example neglecting the fluid–fluid separation solid

We present now results of elastic band structure for a geometry of two-dimensional phononic crystals: the boron-nitride-like structure in which the infinite circular elastic rods are located on the vertices of a regular hexagon and are surrounded by an elastic background [37]. The unit cell of the Bravais lattice contains two kinds of infinitely long parallel cylinders [61,62]. With two cylinders of identical radius, constituted of the same material, the graphite structure is obtained, while if the radius of one of the two cylinders is infinitely small, the widely studied triangular structure [36,28–30] is generated. In the boron-nitride structure, in addition to the contrast in densities and elastic parameters, the numerical studies show that the ratio $\alpha = R_1/R_2$ between radii of the cylinders appears as a pertinent parameter in determining the existence of acoustic band gaps.

We consider two-dimensional composite media, for which the inclusions and matrix are fluids, cylindrical inclusions being disposed on boron-nitride arrays. The physical realization of a two-dimensional fluid/fluid composite system could be achieved by inserting the inclusion material in a latex bladder. The dispersion
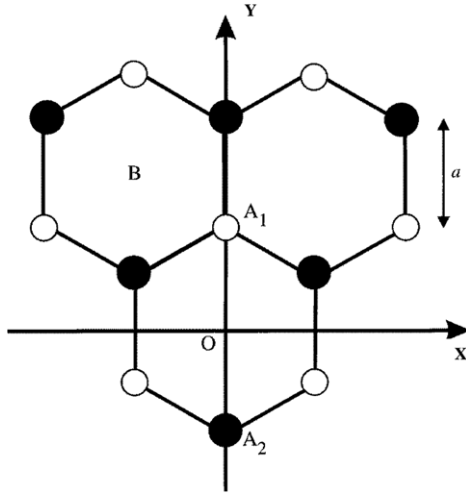
Fig. 11. Two-dimensional boron-nitride array of infinite cylinders, A_1 (white) and A_2 (black), of different radii, R_1 and R_2, periodically distributed in an infinite matrix B. The cylinders are assumed to be parallel to the z axis perpendicular to the transverse plane (xOy) and may be composed of different materials. The distance between the nearest neighbors is a. The unit cell contains one cylinder of each kind. The graphite structure is obtained for cylinders of identical radius and constituted of the same material. When only one kind of site is occupied, the two-dimensional boron-nitride array results in a triangular structure with a lattice parameter $d = a\sqrt{3}$.

curves are computed for water (resp. mercury) cylinders in a mercury (resp. water) background. These band structures will be discussed as a function of the parameter, for different values of the inclusion filling fraction f. For the practical realization of large acoustic band gaps, the graphite structure, and more generally the boron-nitride geometry, can appear as better, similar or worse than the most studied triangular structure, depending on the values of α and f and on the material parameters. In the fluid composites, the graphite structure is more favorable for mercury cylinders in a water background, both for high and low filling fractions. In the opposite case of water rods in mercury, the triangular structure gives rise to the largest band gap but the boron-nitride and graphite geometries may allow several additional gaps of similar magnitude. We show that selective noise filters could be obtained from boron-nitride arrays of cylindrical inclusions of very different radii.

In what follows, the model and the method of calculation are first briefly presented for fluid/fluid binary two-dimensional composite media. We discuss then the numerical results and draw some conclusions.

2.2.1.1. Model and method of calculation. (a) *Model.* The elastic band structures for fluid/fluid two-dimensional binary composite systems was calculated [37]. These periodic systems are modeled as arrays of infinite cylinders of circular cross section made of isotropic materials embedded in an infinite isotropic matrix B. The elastic cylinders, of radius R_i, are assumed to be parallel to the z axis of the Cartesian coordinate system ($Oxyz$) ($\mathbf{e_x}$, $\mathbf{e_y}$, $\mathbf{e_z}$ are unit vectors along the x, y, z axis, respectively). The intersections of the cylinder axes with the (xOy) transverse plane form a two dimensional periodic array which resembles the boron-nitride crystallographic structure with two kinds of cylinders, A_1 and A_2, in each unit cell. The distance between the nearest neighbors is a (see Fig. 11). The graphite structure is obtained with cylinders of identical radius and composed of the same material. The removal of one type of cylinder (A_1 or A_2) from the boron-nitride array results in a triangular array of lattice parameter $d = a\sqrt{3}$. The filling fraction f_i of the cylinder A_i, of radius R_i, is defined as the ratio between the cross-sectional area of the rod i and the surface of the unit cell, i.e. for the boron-nitride structure, $f_i =$

$(2\pi R_i{}^2)/(3\sqrt{3}a^2)$. For the graphite structure ($R_1 = R_2$), in the close packed arrangement ($R_i = a/2$), the maximum value of each f_i is $f_i{}^{max} = \pi/(6\sqrt{3}) \cong 0.302$. In the triangular pattern (with $R_1 = 0$, i.e. $f_1 = 0$ and $\alpha = R_1/R_2 = 0$, for example) the close packed value of $f_2 = f$ corresponds to $R_2 = d/2$, i.e. $f_2{}^{max} = f^{max} = \pi/(2\sqrt{3}) \cong 0.907$. One notices that the maximum filling fraction is lower in the graphite array than in the triangular structure. The propagation of elastic waves in the transverse plane was investigated. With the choice of coordinate axes shown in Fig. 11, the primitive lattice vectors for the boron-nitride structure can be written as

$$\mathbf{a_1} = \frac{a\sqrt{3}}{2}(1, \sqrt{3}), \tag{17}$$

and

$$\mathbf{a_2} = \frac{a\sqrt{3}}{2}(-1, \sqrt{3}). \tag{18}$$

The two infinite cylinders of the primitive unit cell are located at the positions

$$\mathbf{r_1} = -\mathbf{r_2} = a\sqrt{3}\left(0, \frac{1}{\sqrt{3}}\right). \tag{19}$$

The primitive vectors of the reciprocal lattice are given by

$$\mathbf{b_1} = \frac{2\pi}{a\sqrt{3}}\left(1, \frac{1}{\sqrt{3}}\right), \tag{20}$$

and

$$\mathbf{b_2} = \frac{2\pi}{a\sqrt{3}}\left(-1, \frac{1}{\sqrt{3}}\right) \tag{21}$$

and the two-dimensional reciprocal lattice vectors $\mathbf{G}$ are then

$$\mathbf{G} = h_x\mathbf{b_1} + h_y\mathbf{b_2} = \frac{2\pi}{a\sqrt{3}}\left[(h_x - h_y)\mathbf{e_x} + \frac{1}{\sqrt{3}}(h_x + h_y)\mathbf{e_y}\right] \tag{22}$$

where h_x and h_y are two integers.

(b) *Method of calculation.* The method of calculation is the plane wave method. We summarize here this method for fluid/fluid two-dimensional systems. The matrix and inclusions are composed of isotropic materials described by linear elasticity. The mass density and the elastic constants are ρ_{A_i} and C_{11A_i} ($i = 1$ or 2) inside the cylinders A_i and ρ_B and C_{11B} in the background B. These physical characteristics in the composite system, denoted ζ in a general way, are space dependent with respect to the position vector $\mathbf{r} = (x, y)$ in the transverse plane i.e. $\zeta(\mathbf{r}) = \zeta_{\mathbf{A_i}}$ in the cylinder A_i and $\zeta(\mathbf{r}) = \zeta_{\mathbf{B}}$ in the matrix B.

In the two-dimensional fluid/fluid binary composite systems, only longitudinal waves are allowed and the general equation of motion is

$$\rho(\mathbf{r})\frac{\partial^2\mathbf{u}}{\partial t^2} = \nabla(C_{11}(\mathbf{r})\nabla.\mathbf{u}). \tag{23}$$

However the displacement field $\mathbf{u}(\mathbf{r}, t)$ can be obtained from a scalar potential $\Phi(\mathbf{r}, t)$ such that $\rho\mathbf{u} = \nabla\Phi$. Then Eq. (23) may be rewritten as

$$\left(\frac{1}{C_{11}(\mathbf{r})}\right)\frac{\partial^2\Phi}{\partial t^2} = \nabla.\left(\left(\frac{1}{\rho(\mathbf{r})}\right)\nabla\Phi\right). \tag{24}$$

We must keep in mind that in fluids, C_{11} stands for the inverse of the compressibility χ of the material. Taking advantage of the two-dimensional periodicity in the (xy) plane, the quantities $\frac{1}{\rho(\mathbf{r})}$, $\frac{1}{C_{11}(\mathbf{r})}$ for fluid/fluid inhomogeneous media are developed in Fourier series in the form

$$\zeta(\mathbf{r}) = \sum_{\mathbf{G}} \zeta(\mathbf{G})\exp(i\mathbf{G.r}). \tag{25}$$

The Fourier coefficients in Eq. (25) are given as

$$\zeta(\mathbf{G}) = \zeta_B \delta_{\mathbf{G0}} + \sum_i \zeta_{A_i}(\mathbf{G}) \exp(-i\mathbf{G}.\mathbf{r_i}), \tag{26}$$

where $\mathbf{r_i}$ ($i = 1, 2$) are defined in Eq. (19), δ is the *Kronecker* symbol and

$$\zeta_{A_i}(\mathbf{G}) = (\zeta_{A_i} - \zeta_B)F_i(\mathbf{G}). \tag{27}$$

In Eq. (27), $F_i(\mathbf{G})$ stands for the structure factor of the cylinder i defined as

$$F_i(\mathbf{G}) = 2f_i \frac{J_1(GR_i)}{GR_i}, \tag{28}$$

where $J_1(x)$ is the Bessel function of the first kind of order one. After some algebra, Eq. (24) becomes the standard eigenvalue equation for which the size of the involved matrices depends on the number of $\mathbf{G}$ vectors taken into account in the Fourier series.

2.2.1.2. Numerical results for the boron-nitride structure. (a) *Two-dimensional fluid/fluid binary composite systems.* We show now band structures calculated for two-dimensional binary water/mercury composite systems with boron-nitride structure. The choice of these materials is based on the strong contrast in their densities $\rho = 1.025$ and 13.5 g cm^{-3} for respectively water and mercury and elastic properties: speeds of sound 1531 and 1450 m s^{-1} and $C_{11} = 0.2410^{10}$ and 2.8410^{10} N m^{-2} respectively. We shall compare the results on boron-nitride structures with those obtained for triangular arrays of water (resp. mercury) rods in a mercury (resp. water) background [30]. Let us remember that according to the ratio between the radii of the two cylinders in the unit cell, $\alpha = \frac{R_1}{R_2}$, the boron-nitride structure takes into account both the triangular pattern and the graphite structure. Indeed for $\alpha = 0$, one obtains a triangular array of lattice parameter $a\sqrt{3}$. While for $\alpha = 1$, the two cylinders being constituted of the same material, the graphite structure is created. The effect of the parameter α and the influence of the total filling fraction $f = f_1 + f_2$ on the band structure was investigated intensively [37].

The Fourier transform of Eq. (24) for the longitudinal modes of vibrations in two-dimensional fluid/fluid binary composite systems was worked out. In these calculations, the 169 shortest $\mathbf{G}$ vectors were taken into account. These vectors are generated in such a way that they are inscribed in a disk of a certain radius. This way of generating these vectors and this number of $\mathbf{G}$ vectors ensures sufficient convergence and offers a good compromise between accuracy and computing time. The case of water (resp. mercury) cylinders in a mercury (resp. water) background was considered. One can imagine [30] that, in practice, the liquid within the cylinders would be contained by some latex material. The mass density and speed of sound in rubber are comparable to those of water and the effect of this thin latex partition can be neglected. Moreover, it was found that for $f = 0.27$, the triangular band structure of water cylinders in a mercury background exhibits very wide gaps. In the opposite situation, i.e. a triangular pattern of mercury cylinders in a water background, they have shown the existence of band gaps for $0.45 < f < 0.825$, the maximal width of the lowest stop-band being obtained for $f = 0.75$. The dispersion curves of boron-nitride arrays of water/mercury systems were calculated for $f = f_1 + f_2 = 0.27$ and 0.6 and the evolution of the width of the gaps versus the parameter $\alpha = \frac{R_1}{R_2}$ was investigated. Let us notice that the close packed configuration of the graphite structure is obtained for $f = f_1 + f_2 \cong 0.604$.

The dispersion curves for the first ten bands in the principal symmetry directions of the first Brillouin zone (see Fig. 12) were plotted. Fig. 13(a) shows the band structure for the boron-nitride array of water cylinders in a mercury background with
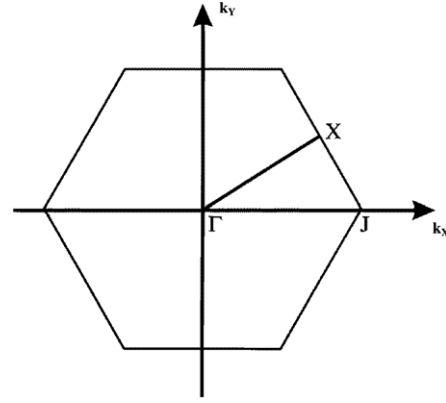
Fig. 12. First Brillouin zone of the boron-nitride array. The irreducible part of this regular hexagon is the triangle $\Gamma J X$ where the reduced coordinates ($\mathbf{k} = \frac{\mathbf{K}a\sqrt{3}}{2\pi}$, $\mathbf{K}$ being a two-dimensional wave vector) of the symmetry points Γ, J and X in the (xOy) plane are respectively $(0, 0)$, $(\frac{2}{3}, 0)$ and $(\frac{1}{2}, \frac{1}{2\sqrt{3}})$.

$f_1 + f_2 = 0.27$ and $\alpha = \frac{R_1}{R_2} = 0.5345$. The plots are given in terms of the reduced frequency $\Omega = \frac{\omega a \sqrt{3}}{2\pi \overline{c_l}}$ with

$$\overline{c_l} = \sqrt{\frac{\overline{\left(\frac{1}{\rho}\right)}}{\overline{\left(\frac{1}{C_{11}}\right)}}}, \tag{29}$$

where

$$\overline{\left(\frac{1}{\rho}\right)} = \left(\frac{1}{\rho}\right)(\mathbf{G} = \mathbf{0}) \tag{30}$$

and

$$\overline{\left(\frac{1}{C_{11}}\right)} = \left(\frac{1}{C_{11}}\right)(\mathbf{G} = \mathbf{0}) \tag{31}$$

versus the reduced Bloch wave vector $\mathbf{k} = \mathbf{K}\frac{a\sqrt{3}}{2\pi}$. There exist five acoustic band gaps in the frequency domain of Fig. 13(a), the largest appearing between the second and the third band with $\Delta\Omega \approx 0.37$. Fig. 13(b) shows the dependence of these gaps versus the parameter α for $f_1 + f_2 = 0.27$. For α varying between 0 and 1, the boron-nitride array evolves from a triangular to a graphite structure. In the range of frequency, $0 < \Omega < 2$, one very large gap appears in the band structure of the triangular pattern ($\alpha = 0$) for $0.27 < \Omega < 0.82$, i.e. $\Delta\Omega = 0.55$. This stop-band corresponds to the widest gap obtained by Kushwaha et al. (see Fig. 2 of Ref. [30]). The width of this gap decreases with increasing α and reaches its minimum value for the graphite structure ($\alpha = 1$). An interesting result is the existence of three additional gaps (second, third and sixth gaps appearing with increasing Ω) in the band structure of the boron-nitride pattern for $0.1 < \alpha < 1$. The widths of these gaps increases with increasing α and are maximal in the graphite structure. One observes also that the width of the fifth gap is maximal for $\alpha \cong 0.5$. Compared to the triangular pattern ($\alpha = 0$), the boron-nitride structure of this two-dimensional binary fluid/fluid composite system presents some large additional gaps in the same range of frequency. The narrowness of the pass bands is also remarkable in this composite. The boron-nitride band structures for this two-dimensional binary composite were also calculated for $f_1 + f_2 = 0.6$ and lead to qualitative similar conclusions although the gaps are narrower in this case. In particular, the largest gap found in the triangular band structure has a width $\Delta\Omega$ equal to 0.42.

The opposite situation was also considered, i.e. the boron-nitride array of mercury cylinders in a water background. Fig. 14(a)
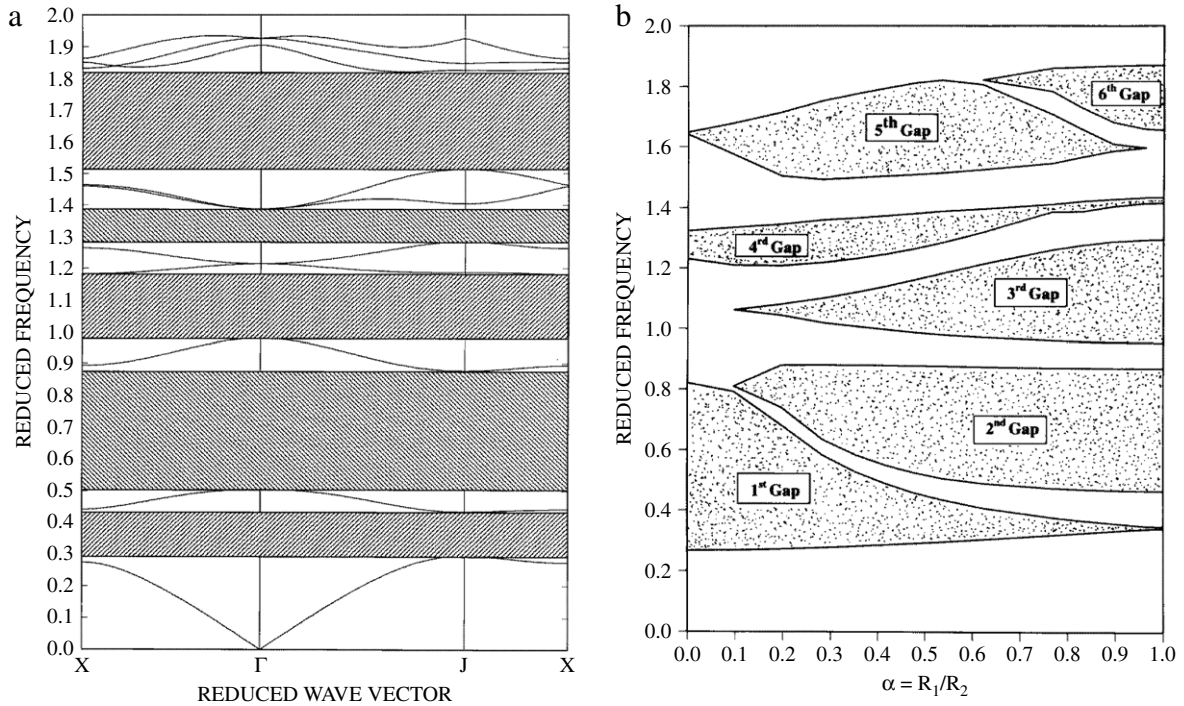
Fig. 13. (a) The plane wave expansion elastic band structure for the boron-nitride array of water cylinders in a mercury background for $f_1 + f_2 = 0.27$ and $\alpha = R_1/R_2 = 0.5345$ (f_i and R_i, $i = 1$ or 2, are respectively the filling fraction and the radius of the two cylinders in the unit cell). The band structure is plotted for the longitudinal modes of vibration in the three high symmetry directions ΓJX of the first Brillouin zone (see Fig. 12). One can notice five gaps in the range of frequency $0 < \Omega < 1.9$. (b) Variation of the width of the gaps appearing in the band structure of the boron-nitride array of water cylinders in a mercury background, for $f_1 + f_2 = 0.27$, as a function of the parameter $\alpha = R_1/R_2$.
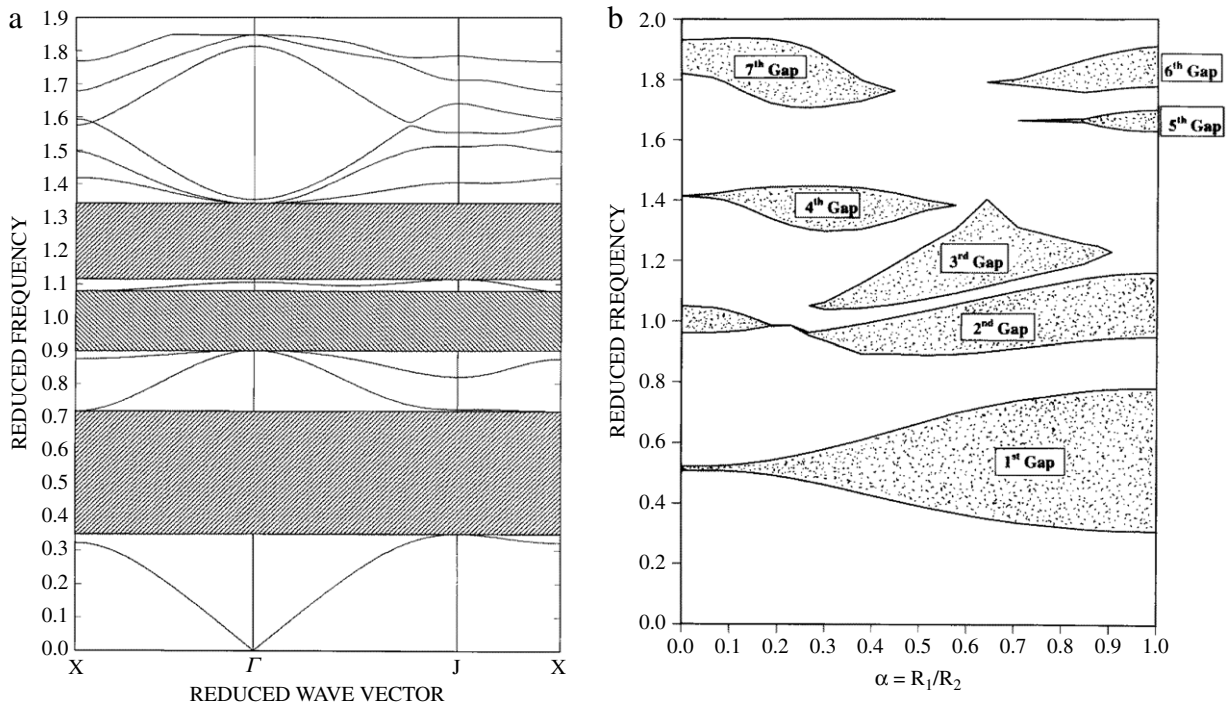
Fig. 14. (a) The plane wave expansion elastic band structure for the boron-nitride array of mercury cylinders in a water background for $f_1 + f_2 = 0.60$ and $\alpha = R_1/R_2 = 0.642$. One can notice three gaps in the range of frequency $0 < \Omega < 1.9$. (b) Variation of the width of the gaps appearing in the band structure of the boron-nitride array of mercury cylinders in a water background, for $f_1 + f_2 = 0.60$, as a function of the parameter $\alpha = R_1/R_2$.

shows the band structure in this case for $f_1 + f_2 = 0.6$ and $\alpha = 0.642$. Three gaps exist in Fig. 14(a), the largest appearing between the first and the second band with $\Delta\Omega \approx 0.368$. Fig. 14(b) shows the width of the gaps versus the parameter α for $f_1 +$

$f_2 = 0.6$ in the range of frequency, $0 < \Omega < 2$. For $\alpha = 0$, the second gap centered on $\Omega = 1$ with a width $\Delta\Omega \cong 0.1$, corresponds to the one observed by Kushwaha et al. (see Fig. 2 of Ref. [30]) in the triangular lattice. One observes that the third

gap (with increasing Ω) exists only in the boron-nitride structure for $0.25 < \alpha < 0.9$ and reaches its maximal width around $\alpha \cong 0.65$. The largest gap is obtained for $\alpha = 1$ between the first and the second band (see Fig. 14(a)). For $f_1 + f_2 = 0.6$, the graphite structure ($\alpha = 1$) is very near to the close-packed configuration for which $f_1 + f_2 = 0.604$ and where each cylinder is in contact with another. The technical realization of this structure would probably be very difficult because the background material separating two cylinders becomes very thin. However the contact between cylinders can be avoided by using the boron-nitride geometry with α quite different from 1, even for this maximum filling fraction. These results reveal that for mercury cylinders in a water background, the general boron-nitride structure and in particular the graphite pattern is more favorable for the opening of large gaps in the band structure while the triangular structure is less appropriate. Moreover, for high filling fraction, the choice of cylindrical inclusions of different diameters allows an easier technical manufacturing together with the possibility of keeping large absolute band gaps. It is noteworthy that for $f_1 + f_2 = 0.6$, the graphite band structure of mercury cylinders in a water background presents some similarities with the triangular band structure of water circular rods in a mercury matrix, especially for the dispersion of the low frequency bands. Following the observations of Cassagne et al. [62] on photonic crystals, this can be understood from the disposition of the cylinders in the graphite structure. From a geometric point of view, in the close-packed arrangement, the graphite array of mercury cylinders in a water background is equivalent to a triangular structure of lattice parameter $a\sqrt{3}$ composed of water rods with non-circular cross section embedded in a mercury matrix.

In order to investigate the effect of the filling fraction on the band structure, the dispersion curves for the boron-nitride array of mercury cylinders in a water background was also calculated for $f_1 + f_2 = 0.30$. There is no gap in the triangular band structure while the graphite pattern gives rise to a single gap between the first and the second band with $\Delta\Omega \simeq 0.142$. One can notice that the density of mercury is greater than that of water while the speeds of sound in these materials are nearly the same. One can think that, for any value of the total filling fraction, in two-dimensional binary fluid/fluid composite systems, the largest acoustic band gaps appear for triangular structures of low density inclusions in a high density background or for a graphite array of high density rods in a low density matrix. This result parallels those of Cassagne et al. [62] for photonic crystals. These authors have shown that the largest photonic absolute band gaps appear for a triangular structure of cylindrical holes in a dielectric or for graphite structures of dielectric rods in air. This is easily understandable by the analogy between Maxwell's equations and those of linear elasticity in fluids. For α quite different from 0 to 1, the boron-nitride array gives rise to additional large gaps in the same range of frequency.

(b) *Two-dimensional solid/solid binary composite systems.* It was shown that the acoustic band structure of a square array of carbon fibres embedded in an epoxy matrix exhibits large absolute band gaps; the widest gaps being obtained for a filling fraction $f = 0.55$ (see figure 2(b) of reference [31]). In complement to this work, we have calculated the dispersion curves for triangular arrays of carbon rods in an epoxy background considering various filling fractions. With this pattern, the widest gap was obtained for $f = 0.65$. Its width is 1.7 times larger than the one obtained for the square array [27]. In this case, the triangular structure is more favorable than the square pattern for the opening of absolute gaps in the acoustic band structure of a two-dimensional binary solid/solid composite material. This observation is in agreement with previous results obtained independently by Sigalas et al. [28] and Kushwaha et al. [29] for other constituents of the two-dimensional inhomogeneous material.

Now, we extend our investigation to two-dimensional composite materials of boron-nitride structure, the constituent materials being C (or W) and epoxy. Both cases of high and low filling fractions of the inclusions will be considered, namely we shall assume either $f_1 + f_2 = 0.6$ (which is the nearest value to 0.65 available in a boron-nitride structure) or $f_1 + f_2 = 0.3$ and discuss the behavior of the acoustic band gaps versus the parameter $\alpha = R_1/R_2$.

The calculation is performed by solving numerically the Fourier transforms of Eqs. (24) and (25) for the *XY* and *Z* modes of vibrations taking into account the 169 shortest **G** vectors. The plots are given in terms of the reduced frequency $\Omega = \frac{\omega a \sqrt{3}}{2\pi c_0}$ (with $c_0 = \sqrt{\overline{C_{44}}/\overline{\rho}}$ where $\overline{C_{44}} = c_{44}$ and $\overline{\rho} = \rho\,(\mathbf{G} = 0)$) versus the reduced Bloch wave-vector $\mathbf{k} = \mathbf{K}\frac{a\sqrt{3}}{2\pi}$.

Let us first consider the filling fraction $f_1 + f_2 = 0.6$. Fig. 15(a) presents the first ten *Z* and *XY* acoustic bands when the ratio between the radii of the two cylinders in the boron-nitride structure is given by $\alpha = 0.186$. One can observe that there are five complete band gaps in this band structure, the largest appearing between the third *XY* band and the second *Z* band with $\Delta\Omega = 0.048$. The presence of nearly flat bands such as the second or the fourth *Z* bands may indicate the existence of localized states in this structure. The effect of the parameter α on the band structure is investigated in Fig. 15(b) where we have superimposed the variations of the width of the *Z* (dashed lines) and *XY* (solid lines) band gaps versus the parameter α for $f_1 + f_2 = 0.6$. Numerous wide *Z* gaps appear for $0 \leq \alpha \leq 0.5$. The existence of a large *XY* gap, between the third and the fourth *XY* bands, see Fig. 15(a) for $0.33 \leq \Omega \leq 0.57$, gives rise to three absolute band gaps where the propagation of acoustic waves of any polarization is forbidden. These absolute gaps are represented as speckled areas in Fig. 15(b). One can notice that the second absolute band gap which opens for $0.4 \leq \Omega \leq 0.5$ exists only in the boron-nitride structure with $0.13 \leq \alpha \leq 0.45$. The maximum width of this gap, obtained for $\alpha \approx 0.3$, is of the same order of magnitude as the largest gap observed in the triangular structure. One can imagine for this kind of composite material engineering applications such as very selective acoustic filters. There is no absolute band gap in the graphite band structure i.e. for $\alpha = 1$. This result shows that the contrast between the diameters of the two cylinders plays an important role in determining acoustic band gaps.

We have also investigated the inverse situation i.e. the boron-nitride array of epoxy cylinders in a carbon background for $f_1 + f_2 = 0.6$. As can be observed in Fig. 16, absolute band gaps appear in this band structure for $0.4 \leq \alpha \leq 1$. The largest absolute gap, centered on $\Omega = 0.45$, is obtained in the graphite structure with $\Delta\Omega \equiv 0.07$. For small α, most of the *Z* and *XY* gaps are very narrow except the first *Z* gap. For α close to 1, there exist some large *Z* gaps. It is noticeable that in the case of square arrays of epoxy cylinders in a carbon matrix, the band structure does not present absolute band gaps [31]. We deduce that, for such a high filling fraction, the existence of band gaps is more favored in a triangular array of inclusions having a density and elastic constants greater than those of the matrix. If the background is the component of greater density and elastic constants, the graphite structure is more appropriate. Similar studies were performed for boron-nitride arrays of W (resp. epoxy) cylinders in an epoxy (resp. W) background for $f_1 + f_2 = 0.6$. Large absolute band gaps were obtained for boron-nitride arrays of W cylinders in an epoxy background with $0 \leq \alpha \leq 0.65$ as well as for boron-nitride arrays of epoxy cylinders in a W background with $0.30 \leq \alpha \leq 0.1$, the largest gaps being observed for the triangular structure in the first case and for the graphite geometry in the second case. The absolute band gaps in composite materials made of W and epoxy are larger than those observed in C-epoxy boron-nitride structures. This result can be explained by the contrast between the densities of W and C (see Table 1).
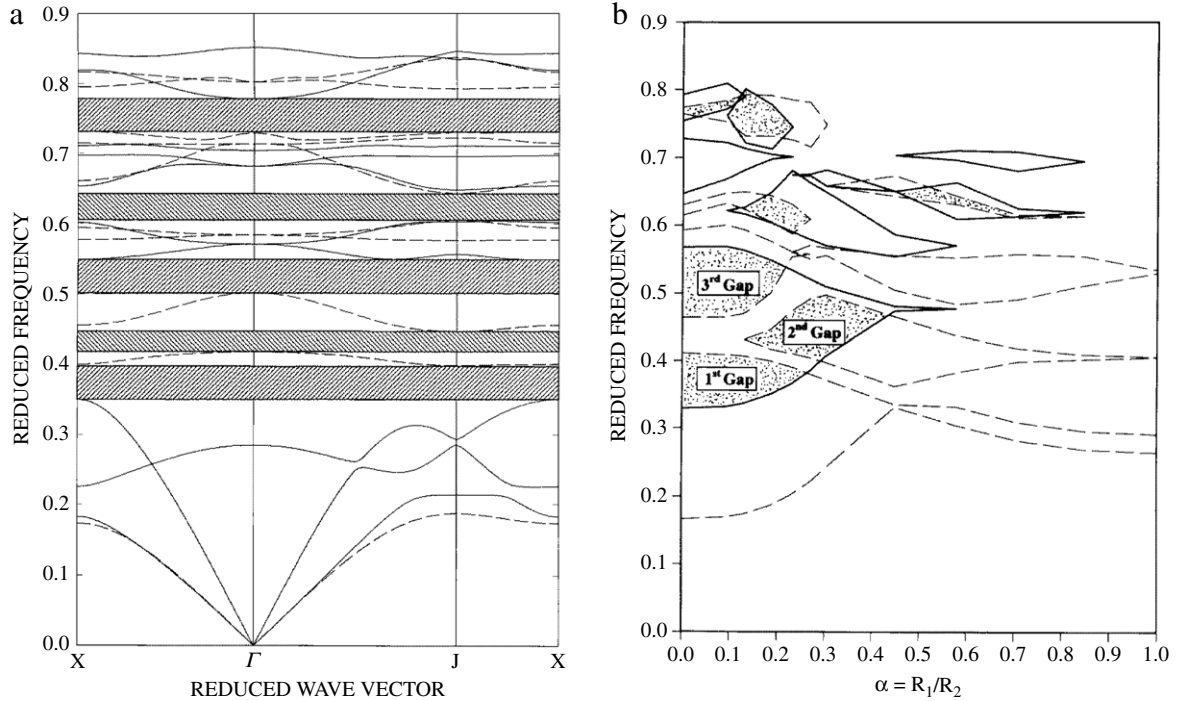
Fig. 15. (a) The plane wave expansion elastic band structure for a boron-nitride array of C cylinders in an epoxy resin matrix for $f_1 + f_2 = 0.6$ and $\alpha = \frac{R_1}{R_2} = 0.186$. The band structure is plotted for Z (dashed lines) and XY (solid lines) modes of vibration in the three high symmetry directions ΓJX of the first Brillouin zone (see Fig. 12). One can notice five complete band gaps in the range of frequency $0 \leq \Omega \leq 0.9$. (b) Variation of the width of the Z (dashed lines) and XY (solid lines) gaps appearing in the band structure of the boron-nitride arrays of carbon cylinders in an epoxy background, for $f_1 + f_2 = 0.6$, as a function of the parameter $\alpha = \frac{R_1}{R_2}$. Each couple of dashed lines (resp. solid lines) represents the variation of the lower and upper frequencies for each Z (resp. XY) gap as a function of α. The overlap of the Z and XY gaps results in absolute band gaps represented as speckled areas in this figure.
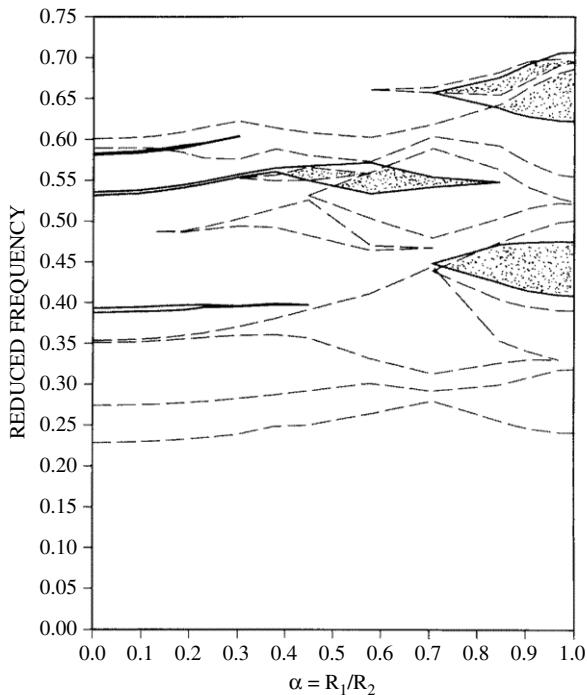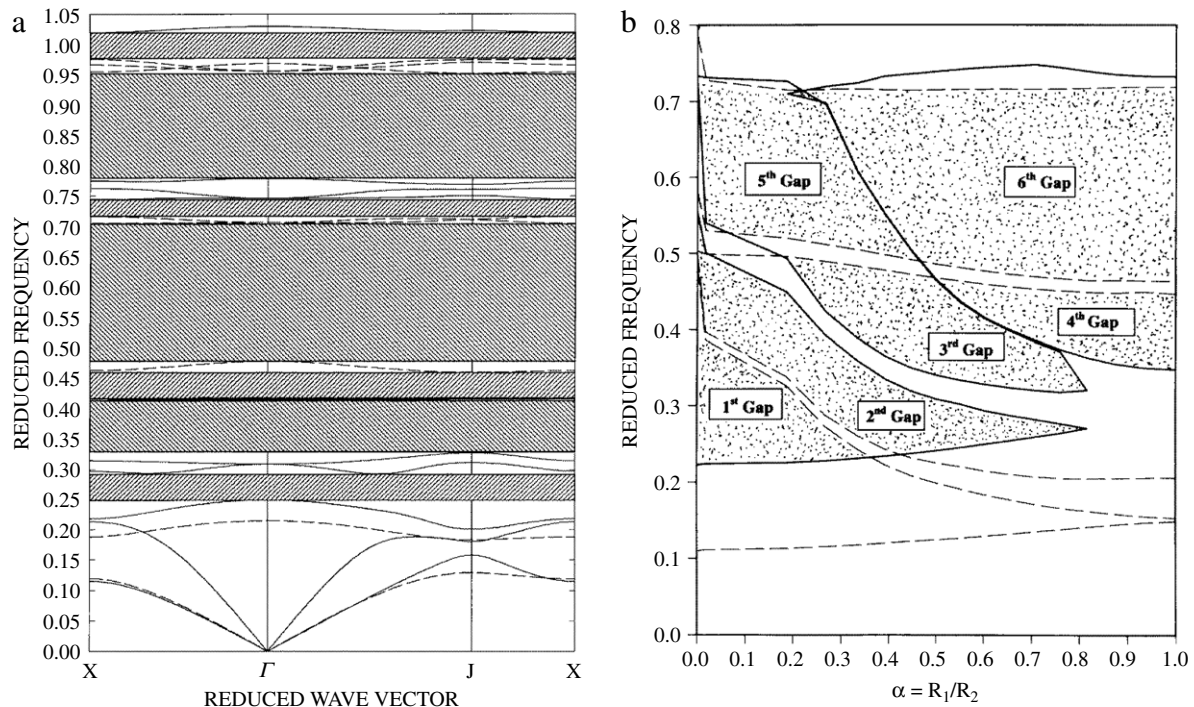

Fig. 16. Variation of the width of the Z (dashed lines) and XY (solid lines) gaps appearing in the band structure of the boron-nitride arrays of epoxy cylinders in a carbon background, for $f_1 + f_2 = 0.6$, as a function of the parameter $\alpha = \frac{R_1}{R_2}$. The absolute band gaps are represented as speckled areas in this figure.

It is noteworthy that for this filling fraction, $f_1 + f_2 = 0.6$, the first few dispersion curves in the graphite band structure of the epoxy/C (or W) system show some similarities with the corresponding curves in the triangular band structure of C (or W)/epoxy composite. A similar observation was made above for two-dimensional binary fluid/fluid composites in relation to the results obtained in photonic crystals [61,62]. Finally we would emphasize that at such a high filling fraction near to the close packed arrangement in the graphite structure, the boron-nitride geometry offers the possibility of avoiding the contact between the cylinders together with the existence of large absolute band gaps.

We now come to consider the case of a low filling fraction such as $f_1 + f_2 = 0.3$. In this case, there is no absolute band gaps in the boron-nitride arrays of epoxy fibers in a C or W background. Absolute gaps were obtained for composites made of C or W fibers in epoxy, the widths of these gaps being much larger for W fibers than with C inclusions. Fig. 17(a) shows the first Z and XY acoustic bands, in the range of frequency $0 \leq \Omega \leq 0.5$, for the boron-nitride array of W cylinders in an epoxy matrix with $f_1 + f_2 = 0.3$ and $\alpha = \frac{R_1}{R_2} = 0.603$. There are seven absolute gaps in this band structure; the largest appearing between the third and the fourth Z bands with $\Delta\Omega = 0.228$. Most of the Z and XY bands, especially those at high frequencies, are very flat. The fourth and the fifth absolute gaps are very much larger than those obtained in Fig. 15(a). In Fig. 17(b), we present the dependence of the Z and XY gaps in the band structure of W/epoxy boron-nitride arrays versus the parameter $\alpha = \frac{R_1}{R_2}$ for $0 \leq \Omega \leq 0.8$. The width of the first absolute band gap is maximum for $\alpha = 0$, strongly depresses for α slightly different from zero and then reaches its minimum value for $\alpha \cong 0.8$. One observes that a very large Z gap exists for all values of α, for $0.5 \leq \Omega \leq 0.7$. This gap appears between the third and the fourth Z bands in the band structure, see Fig. 17(a) and the maximum of its width occurs for $\alpha = 1$. For $0.25 \leq \alpha \leq 0.75$ and $0.4 \leq \Omega \leq 0.7$, the upper limit of the second XY gap and the lower limit of the third XY gap merge together. These two gaps are delimited by the sixth XY band, see Fig. 17(a) which is strictly

Fig. 17. (a) The plane wave expansion elastic band structure for a boron-nitride array of tungsten cylinders in an epoxy resin matrix for $f_1 + f_2 = 0.3$ and $\alpha = \frac{R_1}{R_2} = 0.603$. The band structure is plotted with the same conventions as in Fig. 15(a). One can notice seven complete band gaps in the range of frequency $0 \leq \Omega \leq 1.05$. (b) Variation of the width of the Z (dashed lines) and XY (solid lines) gaps appearing in the band structure of the boron-nitride array of tungsten cylinders in an epoxy background, for $f_1 + f_2 = 0.3$, as a function of the parameter $\alpha = \frac{R_1}{R_2}$ for $0 \leq \Omega \leq 0.8$. The absolute band gaps are represented as speckled areas.

flat for these values of α and Ω. The first and the sixth absolute band gaps (of maximum width for $\alpha = 1$) have widths of the same order of magnitude ($\Delta\Omega = 0.26$ for the first and $\Delta\Omega = 0.244$ for the sixth). One observes also that the third absolute band gap which opens for $0.35 \leq \Omega \leq 0.5$ exists only when the boron-nitride structure with $0 \leq \alpha \leq 0.80$ reaches its maximum width for $\alpha = 0.5$. For $f_1 + f_2 = 0.3$, the boron-nitride array of W cylinders in an epoxy matrix is a good candidate for the opening of absolute band gaps with a configuration far from the close packed arrangement.

### 2.3. Solid–fluid (mixed) phononic crystals

We consider a square array of copper cylinders in an air background. The design of such mixed composites presents several difficulties. Theoretically traditional approaches such as the plane wave expansion method fail to predict accurately the acoustic band structures for such a mixed system. This drawback can be alleviated by imposing the condition of elastic rigidity to the solid inclusions [41,42,45]. Within this condition the solid is effectively treated as a fluid. Surprisingly this assumption works reasonably well but does not account for the chemical nature (Cu, steel, W, etc.) of the solid nor the geometrical differences such as filled or hollow inclusions. Here we compare the approximate plane wave expansion band structure with the transmission coefficients calculated with the finite difference time domain method. The finite difference time domain method enables us to differentiate between filled and hollow inclusions. Finally the predictions of finite difference time domain transmission spectra through finite size Cu/air media and the plane wave expansion band structure are compared to experimental measurements. We demonstrate that filled and hollow Cu inclusions produce very similar sound transmissions suggesting the possibility of realizing light, effective sonic insulators [48].

This subsection is organized as follows. We present briefly first the various theoretical approaches used to analyze the band structure and the transmission of two-dimensional Cu/air mixed composites. The next subsubsection contains the plane wave expansion and finite difference time domain theoretical results, the experimental transmission as well as critical comparisons of the different methods. The conclusions of this subsection are drawn at the end.

2.3.1. Models and methods

2.3.1.1. Model of two-dimensional phononic crystals. The geometry of the two-dimensional phononic crystal is referred to the (O, x, y, z) Cartesian coordinates system. The two-dimensional phononic crystal comprises usually parallel inclusions infinite along the z direction and arranged periodically in the xy plane. We investigate square arrays (lattice parameter, a) of cylinders of circular cross-section. Filled cylinders are characterized by the radius of their cross-section, R. Hollow cylinders or tubes are defined by their thickness δ and inner radius, R_i. The filling factor is $\pi \frac{R^2}{a^2}$ for filled inclusions and $\pi \frac{\delta(\delta + 2R_i)}{a^2}$ for hollow cylinders. The geometry of the square arrays is illustrated in Fig. 18(a) and (b). For the sake of simplicity, all constituent materials are assumed to be elastically isotropic.

2.3.1.2. Plane wave expansion method and band structure. In the most general case of wave propagation in a solid/solid periodic two-dimensional inhomogeneous medium, one makes the assumption that the wave propagation is limited to the xy plane perpendicular to the cylinders. This has the effect of decoupling the elastic displacements in the xy plane (called XY or mixed-polarization modes) and those parallel to the z direction denoted Z modes (transverse modes) [9,37], see Section 2.1.1.1. Since two-dimensional fluid/fluid phononic crystals can support only longitudinal acoustic waves, there is no need to decouple the different
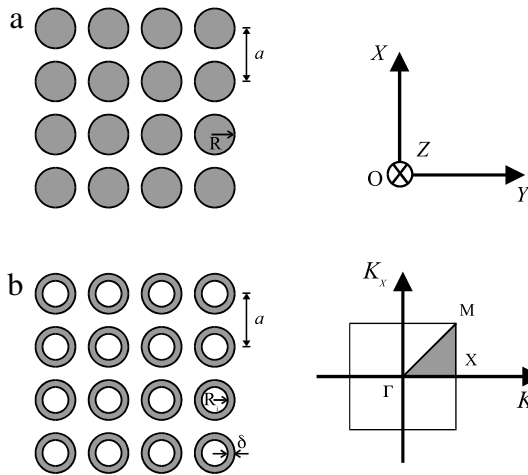
Fig. 18. Two-dimensional cross sections of the square array of circular (a) filled Cu cylinders of radius R, and (b) hollow Cu tubes of inner radius R_i and thickness δ, in air. The Cu cylinders are parallel to the z axis of the Cartesian coordinate system $(0, x, y, z)$. The lattice parameter a is defined as the distance between two nearest neighboring cylinders. The inset shows the two-dimensional irreducible Brillouin zone of the square array. $\mathbf{K}(K_x, K_y)$ is a two-dimensional wave vector.

Fig. 19. Plane wave expansion results for the band structure of the longitudinal modes of vibration in the periodic square array of Cu filled cylinders in air. The radius of the cylinders is $R = 14$ mm and the lattice parameter is $a = 30$ mm. The points Γ, X and M are defined in the inset of Fig. 18. The density ρ and the longitudinal c_ℓ and transverse c_t speeds of sound in air and Cu are $\rho^{Air} = 1.3$ kg m^{-3}, $c_\ell^{Air} = 340$ m s^{-1}, and $\rho^{Cu} = 8950$ kg m^{-3}, $c_\ell^{Cu} = 4330$ m s^{-1}, $c_t^{Cu} = 2900$ m s^{-1}. Absolute band gaps are represented as hatched areas.
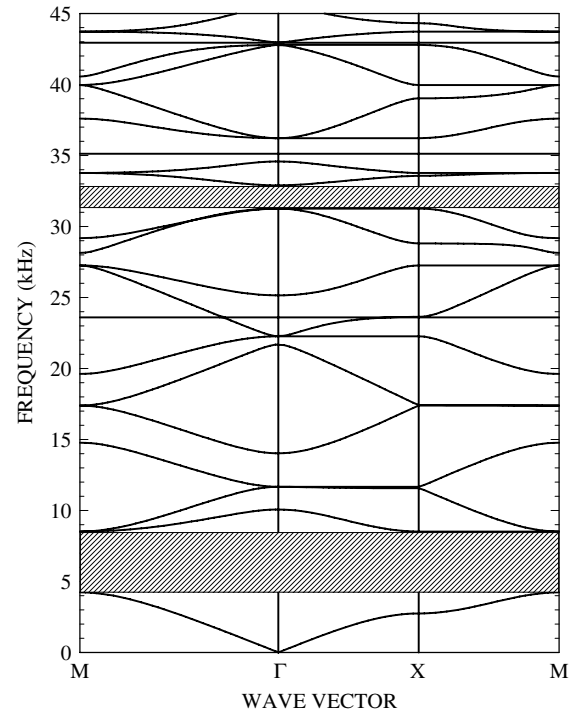
modes and the problem of propagation in the composite is much simpler than for solids [37]. In the plane wave expansion method, numerical difficulties arise when considering mixed solid/fluid composites. While the equations of motion for solid/fluid composites are the same as for solid/solid systems, taking naively the transverse velocity of sound in the fluid equal to 0 results in convergence problems [63,64]. To resolve this difficulty we can make the solid part of the composite, rigid by assuming that its compressibility and its density are infinite. On the practical side, we replace the solid by a fluid with equivalent longitudinal speed of sound and density. In comparison to air, this solid is nearly rigid. This simplifying assumption is well justified for the metallic inclusions (for example, Cu) in air [42,45]. It is, however incapable of differentiating between different metals and filled versus hollow inclusions since the sound waves do not penetrate the inclusions.

2.3.1.3. Finite difference time domain method and transmission coefficient. This method has been already presented in Section 2.1.2. In this section, we consider as the incoming signal a sinusoidal wave of pulsation ω_0 weighted by a Gaussian profile and propagating along the y direction. In Fourier space this signal varies smoothly and weakly in the interval $(0, \omega_0)$. The input signal amplitude does not depend on x. The Fourier transform of that signal normalized to the Fourier transform of a signal propagating through homogeneous material of the same nature as the matrix yields a transmission coefficient.

2.3.2. Results

2.3.2.1. Band structure. Fig. 19 presents the band structure calculated with the plane wave expansion method for a phononic crystal composed of a two-dimensional periodic square array of Cu cylinders of radius $R = 14$ mm in air. The lattice parameter is $a = 30$ mm. Calculations were performed considering filled cylinders made of Cu assumed as an infinitely rigid solid.

The choice of 1089 **G** vectors of the reciprocal lattice for the computation ensures convergence of the eigenvalues over the range of frequencies studied i.e. 0–45 kHz. Fig. 19 shows unambiguously the existence of absolute stop bands i.e. band gaps independent of the direction of propagation. The largest observed absolute band gap appears between the first and the second band and extends from 4.2 to 8.4 kHz which lies in the audible range of frequencies. When considering waves propagating

in the ΓX direction of the irreducible two-dimensional Brillouin zone, the lower bound of the local gap occurs at, approximately, 2.8 kHz. Other local gaps appear at higher frequencies in the directions of propagation ΓX and ΓM. One also notes in both directions of propagation, the existence of relatively flat bands in the band structure. These flat bands are usually associated with the existence of localized states in the composite material [9].

2.3.2.2. Computed transmission coefficients. In Fig. 20(a) and (b), the computed finite difference time domain transmission coefficients through the two-dimensional square array of filled Cu cylinders in air along the two principal directions of propagation are presented. These transmission spectra were obtained numerically by solving the equations of motion over 2^{22} time integration steps with each time step lasting 4 ns. The finite difference time domain samples contain 6 cylindrical inclusions along the y direction of propagation. The space is discretized in both x and y directions with a mesh interval of 10^{-4} m. The location and the width of the first absolute band gap in both directions of propagation compare very well with those observed in the band structure of Fig. 19. At higher frequencies, the location of the local gaps in the ΓX direction overlap in the finite difference time domain spectrum and in the plane wave expansion band structure. Moreover one notes that the flat bands observed in the dispersion curves do not contribute significantly to the transmission. Along the ΓM direction, the finite difference time domain transmission spectrum and the plane wave expansion band structure lead to rather different results. For instance a local gap occurs in Fig. 20(b) between 12 and 14 kHz while longitudinal vibrational modes exist in Fig. 19 in this range of frequency. It appears that some of the vibrational modes observed in the plane wave expansion dispersion curves do not contribute to the transmission as displayed in the finite difference time domain transmission spectrum. These bands are named 'deaf bands'
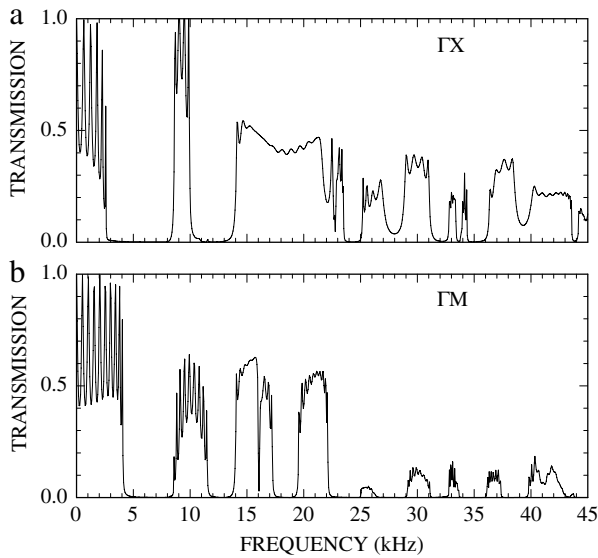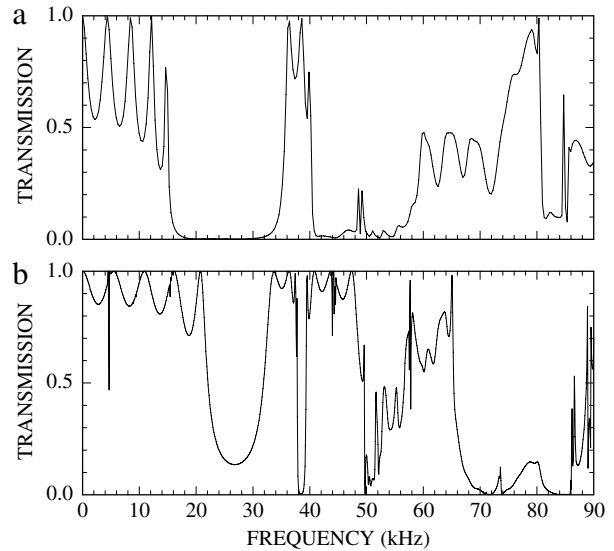
Fig. 20. Transmission coefficient through the square array of filled Cu cylinders in air, computed with the finite difference time domain method along the directions of propagation (a) ΓX and (b) ΓM.
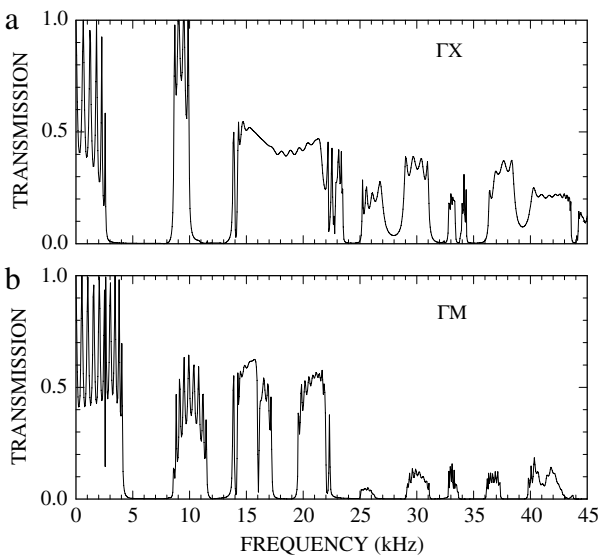
Fig. 21. Same as Fig. 20 but for the square array of Cu tubes of inner radius $R_i = 13$ mm and thickness $\delta = 1$ mm. Air occupies the interior as well as the exterior of the hollow cylinder.

because they cannot be excited by a longitudinal incident wave as can be observed from a detailed analysis of the eigenvectors associated to these vibration modes. In both directions of propagation, one also observes the decreasing of the amplitude of the transmitted computed signal for increasing frequencies.

In contrast to the plane wave expansion method, the two-dimensional finite difference time domain scheme allows one to distinguish between hollow inclusions and filled cylinders. We have then computed the transmission coefficients along the ΓX and ΓM directions of propagation through a square array of Cu tubes of inner radius $R_i = 13$ mm and of thickness $\delta = 1$ mm. The lattice parameter is the same as previously and the computations were done under the same numerical conditions as those of Fig. 20(a) and (b). In particular, with the mesh interval of 10^{-4} m the thickness of the tubes corresponds to 10 spatial discretization points. Fig. 21(a) and (b) present the variation of the computed transmission coefficient as a function of frequency in the direction
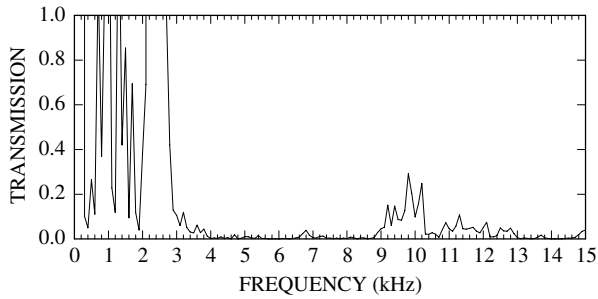

Fig. 22. Transmission coefficient through a square array ($a = 30$ mm) of Cu cylinders in water, computed with the finite difference time domain method along the ΓX direction of propagation for (a) filled cylinders ($R = 14$ mm) and (b) hollow tubes ($R_i = 13$ mm and $\delta = 1$ mm). The density and the longitudinal speed of sound in water are $\rho = 1000$ kg m^{-3} and $c_\ell = 1490$ m s^{-1}. Water occupies the interior as well as the exterior of the hollow cylinder.

ΓX and ΓM respectively, in the range of frequency 0–45 kHz. Except for very slight differences these spectra are surprisingly similar to those obtained with filled cylinders of the same outer radius i.e. $R = 14$ mm (see Fig. 20(a) and (b)). This shows that in this range of frequencies where the thickness of the tubes is very much lower than the wavelength of sound and for constituent materials with extremely different physical characteristics such as Cu and air, the thickness of the inclusions does not affect the transmission of acoustic waves through two-dimensional phononic materials. This theoretical observation agrees with previous experimental results on the transmission of acoustic waves of audible frequencies through square and triangular arrays of hollow and filled stainless steel cylinders in air [47]. However this conclusion is quite dependent upon the choice of the materials constituting the phononic crystal. Therefore, we have considered the case of two-dimensional phononic crystals made of materials whose physical characteristics exhibit a lower contrast. More specifically, a lower contrast can be obtained by replacing air by water in the two-dimensional phononic band gap material previously studied. Fig. 22 shows the finite difference time domain transmission spectra along the ΓX direction of propagation for a square array of filled Cu cylinders immersed in water, see Fig. 22(a), or hollow Cu inclusions surrounded and filled with water, see Fig. 22(b). The geometrical parameters were the same as previously i.e. a lattice parameter $a = 30$ mm, radius $R = 14$ mm for the filled inclusions and an inner radius $R_i = 13$ mm, and a thickness $\delta = 1$ mm for the tubes. Both spectra have been computed with the same numerical conditions and especially with 5 cylinders along the Y direction. These spectra exhibit significant differences in the range of frequencies 0–90 kHz. On the one hand, Fig. 22(a) shows a very large gap of width 18 kHz centered on 25 kHz while in Fig. 22(b) the transmission just depresses around this frequency. The width of this dip is also smaller than that of the gap observed in Fig. 22(a). On the other hand, at higher frequencies, the transmission spectra are completely different. For example, a gap occurs around 45 kHz in Fig. 22(a) while the transmission for hollow inclusions is maximal in this range of frequencies.

Another noticeable difference between the two spectra lies in the existence of a zero of transmission at a frequency of 38 kHz

Fig. 23. Transmission coefficient measured perpendicular to the vertical faces of the sample made of 10×10 Cu tubes ($R_i = 13$ mm and $\delta = 1$ mm) arranged periodically on a square lattice ($a = 30$ mm).

in Fig. 22(b). The mid-frequency of this small gap depends on the thickness of the hollow cylinders. Indeed a more detailed study shows that the zero transmission frequency may be shifted by changing the thickness of the inclusion. These calculations demonstrate clearly that in the peculiar case of a Cu/water composite material, the transmission coefficient of acoustic waves is very sensitive to the thickness of the hollow metallic inclusion.

2.3.2.3. Experimental results. In order to test the theoretical predictions, we have manufactured a phononic crystal composed of a 10×10 square array of hollow Cu cylinders. The physical characteristics of the composite material were those considered in previous sections i.e. an inner radius of the tubes $R_i = 13$ mm, a thickness of the hollow inclusions $\delta = 1$ mm and a period of the square lattice $a = 30$ mm. With this geometry, the filling factor of metallic inclusions is 0.094. It is worth noting that a similar structure built out of filled Cu cylinders would possess a filling factor of 0.684. The tubes of length 450 mm are embedded at one end into a thick steel plate with the other end remaining free. A speaker connected to a low frequency generator and a microphone are employed to produce an incoming signal and record the transmitted one. The transmitted signal is detected by a tracking generator coupled to a spectrum analyzer. The speaker and the microphone are located 40 mm away from the sample faces. Two measurements are conducted with and without the sample. The difference between the Fourier transforms of both temporal signals is calculated to subtract any background effect. Transmission was measured for acoustic waves in the audible frequency range, perpendicularly to the vertical faces of the sample i.e. along the ΓX direction of propagation. The measured acoustic transmission coefficient of Fig. 23 clearly shows one forbidden band between 4 and 8.8 kHz. The width of this forbidden band is slightly lower than that obtained theoretically from the plane wave expansion method and the two-dimensional finite difference time domain scheme (see Figs. 19, 20(a) and 21(a)). On the other hand, the lower and upper edges of the experimental gap appear at frequencies slightly higher than the predicted ones. This discrepancy between measurements and theoretical predictions may be attributed to the divergence of the emitted acoustic signal, i.e. the fact that the input experimental signal is not a plane wave but is composed of a set of wave vectors inside a cone around the incident direction. In other words, experimentally, the transmission through the sample can occur in a cone around the ΓX direction. At frequencies higher than 8.8 kHz, the transmission is maximal for 9.8 kHz with an amplitude very much lower than that at very low frequencies i.e. in the range 0–3 kHz. The transmission is then strongly attenuated and it becomes difficult to define precisely the edges of regions with noise level transmission. But these experiments performed with the usual setup validate fairly well the theoretical

predictions concerning the existence of a forbidden band at audible frequencies.

2.4. Summary

The purpose of Section 2.1.1 was to investigate theoretically the existence of complete band gaps in the acoustic band structure of periodic elastic fiber reinforced composite materials like the carbon–epoxy system. Relatively large complete gaps were obtained where the propagation, perpendicular to the cylinders, of acoustic waves is forbidden. The influence of the geometry of the inclusions and the effect of the composition of the composite material on the band structure was reviewed. In the case of a square array of carbon cylinders embedded in an infinite epoxy background, larger complete band gaps appear for a square section parallel to the lattice than for the other two configurations studied. The existence of a strong contrast between the physical parameters of the inclusions and the matrix seems to be a general rule to obtain complete band gaps in the band structure of elastic composite systems. In the materials used as examples [31] here, carbon and epoxy have rather similar mass densities and very different elastic constants, whereas in W and Al the velocities of sound are in the same range, the elastic constants and mass densities being much higher in W than in Al. With these constituents were obtained complete band gaps for carbon fibers in epoxy and W fibers in an Al matrix, but not in the opposite situations. It was concluded that the contrast between both elastic constants and mass densities is important for the existence of complete band gaps, which cannot be solely predicted by a requirement about the relative velocities of sound.

In Section 2.1.2, the propagation of acoustic waves in a binary two-dimensional phononic crystal constituted of a triangular array of parallel, circular, steel cylinders in an epoxy resin matrix were reviewed. The wave propagation was limited to the plane perpendicular to the cylinders. The measurements and the numerical calculations prove unambiguously the existence of two absolute stop bands independent of the direction of propagation of the acoustic waves. Besides the band gaps, one can establish some qualitative and even semi-quantitative correspondences between the experimental and theoretical transmission spectra inside the pass bands. However, a more quantitative comparison would need to repeat such experiments with other samples (for instance to check the possibility of defects during the sample preparation, different thicknesses of the samples, etc.), and also to include in the finite difference time domain calculation the possibility of three dimensional propagation due to the divergence of the initial pulse. In this respect, an analysis of the eigenvectors associated with the different modes would also be helpful for an understanding of the details of the experimental transmission spectra.

The examples of Section 2.2 show the existence of absolute band gaps in the acoustic band structure of a class of two dimensional binary periodic composite systems: the boron-nitride array of infinite parallel cylinders in a background. In this pattern, the unit cell contains two cylinders of different diameters and the rods are located on the vertices of a regular hexagon. Artificial materials for which the inclusions and matrix are together water cylinders (resp. mercury) in a mercury (resp. water) background were reviewed. Relatively large complete gaps were obtained. In these gaps, the propagation, perpendicular to the inclusions, of phonons in the acoustic region is forbidden. The influence of the cylinder diameters as well as the effect of the composition of the composite material on the band structure were studied.

For high filling fraction, the triangular structure of C or W cylinders embedded in an infinite epoxy matrix is more favorable for the opening of very large gaps in the band structure. In the opposite situation, i.e. epoxy fibers in a C or W background, the

graphite structure, in which all the cylindrical inclusions have the same radius, is more appropriate. For quite low filling fractions, triangular and graphite arrays of W cylinders in an epoxy matrix give rise to large absolute acoustic band gaps of qualitatively similar widths. Our results demonstrate also that two-dimensional solid/solid boron-nitride structures with cylinders of markedly different radii may be used as selective frequency filters. For two-dimensional binary fluid/fluid composites, the graphite structure yielded the largest acoustic band gaps when cylinders of a high density material were embedded in a background of low density; this independent of the filling fraction of the inclusions. In the opposite case of low density fibers embedded in a high density matrix, the triangular structure gives rise to one large absolute band gap (which is the largest one obtained). Moreover in the limit of a high filling fraction, the boron-nitride geometry offers the possibility of an easy technical realization which avoids contact between the fibres.

In solid composites, one may of course be interested in a separate study (or experimental excitation) of Z and XY-polarized modes. In this respect, it is worthwhile to notice the similarities between the wave equation which describes the Z-polarized modes in solid composites and the one giving the fluid composite band structure. This comparison can be made by replacing the parameters ρ and c_{44} in a solid respectively by $\frac{1}{\rho}$ and $\frac{1}{c_{11}}$ in the fluid. Then the conclusions mentioned above in fluid composites can also explain or predict the behaviors of the band structure for Z-polarized modes in solid composites. For instance, in the case of epoxy fibers in a C (or W) matrix (which means c_{44A} much smaller than c_{44B} and ρ_A much smaller than ρ_B) the largest Z-polarized gaps were obtained in the graphite and some boron-nitride geometries. In the opposite case of C (or W) cylinders in an epoxy matrix, the triangular structure gave the largest gap, although the boron-nitride patterns with α different from 0, and in particular the graphite structure, show richer band gap structures.

The calculation of the acoustic band structure was performed in this example for waves propagating parallel to the ($x0y$) plane, perpendicular to the z axis of the fibers. For infinitely long cylinders, it is likely that these gaps will close, if we take account of wave propagation along the z direction, in addition to the propagation along the x, y directions. However, one may think that these gaps will still exist either if the cylinders are of finite dimension with a length of order π/a, or if they are composed of a periodic structure with a repeating period of the same order of magnitude [65].

Finally, it could be interesting to extend these calculations to two-dimensional mixed periodic composite media where the inclusions and matrix are of different nature, i.e. fluid (resp. solid) cylinders, arranged on patterns of various geometries, in a solid (resp. fluid) matrix. The experimental manufacturing of these systems will of course be very easy.

In Section 2.3, we have reviewed theoretically and experimentally the propagation of acoustic waves in a two-dimensional elastic band gap material composed of a square array of parallel, circular, Cu cylinders in air. The experiments and the theoretical calculations prove the existence of a forbidden band for frequencies in the audible regime. From a theoretical point of view, the comparison between our plane wave expansion and finite difference time domain results have shown that the assumption of an infinitely rigid solid made for the computation of the band structure is realistic at low frequencies i.e. for frequencies lower than 10 kHz. At higher frequencies the two theoretical methods give rather different results especially in the ΓM direction of propagation of the irreducible square Brillouin zone. On the other hand, the finite difference time domain method enabled us to differentiate between filled inclusions and hollow tubes. The plane wave expansion method is not well adapted to the study of fluid–solid

systems. The finite difference time domain method is, on the contrary, well suited for such systems. These calculations demonstrate undoubtedly that for frequencies in the range 0–45 kHz, filled and hollow metallic inclusions placed in air lead to very similar transmission coefficients in agreement with other experimental results. In contrary, the transmission coefficient strongly depends on the thickness of the hollow inclusion when air has been replaced by water in the two-dimensional structure. From a practical point of view, the Cu/air composite material, which can be very easily manufactured, is a good candidate for an effective light, sonic insulator. It should also be possible to shift the forbidden band to much lower audible frequencies by changing the geometry of the array of inclusions. We will, in what follows, illustrate the applications of two-dimensional phononic crystals by four different kinds of examples: first the filtering of acoustic waves, next the demultiplexing of acoustic waves, then some high-frequency radio-frequency devices using phononic crystal plates and finally some sonic insulators.

3. Filtering and multiplexing of acoustic waves

Manipulation of light in waveguides inside photonic crystals allows low loss transmission through sharp bends, filtering or wavelength division multiplexing [66–70]. The coupling of a waveguide with resonant cavities can alter drastically the transmission spectrum and may find useful applications [71–73]. The filtering technology enables us in particular to construct multiplexing and demultiplexing devices. Multiplexing is the operation which enables us to inject in one waveguide frequencies incoming from two or more different waveguides. Demultiplexing is the inverse operation enabling us to extract from one waveguide one frequency and to send it to another waveguide. Inspired by waveguides in photonic crystals, similar research appeared for phononic crystals.

We review in what follows the propagation of acoustic waves through perfect and defect-containing waveguide structures created inside a phononic crystal composed of solid constituents. The removal of inclusions along some pathway in the phononic crystal produces acoustic waveguides [74–84]. Acoustic waves that would not propagate otherwise in a phononic crystal can be guided with minimal loss along such waveguides. Low loss transmission can be achieved in linear waveguides as well as guides with sharp bends. Furthermore, the passing band of a guide can be altered by attaching resonators to its side. For instance, side branch resonators obtained by removing additional inclusions in a direction perpendicular to a linear waveguide in a two-dimensional phononic crystal induce zeros of transmission in the spectrum of the unperturbed guide [78,81]. The zeros of transmission appear as narrow dips with frequencies depending on the geometry of the resonator. Such resonant filters rejecting specific frequencies may serve as building elements for the design of specific functions in the treatment of acoustic signals.

Experimental observation of a phononic crystal waveguide was reported [85–88] following several numerical studies of similar guides [78–81]. In support of a recent theoretical study showing the existence and properties of resonant filters in two-dimensional phononic crystal waveguides [78], it was shown experimentally that the presence of resonators in the vicinity of a waveguide induces narrow zeros of transmission in the passing band of the guide. The experimental results were supplemented by numerical calculations of dispersion curves and transmission coefficients based on the plane wave expansion and the finite difference time domain methods.

In this section, we present first examples for filtering in solid/fluid systems and then in solid/solid systems. Then we review the wavelength division multiplexing of acoustic waves.
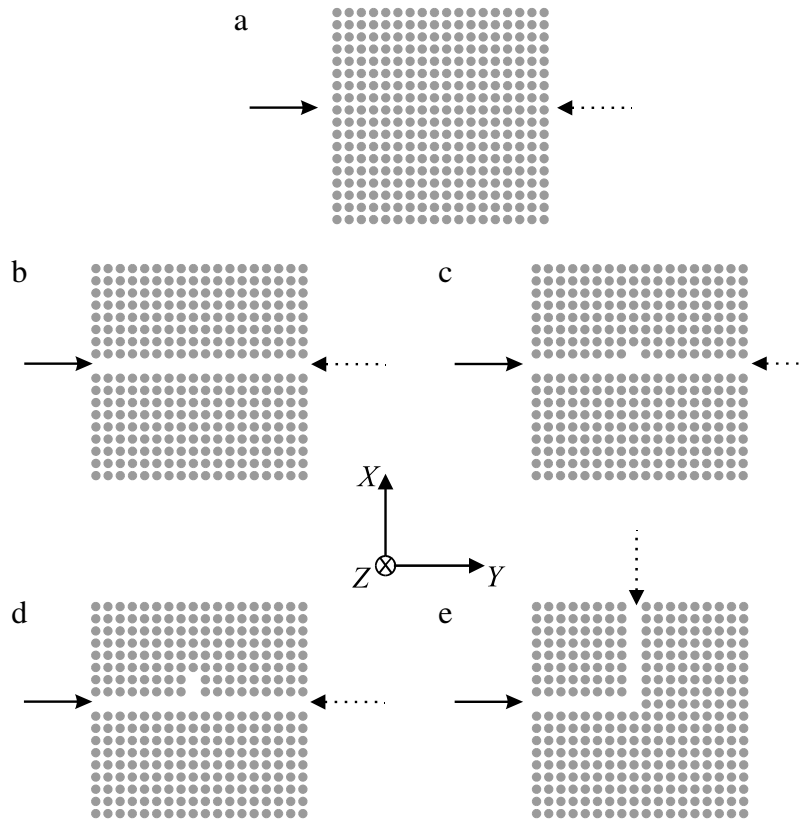
Fig. 24. Cross sections of the phononic crystals for the directions of propagation and the geometries considered in this section. The PVC cylinders are parallel to the *z* direction of the Cartesian coordinate system (O, x, y, z). The full and dashed arrows symbolize the location of the speaker and the microphone during the experimental process. (a) The *x* direction of propagation along the perfect phononic crystal, (b) the perfect linear waveguide, (c) a stub of length equal to one period attached vertically to the waveguide, (d) a stub two periods long, and (e) a guide with a sharp bend.

## 3.1. Filtering in solid/fluid systems

3.1.1. Systems

The basic experimental system is a two-dimensional solid/fluid phononic crystal composed of 18 × 18 polyvinyl chloride (PVC) cylinders in air. The cylinders are one meter long, parallel to the *z* direction of the (O, x, y, z) Cartesian coordinate system (see the inset in Fig. 24) and are arranged on a square array with lattice parameter $a = 2.7$ cm, see the illustration in Fig. 24(a). The cylinder radius is $r = 1.29$ cm. This results in a filling factor, $f = \pi r^2/a^2 = 0.717$. We have chosen a PVC/air phononic crystal with lattice parameter in the centimeter range to achieve acoustic band gaps in the audible range of frequency [26,9,31]. Acoustic waveguides and resonators are easily created in this structure by removing cylinders. More specifically, we have constructed a linear waveguide (Fig. 24(b)), two resonators of different lengths coupled to a linear guide (Fig. 24(c) and (d)) and a guide with a sharp bend (Fig. 24(e)).

3.1.1.1. Experiments. We measure the transmission across the phononic crystal and along the guides with a speaker connected to a function generator (HP3324A) and a microphone whose frequency response lies in the range [40 Hz–12 kHz]. The speaker produces the incoming signal and the microphone records the transmitted one. The transmitted signal is detected with a tracking generator coupled to a spectrum analyzer (HP89410A). The speaker and microphone are placed against the walls of the structures in the same plane perpendicular to the cylinders. For each system, two measurements are conducted with and without the structure. The difference between these frequency signals is calculated to subtract any background effect.

3.1.1.2. Theoretical methods. In this section, we apply the plane wave expansion method for computing the band structure of the phononic crystal by imposing the condition of infinite rigidity of the solid constituent (as described in Section 2.3.1.2). We used again the finite difference time domain method described previously for computing the transmission coefficients through phononic crystal samples.

In the present case, the transmission spectrum along the *x* direction of propagation in the irreducible Brillouin zone of the phononic crystal is calculated with an inhomogeneous region of thickness 18*a* along the *y* direction and a width *a* along the *x* direction (i.e. 18 cylinders). For these structures the transmitted signal is averaged over the entire width of the system. A transmission coefficient is obtained by Fourier transforming the transmitted temporal signal and normalizing it to that of a homogeneous system composed of air. The central regions for the linear waveguide and the waveguides with a side branch resonator are constructed from a structure composed of 18 × 18 periods. For this, cylinders are removed along the *y* direction to form the guide and along the *x* direction to create the resonator. The signal exiting the guides is averaged over their width. The Fourier transform of the average exciting signal is again normalized to the Fourier transform of a signal propagating inside homogeneous air. In contrast to the case of the perfect phononic crystal, the normalization of the guided signal can give values of transmission exceeding 1 in linear scale or equivalently slightly positive values in dB.

To avoid difficulties encountered in the calculation of the band structure of mixed composites with the plane wave expansion method, Tanaka et al. [63] have reported an extension of the finite difference time domain method for the calculation of dispersion relations of acoustic waves in two-dimensional phononic crystals. In
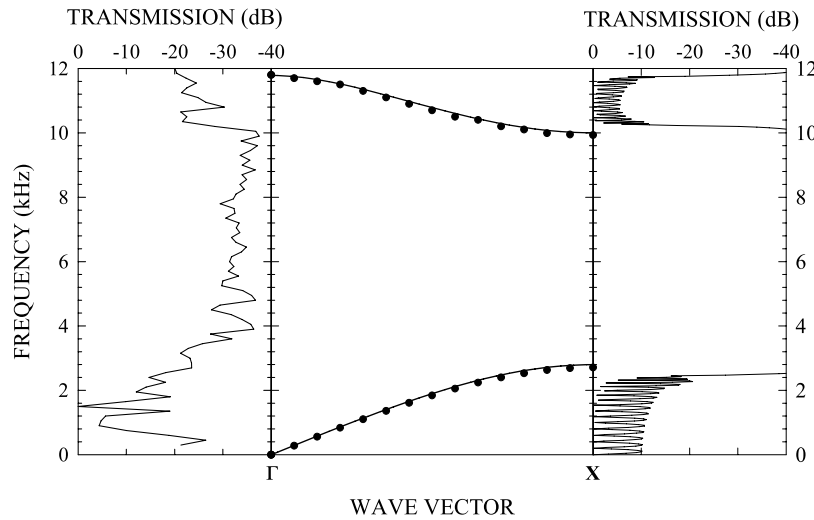
Fig. 25. (a) Band structures of the perfect PVC/air phononic crystal along the *X* direction of propagation of the irreducible Brillouin zone (see inset) computed with the plane wave expansion (solid lines) and the finite difference time domain (dots) methods. Experimental (b) and theoretical (c) transmission coefficients along the *ΓX* direction.

contrast with the standard finite difference time domain approach, the band structure finite difference time domain technique implies a periodic system in the *XY* plane.

The displacement field and the stress tensor must satisfy the Bloch theorem

$$\mathbf{u}(\mathbf{r}, t) = e^{i\mathbf{K}.\mathbf{r}}\mathbf{U}(\mathbf{r}, t), \tag{32}$$

and

$$\vec{\sigma}(\mathbf{r}, t) = e^{i\mathbf{K}.\mathbf{r}}\vec{\Sigma}(\mathbf{r}, t), \tag{33}$$

where $\mathbf{r}(\mathbf{x}, \mathbf{y})$ is the position vector in the *xy* plane and $\mathbf{K}(K_x, K_y)$ is the Bloch wave vector. $\mathbf{U}(\mathbf{r}, t)$ and $\vec{\Sigma}(\mathbf{r}, t)$ are spatial periodic functions of period *a*, the lattice translation vector. One inserts Eqs. (32) and (33) into the equations of propagation of the elastic waves

$$\rho(x, y)\frac{\partial^2 \mathbf{u}}{\partial t^2} = \nabla.\vec{\sigma}. \tag{34}$$

To solve them, one first specifies a 2D wave vector, **K**, along the principal direction of the irreducible Brillouin zone. An assumption on the initial displacement $\mathbf{U}(\mathbf{r}, t = 0)$ in the form of a delta stimulus at some random location within the unit cell is then made. The equations of motion are solved by discretizing both space and time. The time evolution of $\mathbf{U}(r_i, t)$ at several predetermined locations within the unit cell is recorded. Peaks in the frequency space of the Fourier-transformed signals are identified as the eigenfrequencies of the normal modes of the system for the wave vector, **K**. In contrast to the plane wave expansion method, the band structure finite difference time domain technique allows us to compute the band structure of periodic mixed solid/fluid composite materials without requiring the assumption of solid rigidity.

The physical parameters used in these calculations are the longitudinal C_l, transverse C_t, speeds of sound and the mass density ρ for the solid. The acoustic properties of a fluid like air are the longitudinal speed of sound and the density. For all calculations we use $c_l = 2230$ m/s, $c_t = 1000$ m/s and $\rho = 1364$ kg/m^3 for PVC, and $C_l = 340$ m/s and $\rho = 1.3 \times 10^{-3}$ kg/m^3 for air.

3.1.2. Results

3.1.2.1. Perfect phononic crystal. Fig. 25(a) presents the band structures along the *x* direction of propagation computed with both the plane wave expansion and the finite difference time domain methods. The plane wave expansion band structure was

calculated with 169 **G** vectors of the reciprocal space. In the range of frequencies of Fig. 25(a), there exists a large stop band between 2.8 and 10 kHz. The very good agreement between the two theoretical methods validates the assumption of the rigidity of the solid in the peculiar case of the PVC/air composite in this range of frequencies. Fig. 25(b) and (c) show the experimental and theoretical transmission spectra of the PVC/air phononic crystal along the *x* direction of propagation, respectively. The measured transmission is drastically depressed in the interval of frequencies [3, 10] kHz. This stop band is also confirmed by the computed transmission and agrees with the band structure calculations. On the other hand, we have verified experimentally and theoretically via plane wave expansion and finite difference time domain calculations, that along the *ΓM* direction a stop band extends from 4 to 10 kHz. This shows that the PVC/air phononic crystal possesses an absolute band gap in the audible frequency range between 4 and 10 kHz. This interval of frequency is the intersection of the gaps in the *ΓX* and *ΓM* directions.

3.1.2.2. Linear waveguide. In this section, we investigate the properties of a two-dimensional phononic crystal made of PVC cylinders surrounded by air and containing a straight waveguide (see Fig. 24(b)). Fig. 26(a) reports its band structure. These dispersion curves were obtained numerically, on the one hand, using the plane wave expansion method (solid lines) with a supercell of 7 periods. The supercell contains 7 unit cells, one of which is filled with air only. The supercell is also repeated periodically in the *x* direction leading to a stack of waveguides separated by 7 periods in this direction. This separation is sufficient to avoid coupling between neighboring guides. The plane wave expansion band structure was calculated with 1105 **G** vectors. On the other hand, the band structure was also computed with the help of the finite difference time domain method (dots) and the agreement with the plane wave expansion calculations is again quite good. The slight difference in frequency of the finite difference time domain bands compared to those obtained with the plane wave expansion method results from the fact that the plane wave expansion calculation has not fully converged with respect to the **G** vectors [63]. The dispersion curves numbered 6, 7, 8 and 9 are related to localized modes in the straight waveguide. The measured and calculated transmission spectra of the linear waveguide are presented in Fig. 26(b) and (c), respectively. Experimentally, the waveguide permits transmission of waves that otherwise would be forbidden in the perfect phononic crystal. There are two waveguide passing bands with frequency intervals
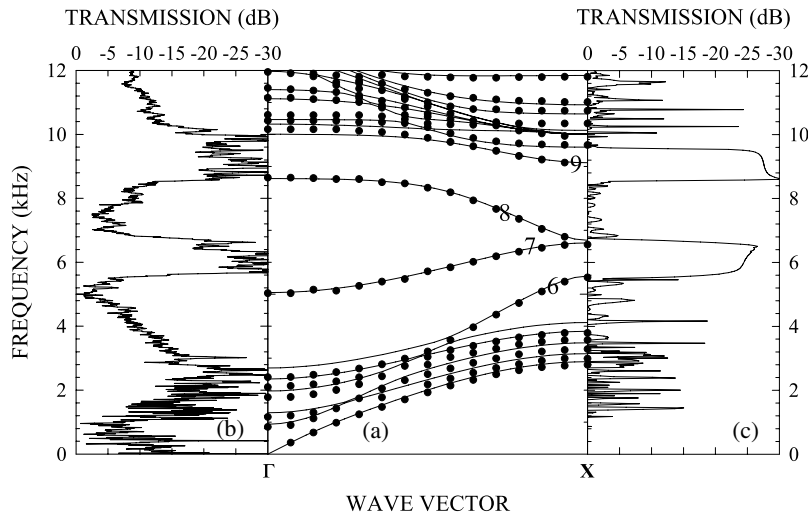
Fig. 26. (a) Plane wave expansion (solid lines) and finite difference time domain (dots) band structures of a PVC/air phononic crystal containing a straight waveguide along the *Y* direction (see Fig. 24(b)). The supercell contains 1 × 7 unit cells. Experimental (b) and theoretical (c) transmission spectra along the linear waveguide. The bands numbered 6, 7, 8 and 9 in (a) are associated with waveguide modes. Bands 7 and 9 are "deaf bands" and do not contribute to the transmission (see text for details).

[2.4, 5.6] kHz and [6.8, 8.5] kHz. Transmission of waves with frequencies in these intervals takes place along the waveguide without any loss. Stop bands still exist for frequencies between 5.6 and 6.8 kHz and 8.5 and 10 kHz. The experimental spectrum is confirmed by the finite difference time domain calculation. Indeed the right panel of Fig. 26 shows two passing bands from 0 to 5.5 kHz and 6.8 to 8.5 kHz, separated by a region with low transmission that extends from 5.5 to 6.8 kHz. The gap of the perfect phononic crystal persists for frequencies in the range [8.5, 9.6] kHz.

A comparison between the transmission spectra and the band structures indicates that the dispersion curves labeled 7 and 9 in Fig. 26(a) do not contribute to the transmission. An analysis of the symmetry of these modes may explain this singular effect. For this, using the plane wave expansion method, we compute some eigenvectors associated with bands 6 through 9 at a given wave vector. The Fourier transform of the eigenvectors yields the pressure field inside the phononic crystal [47]. Fig. 27 illustrates the pressure field pattern corresponding to the 6th, 7th, 8th and 9th bands at the *X* point of the irreducible Brillouin zone. It is important to note that the 6th and 8th modes have a symmetry readily excitable by an incident wave of longitudinal polarization. In contrast, the 7th and 9th modes are anti-symmetric with respect to the symmetric plane of the waveguide. Consequently, these antisymmetric modes cannot be excited by a longitudinal incident wave and will not contribute to the transmission. Modes of this kind, named "deaf bands", were reported for perfect photonic or phononic crystals [47,89–92]. Let us stress again that the deaf modes reported in this paper are not modes of perfect crystals but waveguide modes.

In Fig. 27, the centers of the cylinders in the phononic crystal are located at integer values of the ratios x/a and y/a, excluding $x/a = 3$ which is the position of the symmetry plane of the waveguide. The rigidity of the inclusions explains that the acoustic waves do not penetrate inside the cylinders and this leads to a vanishing pressure field inside the inclusions. The air waveguide is bound by PVC cylinders at $x/a = 2 + r/a = 2.48$ and $x/a = 4 - r/a = 3.52$, that is, its width is equal to $1.04a$. The acoustic pressure field extends significantly beyond these bounds, showing that the waveguide modes are not strictly confined inside the waveguide. At larger distances from the waveguide boundaries, the pressure field vanishes everywhere since the frequency of the propagating waves falls inside the stop band of the perfect phononic crystal. In another study of a waveguide in air/water and steel/water two-dimensional phononic crystals, the guiding modes

were shown to obey classical waveguide models with strictly perfectly reflecting walls [78]. The extent of the pressure field outside the limits of the waveguide in the PVC/air system indicates that in this particular case the waveguide modes cannot be derived analytically from simple waveguide theory. It therefore appears that straightforward and generalized application of this theory to waveguides in phononic crystals can be misleading.

3.1.2.3. Linear waveguides with side branch resonator. The effect of a side branch resonator on the transmission spectrum of the waveguide is illustrated in Figs. 28 and 29. The removal of a single cylinder adjacent to the waveguide produces a resonator of nominal length *a*. The calculated transmission spectrum in Fig. 28(a) retains the general characteristics of the linear waveguide (see Fig. 26(c)) with two additional features. Narrow dips appear in the calculated transmission spectrum at two frequencies, namely 4.7 and 7.5 kHz. These reductions in transmission are similar in nature to those observed in a theoretical study of waveguides with side branch resonators in water/air and steel/water phononic crystals [78]. The transmission in the waveguide is significantly altered due to interference phenomena between the acoustic modes of the guide and those of the resonator. The characteristics of the experimental spectrum of the guide with a resonator of length *a* are best seen by calculating the difference between the transmission along the guide with a resonator and that of the perfect linear guide as reported in the insets of Fig. 28(b). A small depression in transmission occurs in the first passing band of the linear guide at 4.85 kHz. This agrees quite well with the theoretically predicted dip at 4.7 kHz (see Fig. 28(a)). In the range [7, 8.5] kHz, the experimental transmission spectrum exhibits two depressions around 7.5 and 8.2 kHz. Since the first depression is in accordance with the one observed in the theoretical transmission, the feature at 8.2 kHz have no analog in Fig. 28(a). Nevertheless, one notes that this feature appears in the very near vicinity of the edge of the second waveguide passing band and this renders its analysis very difficult.

Lengthening the resonator increases the number of resonant modes and therefore the number of narrow dips in the transmission spectrum of the guide with a resonator. For instance, in the case of Fig. 29(a) where the resonator is twice as long as in Fig. 28, the theoretical transmission spectrum exhibits four narrow dips in transmission at 3.95, 7.3, 9.7 and 9.8 kHz. The experimental spectrum of the guide with a resonator of length 2*a* possesses a significant reduction in transmission at 4.1 kHz in very good agreement with the first calculated dip (see Fig. 29(a)). Two additional and
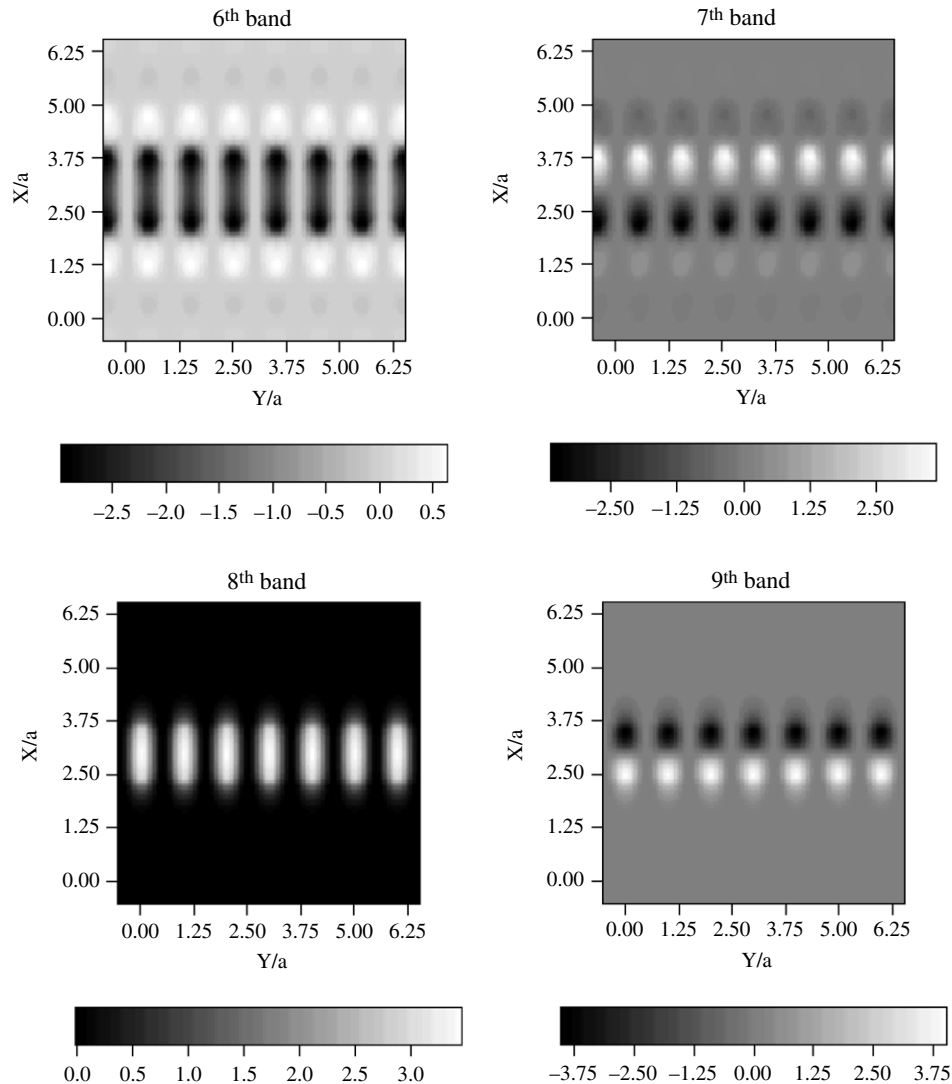
Fig. 27. Pressure fields inside the PVC/air phononic crystal containing a straight waveguide. The grey scale indicates the relative amplitude of the pressure field. These maps were obtained from the plane wave expansion computations of the eigenvectors associated with the 6th, 7th, 8th and 9th eigenfrequencies at the *X* point of the irreducible Brillouin zone (see Fig. 26(a)).

well-defined depressions in transmission are observed in the second passing band of the guide at the frequencies 7.4 and 8.2 kHz. As in the previous case, the first of these two features is in good agreement with the theoretical predictions but the second one which appears in the near vicinity of the stop band has no equivalent in Fig. 29(a). Because the second stop band in the experimental spectrum (see Fig. 26) is larger than the theoretically predicted transmission band gap, the dips calculated around 9 kHz cannot be observed experimentally.

A comparison between Figs. 28(b) and 29(b) reveals that the influence of the resonator on the waveguide transmission is much more pronounced with a longer resonator. For instance, the first depression in transmission which occurs around 4.5 kHz in these two figures is much more important with a resonator of nominal length 2*a* than *a*. As noted before, the waveguide modes extend significantly beyond the physical bounds of the guide. The interference between these modes and those of a short resonator are therefore anticipated to be weak. Simple models based on one-dimensional waveguides coupled to one-dimensional resonators introduced in [78] will not be applicable to systems such as those

studied here where the guiding modes are not strictly confined inside the bounds of the guide.

3.1.2.4. Bent waveguide. The transmission spectrum along a bent waveguide (Fig. 30) is similar to that of the linear guide. This spectrum is measured by emitting sound waves at the entrance of the guide and collecting the signal at its exit. This result demonstrates that acoustic waves can be transmitted without significant loss along a guide with sharp bends. To verify that transmission occurs without much loss, we have also measured the transmission by placing the speaker at the entrance of the bent guide and the microphone on the opposite side. In this case one recovers the transmission spectrum in the ΓX direction of the perfect phononic crystal. The most significant difference between the transmission spectra of the linear and bent waveguide arises in the form of dips in the passing bands of the latter. The most notable features occur at 4.5 and 7.3 kHz and are reminiscent of the dips in the transmission spectrum of a guide with a side branch resonator of nominal length 2*a*. The observed features appear therefore to be due to interferences between the incident wave and waves reflected by the bend.
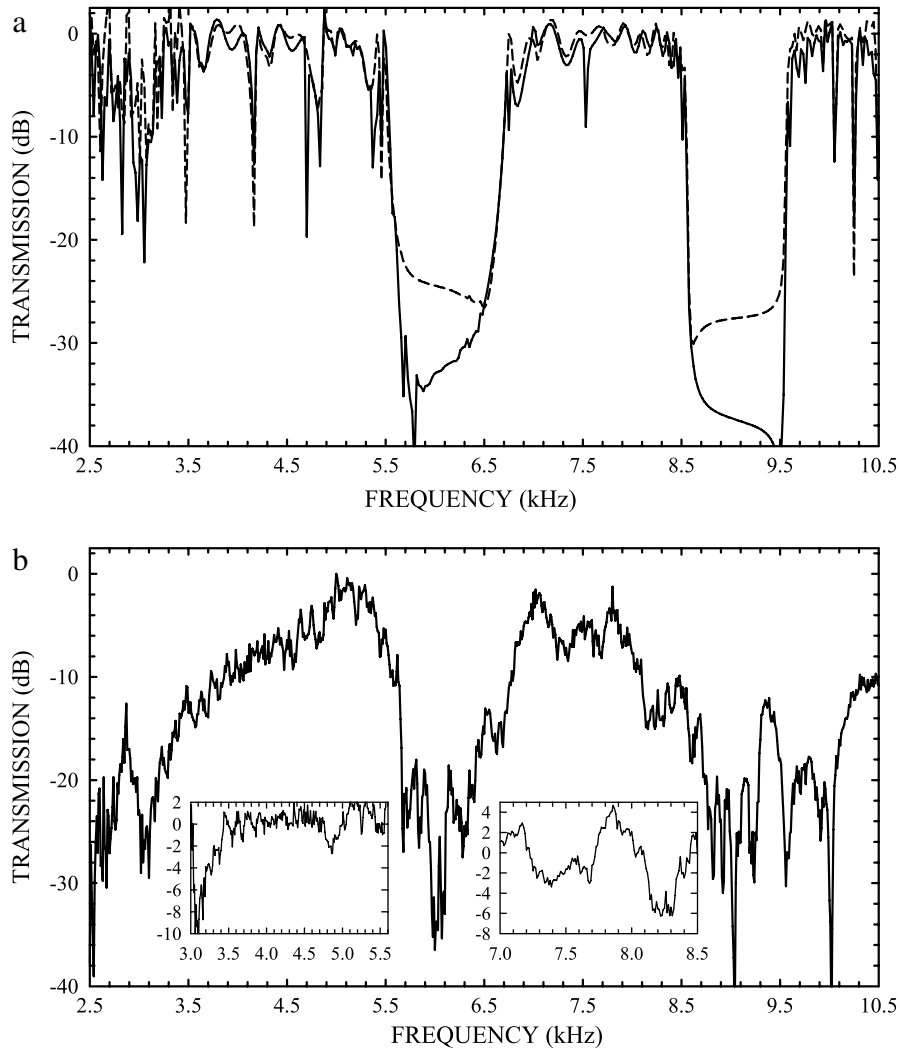
Fig. 28. Theoretical (a) and experimental (b) transmission spectra along the linear waveguide with a side branch of nominal length *a*. The insets represent the difference between the transmission in the guide with resonator and the transmission in the linear waveguide in the range of frequencies associated with the passing bands of the linear guide. The dashed line in (a) represents the computed transmission along the linear waveguide of Fig. 26(c).

3.2. Filtering in solid/solid systems

3.2.1. Geometrical models

We consider now a solid/solid two-dimensional phononic crystal composed of steel cylinders in epoxy. The physical parameters characterizing the acoustic properties of the constituent materials are the longitudinal, c_ℓ and transverse, c_t, speeds of sound as well as the mass density ρ. We take $c_\ell = 5825$ m/s, $c_t = 3226$ m/s, $\rho = 7780$ kg/m^3 for steel, and $c_\ell = 2569$ m/s, $c_t = 1139$ m/s, $\rho = 1142$ kg/m^3 for epoxy. The inclusions have the cylindrical symmetry and are arranged periodically on a square lattice. The parameters specifying the geometry of the crystal are the lattice parameter, a, and the radius of the inclusion, r. The filling fraction of the composite medium is defined as the ratio $\beta = \pi r^2/a^2$. We assume $a = 9$ mm and $r = 3.5$ mm (or $\beta = 0.475$). This insures that the phononic crystal displays a large band gap extending from 85 to 200 kHz.

Fig. 31 displays the cross sections of the phononic crystal for the geometries considered here. Simple linear waveguides of different width, d, are created in the phononic crystal by removing one or several rows of cylinders along the y direction of the square array, Fig. 31(a). Stubs of varying lengths and widths can be obtained by removing cylinders in the direction x perpendicular to the waveguide, Fig. 31(b). A cavity can be inserted at the side of the

waveguide, Fig. 31(c). The coupling between the cavity and the waveguide can be modified by changing their separation, although we limit ourselves to a separation of one unit cell. Resonating cavities can also be built out of two basic cylindrical inclusions inserted within the waveguide, Fig. 31(d).

We study the transmission through the above structures as well as dispersion relations of the perfect waveguide and of an isolated cavity. Our calculations of the dispersion relations and transmittivity are performed by a combination of the plane wave expansion method and of the finite difference time domain method.

3.2.2. Dispersion relations and transmissions of linear waveguides

In solid/solid two-dimensional phononic crystal, by limiting the wave propagation to the plane xy perpendicular to the cylinders, the propagation modes decouple in the Z modes (with elastic displacement **u** parallel to the z direction) and in the XY modes (with **u** in the plane xy). Here, we focus on XY modes. The band structure of the XY modes of the perfect phononic crystal considered here possesses a wide absolute band gap extending from 85 to 200 kHz. This result is obtained from a calculation of the band structure by means of the plane wave expansion method using 882 wave vectors of the reciprocal space. It is also confirmed in the transmission spectra of the phononic crystal
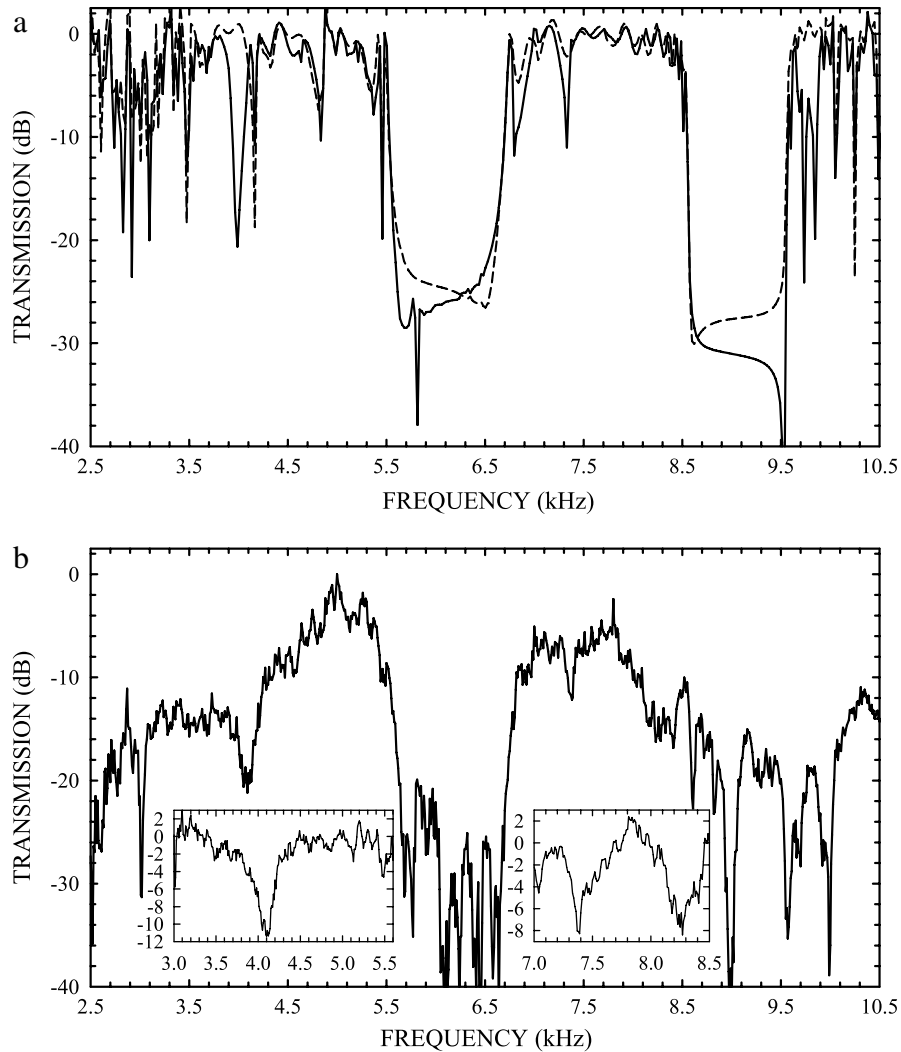
Fig. 29. Theoretical (a) and experimental (b) transmission spectra along the linear waveguide with a side branch of nominal length 2*a*. The insets represent the difference between the transmission in the guide with a resonator and the transmission in the linear waveguide in the range of frequencies associated with the passing bands of the linear guide. The dashed line in (a) represents the computed transmission along the linear waveguide of Fig. 26(c).
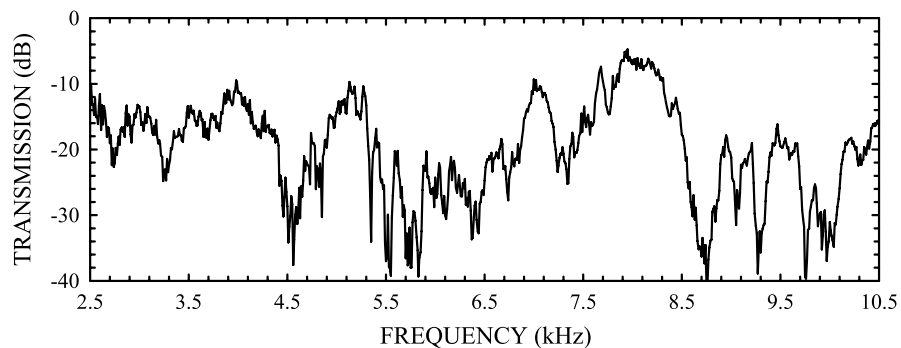

Fig. 30. Experimental transmission spectrum for propagation along the bent waveguide.

calculated by the finite difference time domain method along two high symmetry axes of the Brillouin zone. We review now the properties of a phononic crystal containing a simple straight waveguide. As a basis for further discussions, we first consider a guide simply built by removing one row of cylindrical inclusions along the *y* direction. This is analogous to the examples considered in Refs. [78,79]. The width *d* of the guide, defined by the distance between neighboring cylinders on both sides of the guide, equals *d* = 11 mm, Fig. 31(a). Fig. 32(a) reports its band structure.

The band gap of the perfect phononic crystal is delimited by the two thick horizontal lines. In order to perform this calculation, a supercell of 5 periods is repeated periodically in the *x* direction. This means that the waveguide is repeated every 5 periods in the *x* direction. The band structure is calculated with 1586 vectors of the reciprocal space.

The dispersion curves appearing inside the gap of the perfect phononic crystal are related to localized modes associated with the linear waveguide. The number and dispersion of the localized
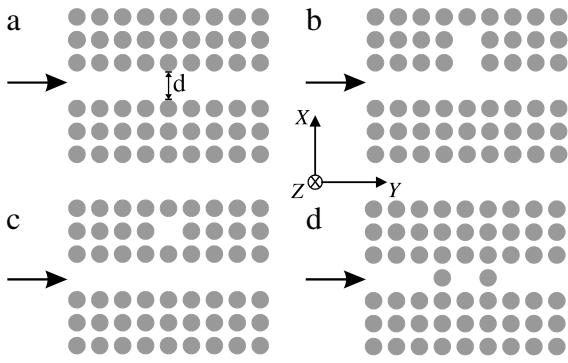
Fig. 31. Cross sections of the phononic crystals for the geometries considered in this subsection. (a) A perfect linear waveguide of width, *d*. (b) A stub attached vertically to the waveguide. (c) A side-coupled waveguide cavity. (d) A cavity inside the linear waveguide.
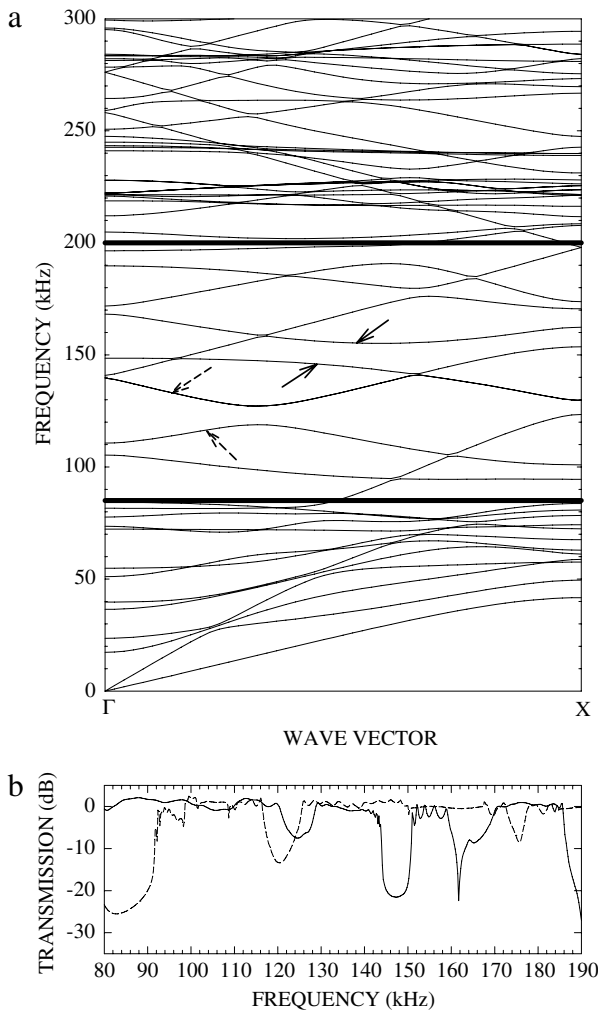
Fig. 32. (a) Band structure of the *XY* modes of propagation of a phononic crystal containing a linear waveguide along the *Y* direction as in Fig. 31(a). The calculation is performed by considering a supercell of 5 periods along the *x* direction. The band gap of the perfect phononic crystal is delimited by the two thick horizontal lines. The filled arrows indicate two symmetrical dispersion curves that anti-cross each other giving rise to the dip in the transmission spectrum around 145 kHz. The dashed arrows indicate two anti-symmetrical branches that anti-cross each other giving rise to the dip in the transmission spectrum around 120 kHz. (b) Transmission through the waveguide for two polarizations of the incident wave, longitudinal (solid line) or transverse (dashed line).

modes can be understood, and qualitatively explained, by considering the propagation of elastic waves in a classical linear guide with rigid boundary conditions for which the dispersion relations can be derived analytically [93]. Indeed this analogy is possible since the displacement field of a wave propagating along the guide in the phononic crystal remains almost confined inside the guide and only penetrates weakly around the steel cylinders situated on both sides of the guide. The main difference between the guide in the phononic crystal and the classical one is that the former has rough instead of planar walls. The roughness of the walls results from the periodicity of *a* of the inclusion that bound them along the *Y* direction. Therefore, for comparison, the dispersion curves of a guide with planar walls should be essentially folded back into a reduced Brillouin zone of dimension π/a. The numerous localized branches inside the gap of the phononic crystal, Fig. 32(a), are the result of this folding and the resulting interaction between branches that cross each other. The results of Fig. 32(a) resemble qualitatively those of Ref. [79] dealing also with a solid/solid composite, constituted by Pb cylinders in epoxy. On the other hand, in the case of the solid/fluid composite (steel cylinders in water) studied in Ref. [78], the number of localized branches in the band gap is much smaller because the matrix is now constituted by a fluid that can only support compressional waves, but not shear waves.

Like in a classical guide, the vibrational modes of the phononic crystal waveguide can be distinguished according to their symmetric or anti-symmetric character with respect to the plane cutting through its middle. Consequently, these modes can be excited with an incident wave of appropriate symmetry. We have calculated, see Fig. 32(b), the transmission through the guide as a function of the frequency, the probing signal being initially of either longitudinal or transverse polarization. Indeed, as discussed below, these waves are respectively symmetrical or antisymmetrical with respect to the symmetry plane.

To calculate the transmission coefficient, we construct a sample in three parts along the *y* direction, a central region containing the finite phononic crystal sandwiched between two homogeneous regions. A traveling wave packet is launched in the first homogeneous part and it propagates in the direction of increasing *y* along the whole sample. Periodic boundary conditions are applied in the *x* direction and absorbing Mur's boundary conditions [94] are imposed at the free ends of the homogeneous regions along the *y* direction. The incoming signal is a sinusoidal wave of frequency $f_0 = 400$ kHz weighted by a Gaussian profile and propagates along the *y* direction. In Fourier space, this signal varies smoothly and weakly in the interval $(0, f_0)$. The amplitude of the input signal does not depend on *x*; it is directed along the *y* direction (resp. *x* direction) when the input signal is of longitudinal (resp. transverse) polarization. Thus, the incident probing signal is either symmetrical or anti-symmetrical with respect to the mirror plane of the guide. The transmittance is obtained by averaging the displacement field at the guide's exit along a line normal to its axis, followed by a Fourier transformation and by normalizing to the same quantity calculated for the incoming wave packet in the absence of the phononic crystal. It should be pointed out that, with this definition, the transmission can exceed one. Depending on whether the input signal is of longitudinal or transverse polarization, the average is taken over the *y* component or the *x* component of the displacement field.

With an incident wave of longitudinal polarization, the transmittance, Fig. 32(a), in the frequency range corresponding to the gap of the phononic crystal takes on a value near 1 except for the secondary gaps appearing respectively around 125, 145 and 170 kHz. The first dip around 125 kHz results from the folding of the symmetrical branches at the Brillouin zone boundary. The second dip at 145 kHz is associated with the anti-crossing between two symmetrical branches marked by arrows in Fig. 32(a). In this example, the length of the guide is taken to be $\ell = 15a$.

The attenuation of the transmitted signal in these secondary gaps is significantly dependent upon the length of the waveguide. Decreasing this length will result in the weakening of the dips. For instance, the dip at 125 kHz will become very small for a length $\ell = 7a$ of the guide, whereas the dip at 145 kHz is less affected by this length. It is likely that this effect is due to the large flat part of the two dispersion curves that anti-cross each other.

Finally, launching a probing signal of transverse polarization (dashed curve in Fig. 32(b)) yields a high transmittance from 93 kHz where the anti-symmetric modes of the waveguide start to exist. This transmission spectrum displays a dip in the frequency interval [118–125] kHz due to the anti-crossing between two anti-symmetric branches (indicated by dashed arrows in Fig. 32(a)).

Now, we review another example dealing with a case that has not been mentioned in the literature, namely the possibility of decreasing the number of dispersion curves (and even yielding the guide monomode) by narrowing the width of the waveguide. Indeed, similarly to the case of a classical linear guide, the cut-off frequency of the guided modes in the phononic crystal can be increased by decreasing the width of the guide. This operation can be performed by assuming that the cylindrical inclusions on both sides of the waveguide are separated by a distance smaller than the period a. Decreasing the thickness of the guide will have, at the same time, the effect of reducing the number of guided mode branches that appears in the gap of the phononic crystal. As a consequence, the guide can even be made monomode over a large frequency range. This effect is sketched in Fig. 33 where we present the band structure of the guided modes and the corresponding transmission coefficients for a narrow waveguide of width $d = 6.5$ mm. One notices the existence of a small (secondary) gap around 150 kHz at the edge of the Brillouin zone, between two symmetric branches. This gap gives rise to a dip in the transmission spectrum. This dip becomes less pronounced when decreasing the length of the waveguide. On the other hand, the dispersion curves display two almost flat antisymmetric branches around 140 kHz, and therefore the transmission with a probing signal of transverse polarization mainly extends over the limited frequency domain of [130–147] kHz.

On contrary, increasing the width of the guide (for instance by removing two or several rows of cylinders along the y direction) will increase the number of localized mode branches in the band gap of the phononic crystal and the transmission becomes mainly multimode.

3.2.3. Waveguides containing a cavity or side-coupled with a cavity.

We now turn to the behavior of a defect cavity in the phononic crystal. The cavity is simply obtained by removing one cylindrical inclusion thus creating a vacant lattice site. The band structure of such a system is calculated for a supercell of 3×3 cylinders with one vacancy in its center. The number of reciprocal lattice vectors used in the calculation is 2738. The band structure reported in Fig. 34 shows the stop band of the phononic crystal containing several nearly flat bands. These flat bands are representative of the vibrational modes characteristic of the cavity. Let us notice that the cavity possesses two perpendicular symmetry axes x and y. Thus, its eigenmodes can be labeled according to their symmetry with respect to these axes as SS, AS, SA and AA, where S and A respectively stand for symmetric and anti-symmetric (for instance SS means symmetric with respect to both x and y axes). We have created excitations inside the cavity having each of the four above symmetries. The characteristic frequencies of the cavity, falling in the band gap of the phononic crystal, coincide with those obtained by the plane wave expansion method (34) within a few per cent. In Fig. 35, we give a map of the eigenvectors for some of the cavity modes. These maps are obtained by exciting with an incident probe an eigenmode of the cavity, contained inside a waveguide. We
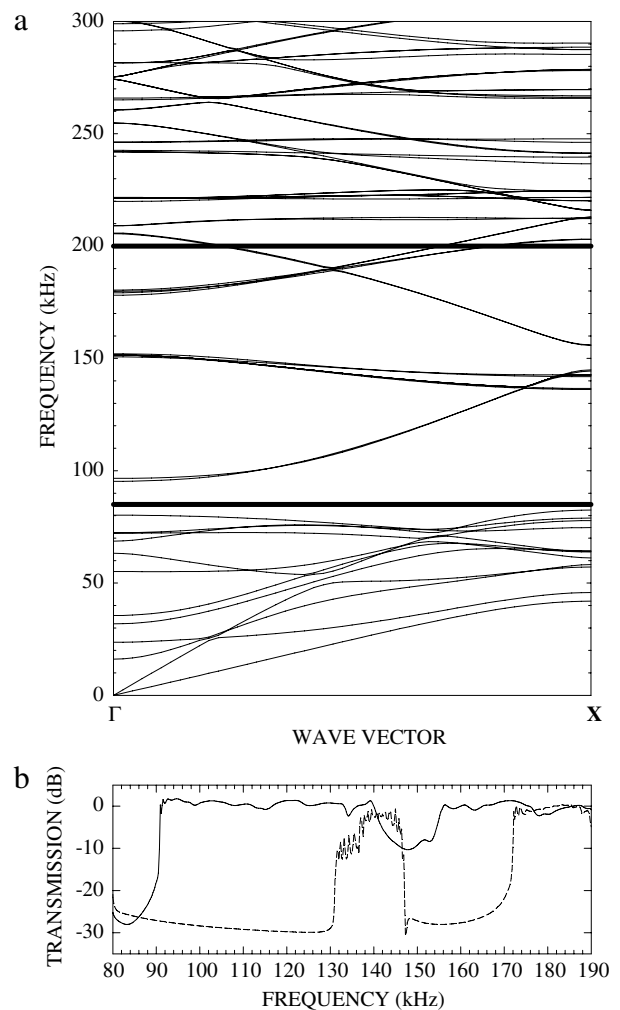

Fig. 33. Same as in Fig. 32, but the width of the waveguide is taken to be $d = 6.5$ mm instead of $d = 11$ mm in Fig. 32.

shall again refer to this point in connection with the explanation of transmission spectra shown in Fig. 36.

The eigenmodes of the cavity can be used advantageously to induce either narrow passing bands within the stop band of the phononic crystal or very narrow stopping bands in the pass band of a waveguide. To that effect we consider (i) a waveguide with a side-branch resonator constituted by a cavity, Fig. 31(c), and (ii) a waveguide in the phononic crystal containing a single cavity, Fig. 31(d). Indeed, a single cavity incorporated into the waveguide may limit the transmission mainly to the frequencies situated in the neighborhood of the eigenfrequencies of the cavity. On contrary, a side-coupled waveguide cavity is expected to induce zeros in the transmission spectrum of the perfect waveguide [74, 75] that occur at the characteristic frequencies of the cavity. So, the same cavity can have two opposite effects depending on whether it is incorporated inside or at the side of the waveguide.

In the following examples, the length of the waveguide is chosen to be $\ell = 9a$ as displayed in Fig. 31. Fig. 36 summarizes the transmittance of the two systems. The cavity-containing guide is probed with a longitudinal, Fig. 36(a), as well as a transverse, Fig. 36(b), incident wave packet. The longitudinal incident wave is symmetrical with respect to the y axis and, thus, can probe the eigenmodes of the cavity that have SS and AS symmetries with respect to the xy axes. On the other hand, the transverse incident wave can excite eigenmodes of only SA and AA symmetries. This is confirmed by the transmission spectra shown in Fig. 36(a)
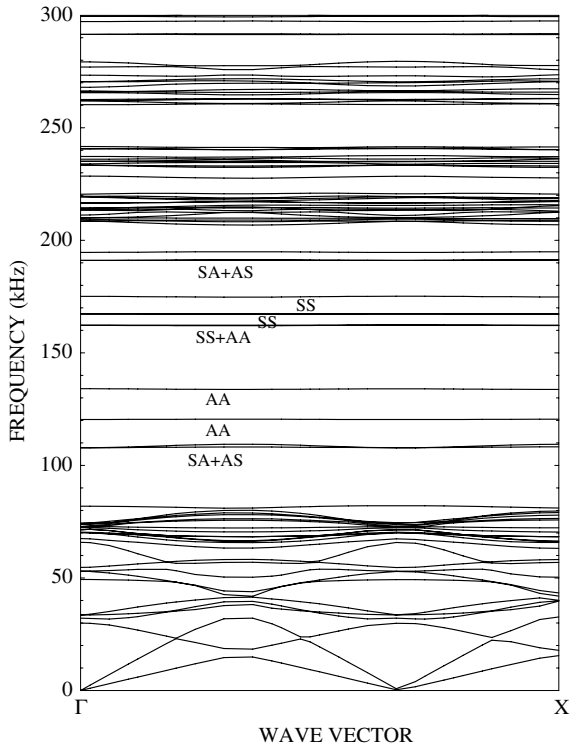
Fig. 34. Band structure of the *XY* modes in a phononic crystal containing a square cavity obtained by removing one cylinder. The calculation is performed by using a supercell 3 × 3. The symmetry of the cavity modes with respect to the *x* and *y* axes are indicated by the letters *S* and *A*, where *S* and *A* stand for symmetric and anti-symmetric respectively (for instance *SS* means symmetric with respect to both *x* and *y* axes).
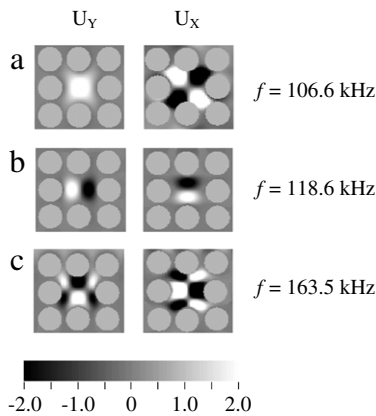
Fig. 35. Map of the components u_x and u_y of some of the eigenvectors of the cavity modes shown in Fig. 34. *f* stands for the frequency of each eigenmode. These maps were obtained by using an incident probing signal of either longitudinal polarization ((a) and (c)) or transverse polarization (b).

and (b) that are mainly composed of peaks in the vicinity of the characteristic frequencies of the cavity with the appropriate symmetry. It is worthwhile to notice that the maps sketched in Fig. 35 are obtained by using an incident probing signal of either longitudinal polarization, Fig. 35(a) and (c), or transverse polarization, Fig. 35(b), at the frequencies of the peaks in the transmission spectra of Fig. 36(a) and (b). Finally, one can remark that the peaks appearing in the transmission spectra can be made sharper if the isolation of the cavity is increased, for instance by bordering the cavity on each side by two cylindrical inclusions instead of one as was shown in Fig. 31.

In Fig. 36(c), we show the transmittance through the side-coupled waveguide cavity, Fig. 31(c). Since this system does not
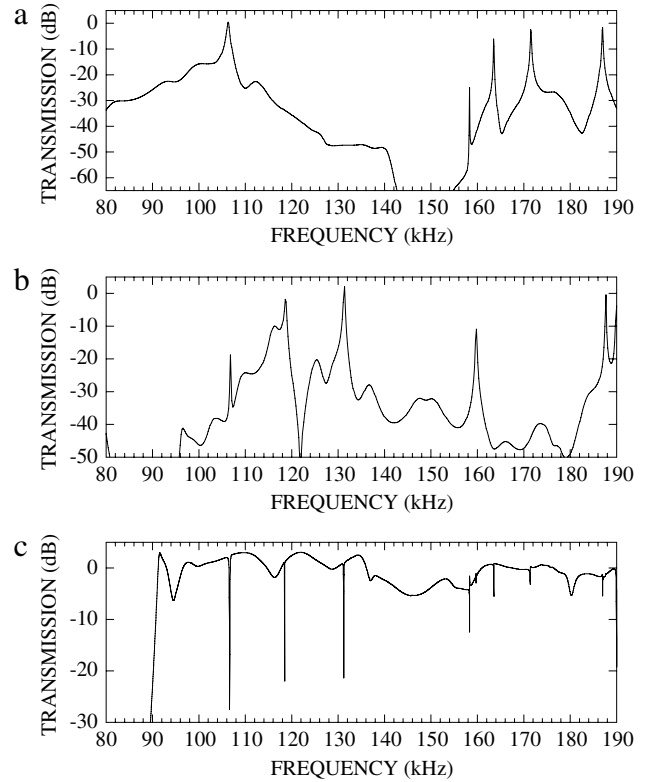
Fig. 36. (a) and (b) Transmittance through a cavity containing waveguides such as in Fig. 31(d). In these figures the polarization of the incident wave is respectively longitudinal or transverse and the width of the cavity is $d = 11$ mm. (c) Transmittance through a waveguide coupled to a cavity along its side as illustrated in Fig. 31(d). The width of the waveguide is taken here to be $d = 6.5$ mm to insure the monomode behavior of the propagation in a wide frequency range of the phononic crystal bandgap.

display any particular symmetry, an incident longitudinal wave can probe in principle all the eigenmodes of the cavity. To enhance the zeros of transmission induced by the side branch resonator, we have chosen a linear guide of narrower width than the period, namely $d = 6.5$ mm, to yield monomode guiding character from 90 kHz up to approximately 150 kHz (see Fig. 33). Transmission takes place for most frequencies below 140 kHz but zeros of transmission occur at several frequencies corresponding to the characteristic frequencies of the cavity. It should be mentioned that with a wider guide, for instance of width $d = 11$ mm, the dips in the transmission still exist, but the transmission does not decrease as much as in Fig. 36(c). It is interesting to notice that the dips in the transmission spectrum of Fig. 36(c) occur exactly at the same frequencies as the peaks in Fig. 36(a) and (b).

Finally, we have also investigated the transmission through a stubbed waveguide such as in Fig. 31(b). The results for the transmission spectra are presented in Fig. 37 where we have considered two different lengths of the stub and two different widths of the waveguide, the incident wave being of longitudinal polarization. In Fig. 37(a) and (b), the width of the linear guide is chosen to be $d = 6.5$ mm in order to have a monomode regime over a broad frequency range (see Fig. 33). One can notice that the main effect of the stub is to induce dips, or zeros of transmission, in the spectrum. The existence of such zeros of transmission has been demonstrated in modellistic calculations [74,75], especially using perfect boundary conditions on the walls of the guide, and also proved in a numerical simulation of stubbed waveguide in phononic crystals made of fluid/fluid or solid/fluid constituents [78]. They are associated with the resonance frequencies of the
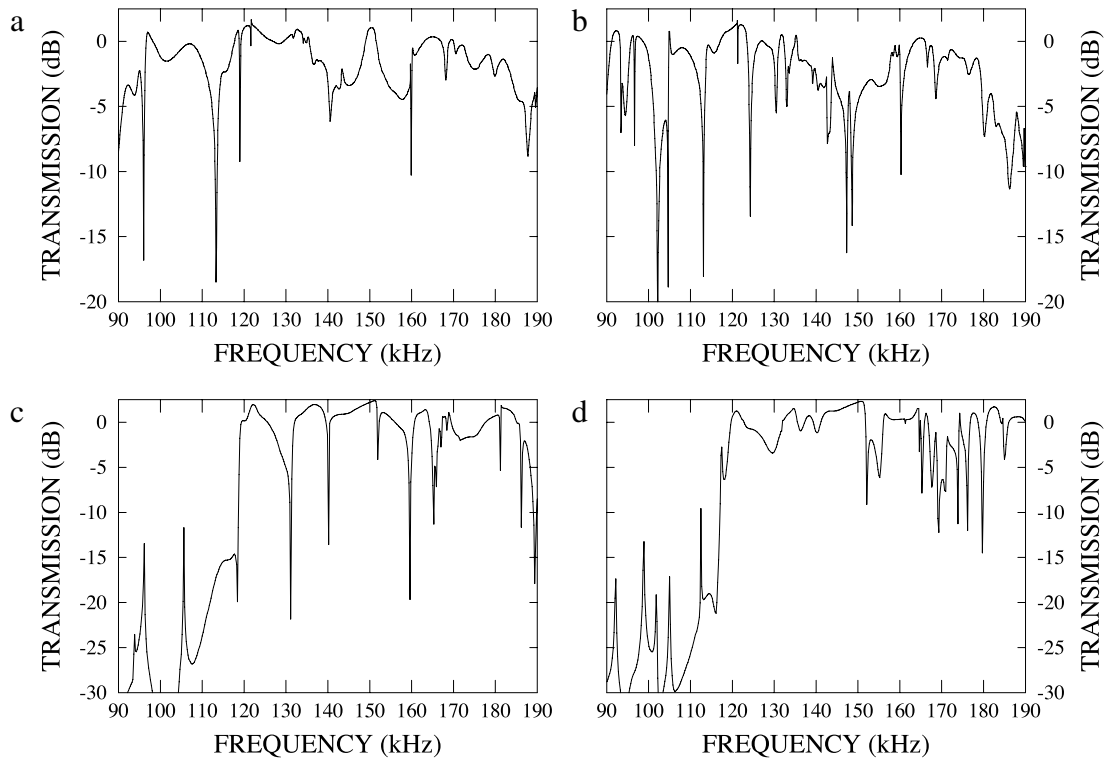
Fig. 37. Transmission through a stubbed waveguide such as in Fig. 31(b). In (a) and (b) the width of the waveguide is $d = 6.5$ mm and the length of the stub is respectively equal to one or two periods of the phononic crystal (i.e. one or two cylinders have been removed perpendicularly to the waveguide). In (c) and (d) the width of the waveguide is only $d = 4$ mm to show the possibility of selective transmission in a frequency range in which the propagation is prohibited along the guide.

resonators that are attached to the waveguide. However, the number of such zeros of transmission is relatively smaller in the case the matrix of the phononic crystal is constituted by a fluid [78] because the fluid can only support compressional waves. In the case of a solid/solid composite considered here, both shear and compressional waves can propagate inside the waveguide and resonators. As a consequence the transmission spectrum appears to be more rich and also more complicated due to this coupling between longitudinal and transverse vibrations in solid materials. The results of Fig. 37 show that the transmission spectra still contain very deep negative peaks, as well as some smaller dips. Nevertheless, it is difficult to predict the exact frequencies of the dips, in contrast to the case of phononic crystals in which the background is a fluid material that can support only compressional waves [78]. From a qualitative point of view, the number of such zeros of transmission increases by increasing the length of the stub, as can be seen from a comparison of Fig. 37(a) and (b). This is expected since the resonator constituted by the stub can support an increasing number of modes when increasing its length.

In Fig. 37(c) and (d), the width of the waveguide is made even smaller, i.e. $d = 4$ mm only. This has the effect of shifting upwards the dispersion curves of the waveguide, therefore leaving the lower part of the phononic crystal bandgap (from 80 to 120 kHz) free of modes. In other words, the waves are prohibited from propagation along the waveguide in the above frequency range. In this region, due to the presence of the stub, selective transmission becomes possible by the well known quantum tunneling effect at the frequencies of the modes induced by the stub. One can notice a good correspondence between some of these peaks and the strongest dips in Fig. 37(a). Therefore, the same stub can induce selective transmissions or zeros of transmission depending on whether the propagation is forbidden or allowed through the waveguide.

3.3. Multiplexing of acoustic waves

Demultiplexing of acoustic waves has been predicted theoretically and/or observed experimentally in two-dimensional phononic crystals [95,96]. In particular, a great deal of theoretical and experimental work was devoted to the study of the propagation of acoustic waves in a guide (created by removing a row of cylinders) in a two-dimensional phononic crystal composed of steel cylinders in water, as well as the interaction of such a guide with a cavity or a stub. For instance [78,81], a cavity inside the guide permits us to select a particular frequency to be transmitted, while the presence of a stub at the side of a waveguide leads to zeros of transmission, removing a few frequencies from the transmission spectrum.

Based on the above knowledge, the aim of this section is to review, both theoretically and experimentally, the acoustic channel drops tunneling in a phononic crystal, namely the possibility of transferring one particular acoustic wavelength between two parallel waveguides coupled through an appropriate coupling element. The basic theoretical ideas for such a selective transfer to occur, leaving all other neighboring states unaffected, have been discussed thoroughly a few years ago by Fan et al. [97,98]. The phenomenon was also demonstrated by a numerical simulation in a photonic crystal. Subsequent works have adapted the same idea to other systems or models [4,99]. In the case of the phononic crystal discussed below, the coupling element is composed of two coupled cavities interacting with stubs located at the sides of the two parallel guides (see Fig. 38).

Our ultrasonic crystal is composed of a two dimensional square array of steel cylinders in water. The elastic parameters of the materials are summarized in Table 2. The lattice parameter, a, is 3 mm and the diameter of cylinders is 2.5 mm, resulting in a filling fraction of 55%. Such a phononic crystal displays an absolute
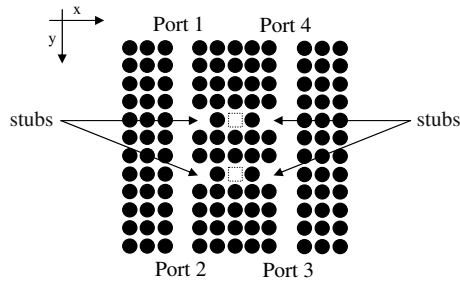
Fig. 38. Schematic view of the phononic crystal with two waveguides coupled through an element composed by two cavities (represented by dotted squares). Stubs along the guides ensure the efficiency of the coupling. Extremities of the two waveguides are labeled as ports 1–4.

Table 2
Mass density ρ, longitudinal speed of sound c_L and transverse speed of sound c_T of water and steel.

Material	ρ (kg m^{-3})	c_L (m s^{-1})	c_T (m s^{-1})
Water	1000	1490	–
Steel	7780	5825	3226

band gap ranging from 250 to 325 kHz [79]. The waveguides are formed (Fig. 38) by removing two parallel rods of steel cylinders along the direction of propagation (ΓX). The coupling element is constituted by two single-mode cavities. However, to ensure an efficient coupling between each cavity and the neighboring guides, we have grafted a stub to the side of the guide (Fig. 38). Let us notice that due to the simplicity of the geometrical model we were able to perform an experiment which is described in the second part of this section.

Numerical simulations of the transmission responses were obtained by using a finite-difference time-domain program.

The sample is constructed in three parts along the direction of propagation y. The central region, which contains the finite

size inhomogeneous phononic crystal, is sandwiched between two homogeneous media used for launching and probing the acoustic waves. In our finite difference time domain calculation, the structure is periodically repeated along the x direction; for instance, in the case of Fig. 38, the unit cell along x contains 13 rows of cylinders. This number is chosen in order to obtain a good compromise between the time needed for numerical simulations and the efficiency of isolating each unit cell from the neighboring ones. The space is discretized in both x and y directions with a mesh interval of ($a/50$). The equations of motion are solved with a time integration step of 4 ns with a number of steps equal to 2^{21}.

A broad band wave packet is launched in the first homogeneous region. The incoming wave is a longitudinal pulse, with a Gaussian profile along the x and y directions. In the x direction, the incoming signal covered the entrance of port 1, leaving port 2 without any signal. The transmitted signals are recorded as a time function at ports 2, 3 and 4 and are integrated over the cross section of each waveguide. All transmitted spectrum, presented below in decibels (dB) without any normalization, correspond to the Fourier transform of the recorded signal.

Fig. 39 displays the theoretical transmission along a single straight wave guide, either when the guide is perfect, or when a stub is inserted at the side of the guide and when a single cavity is inserted inside the crystal. The guide exhibits a full transmission band of acoustic waves in the frequency range [270 kHz, 300 kHz] that covers a large part of the phononic crystal stop band. The insertion of the cavity (resp. a stub) gives rise to a filtering (resp. a rejecting) of a narrow frequency domain around 290 kHz in the transmission spectrum. It is interesting to notice that the resonances of both defects occur almost at the same frequency ($f = 290$ kHz), which again is in favor of the coupling geometry shown in Fig. 38.

In Fig. 40, we present the theoretical transmission through different ports of Fig. 38 when the incident signal is launched from port 1. One can observe that the direct transmission at port
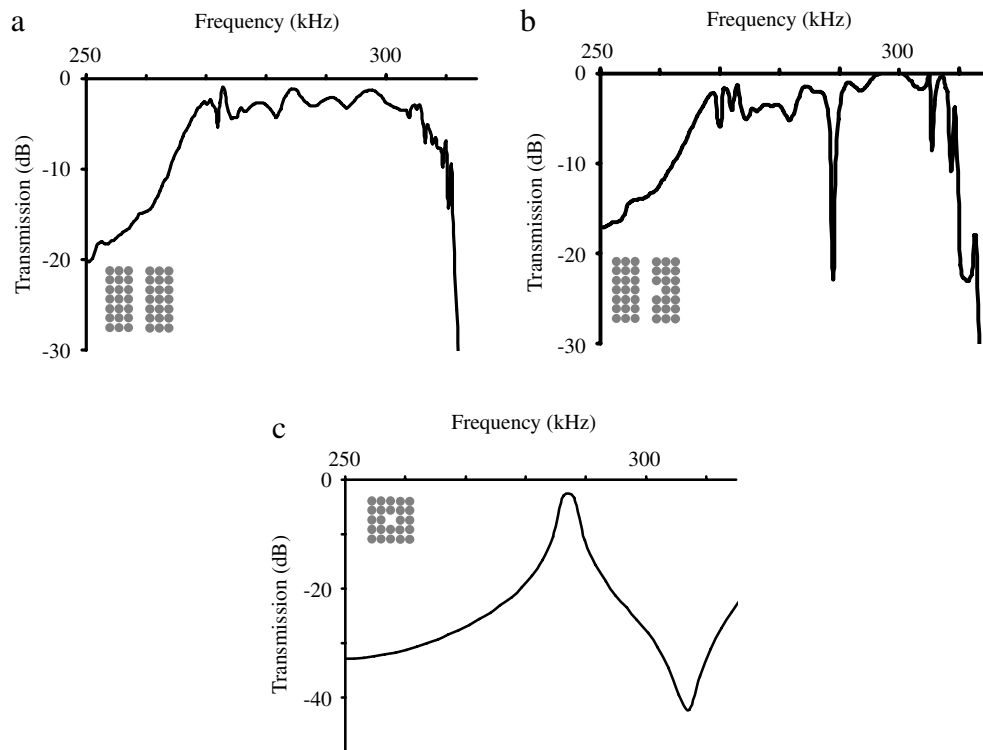
Fig. 39. Modelised transmission spectrum (a) through a straight waveguide in the phononic crystal, in the frequency range of the absolute band gap (from 250 to 320 kHz), (b) through a straight waveguide when a stub is inserted at the side of the guide and (c) for a single cavity inside the crystal.
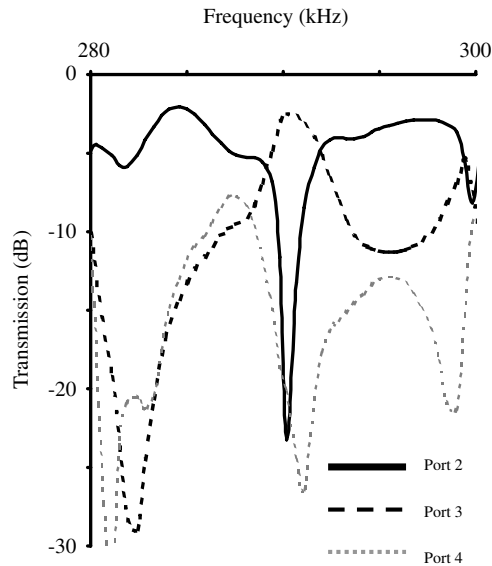
Fig. 40. Numerical transmission spectra at outputs 2, 3 and 4 for an input Gaussian excitation coming from port 1. At the frequency of 290 kHz, the incident wave drops from the first to the second waveguide.

Fig. 42. Experimental transmission spectra for the phononic crystal structure. The channel drop process from port 1 to 3 is observed at 290 kHz as predicted numerically.

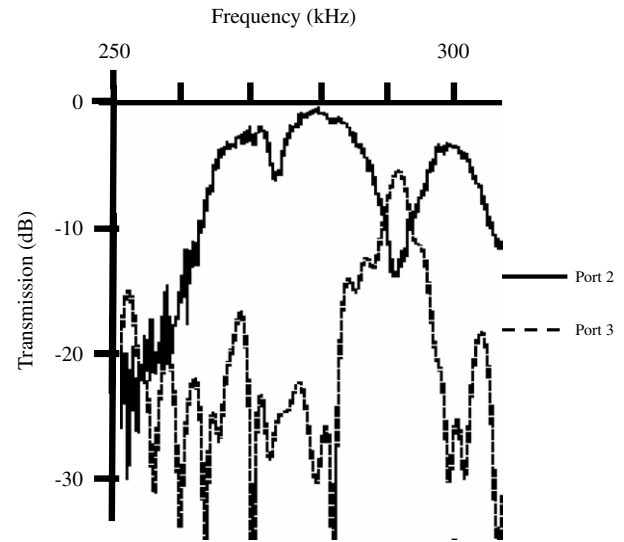**Fig. 41.** (Color online). Calculated displacement field along the direction of propagation (averaged over one period of oscillation) at the frequency $f = 290$ kHz. Red color (respectively blue) corresponds to the highest (respectively lowest) value of the displacement field given in arbitrary units.

2 drops almost to zero at the frequency of 290 kHz. At the same time a significant peak of transmission occurs at port 3, with magnitude comparable to the loss at port 2, while the signal at port 4 remains weak. This means that, at this frequency, the incoming signal is essentially transferred to the second waveguide towards port 3, leaving all other exits of the structure unaffected. In other words, the input signal tunneled through the coupling element and dropped inside the second waveguide.

To obtain a direct confirmation of the multiplexing phenomenon, the finite difference time domain computation has been used to simulate a monochromatic source at the frequency $f = 290$ kHz. The computed displacement field along the direction of propagation is displayed in Fig. 41. The transfer of the input signal from port 1 to port 3 is clearly apparent with an absence of signal

at port 2. Let us recall that, due to the periodicity of the structure along the x direction, the displacement field in the exit domain results from a superposition of the signals coming out of port 3 in two neighboring cells. At port 4, a weak signal is still observed, probably due to the incident waves launched from the sources in two neighboring cells.

As already mentioned, the simplicity of the structure has been chosen with the aim of realizing the corresponding experiment. The experimental set-up is based on the ultrasonic immersion transmission technique [100]. A couple of wide-band-width transmitter–receiver generators (Panasonic model 5800) produce a short duration pulse which is applied to the source transducer launching the probing longitudinal waves. The signal detected by the receiving transducer is acquired by the pulser/receiver, post amplified, and then digitized by a digital sampling oscilloscope. To reduce random errors, 500 measurements are averaged before a fast Fourier transform is performed to obtain the transmission spectrum. The system is first calibrated with no sample present; a reference signal is digitized and its spectrum is used to normalize the subsequent transmission spectra.

The measured transmissions are displayed in Fig. 42. The continuous and dashed lines represent the transmission spectra at ports 2 and 3 respectively. As a first comment, we can observed that the maximum value of the experimental transmission in port 2 is 10 dB less than the theoretical one (-62 dB instead of -52 dB). This is due to the position of the detector which is not exactly positioned at the exit waveguide in the experimental device. However, inside the transmission band of the main waveguide, extending from 250 to 320 kHz, we observe a drop of the amplitude at port 2 at the frequency of 290 kHz together with an increase of the amplitude at port 3. The amplitude at port 2 is estimated to be 15 dB lower than the incoming signal amplitude. This means that at this frequency the input signal is almost completely transferred from the first continuum waveguide to the second one through the coupling element. On the other hand, the transmission peak which occurs at port 3 presents a magnitude lower than the loss at port 2. This signifies that, at $f = 290$ kHz, the totality of the signal has not been transmitted from port 1 to 3. We expect that the difference has been linked to the absorption of the signal during the transfer via the coupling element. Nevertheless, these experimental results are in good agreement with the numerical transmission spectra presented in Fig. 40 in regards to the frequency of the phenomenon.

3.4. Summary

The experimental results presented in this section report first on the transmission of audible acoustic waves along waveguides in a two-dimensional phononic crystal. We show the existence of deaf modes in the band structure of the waveguide. We demonstrate the possibility of resonant filtering in a linear phononic crystal waveguide with one single side branch resonator. Frequency filtering takes place by reduction of the transmission at specific frequencies within the passing band of the waveguide. These frequencies depend on the length of the resonator. The experimental results are in fair agreement with theoretical calculations, especially at the lowest frequencies studied. A waveguide with a sharp bend appears to transmit acoustic waves without significant loss over most of the passing band of a linear guide. Similarly to the linear guide with a resonator, transmission along the bent waveguide is significantly reduced at some specific frequencies which is believed to be due to interference between incident and reflected waves near the bend. Such structures may serve as an element in the design of devices for the treatment of acoustic signals such as filtering.

Then we reviewed the propagation of acoustic waves through defect-containing waveguide structures in phononic crystals composed of solid constituents. First, we have considered the case of perfect waveguides, mainly to show that the number and dispersion of the localized branches that contribute to transmission can be adjusted by varying the width of the guide. In particular, the guide can be made monomode over a large frequency range of the phononic crystal band gap. Other geometrical structures of the waveguide would also be interesting [71] for applications.

The transmission through the waveguide can be significantly altered by incorporating a cavity inside or at the side of the guide. In a cavity-containing waveguide, the transmission can be limited to narrow frequency domains situated in the vicinity of the characteristic frequencies of the cavity. Depending on their symmetry, different modes can be excited and contribute to transmission when either a longitudinal or a transverse incident wave is launched onto the phononic crystal. The transmission peaks can be made sharper by increasing the isolation of the cavity. In the case of a waveguide with a cavity along its side, the main modification in the transmission as compared to the case of a perfect waveguide is the existence of notches that occur at the characteristic frequencies of the cavity. The dips in the transmission become in general deeper when the propagation along the waveguide is made monomode. Zeros of transmission can also be induced in the transmission spectrum by simply coupling the waveguide to a stub. However, unlike the case of an isolated cavity, it is more difficult to find a simple interpretation of their frequencies, especially in the case of solid/solid composites because the longitudinal and transverse waves are strongly coupled together.

It would be interesting to investigate the above phenomena in more detail for different shapes of the cavities and different strengths of their coupling with the guide, as well as a combination of such defects [69–72]. A rich variety of situations may occur, especially in view of the fact that the phononic crystal can be composed of both solid and fluid constituents that can support different polarizations of the waves.

We reviewed in the last subsection experimentally and numerically an acoustic model of channel drop processes. The general device is composed of two continuum waveguides and a coupling element constituted by two cavities inserted in a phononic crystal made of steel cylinders in water. The cavities are coupled to the waveguides through stubs grafted at the sides of the guides. This basic model has been chosen to realize experimental measurement in comparison with the theoretical simulation. We have demonstrated that at the frequency of $f = 290$ kHz, we have a complete transfer of the wave between the two continuum through localized states of the coupling element. We have shown that this frequency corresponds to the resonant mode of the coupling element. Of course, the multiplexing phenomenon could be improved or tuned by adjusting other parameters in the model such as the diameters and the nature of the cylinders surrounding the cavities in order to modify their interaction. Such devices could find their applications for frequency division multiplexing in acoustical systems.

4. Crystal plates and high-frequency radio-frequency devices

Earlier studies of bulk phononic crystals i.e. phononic crystals assumed of infinite extent along the 3 spatial directions, have shown that the bandwidth of the forbidden band depends strongly on the contrast between the physical characteristics (density and elastic moduli) of the inclusions and the matrix, as well as the geometry of the array of inclusions, the inclusion shape and the filling factor of inclusions [31,26,37,101]. More recently, various authors have studied theoretically the existence of surface acoustic waves localized at the free surface of a semi-infinite two-dimensional phononic crystal [102–105],whereas the case of three-dimensional phononic crystals has only been dealt more recently [106]. A few works have also investigated the dispersion curves of acoustic waves in a free or supported plate for one-dimensional [107–109] or two-dimensional [110–116] phononic crystals. The existence of band gaps in such geometries may be useful for the purpose of introducing functionalities such as waveguiding and filtering in integrated structures. They can operate at the frequencies of telecommunications (about 1 GHz) when the thickness of the plate is in the micron range. Let us also mention two experiments dealing with the study of vibrations in a periodical array of dots deposited on a substrate in the GHz regime [117,118].

4.1. The phononic crystal plate

4.1.1. Introduction

In this subsection, we report on band gap properties and applications of two phononic crystal based structures, namely the phononic crystal plate and the periodical array of dots deposited on a thin substrate.

For the first geometry considered in this section, the parallel inclusions are of cylindrical shape and the surface considered is perpendicular to their axis. Various arrays of inclusions [102,103], crystallographic symmetries of the component materials [104], and also the piezoelectricity of one of the constituents [105] were taken into account by several authors. In these studies, the same method of computation of the surface acoustic wave band structure was applied. This method is based on the plane wave expansion method [31,26,37] with surface acoustic waves explicitly searched as solutions of the Fourier-transformed equation of propagation, exponentially decreasing along the cylinders' direction and by imposing the proper boundary conditions on the free surface. This method initially developed by Tanaka et al. [102] for semi-infinite two-dimensional phononic crystals exhibiting a single free surface was applied to compute the band structures of two-dimensional phononic crystal plates, with two free surfaces [119,120]. For example, the symmetric Lamb mode band structures of two-dimensional phononic crystal plates composed of triangular arrays of W cylinders in an Si background were calculated [119]. More recently, Charles et al. [120] reported on the band structure of a slab made of a square array of Fe cylinders embedded in a Cu matrix. Nevertheless, no absolute stop bands were reported in these studies. Hsu and Wu [111] combined Mindlin's

plate theory and the plane wave expansion method for the calculation of the lower dispersion curves in the band structure of two-dimensional gold/epoxy phononic crystal plates. While accurate, this method however is restricted to thin plates. Moreover, Manzanares-Martinez and Ramos-Mendieta have also considered the propagation of acoustic waves along a surface parallel to the cylinders in a two-dimensional phononic crystal [121]. R. Sainidou et al. investigated with the help of the layer-multiple scattering method, the guided elastic waves in a glass plate coated on one side with a periodic monolayer of polymer spheres immersed in water [122]. From the experimental point of view, Wu et al. [123, 124] observed high frequency surface acoustic waves with a pair of interdigital transducers placed on both sides of a very thick silicon plate in which a square array of holes was drilled. Similar experiments were conducted by S. Benchabane et al. on a two-dimensional square lattice piezoelectric phononic crystal etched into lithium niobate [125]. Zhang et al. [126] have shown the existence of gaps for acoustic waves propagating at the surface of an air/aluminium two-dimensional phononic crystal plate through laser ultrasonic measurements.

In this subsection [115,113], we use a supercell plane wave expansion method to calculate the band structure of a two-dimensional phononic crystal plate of finite thickness along the axis of the cylinders. We highlight the differences between two-dimensional bulk phononic crystal dispersion curves and the band structure of the phononic crystal plate. We investigate the influence of the constituent materials, of the plate thickness, and of the geometry of the array on the band structure. Furthermore we identify the conditions for convergence of the supercell plane wave expansion method in terms of the contrast in the physical properties of the constituent materials of the phononic crystal plate. We focus on two-dimensional phononic crystal plates made of solid cylindrical inclusions embedded in a solid material and on arrays of air holes drilled in a solid matrix. In the case of air holes/solid matrix phononic crystal plates, we characterize the optimum conditions for the existence of wide absolute forbidden bands upon variations of the thickness of the plate. We demonstrate that removing cylinders in a phononic crystal plate with a forbidden band to form a waveguide leads to the existence of guided acoustic modes.

4.1.2. Models and plane wave expansion

4.1.2.1. Plane wave expansion method for bulk phononic crystals. We first briefly recall the basic principles of the plane wave expansion method used for the calculation of the band structures of bulk two-dimensional phononic crystals. The presentation given here is more general than the one of Section 2 where we assumed that the transverse modes can be decoupled from the modes with the two other polarizations. Two-dimensional phononic crystals are modeled as periodic arrays of infinite cylinders of different shapes (circular, square, etc.) made up of a material *A* embedded in an infinite matrix *B*. Elastic materials *A* and *B* may be isotropic or of specific crystallographic symmetry. The elastic cylinders are assumed parallel to the *z* axis of the Cartesian coordinate system (O, x, y, z). The intersections of the cylinders axis with the (xOy) transverse plane form a two-dimensional periodic array and the nearest neighbor distance between cylinders is *a*. The two-dimensional primitive unit cell may contain one cylinder, or more. The filling factor, f_i, of each inclusion is defined as the ratio between the cross-sectional area of a cylinder and the surface of the primitive unit cell.

In the absence of an external force, the equation of propagation of the elastic waves in any composite material is given as:

$$\rho(\mathbf{r}) \frac{\partial^2 u_i(\mathbf{r}, t)}{\partial t^2} = \sum_{j,m,n} \frac{\partial}{\partial x_j} \left(C_{ijmn}(\mathbf{r}) \frac{\partial u_n(\mathbf{r}, t)}{\partial x_m} \right) \quad (35)$$
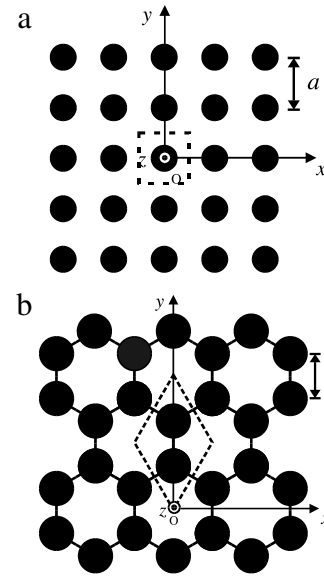
Fig. 43. Transverse cross-section of the square (a) and of the graphite (b) arrays. The cylinders are parallel to the *z* direction. The dotted lines represent the primitive unit cell of the two-dimensional array.

where $u_i(\mathbf{r}, t)$ is a component $(i \equiv x, y, z)$ of the elastic displacement field. The elements C_{ijmn} $(i, j, m, n = 1, \ldots, 6)$ of the elastic stiffness tensor and the mass density ρ are periodic functions of the position vector, $\mathbf{r} = (\mathbf{r}_{//}, z) = (x, y, z)$.

In the particular case of bulk phononic crystals, i.e. assumed of infinite extent along the three spatial directions *x*, *y* and *z*, the elastic constants and the mass density do not depend on *z*. Then taking advantage of the two-dimensional periodicity in the (xOy) plane, they can be expanded in Fourier series in the form:

$$C_{ijmn}(\mathbf{r}_{//}) = \sum_{\mathbf{G}_{//}} C_{ijmn}(\mathbf{G}_{//}) e^{i\mathbf{G}_{//} \cdot \mathbf{r}_{//}} \quad (36)$$

$$\rho(\mathbf{r}_{//}) = \sum_{\mathbf{G}_{//}} \rho(\mathbf{G}_{//}) e^{i\mathbf{G}_{//} \cdot \mathbf{r}_{//}} \quad (37)$$

where $\mathbf{G}_{//} = (G_x, G_y)$ is a two-dimensional reciprocal-lattice vector. One writes, with the help of the Bloch theorem, the elastic displacement field as:

$$\mathbf{u}(\mathbf{r}) = e^{i(\omega t - \mathbf{K}_{//} \cdot \mathbf{r}_{//} - K_z z)} \sum_{\mathbf{G}_{//}} \mathbf{u}_{\mathbf{K}}(\mathbf{G}_{//}) e^{i\mathbf{G}_{//} \cdot \mathbf{r}_{//}} \quad (38)$$

where $\mathbf{K} = (\mathbf{K}_{//}, K_z) = (K_x, K_y, K_z)$ is a wave vector and ω an angular frequency. If one assumes that $K_z = 0$ then the vibrations in the (xOy) plane (called *XY* or mixed-polarization modes) decouple from those parallel to the *z* direction denoted *Z* modes (transverse modes) [31,37]. Substituting Eqs. (36)–(38) into Eq. (35) leads to a standard eigenvalue equation for which the size of the matrices involved depends on the number of two-dimensional $\mathbf{G}_{//}$ vectors taken into account in the Fourier series. The numerical resolution of the eigenvalue equation is performed along the principal directions of propagation of the two-dimensional irreducible Brillouin zone of the array of inclusions.

In this subsection, phononic crystals with square lattice and graphite array are considered (see Fig. 43). For a square lattice of inclusions (see Fig. 43(a)), with one cylinder of filling factor *f* located at the center of the two-dimensional primitive unit cell, the Fourier coefficients in Eqs. (36) and (37) are given as:

$$\zeta(\mathbf{G}_{//}) = \frac{1}{A_u} \iint_{\left(\substack{\text{primitive} \\ \text{unit cell}}\right)} \zeta(\mathbf{r}_{//}) e^{-i\mathbf{G}_{//} \cdot \mathbf{r}_{//}} d^2 \mathbf{r}_{//}$$

$$= \begin{cases} f\zeta_A + (1-f)\zeta_B, & \text{if } \mathbf{G}_{//} = \mathbf{0} \\ (\zeta_A - \zeta_B)F(\mathbf{G}_{//}), & \text{if } \mathbf{G}_{//} \neq \mathbf{0} \end{cases} \quad (39)$$

where $\zeta \equiv \rho$, C_{ijmn}, and A_u, is the area of the two-dimensional primitive unit cell. $F(\mathbf{G}_{//})$ is the structure factor defined as:

$$F(\mathbf{G}_{//}) = \frac{1}{A_u} \iint_{(A)} e^{-\iota \mathbf{G}_{//} \cdot \mathbf{r}_{//}} d^2 \mathbf{r}_{//}. \tag{40}$$

In Eq. (40), the integral is performed over the cross-section of the inclusion. For cylinders of circular cross-section of radius R, the structure factor is:

$$F(\mathbf{G}_{//}) = 2f \frac{J_1(G_{//}R)}{G_{//}R} \tag{41}$$

where J_1 is the Bessel function of the first kind, $f = \pi R^2/a^2$ and $0 \le f \le \pi/4$. The components of the two-dimensional reciprocal lattice vectors $\mathbf{G}_{//}$ are $G_x = \frac{2\pi}{a} n_x$ and $G_y = \frac{2\pi}{a} n_y$ where n_x and n_y are integers. In the course of the numerical calculations, we consider $-M_x \le n_x \le +M_x$ and $-M_y \le n_y \le +M_y$ (with M_x and M_y positive integers) i.e. that $(2M_x+1)(2M_y+1)$ two-dimensional $\mathbf{G}_{//}$ vectors (G_x and G_y have $(2M_x+1)$ and $(2M_y+1)$ different values, respectively) are taken into account. This gives $3(2M_x+1)(2M_y+1)$ eigenfrequencies ω for a given wave vector $\mathbf{K}$.

In the graphite network (see Fig. 43), the inclusions are located at the vertices of a regular hexagon and the distance between two nearest neighbors is a. The two-dimensional primitive unit cell with a lozenge pattern of side $a\sqrt{3}$ contains two identical cylinders of filling factors f_1 and f_2, located at $\boldsymbol{\tau_i}$ ($i = 1, 2$) and the Fourier coefficients become:

$$\zeta(\mathbf{G}_{//}) = \begin{cases} f\zeta_A + (1-f)\zeta_B, & \text{if } \mathbf{G}_{//} = \mathbf{0} \\ (\zeta_A - \zeta_B)F(\mathbf{G}_{//})\left(\dfrac{e^{-\iota \mathbf{G}_{//} \cdot \boldsymbol{\tau}_1} + e^{-\iota \mathbf{G}_{//} \cdot \boldsymbol{\tau}_2}}{2}\right), \\ \qquad \text{if } \mathbf{G}_{//} \ne \mathbf{0} \end{cases} \tag{42}$$
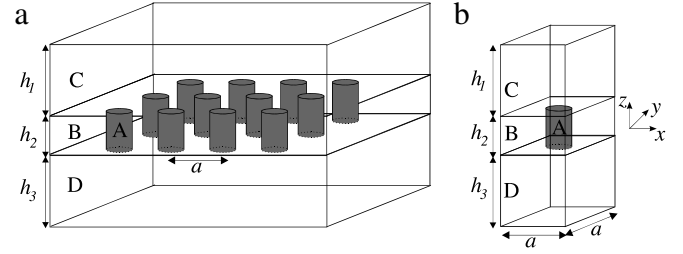
where $F(\mathbf{G}_{//})$ has the same meaning as above, $f = f_1 + f_2$ is the total filling factor of inclusion with $f_1 = f_2 = 2\pi R^2/3\sqrt{3}a^2$ ($0 \le f_1, f_2 \le \pi/6\sqrt{3}$) for cylindrical inclusions. The components of the two-dimensional reciprocal lattice vectors $\mathbf{G}_{//}$ are $G_x = \frac{2\pi}{a\sqrt{3}}(n_x - n_y)$ and $G_y = \frac{2\pi}{a\sqrt{3}}(\frac{n_x+n_y}{\sqrt{3}})$ where n_x and n_y are integers [37].

4.1.2.2. Plane wave expansion method for phononic crystal plates. To calculate the elastic band structures of two-dimensional phononic crystal plates, one modifies the plane wave expansion method presented above. The phononic crystal plate of thickness, h_2, is assumed infinite in the (xOy) plane of the Cartesian coordinate system (O, x, y, z). The plate is sandwiched between two slabs of thicknesses h_1 and h_3, made of elastic homogeneous materials C and D, see Fig. 44(a). In the course of the numerical calculations, one considers the parallelepipedic supercell depicted in Fig. 44(b). The basis of the supercell in the (xOy) plane includes that of the two-dimensional primitive unit cell (which may contain one cylinder or more) of the array of inclusions and its height along the z direction is $\ell = h_1 + h_2 + h_3$. This supercell is repeated periodically along the x, y and z directions. This triple periodicity allows one to develop the elastic constants and the mass density of the constituent materials as Fourier series as:

$$\zeta(\mathbf{r}) = \sum_{\mathbf{G}} \zeta(\mathbf{G}) e^{\iota \mathbf{G} \cdot \mathbf{r}} \tag{43}$$

where $\mathbf{r} = (\mathbf{r}_{//}, z) = (x, y, z)$ and $\mathbf{G} = (\mathbf{G}_{//}, G_z) = (G_x, G_y, G_z)$ are *three-dimensional position vectors and reciprocal lattice vectors* respectively. Moreover the elastic displacement field can be written as

$$\mathbf{u}(\mathbf{r}) = e^{\iota(\omega t - \mathbf{K}_{//} \cdot \mathbf{r}_{//} - K_z z)} \sum_{\mathbf{G}} \mathbf{u}_{\mathbf{K}}(\mathbf{G}) e^{\iota \mathbf{G} \cdot \mathbf{r}}. \tag{44}$$

Fig. 44. (a) Two-dimensional phononic crystal plate sandwiched between two slabs of homogeneous materials, and (b) three-dimensional supercell considered in the course of the supercell-plane wave expansion computation.

The components in the (xOy) plane of the $\mathbf{G}$ vectors depend on the geometry of the array of inclusions (see above) while along the z direction, $G_z = \frac{2\pi}{\ell} n_z$ where n_z is an integer. The Fourier coefficients in Eq. (44) are now given as:

$$\zeta(\mathbf{G}) = \frac{1}{V_u} \iiint_{(\text{super cell})} \zeta(\mathbf{r}) e^{-\iota \mathbf{G} \cdot \mathbf{r}} d^3 \mathbf{r} \tag{45}$$

with $V_u = A_u.\ell$ is the volume of the supercell.

For a square array of inclusions, the Fourier coefficients become:

$$\zeta(\mathbf{G}) = \begin{cases} f\zeta_A\left(\dfrac{h_2}{\ell}\right) + (1-f)\zeta_B\left(\dfrac{h_2}{\ell}\right) + \zeta_C\left(\dfrac{h_1}{\ell}\right) \\ \quad + \zeta_D\left(\dfrac{h_3}{\ell}\right), \quad \text{if } \mathbf{G} = \mathbf{0} \\ (\zeta_A - \zeta_B)F^s_I(\mathbf{G}) + (\zeta_C - \zeta_B)F^s_{II}(\mathbf{G}) \\ \quad + (\zeta_D - \zeta_B)F^s_{III}(\mathbf{G}), \quad \text{if } \mathbf{G} \ne \mathbf{0} \end{cases} \tag{46}$$

with

$$\begin{aligned} F^s_I(\mathbf{G}) &= \frac{1}{V_u} \iiint_{(A)} e^{-\iota \mathbf{G} \cdot \mathbf{r}} d^3 \mathbf{r} \\ &= F(\mathbf{G}_{//}) \left(\frac{\sin\left(G_z \frac{h_2}{2}\right)}{\left(G_z \frac{h_2}{2}\right)}\right) \cdot \left(\frac{h_2}{\ell}\right) \end{aligned} \tag{47a}$$

$$\begin{aligned} F^s_{II}(\mathbf{G}) &= \frac{1}{V_u} \iiint_{(C)} e^{-\iota \mathbf{G} \cdot \mathbf{r}} d^3 \mathbf{r} \\ &= \left(\frac{\sin\left(G_x \frac{a}{2}\right)}{\left(G_x \frac{a}{2}\right)}\right) \cdot \left(\frac{\sin\left(G_y \frac{a}{2}\right)}{\left(G_y \frac{a}{2}\right)}\right) \cdot \left(\frac{\sin\left(G_z \frac{h_1}{2}\right)}{\left(G_z \frac{h_1}{2}\right)}\right) \\ &\quad \times \left(\frac{h_1}{\ell}\right) . e^{-\iota G_z \left(\frac{h_1+h_2}{2}\right)} \end{aligned} \tag{47b}$$

$$\begin{aligned} F^s_{III}(\mathbf{G}) &= \frac{1}{V_u} \iiint_{(D)} e^{-\iota \mathbf{G} \cdot \mathbf{r}} d^3 \mathbf{r} \\ &= \left(\frac{\sin\left(G_x \frac{a}{2}\right)}{\left(G_x \frac{a}{2}\right)}\right) \cdot \left(\frac{\sin\left(G_y \frac{a}{2}\right)}{\left(G_y \frac{a}{2}\right)}\right) \cdot \left(\frac{\sin\left(G_z \frac{h_3}{2}\right)}{\left(G_z \frac{h_3}{2}\right)}\right) \\ &\quad \times \left(\frac{h_3}{\ell}\right) . e^{-\iota G_z \left(\frac{h_2+h_3}{2}\right)}. \end{aligned} \tag{47c}$$

In Eq. (47), the integration is performed over the volume occupied by each material A, C, or D inside the unit cell. In Eq. (47a), $F(\mathbf{G}_{//})$ is the structure factor defined by Eq. (41) for cylindrical inclusions. For the graphite network, the Fourier coefficients become

$$\zeta(\mathbf{G}) = \begin{cases} f\zeta_A\left(\dfrac{h_2}{\ell}\right) + (1-f)\zeta_B\left(\dfrac{h_2}{\ell}\right) + \zeta_C\left(\dfrac{h_1}{\ell}\right) \\ \quad + \zeta_D\left(\dfrac{h_3}{\ell}\right), \quad \text{if } \mathbf{G}_{//} = \mathbf{0} \\ (\zeta_A - \zeta_B)F^g_{I}(\mathbf{G})\left(\dfrac{e^{-\imath\mathbf{G}_{//}\cdot\boldsymbol{\tau}_1} + e^{-\imath\mathbf{G}_{//}\cdot\boldsymbol{\tau}_2}}{2}\right) \\ \quad + (\zeta_C - \zeta_B)F^g_{II}(\mathbf{G}) + (\zeta_D - \zeta_B)F^g_{III}(\mathbf{G}), \\ \quad \text{if } \mathbf{G} \neq \mathbf{0} \end{cases} \quad (48)$$

with

$$F^g_{I}(\mathbf{G}) = \frac{1}{V_u}\iiint_{(A)} e^{-\imath\mathbf{G}\cdot\mathbf{r}}d^3\mathbf{r}$$

$$= F(\mathbf{G}_{//})\left(\frac{\sin\left(G_z\frac{h_2}{2}\right)}{(G_z\frac{h_2}{2})}\right)\cdot\left(\frac{h_2}{\ell}\right) \quad (49a)$$

$$F^g_{II}(\mathbf{G}) = \frac{1}{V_u}\iiint_{(C)} e^{-\imath\mathbf{G}\cdot\mathbf{r}}d^3\mathbf{r}$$

$$= \left(\frac{\sin\left(G'_x\frac{a\sqrt{3}}{2}\right)}{(G'_x\frac{a\sqrt{3}}{2})}\right)\cdot\left(\frac{\sin\left(G'_y\frac{a\sqrt{3}}{2}\right)}{(G'_y\frac{a\sqrt{3}}{2})}\right)\cdot\left(\frac{\sin\left(G_z\frac{h_1}{2}\right)}{(G_z\frac{h_1}{2})}\right)$$

$$\times \left(\frac{h_1}{\ell}\right).e^{-\imath G_z\left(\frac{h_1+h_2}{2}\right)} \quad (49b)$$

$$F^g_{III}(\mathbf{G}) = \frac{1}{V_u}\iiint_{(D)} e^{-\imath\mathbf{G}\cdot\mathbf{r}}d^3\mathbf{r}$$

$$= \left(\frac{\sin\left(G'_x\frac{a\sqrt{3}}{2}\right)}{(G'_x\frac{a\sqrt{3}}{2})}\right)\cdot\left(\frac{\sin\left(G'_y\frac{a\sqrt{3}}{2}\right)}{(G'_y\frac{a\sqrt{3}}{2})}\right)\cdot\left(\frac{\sin\left(G_z\frac{h_3}{2}\right)}{(G_z\frac{h_3}{2})}\right)$$

$$\times \left(\frac{h_3}{\ell}\right).e^{-\imath G_z\left(\frac{h_2+h_3}{2}\right)} \quad (49c)$$

where

$$\begin{cases} G'_x = \dfrac{G_x + \sqrt{3}G_y}{2} \\ G'_y = \dfrac{-G_x + \sqrt{3}G_y}{2}. \end{cases} \quad (50)$$

As for the bulk phononic crystals, the equation of motion is Fourier transformed by substituting Eqs. (43) and (44) in Eq. (35) and one has again to resolve a standard eigenvalue equation. The numerical resolution of this eigenvalue equation is performed along the principal directions of propagation of the two-dimensional irreducible Brillouin zone of the array of inclusions while K_z is fixed to any value lower than $\frac{\pi}{\ell}$. In the course of the numerical calculations, G_x, G_y and G_z take respectively $(2M_x + 1)$, $(2M_y + 1)$ and $(2M_z + 1)$ discrete values and this leads to $3(2M_x + 1)(2M_y + 1)(2M_z + 1)$ eigenfrequencies for a given wave vector $\mathbf{K}$.

The supercell method requires an interaction as low as possible between the vibrational modes of neighboring periodically repeated phononic crystal plates. Then, in order to allow the top surface of the plate to be free of stress, medium C should behave, for instance, like a vacuum [121]. But, as already observed by various authors [121,127,63], the choice of the physical parameters characterizing vacuum in the course of the plane wave expansion computations is of critical importance. Indeed, in the framework of the plane wave expansion method, taking abruptly $C_{ijmn} = 0$ and $\rho = 0$ for vacuum leads to numerical instabilities and unphysical results [121,127,63]. Then the vacuum must be modeled as a pseudo-solid material with very low C_{ijmn} and ρ. For the sake of simplicity, this low impedance medium is supposed elastically

isotropic and is characterized by a longitudinal speed of sound c_ℓ, and a transversal speed of sound c_t or equivalently by two elastic moduli expressed with the Voigt notation as $C_{11} = \rho c_\ell{}^2$ and $C_{44} = \rho c_t{}^2$. The choice of the values of these parameters is governed by the boundary condition between any solid material and vacuum. Indeed, one knows that this interface must be free of stress and this requires that $C_{11} = 0$ and $C_{44} = 0$ rigorously in vacuum [105,121]. Then, using the low impedance medium to model the vacuum in the plane wave expansion computations, the non-vanishing values of these parameters must be as small as possible and we consider that the ratio between the elastic moduli of the low impedance medium and those of any other solid material constituting the phononic crystal must approach zero. We choose c_ℓ and c_t to be much larger than the speeds of sound in the usual solid materials in order to limit propagation of acoustic waves to the solid. Large speeds of sound and small elastic moduli impose a choice of a very low mass density for the low impedance medium. More specifically, we choose $\rho = 10^{-4}$ kg m^{-3} and $c_\ell = c_t = 10^5$ m s^{-1} i.e. the acoustic impedances of the low impedance medium are equal to 10 kg m^{-2} s^{-1}. With these values $C_{11} = C_{44} = 10^6$ N m^{-2} and the elastic constants of the low impedance medium are approximately 10^4 times lower than those of any usual solid material that are typically of the order of 10^{10} N m^{-2}. The values we choose for C_{11} and C_{44} are a compromise to achieve satisfactory convergence of the plane wave expansion method and still satisfy boundary conditions. Values of the elastic constants of the low impedance medium lower than 10^4 N m^{-2} can have, in some cases, effects on the numerical convergence. We choose $C_{11} = C_{44}$ for convenience. In the course of the plane wave expansion calculations, these values of the low impedance medium physical characteristics allow one to model the vacuum without numerical difficulties. One can also note that our choice of unphysical high speeds of sound for the low impedance medium such as $\frac{1}{c_\ell^2} = \frac{1}{c_t^2} \longrightarrow 0$ is consistent with the numerical condition $\frac{\rho^{Air}}{C^{Air}_{ijmn}} \longrightarrow 0$, derived by Y. Tanaka et al. for computing accurately the plane wave expansion bulk band structures of air/solid two-dimensional phononic crystals [63].

In the supercell, medium D can be either a vacuum or a homogeneous material depending on whether one wants to model a phononic crystal plate or a structure made of a phononic crystal plate deposited on a substrate of finite thickness. Throughout the present section, we restrict ourselves to isotropic materials A, B and D or to constituents of cubic crystallographic symmetry. Finally with our numerical method, computations of dispersion curves of phononic crystal plates with $K_z = 0$ and with any other non-vanishing value of K_z, lower than $\frac{\pi}{\ell}$, lead to nearly the same result. Indeed the eigenvalues computed with $K_z = 0$ and $K_z \neq 0$ differ only in their third decimal. This indicates that the homogeneous slabs C and D made of the low impedance medium modeling a vacuum rigorously provide appropriate decoupling of the plate modes of vibration in the z direction. Then, throughout this section, the value of K_z has been fixed to zero.

In what follows, we give numerical results for different types of crystal plates.

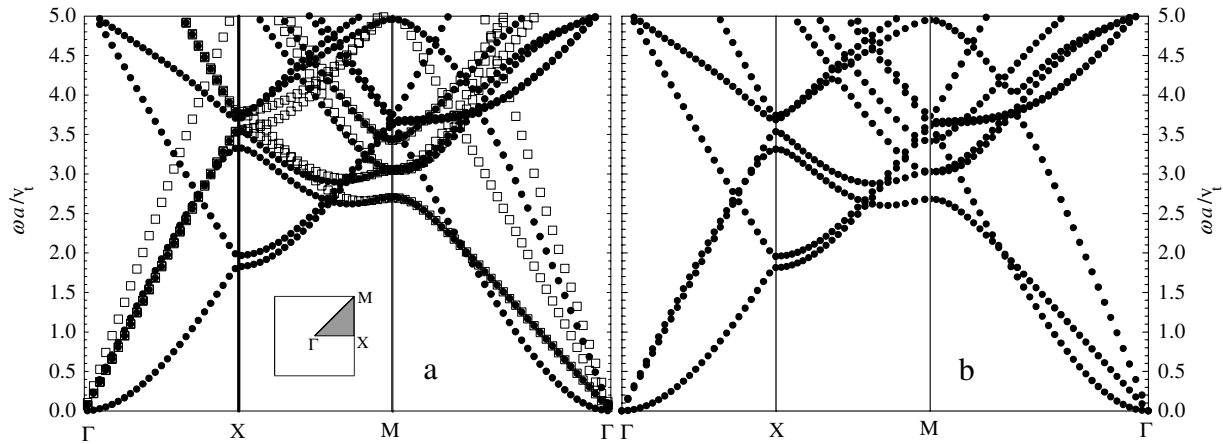### 4.1.3. Solid/solid two-dimensional phononic crystal plates

4.1.3.1. Low contrast solid/solid systems. We first apply our supercell plane wave expansion method to the calculation of the band structure of a phononic crystal plate made of a square array (lattice parameter a) of iron cylinders, of circular cross section of radius R, embedded in a copper background. Fe and Cu are materials of cubic crystallographic symmetry and their physical properties (density and elastic constants) present a low contrast [120] (see Table 3).

The filling factor ($f = \pi R^2/a^2$) and the thickness of the plate are $f = 0.564$ and $h_2 = 0.7a$, respectively. Fig. 45(a) shows the

Table 3
Mass density ρ and elastic constants C_{11}, C_{12} and C_{44} of Fe, Cu, steel, epoxy and Si.

Material	ρ (kg m^{-3})	C_{11} (10^{10} N m^{-2})	C_{12} (10^{10} N m^{-2})	C_{44} (10^{10} N m^{-2})
Fe (cubic)	7867	22.6	14.0	11.6
Cu (cubic)	8932	16.83	12.21	7.57
Steel (isotropic)	7780	26.4	–	8.1
Epoxy (isotropic)	1142	0.754	–	0.148
Si (cubic)	2331	16.578	6.394	7.962

Fig. 45. (a) Plane wave expansion elastic band structures for the bulk two-dimensional phononic crystal (open squares) and the phononic crystal plate of thickness $h_2 = 0.7a$ (black filled circles) made of a square array of Fe cylinders of cylindrical cross section embedded in a Cu background with $f = 0.564$. 169 and 343 (i.e. $M_x = M_y = 6$ and $M_x = M_y = M_z = 3$) reciprocal lattice vectors were taken into account for the computations of the plane wave expansion band structures of the bulk phononic crystal and of the phononic crystal plate, respectively. The inset represents the first Brillouin zone ($\Gamma X M$) of the square array. The components of the wave vector **K** at the Γ, X and M points are $\frac{2\pi}{a}(0,0)$, $\frac{2\pi}{a}(\frac{1}{2},0)$ and $\frac{2\pi}{a}(\frac{1}{2},\frac{1}{2})$. A dimensionless frequency $\omega a/c_t{}^{Cu}$ where $c_t{}^{Cu}$ is the transverse speed of sound in Cu, is reported on the vertical axis. (b) Supercell-plane wave expansion (black filled dots) and finite element method (black crosses) band structures of the same plate. Note the excellent agreement between the band structures of the plate derived from the two methods of calculation.

band structure of the bulk phononic crystal (hollow squares) and of the phononic crystal plate (black filled dots). The band structure of the bulk phononic crystal was computed with the classical plane wave expansion method (see the above subsection on the plane wave expansion method for bulk phononic crystals). Applying the supercell plane wave expansion method, one obtains the dispersion curves of the plate. In this case, materials C and D are made of a low impedance medium and the thicknesses h_1 and h_3 were chosen equal to a. 169 and 343 (i.e. $M_x = M_y = 6$ and $M_x = M_y = M_z = 3$) reciprocal lattice vectors were taken into account for the computations of the band structures of the bulk phononic crystal and of the phononic crystal plate, respectively. This choice of the number of reciprocal lattice vectors assures a good precision for the dispersion curves. One observes the characteristic nearly-parabolic shape in the vicinity of the Γ point of the antisymmetric Lamb mode A_0. This is the slowest of the modes starting at the Γ point. In this particular structure, the symmetric Lamb mode S_0 and the first transverse mode nearly overlap. These band structures are nearly the same as those published in Ref. [120]. In this reference, the dispersion curves of the plate were derived with the help of the plane wave expansion method, by imposing the stress free boundary conditions on the top and bottom surfaces of the plate [120]. However this latter method requires sampling of both wave vector and frequency while the supercell plane wave expansion method generates the eigenvalues (frequencies) by sampling only over the wave vector. In the case of the Fe/Cu system, the supercell plane wave expansion method achieves satisfactory convergence at a lower computational cost than the plane wave expansion method with stress free surface boundary conditions. Slight differences occur between the values of the eigenfrequencies computed with our supercell plane wave expansion method and those obtained by C. Charles et al., especially for modes of higher order. This can be attributed to a better convergence of our method due to the larger

number of reciprocal lattice vectors taken into account (343 compared to 25). Moreover, Fig. 45(a) does not exhibit some pseudomodes without physical meaning which can occur when solving the Fourier transform of the equations of propagation with stress free boundary conditions at the surfaces [102,103]. One notes also that due to the very low contrast between the elastic constants and density of Fe and Cu, these band structures do not exhibit an absolute band gap. To verify the validity of the application of the supercell-plane wave expansion method to low contrast solid/solid systems, the band structure of the same plate was also calculated using the finite element method [128,129]. In all finite element calculations reported in this paper, we have insured that the finite element mesh is fine enough for complete convergence of the finite element band structure. These finite element band structures are subsequently used as reference for characterizing the rate of convergence of the supercell plane wave expansion method. The supercell plane wave expansion (black filled dots) and finite element (black crosses) plate band structures are plotted in Fig. 45(b). One observes the excellent agreement between the results derived from the two calculation methods. This indicates the very good convergence of our supercell plane wave expansion method for low contrast solid/solid two-dimensional phononic crystal plates with a reasonably small number of plane waves (i.e. 343) taken into account. The calculations reported in Fig. 45(b) were done with $h_1 = h_3 = a$. We have verified the agreement between the supercell plane wave expansion and the finite element band structures for h_1 and h_3 varying from $0.5a$ to $1.5a$. This range of thickness for media C and D effectively forbid the interaction between the vibrational modes of neighboring periodically repeated phononic crystal plates. Subsequently we fixed $h_1 = h_3 = a$.

Finally, we also checked that our supercell-plane wave expansion method leads to similar results to those published by Tanaka et al. [102] for another low contrast solid/solid system namely

a two-dimensional semi-infinite phononic crystal composed of a square array of AlAs cylinders in a GaAs matrix. For this, we increased the thickness of the plate to a value of three times the lattice parameter and verified that the zero order symmetric and antisymmetric plate modes fuse into the Rayleigh wave propagating at the free surface of a two-dimensional semi-infinite phononic crystal. Our supercell plane wave expansion band structure includes additional bands that arise from the finite thickness of the plate. As the thickness increases further the number of extra bands increases. However due to the limited number of reciprocal vectors that can be taken into account, the convergence of the numerical calculations fails when considering a very large thickness of the plate [112].

4.1.3.2. High contrast solid/solid systems. Here we consider the case of two-dimensional phononic crystal plates made of arrays of steel inclusions embedded in epoxy resin. These solids possess very different densities and elastic constants and the bulk phononic crystal exhibits very large absolute band gaps provided the filling factor of inclusion is sufficiently large [26]. Steel and epoxy resin are isotropic materials and their physical characteristics are reported in Table 3 [60].

Fig. 46(a) shows the supercell plane wave expansion band structure in the ΓX direction of propagation, of a phononic crystal plate composed of inclusions of circular cross section placed on a square array with thickness $h_2 = a$. The filling factor f (= $\pi R^2/a^2$) is equal to 0.564. The results are rendered in terms of a reduced frequency $\Omega = \omega a/2\pi \overline{c_t}$, versus a reduced wave vector $\mathbf{k} = \mathbf{K}a/2\pi$ where $\overline{c_t} = \sqrt{C_{44}/\overline{\rho}} = \sqrt{C_{44}(\mathbf{G}=\mathbf{0})/\rho(\mathbf{G}=\mathbf{0})}$ is an average transverse speed of sound. Here the calculation is done with $M_x = M_y = 6, M_z = 2$. For comparison, the finite element band structure of the same plate is reported in Fig. 46(b). Although the shape of the dispersion curves is quite similar in the supercell plane wave expansion and finite element calculations, the values of the eigenfrequencies differ significantly by about 15%. This result suggests that the supercell plane wave expansion method with $M_x = M_y = 6, M_z = 2$ has not converged for the high contrast solid/solid phononic crystal plate. In Fig. 47, we analyze the convergence of the supercell plane wave expansion method at the X point of the square Brillouin zone for a steel/epoxy phononic crystal plate of thickness $h_2 = a$ and $f = 0.564$ by varying M_x, M_y and M_z i.e. the number of plane waves. On the one hand, for this relatively small thickness of the plate, the supercell plane wave expansion eigenfrequencies appear to be significantly less sensitive to the choice of M_z than $M_x = M_y$. On the other hand, comparison with the finite element method shows that even with 1575 plane waves (i.e. $M_x = M_y = 8, M_z = 2$) the frequencies have not converged and remain about 10% above the finite element results. Note that this pathological lack of convergence for high contrast solid/solid systems is also observed in the plane wave expansion method with stress free boundary conditions [120,111]. This problem also arises in the calculation of the band structure of bulk high contrast two-dimensional phononic crystals [31,26,101, 37]. For example, in steel/epoxy bulk two-dimensional phononic crystals, the plane wave expansion eigenvalues start to converge satisfactorily for $M_x = M_y = 12$. It seems that all the plane wave expansion-based methods introduced to date for computing the band structures of high contrast solid/solid two-dimensional phononic crystal plates suffer from convergence difficulties and do not constitute a reliable numerical tool in this case [111,112].

### 4.1.4. Air inclusion phononic plates and wave guiding

Since in all band structures reported previously the reduced frequency Ω scales as the inverse of the lattice parameter of the array of inclusions, a, the domain of frequency where forbidden
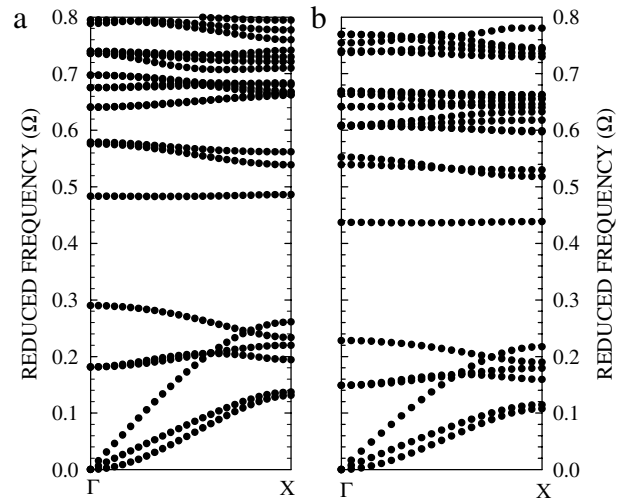

Fig. 46. Band structures along the ΓX direction of propagation of a two-dimensional phononic crystal plate composed of a square array of steel cylinders embedded in an epoxy matrix calculated with (a) the supercell-plane wave expansion method and (b) the finite element method. The supercell-plane wave expansion calculation used $M_x = M_y = 6, M_z = 2$ i.e. 845 plane waves. The filling factor of inclusions and the thickness of the plate are $f = 0.564$ and $h_2 = a$.

band gaps may occur also scales as $1/a$. The design of phononic crystal plates with forbidden gaps in the mega- or gigahertz range requires periodicity of the array of inclusions of the order of the micro- or the nanometer. From an experimental point of view, the realization at this scale of two-dimensional phononic crystals composed of two different solid materials is a very challenging task while actual techniques based, for example, on reactive ion etching (RIE), focused ion beam (FIB) or interference lithography allow one to drill relatively easily a regular network of holes in a solid [105,130]. Consequently, with the aim of designing structures exhibiting absolute band gaps at very high frequencies that can be fabricated experimentally, we focus our attention on arrays of holes drilled in a solid matrix. We consider two types of matrix materials, namely steel and silicon.

4.1.4.1. Air/isotropic matrix systems. Fig. 48 shows the elastic band structure of a phononic crystal plate made of a square array of cylindrical holes in steel calculated with the supercell plane wave expansion method with $M_x = M_y = 4, M_z = 2$ and the finite element method. With these constituent materials, the choice of the filling factor is of particular importance. Indeed, most of the theoretical and experimental studies conducted on bulk two-dimensional phononic crystals have shown that larger gaps are obtained when the inclusions are made of the stiffer material [31, 37]. Nevertheless, a very compact array of holes, for example, a square array of holes drilled in a solid with a filling factor near the close packed value (i.e. $f = \pi/4$ or $R/a = 0.5$), can be visualized as a square array of singular shape solid inclusions embedded in air. Consequently one may expect large gaps for a high filling factor of holes [131]. This is indeed observed in Fig. 48 where $f = 0.7$ i.e. $R/a = 0.472$. In the course of the supercell plane wave expansion numerical calculations, the material inside the holes i.e. air was modeled by the low impedance medium depicted in the subsection on the plane wave expansion method for plates. With these very large contrast material constituents the supercell plane wave expansion band structure has converged to the finite element results with 405 plane waves. It is worth noting that the air inclusions are not included in the finite element mesh and their effect is accounted for through stress free boundary conditions at the surface of the holes. We further analyze the rate of convergence of the supercell plane wave expansion method as a function of the
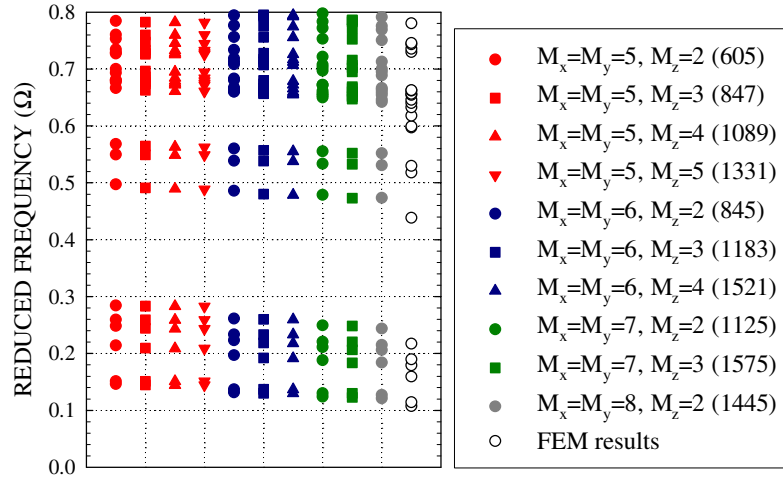
Fig. 47. (Color online) Eigenvalues at the *X* point of the Brillouin zone calculated with the supercell-plane wave expansion method as a function of M_x, M_y and M_z (i.e. the number of plane waves) for the steel/epoxy phononic crystal plate of Fig. 46. The open circles represent the eigenvalues computed with the finite element method and serve as a fully converged reference. The integer $N = (2M_x + 1)(2M_y + 1)(2M_z + 1)$ in parentheses indicates the number of plane waves taken into account in the supercell-plane wave expansion calculations. The standard eigenvalue equation to be resolved involves square matrices of size equal to $3N \times 3N$. Note the poor convergence of the supercell-plane wave expansion method and the relative insensitivity to M_z for our relatively thin plate.
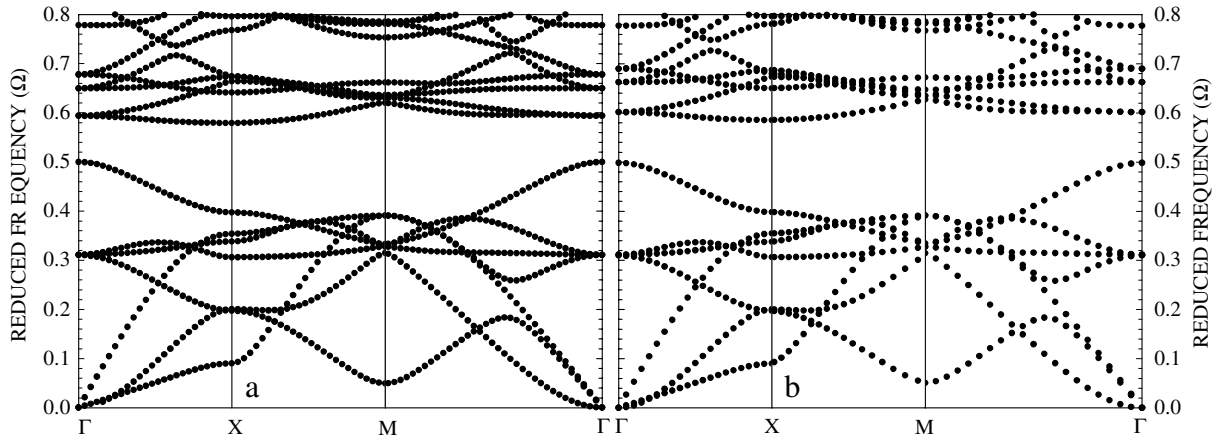
Fig. 48. Band structure of a two-dimensional phononic crystal plate composed of a square array of holes drilled in a steel plate calculated with (a) the supercell-plane wave expansion method and (b) the finite element method. The supercell-plane wave expansion calculation used $M_x = M_y = 4$, $M_z = 2$ i.e. 405 plane waves and the air holes were modeled with the low impedance material. The filling factor of inclusions and the thickness of the plate are $f = 0.7$ and $h_2 = a$. Note the excellent agreement between the eigenvalues of the two band structures.
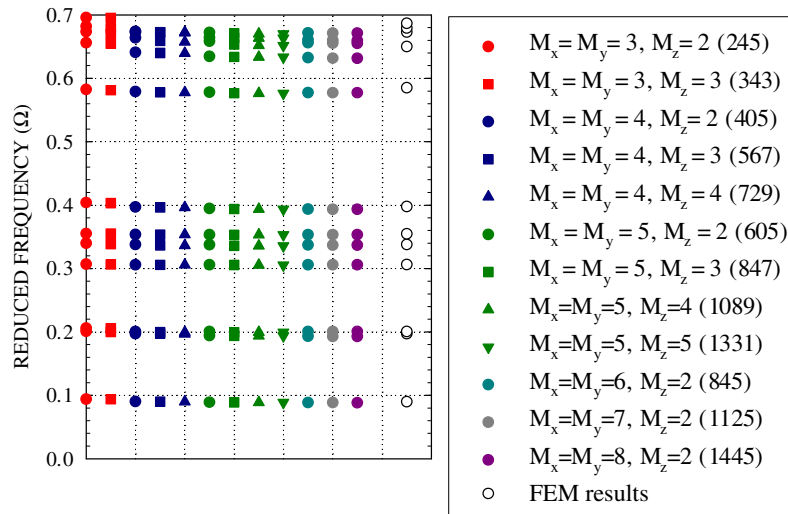

Fig. 49. (Color online) Eigenvalues at the *X* point of the Brillouin zone calculated with the supercell-plane wave expansion method as a function of M_x, M_y and M_z (i.e. the number of plane waves) for the air/steel phononic crystal plate of Fig. 48. The open circles represent the eigenvalues computed with the finite element method and serve as a fully converged reference. Note the excellent convergence of the supercell-plane wave expansion method starting at a relatively small number of plane waves.
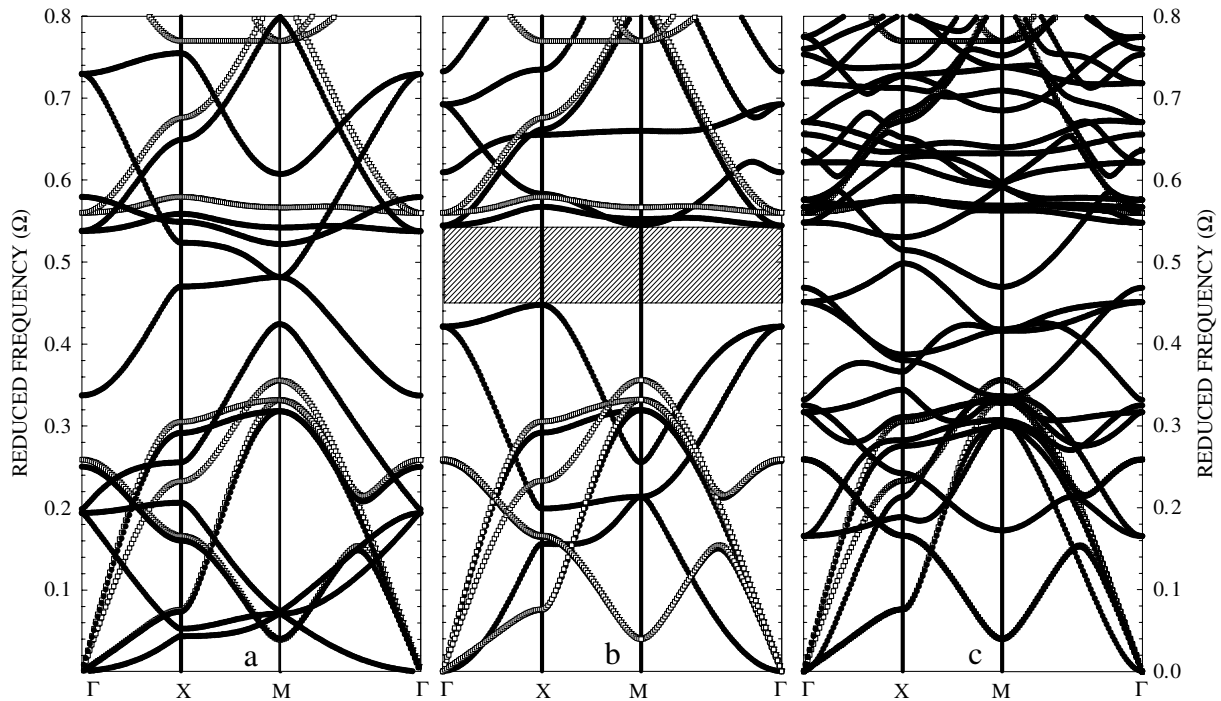
Fig. 50. Supercell-plane wave expansion band structures for the bulk two-dimensional phononic crystal (open squares) and the phononic crystal plate of thickness h_2 (black filled circles) made of a square array of air (low impedance material) holes embedded in silicon with $f = 0.7$. (a) $h_2 = 0.1a$; (b) $h_2 = 0.55a$; (c) $h_2 = 2a$. The dashed area in (b) shows the absolute band gap for the plate. The supercell-plane wave expansion calculation used $M_x = M_y = 4$, $M_z = 2$ i.e. 845 plane waves.

number of plane waves taken into account in the Fourier series expansion in Fig. 49 at the X point of the Brillouin zone. This figure shows that good convergence is achieved for the lower 20 bands with the number of plane waves greater or equal to 405. In the case of Fig. 48, where 405 plane waves were taken into account, the worst convergence in reduced frequency is less than 2% of the fully converged finite element eigenfrequency. We also observed an overall agreement between the band structures obtained by Langlet on arrays of cylindrical holes drilled in PVC plates applying the finite element method [128] and that calculated with the supercell plane wave expansion method using a low impedance medium as the inclusion material. This agreement is achieved with $M_x = M_y = M_z = 3$. All our numerical results using the low impedance medium as the inclusion material suggest that the supercell plane wave expansion method provides a mean of calculating the band structure of air/solid two-dimensional phononic crystal plates reliably with a reasonably small number of plane waves in the Fourier series expansion and this over a wide range of matrix materials.

4.1.4.2. Air/cubic matrix systems. With a reasonably fast converging supercell plane wave expansion method for air/solid systems, we now investigate a two-dimensional phononic crystal plate composed of a material commonly used in micro-fabrication, namely silicon. The first plate is composed of a square array of air holes. Fig. 50 reports the elastic band structures of the bulk phononic crystal and of phononic crystal plates with varying thicknesses for a filling factor fixed to 0.7. The plate modes differ significantly from the bulk band structures. The thin ($h_2 = 0.1a$) and thick plates ($h_2 = 2a$) of Fig. 50(a) and (c) do not exhibit a band gap. An absolute band gap occurs in Fig. 50(b) for a plate thickness of 0.55a. The complete evolution of the gap width with the ratio h_2/a is presented in Fig. 51 showing the closing of the gap for thicknesses below 0.2a and above 0.9a. One may search for larger band gaps with the same constituent materials by changing the geometry of the array of inclusions. Indeed, it is well known that
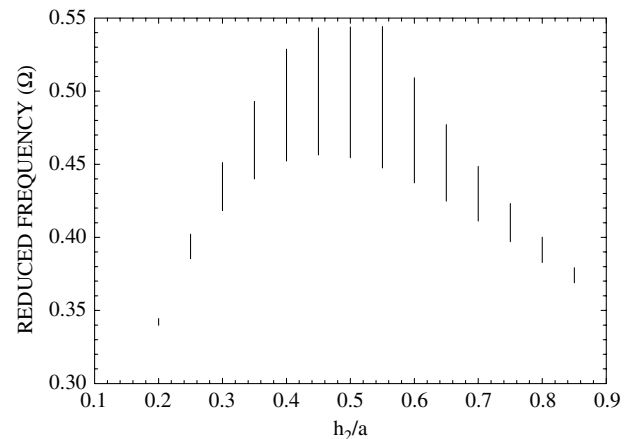
Fig. 51. Location and width of the band gap versus the ratio of the plate thickness h_2 to the lattice parameter a for air/silicon phononic crystal plate with a square array of holes. All other parameters (f, M_x, M_y, M_z) are the same as those of Fig. 50.

bulk phononic crystal geometry plays a fundamental role in designing large elastic band gaps. Subsequently we investigated the dispersion curves of two-dimensional phononic crystal plates with the graphite structure. Fig. 52 shows the bulk band structure (hollow squares) and the dispersion curves of a phononic crystal plate (black filled circles) for a graphite array of holes in silicon with $f_1 = f_2 = 0.25$ i.e. a total filling factor f of inclusions equal to 0.5, smaller than the close-packing value of 0.604. We consider plates of varying thicknesses. The characteristic "lattice" parameter of the graphite array is not a but rather $a\sqrt{3}$ i.e. the length of the sides of the two-dimensional primitive unit cell of the graphite array (see Fig. 43). Then we study the evolution of the band structure of the plate as a function of the ratio between the plate thickness h_2 and $a\sqrt{3}$. As in the previous cases, the band structure of the plate differs from that of the infinite phononic crystal. On the other hand, the
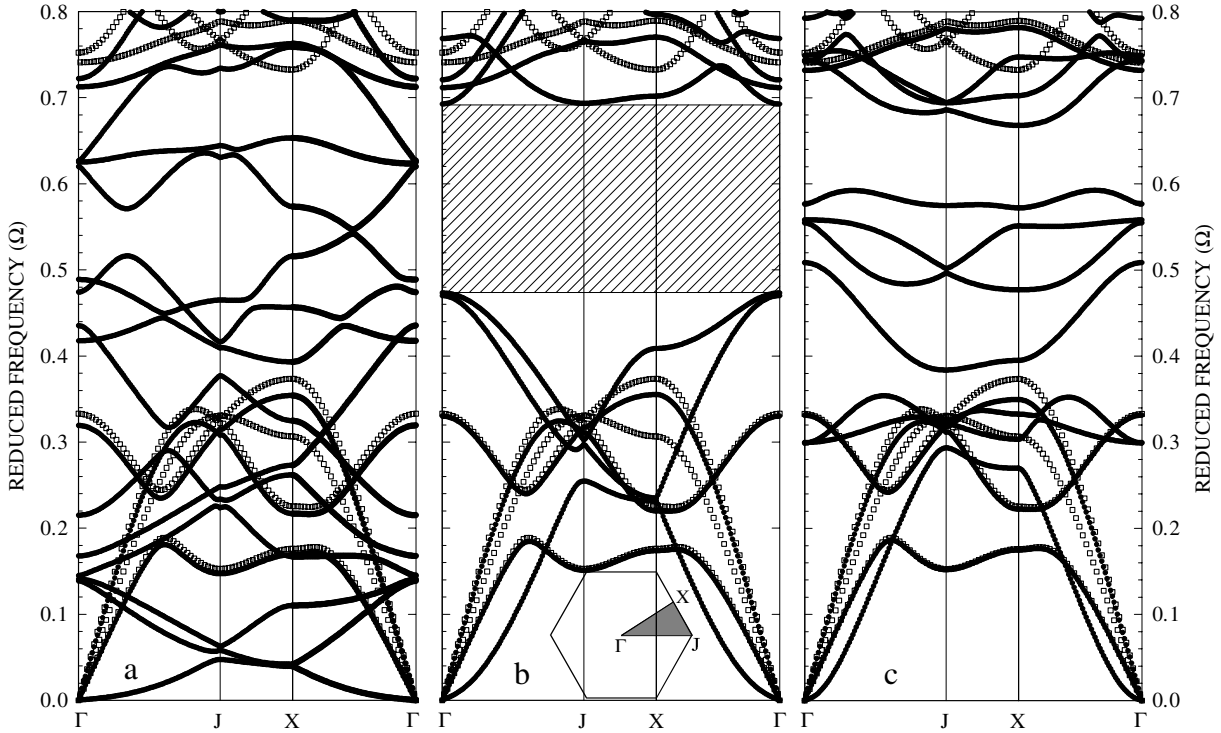
Fig. 52. Supercell-plane wave expansion band structures for the bulk two-dimensional phononic crystal (open squares) and the phononic crystal plate of thickness h_2 (black filled circles) made of a graphite array of air (low impedance material) holes embedded in silicon with $f = f_1 + f_2 = 0.5$. (a) $\frac{h_2}{a\sqrt{3}} = 0.1$; (b) $\frac{h_2}{a\sqrt{3}} = 0.58$; (c) $\frac{h_2}{a\sqrt{3}} = 1.15$. The results are rendered in terms of a reduced frequency $\Omega = \omega a\sqrt{3}/2\pi \overline{c_t}$ versus a reduced wave vector $\mathbf{k} = \mathbf{K}a\sqrt{3}/2\pi$ where $\overline{c_t} = \sqrt{C_{44}/\overline{\rho}} = \sqrt{C_{44}(\mathbf{G}=\mathbf{0})/\rho(\mathbf{G}=\mathbf{0})}$ is an average transverse speed of sound. The inset represents the first Brillouin zone ($\Gamma J X$) of the graphite array. The components of the wave vector $\mathbf{K}$ at the Γ, J and X points are $\frac{2\pi}{a\sqrt{3}}(0,0)$, $\frac{2\pi}{a\sqrt{3}}(\frac{2}{3},0)$ and $\frac{2\pi}{a\sqrt{3}}(\frac{1}{2},\frac{1}{2\sqrt{3}})$. The supercell-plane wave expansion calculation used $M_x = M_y = 4$, $M_z = 2$ i.e. 845 plane waves.

width of the full band gap centered around $\Omega \approx 0.6$ in Fig. 52(b) is markedly larger than the gaps reported in the case of the square array. As previously, the existence of this absolute stop band depends on the thickness h_2 of the plate and the optimum value of h_2 is of the order of magnitude of $0.58a\sqrt{3}$. In Fig. 52(c), the absolute band gap remains for a thickness of $2a\sqrt{3}$. In Fig. 53, we present the position and width of the first band gap as a function of the ratio $h_2/a\sqrt{3}$. Fig. 53 shows that the absolute band gap vanishes for $h_2/a\sqrt{3} < 0.2$. For the graphite structure, the band gap does not close before the ratio $h_2/a\sqrt{3}$ exceeds 1.15. One observes that the larger gap appears for $h_2/a\sqrt{3} \approx 0.58$. Then the variation of the gap width with the ratio between the thickness of the plate and the characteristic "lattice" parameter for both square and graphite networks of holes scales in a similar way. Moreover, while for the square array of holes, absolute band gaps were obtained for filling factors approaching the close-packed value for which cylinders are in contact with one another, the graphite network shows wide gaps for non-contacting cylinders. Consequently, the technical realization of phononic crystals made of holes in a solid matrix exhibiting absolute stop bands at very high frequencies is probably much easier when the holes are arranged upon a graphite array than a square network especially at the scale of a thin plate. Moreover, we have verified that the effect of the geometry of the inclusion (square rather than cylindrical inclusion) in that case of an air/solid two-dimensional phononic crystal plate is minimal as already observed in bulk phononic crystals [101].

4.1.4.3. Waveguide in air/silicon two-dimensional phononic crystal plate. Bulk phononic crystals containing rectilinear defects have been shown to guide elastic waves efficiently [95,88,132,16]. Moreover surface acoustic waves can also be guided in defective semi-infinite two-dimensional phononic crystals [133]. Sun et al.
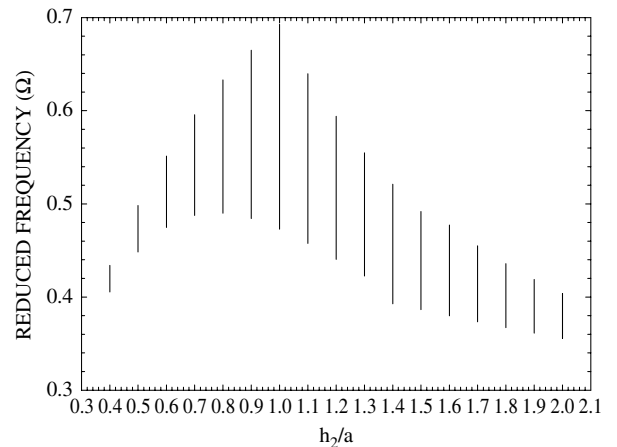
Fig. 53. Location and width of the band gap versus the ratio of the plate thickness h_2 to the characteristic lattice parameter $a\sqrt{3}$ for an air/silicon phononic crystal plate with a graphite array of holes. All other parameters (f, M_x, M_y, M_z) are the same as those of Fig. 52.

and Chen et al. investigated the propagation of elastic waves through waveguides in a two-dimensional phononic crystal plate made of solid constituents [134,135]. In addition to the calculation of band structures of perfect two-dimensional phononic crystal plates, the supercell plane wave expansion method can also be extended to study wave propagation in defective plate structures. More specifically, we consider a phononic crystal composed of a square array of low impedance medium holes in an Si plate with a filling fraction $f = 0.7$. Here we extend the supercell plane wave expansion method to the calculation of the band structure of two-dimensional phononic crystal plates with a linear defect of

variable width. The guide is obtained by removing a row of holes along the x direction and varying the distance between the two neighboring rows of holes. This is done numerically by considering a rectangular supercell of width along the x direction equal to a and a length along the y direction, $L_y > a$. The thickness of the supercell along the z direction remains equal to $\ell = h_1 + h_2 + h_3$. The structure of the defected supercell is illustrated in Fig. 54. In this figure, αa represents the separation distance between the edges of the two unit cells adjacent to the waveguide. αa is an adjustable geometrical parameter. For $\alpha = 0$, the structure is that of a supercell containing N_{cyl} holes arranged on a perfect square lattice, namely a supercell of the perfect phononic crystal plate. If $\alpha = 1$ the structure is that of a two-dimensional phononic crystal plate with one row of holes filled with the matrix material. One can vary the width of the waveguide by setting $\alpha \neq 0$. The width W of the guide defined as the closest distance between the surface of the holes on either side of the guide is given by $W = (1+\alpha)a - 2R$. This supercell is repeated periodically in the x, y and z directions. We choose the thickness h_2 of the slab equals to $0.55a$ for insuring the existence of the largest gap in the perfect phononic crystal plate. The thickness h_1 and h_3 of the low impedance medium slabs are equal to a. Due to the periodicity in the y direction, the expression of the Fourier coefficients defined by Eq. (46) must be modified as

$$\zeta(\mathbf{G}) = \begin{cases} \zeta_A f \dfrac{N_{cyl}}{(L_y/a)} \left(\dfrac{h_2}{\ell}\right) + \zeta_B \left(1 - \dfrac{N_{cyl}}{(L_y/a)}f\right)\left(\dfrac{h_2}{\ell}\right) \\ \quad + \zeta_C \left(\dfrac{h_1}{\ell}\right) + \zeta_D \left(\dfrac{h_3}{\ell}\right), \quad \text{if } \mathbf{G} = \mathbf{0} \\[2mm] (\zeta_A - \zeta_B)\dfrac{1}{(L_y/a)}\displaystyle\sum_i^{N_{cyl}} e^{-\iota\mathbf{G}\cdot\mathbf{r}_i}.F^{wg}{}_I(\mathbf{G}) \\ \quad + (\zeta_C - \zeta_B)F^{wg}{}_{II}(\mathbf{G}) + (\zeta_D - \zeta_B)F^{wg}{}_{III}(\mathbf{G}), \\ \quad \text{if } \mathbf{G} \neq \mathbf{0}, \end{cases} \tag{51}$$

with

$$F^{wg}{}_I(\mathbf{G}) = \frac{1}{V_u}\iiint_{(A)} e^{-\iota\mathbf{G}\cdot\mathbf{r}}d^3\mathbf{r}$$

$$= F(\mathbf{G}_{//})\left(\frac{\sin\left(G_z\frac{h_2}{2}\right)}{\left(G_z\frac{h_2}{2}\right)}\right).\left(\frac{h_2}{\ell}\right) \tag{52a}$$

$$F^{wg}{}_{II}(\mathbf{G}) = \frac{1}{V_u}\iiint_{(C)} e^{-\iota\mathbf{G}\cdot\mathbf{r}}d^3\mathbf{r}$$

$$= \left(\frac{\sin\left(G_x\frac{a}{2}\right)}{\left(G_x\frac{a}{2}\right)}\right).\left(\frac{\sin\left(G_y.\frac{L_y}{2}\right)}{\left(G_y\frac{L_y}{2}\right)}\right).\left(\frac{\sin\left(G_z\frac{h_1}{2}\right)}{\left(G_z\frac{h_1}{2}\right)}\right)$$

$$\times \left(\frac{h_1}{\ell}\right).e^{-\iota G_z\left(\frac{h_1+h_2}{2}\right)} \tag{52b}$$

$$F^{wg}{}_{III}(\mathbf{G}) = \frac{1}{V_u}\iiint_{(D)} e^{-\iota\mathbf{G}\cdot\mathbf{r}}d^3\mathbf{r}$$

$$= \left(\frac{\sin\left(G_x\frac{a}{2}\right)}{\left(G_x\frac{a}{2}\right)}\right).\left(\frac{\sin\left(G_y.\frac{L_y}{2}\right)}{\left(G_y\frac{L_y}{2}\right)}\right).\left(\frac{\sin\left(G_z\frac{h_3}{2}\right)}{\left(G_z\frac{h_3}{2}\right)}\right)$$

$$\times \left(\frac{h_3}{\ell}\right).e^{-\iota G_z\left(\frac{h_2+h_3}{2}\right)}. \tag{52c}$$

In order to follow the evolution of the dispersion curves of the defective phononic crystal plate as a function of the waveguide width, we have investigated seven systems. The first system corresponds to a perfect phononic crystal plate with a supercell containing $N_{cyl} = 5$ with $\alpha = 0$. For the seventh system, we have chosen $\alpha = 1$ and $N_{cyl} = 4$. This structure is equivalent
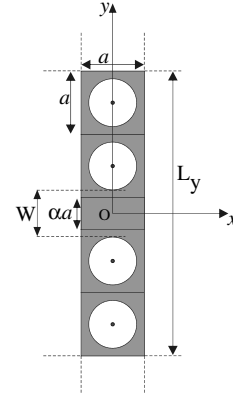

Fig. 54. Schematic illustration of the supercell used for the supercell-plane wave expansion calculation of the band structure of a defected phononic crystal plate.

to filling, with silicon, one of the five holes in the first system, effectively resulting in a linear defect along the x direction. The other systems with $N_{cyl} = 4$ and α ranging from 0.25 to 0.85 by steps of 0.15 are similar to the seventh system but with a narrower waveguide. Because of the periodicity, the waveguide is repeated in the y direction leading to a stack of waveguides separated by 4 air holes. This separation is sufficient to avoid significant coupling between neighboring guides.

The band structures, computed along the ΓX direction (i.e. the direction of propagation of a wave along the linear waveguide) of the seven systems, are reported in Fig. 55. Since the supercell is longer in the y direction, a larger number of reciprocal vectors is required along the y direction for satisfactory convergence. $(2M_x + 1)(2M_y.M_y' + 1)(2M_z + 1) = 1845$ (with $M_x = M_y = 4$, $M_z = 2$ and $M_y' = 5$) reciprocal lattice vectors were taken into account for computing these dispersion curves. Fig. 55(a) exhibits numerous additional branches than that of Fig. 50(b) (i.e. the band structure calculated with a single unit cell along the y direction) as the result of the folding of the bands in the y direction due to the 5 unit cell periodicity in that direction. This system still shows the forbidden band. Formation of a waveguide in that structure inserts guided modes inside the band gap of the perfect phononic crystal as illustrated in Fig. 55(b)–(g). Fig. 55 shows that when the width of the waveguide increases, the number of guided modes in the band gap increases. This is the standard behavior observed in waveguide theory. One considers now a specific waveguide mode that falls inside the band gap of the perfect phononic crystal plate. This mode is represented with red dots in Fig. 55(b)–(e). One observes that the location of this mode inside the stop band of the perfect phononic crystal plate depends strongly on the width of the waveguide. This mode evolves from a location near the top of the gap to near the bottom of the gap as the width of the waveguide increases. This mode merges with the pass band below the band gap for α larger than 0.7. We characterize this guided mode further by calculating the modulus of the complex components of the displacement field for different values of α. For example, Fig. 56 shows the maps of the modulus of these components for this specific mode for a fixed value of the wave vector i.e. $K_x = 0.14.(2\pi/a)$ (blue square in Fig. 55(b)–e)). Fig. 56(a1–c4) correspond to cuts of the three-dimensional displacement field in the (xOy) plane at a position $z = 0.2a$, that is near the top surface of the plate. One observes that for $\alpha = 0.25$, the guided mode which appears approximately at the center of the stop band (see Fig. 55(b)) is confined within or in the close vicinity of the waveguide (see the top panel of Fig. 56). The displacement field penetrates the inner space between the adjacent cylinders but becomes negligible once one leaves the close vicinity of the guide [87]. For a larger waveguide, while the z component of this mode remains well
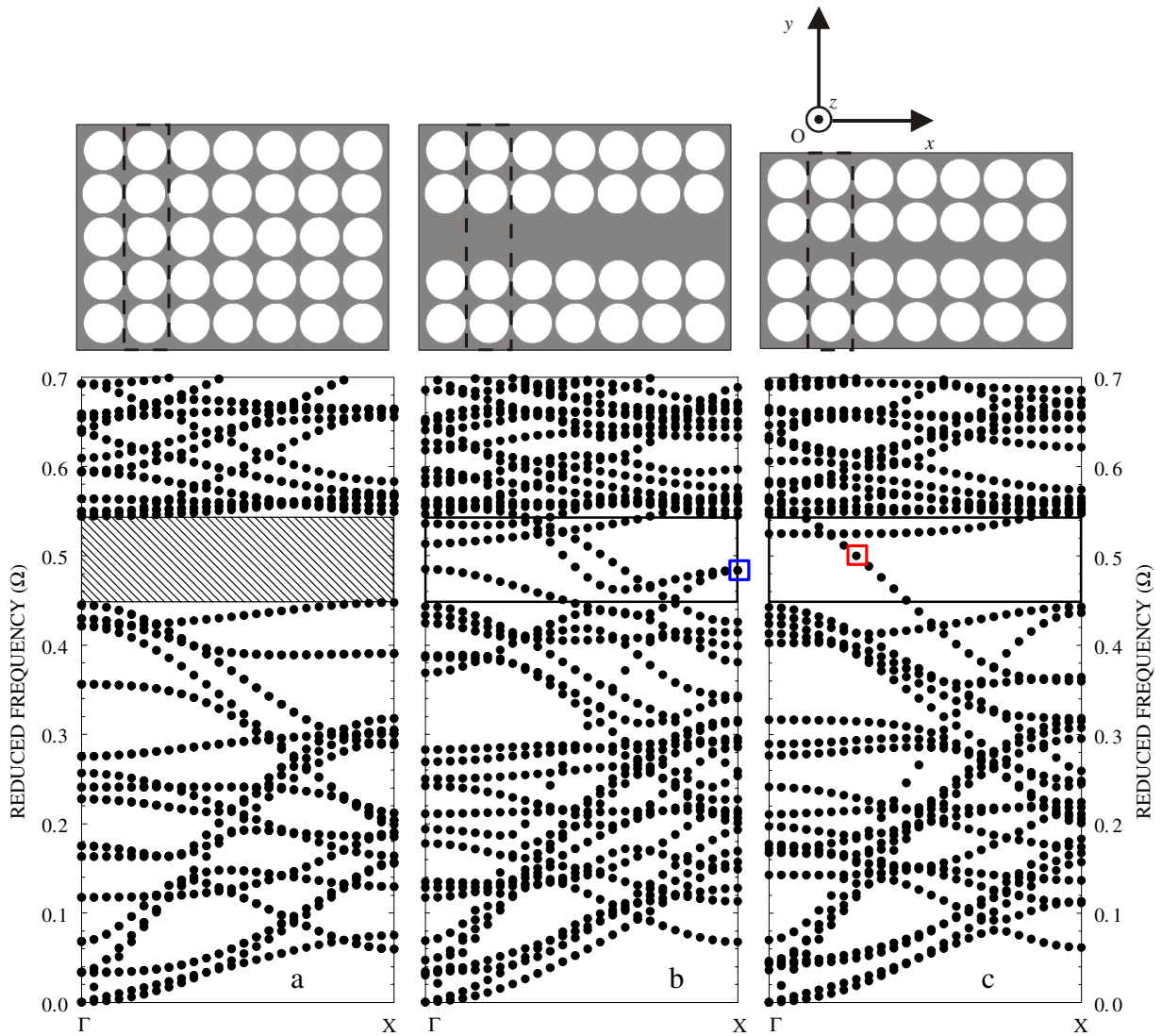
Fig. 55. Band structures along the ΓX direction of (a) the perfect phononic crystal plate ($\alpha = 0$ and $N_{cyl} = 5$), (b) the phononic crystal plate containing a waveguide with $\alpha = 0.25$ and $N_{cyl} = 4$, (c) the same as in (b) but with $\alpha = 0.4$, (d) the same as in (b) but with $\alpha = 0.55$, (e) the same as in (b) but with $\alpha = 0.7$, (f) the same as in (b) but with $\alpha = 0.85$, (g) the same as in (b) but with $\alpha = 1.0$. αa represents the separation distance between the edges of the two unit cells adjacent to the waveguide. The supercell-plane wave expansion calculation used $M_x = 4$, $M_y * M_y' = 4 * 5 = 20$, $M_z = 2$ i.e. 1845 plane waves. The dashed area in (a) shows the absolute band gap for the plate. In (b)–(e) (resp. (g)), the blue (resp. green) square indicates the location of the guided modes analyzed in Fig. 56 (resp. Fig. 57). (For interpretation of the references to colour in this figure legend, the reader is referred to the web version of this article.)

confined into the waveguide, the other components leak out into the phononic crystal structure. The mode becomes less and less confined to the waveguide as the width of the waveguide increases. In Fig. 55(c) and (d), one notes that the mode we consider crosses another mode for this value of K_x. These two modes may interact strongly together and this has probably a detrimental effect on the waveguide mode confinement. For $\alpha = 0.7$, the mode is very close to the bottom of the stop band (see Fig. 55(e)) and this may explain the very weak confinement of the mode. The bottom panel of Fig. 56 shows cuts of the displacement field in the (xOz) plane located at a position along the y direction corresponding to the center of the guide for the waveguide mode considered in Fig. 55(b) for $\alpha = 0.25$ and $K_x = 0.14.(2\pi/a)$. We use these figures to define the polarization of the mode in the (xOz) plane. At the center of the waveguide, due to the symmetry of the mode, the y component of the displacement field is negligible while the x component is fairly localized near the surfaces of the plate. The z component varies slowly along the x direction. We checked that the modes depicted by a blue square in Fig. 55(b)–(e) possess the same polarization in the (xOz) plane than that described in the bottom panel of

Fig. 56. Fig. 57 presents the maps of the displacement field for the waveguide mode with $\Omega = 0.4834$ at the X point for the wider guide. This mode is represented with a green square in Fig. 55(g). In this case, the wave vector corresponds to one of the highest symmetry points in the square Brillouin zone. Note that at this **K** point another mode appears at a slightly higher reduced frequency i.e. $\Omega = 0.4836$. One observes in the top panel of Fig. 57 that the confinement of the waveguide mode with $\Omega = 0.4834$ is very good in this large waveguide and does not suffer from the possible interaction between these two modes. The bottom panel of Fig. 57 shows that, in that case, the z component of the displacement field is localized to the vicinity of the surfaces of the plate. The polarization of this mode differs from that depicted in Fig. 56(d–f) for the guided mode of the narrowest waveguide. A comparison between the bottom panels of Figs. 56 and 57 indicates that depending upon the polarization of the mode, the x or z component of the displacement field of the guided mode may be localized on the surfaces of the plate. Moreover the thickness of the plate governs the width of the absolute band gap of the perfect phononic crystal plate. As observed in these results (see Figs. 56

(a) u_x.

(b) u_y.

(c) u_z.

(d) u_x.

(e) u_y.

(f) u_z.
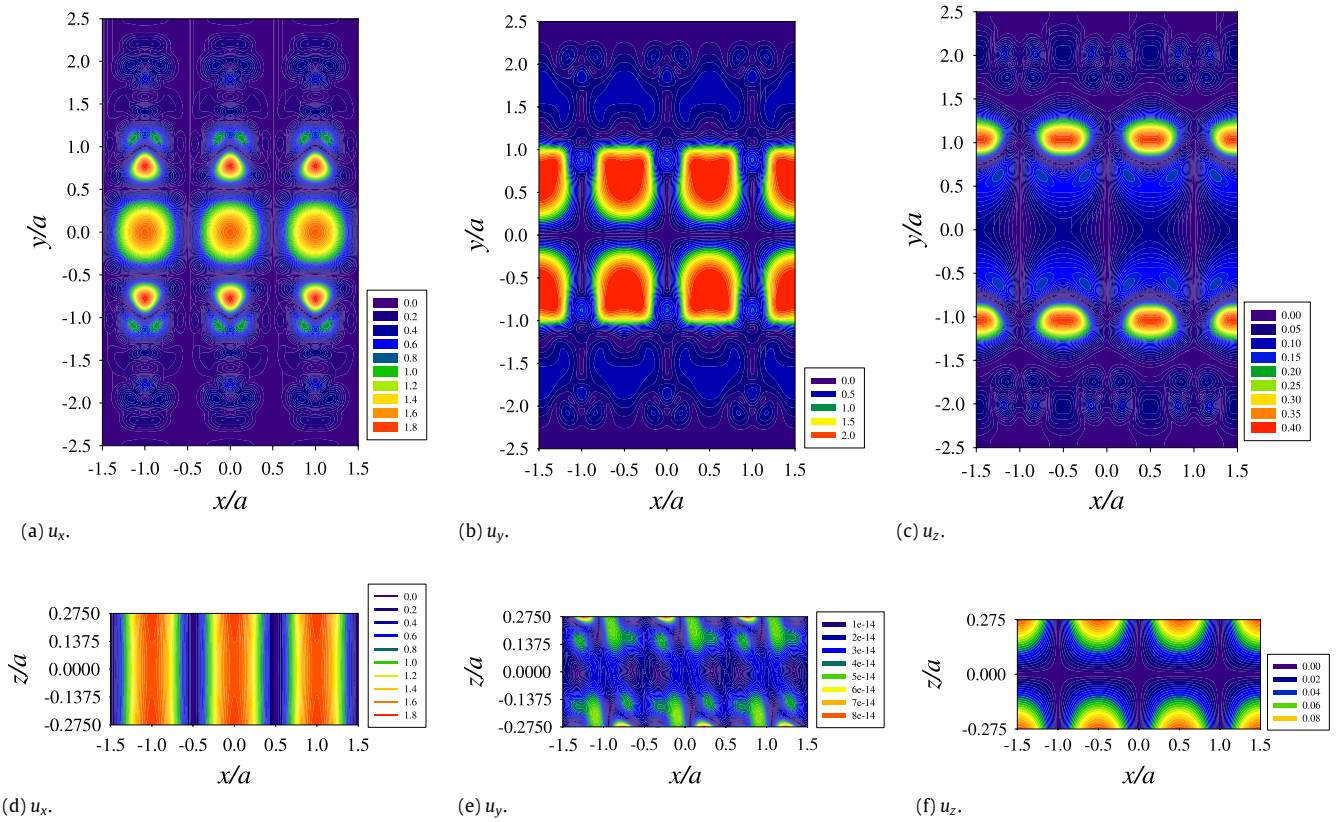
Fig. 56. (Color online) Maps of the modulus (in arbitrary units) of the complex components of the elastic displacement field in (a1), (b1), (c1) the xOy ($z = 0.2a$) plane and (d)–(f) the xOz plane at the center of the waveguide for the waveguide mode with $\Omega = 0.5001$ at the $K_x = 0.14.(\frac{2\pi}{a})$ point for the narrowest waveguide (see blue square in Fig. 55(b)). (a2), (b2) and (c2): the same as in (a1), (b1) and (c1) but for the mode represented with a blue square in Fig. 55(c); (a3), (b3) and (c3): the same as in (a1), (b1) and (c1) but for the mode represented with a blue square in Fig. 55(d); (a4), (b4), (c4): the same as in (a1), (b1) and (c1) but for the mode represented with a blue square in Fig. 55(e).

(a) u_x.

(b) u_y.

(c) u_z.

(d) u_x.

(e) u_y.

(f) u_z.
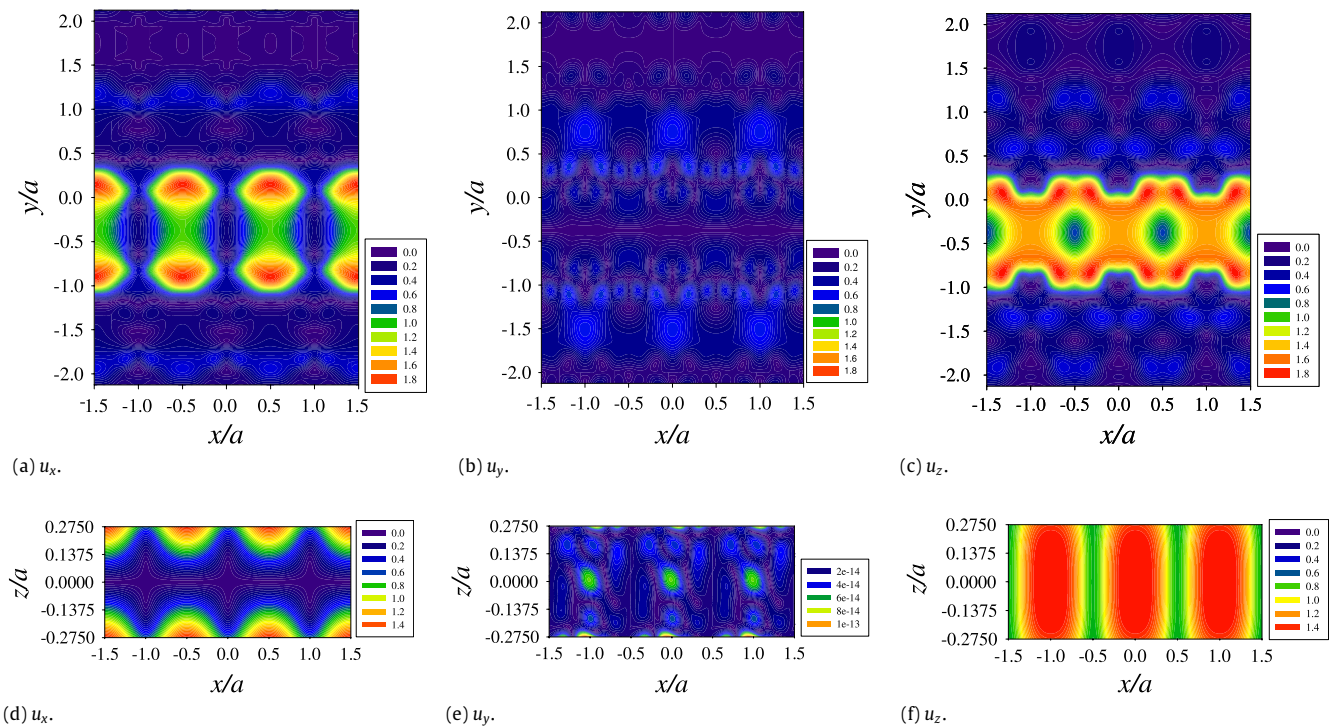
Fig. 57. (Color online) Maps of the modulus (in arbitrary units) of the complex components of the elastic displacement field in (a)–(c) the xOy ($z = 0.2a$) plane and (d)–(f) the xOz plane at the center of the waveguide for the waveguide mode with $\Omega = 0.4834$ at the X point for the widest waveguide (see green square in Fig. 55(g)).
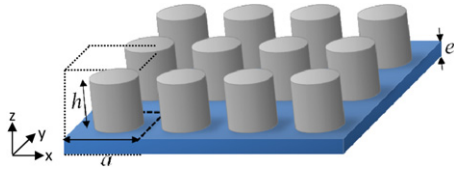
Fig. 58. (Color online) Schematic view of a phononic crystal made of a square lattice of finite cylinders deposited on a homogeneous plate. The lattice parameter is denoted *a*, the height of the cylinder *h* and the thickness of the plate *e*. The dashed cube ($a \times a \times b$) represents one unit cell of the periodic structure.

and 57) and also in the case of guided modes in bulk phononic crystals [87], a guided mode is confined more effectively inside the waveguide if it appears in the band structure far away from the edges of the stop band. One may suppose that due to the narrower stop band, a guided mode will be less confined inside the waveguide when considering a thinner or thicker phononic crystal plate.

4.2. Cylindrical dots deposited on a thin homogeneous plate and high-frequency radio-frequency devices

In this subsection, we are dealing with the band structure of a finite thickness structure composed of a square array of cylindrical dots deposited on a thin homogeneous plate. The new effect observed in this geometry is the possibility of finding a low frequency gap, which means a frequency at which the wavelengths in the constituting materials are much longer than the typical lengths in the structure such as the period of the lattice or the thickness of the plate. The opening of this gap results from a sharp bending of the dispersion curves at a given frequency. We shall discuss the existence and evolution of this gap as a function of the geometrical parameters of the structure and the material parameters of the two constituents namely the dots and the plate. The band structure can also display one or more higher gaps which will also be investigated. Finally, we show the possibility of confinement and wave guiding when a guide is created inside the phononic crystal by removing or modifying a row of dots. The calculations presented in this subsection are based on both the finite difference time domain and the finite element methods.

4.2.1. First model and gap study [116]

4.2.1.1. Introduction. As shown in Fig. 58, the physical model considered is a square lattice of cylindrical dots deposited on a plate. The *z* axis is chosen to be perpendicular to the plate and parallel to the cylinders axis. The lattice parameter *a* of the phononic crystal is chosen to be $a = 1$ mm except if stated otherwise. The filling factor is defined as $\beta = \pi r^2/a^2$, where *r* represents the radius of the cylinders. The height of the cylinders is denoted by *h* and the thickness of the plate by *e*. The materials constituting the dots and the plate (which are taken in most of the numerical calculations to be steel and silicon) are assumed to be isotropic or of cubic symmetry with their crystallographic axes oriented along the coordinate axes *x*, *y* and *z*. The elastic constants and mass densities of the materials involved in the calculations are given in Table 4.

The band structures were computed using the finite difference time domain method. Dispersion curves were calculated using a three dimensional unit cell (see the dashed lines in Fig. 58), with dimensions ($a \times a \times b$), which is repeated in the three directions of space and by using the Bloch theorem which introduces the wavevector **K**. In the *z* direction, the length of the unit cell, *b*, is chosen in such a way as to embed the plate and the cylinder as well as a thin layer of vacuum on both sides in order to decouple the interaction between neighboring cells. Therefore, with respect
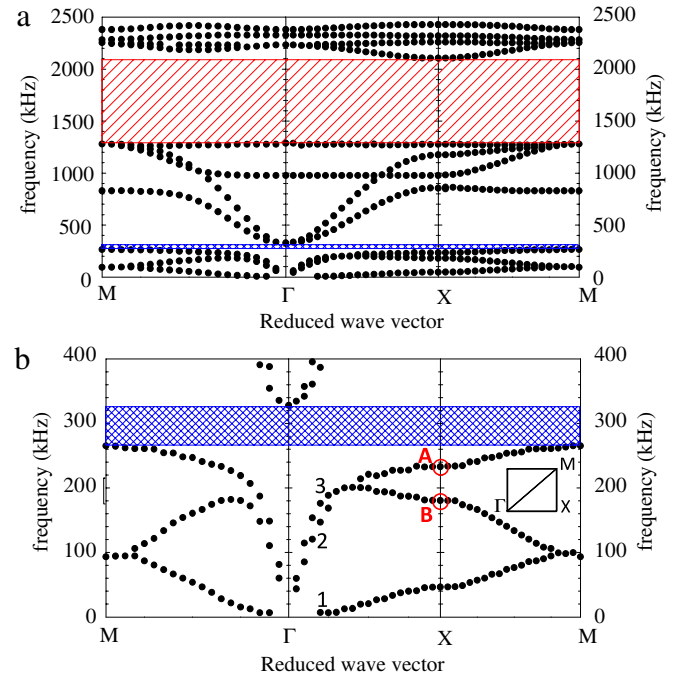

Fig. 59. (Color online) (a) Band structure in the frequency range [0, 2500 kHz] of the model of Fig. 58 for steel cylinders on a silicon plate, calculated in the first irreducible Brillouin zone of the phononic crystal. The lattice parameter is $a = 1$ mm ($\beta = 0.564$), the height of the cylinders $h = 0.6$ mm and the thickness of the plate $e = 0.1$ mm. (b) Same as (a) in the magnified frequency range [0, 400 kHz]. Points *A* and *B* correspond respectively to the extremities of branches 2 and 3 at the *X* point of the Brillouin zone.

to the wavevector K_z along *z*, the dispersion curves are flat and the calculation can be limited to $K_z = 0$. The space is discretized in *x*, *y* and *z* directions using a mesh interval equal to $\Delta x = \Delta y = \Delta z = a/30$. The equations of elasticity are solved with a time integration step $\Delta t = \Delta x/(4c_l)$ where c_l is the highest longitudinal velocity involving the structure. The number of time steps in general is equal to 2^{19} which is the necessary test time for a good convergence of the numerical calculation. For each value of the wavevector parallel to the plate, an initial random displacement is applied inside the unit cell at the origin of time. Then, the displacement field is recorded at every position in the unit cell as a function of time and finally Fourier transformed to obtain the eigenmodes of the structure for the chosen wavevector. Therefore, the band structures are rendered in terms of frequency as a function of the wave vector and plotted along the principal directions of the two-dimensional irreducible Brillouin zone.

We have made the calculation of the band structure for the system described in Fig. 58 with propagation in the (*x*, *y*) plane, along the high symmetry axes of the first Brillouin zone. The following parameters are used: filling factor $\beta = 0.564$, height of the cylinders $h = 0.6$ mm and thickness of the plate $e = 0.1$ mm. The band structure is presented, Fig. 59(a), in the frequency range [0–2500 kHz], and magnified in Fig. 59(b) for its lowest part ([0–400 kHz]). The choice of the geometrical parameters insures the existence of two absolute band gaps extending respectively from 265 to 327 kHz and from 1280 to 2110 kHz. The direction *XM* of the Brillouin zone does not change the existence and the width of the gaps and will not been drawn in the rest of this subsection so as to reduce the representations of the figures of dispersion. It should be noticed that the lowest band gap happens in a frequency range where the smallest wavelength in the constituent materials is ten times larger than the period of the phononic crystal. In the vicinity of the Brillouin zone center, the three lowest branches 1–3, starting at the Γ point, are quite similar to those of a homogeneous slab.

Table 4
Physical characteristics of materials used: ρ is the density, C_{11}, C_{12} and C_{44} are the three independent elastic moduli of cubic structure.

Constant	Silicon	Steel	Tungsten	Aluminium	Epoxy
ρ (kg/m^3)	2331	7780	18 700	2730	1142
C_{11} (N/m^2)	16.57×10^{10}	26.4×10^{10}	50.23×10^{10}	10.82×10^{10}	0.754×10^{10}
C_{12} (N/m^2)	6.39×10^{10}	10.2×10^{10}	20.27×10^{10}	5.12×10^{10}	$C_{12} = C_{11} - 2C_{44}$
C_{44} (N/m^2)	7.962×10^{10}	8.10×10^{10}	14.98×10^{10}	2.85×10^{10}	0.148×10^{10}
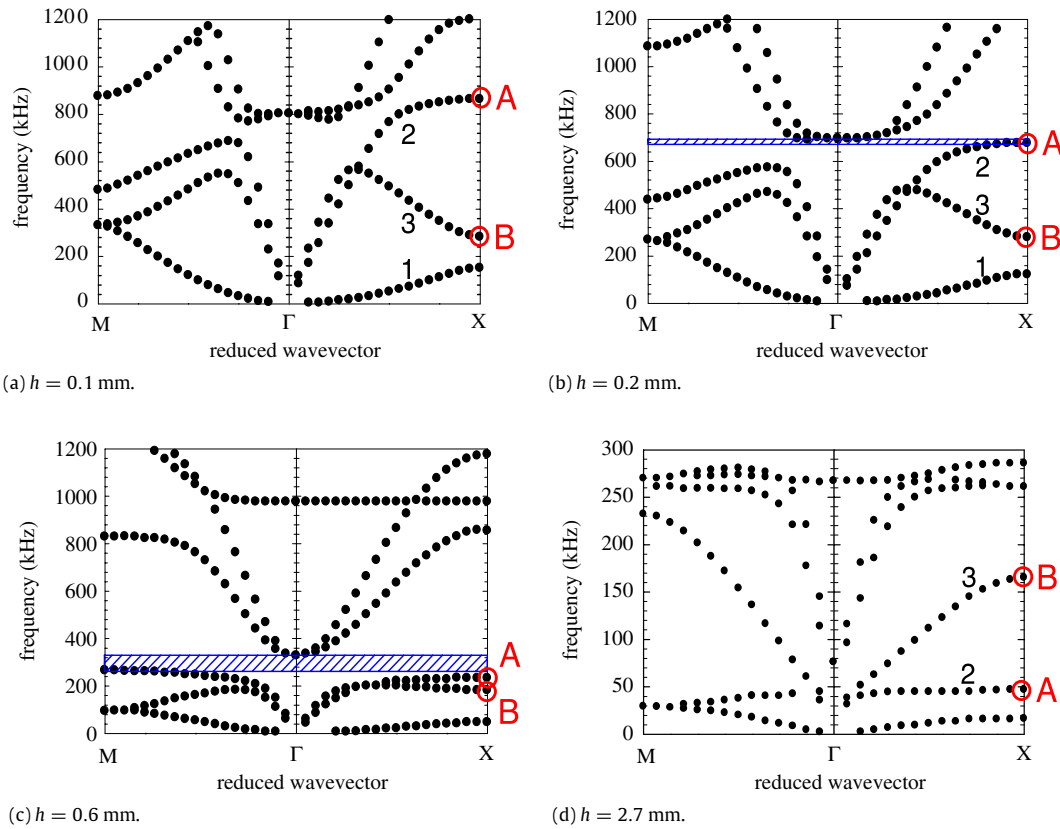
Fig. 60. (Color online) Evolution of the band structure as a function of the height of the dots, keeping constant the thickness of the plate ($e = 0.1$ mm) and the filling factor ($\beta = 0.564$). (a) $h = 0.1$ mm, (b) $h = 0.2$ mm, (c) $h = 0.6$ mm and (d) $h = 2.7$ mm.

They respectively correspond to the antisymmetric Lamb mode (A_0), the shear horizontal mode (SH), and the symmetric Lamb mode (S_0). Dispersion curve calculations of Fig. 59 have also been performed using the finite element method and present a good agreement except for the flat band at 1280 kHz which does not exist. This discrepancy does not affect the conclusions of this study.

4.2.1.2. Behavior of the low frequency gap. The behavior of the band structure of Fig. 59(b) has been studied as a function of the geometrical parameters h, e and β, for the high symmetry axes ΓX and ΓM of the irreducible Brillouin zone (Figs. 60–62).

First, in Fig. 60, we fix the value of the filling fraction ($\beta = 0.564$) and the thickness of the plate ($e = 0.1$ mm) while increasing the height h of the dots. For a small thickness $h = 0.1$ mm, Fig. 60(a), the band structure does not display any band gap in the range [0–1200 kHz], although one can notice a bending of both shear horizontal mode (branch 2) and more particularly of symmetric Lamb mode which becomes a negative slope branch (branch 3). Increasing the height of the cylinders from 0.1 mm to 0.2 mm, Fig. 60(b), the first three dispersion curves shift downwards and the band structure shows the opening of a small absolute gap in the range [675.5–695.2 kHz] which results from a most important bending of the shear horizontal mode (branch 2). With increasing h, the dispersion curves continue to

shift downwards. Until $h = 0.6$ mm, the central frequency of the first gap decreases and its width becomes larger, Fig. 60(c). Increasing h further, one can notice a slower decrease of point B, situated at the boundary X of the Brillouin zone on branch 3, with respect to the other branch extremities, leading to the closing of the gap. This occurs first in the ΓM direction for $h \geq 1.0$ mm, and then in both directions of the Brillouin zone as seen for example in Fig. 60(d) for $h = 2.7$ mm in the magnified frequency range [0–300 kHz].

Fig. 61 presents the evolution of the dispersion curves as a function of the thickness of the plate for constant values of $\beta = 0.564$ and $h = 0.6$ mm. Increasing e from 0.1 to 0.4 mm, the dispersion curves shift to higher frequencies and the gap closes first in the ΓM direction, Fig. 61(b), and finally in both directions of the Brillouin zone as sketched in Fig. 61(c) for $e = 0.6$ mm. This result is due to a faster upward shift of point B with respect to the other branch boundaries.

On the basis of a closed gap ($e = 0.4$ mm), we show in Fig. 62 the influence of the filling factor β on the dispersion curves. The reduction of the filling factor is obtained by increasing the lattice parameter a from 1.0 to 1.6 mm, keeping constant all the other parameters of the structure ($r = 0.42$ mm, $e = 0.4$ mm and $h = 0.6$ mm). In Fig. 62(a), with $a = 1.0$ mm, the gap is closed in the ΓM direction of the Brillouin zone. Increasing a to 1.2 mm, the dispersion curves move downwards and the gap appears in the

(a) $e = 0.1$ mm.
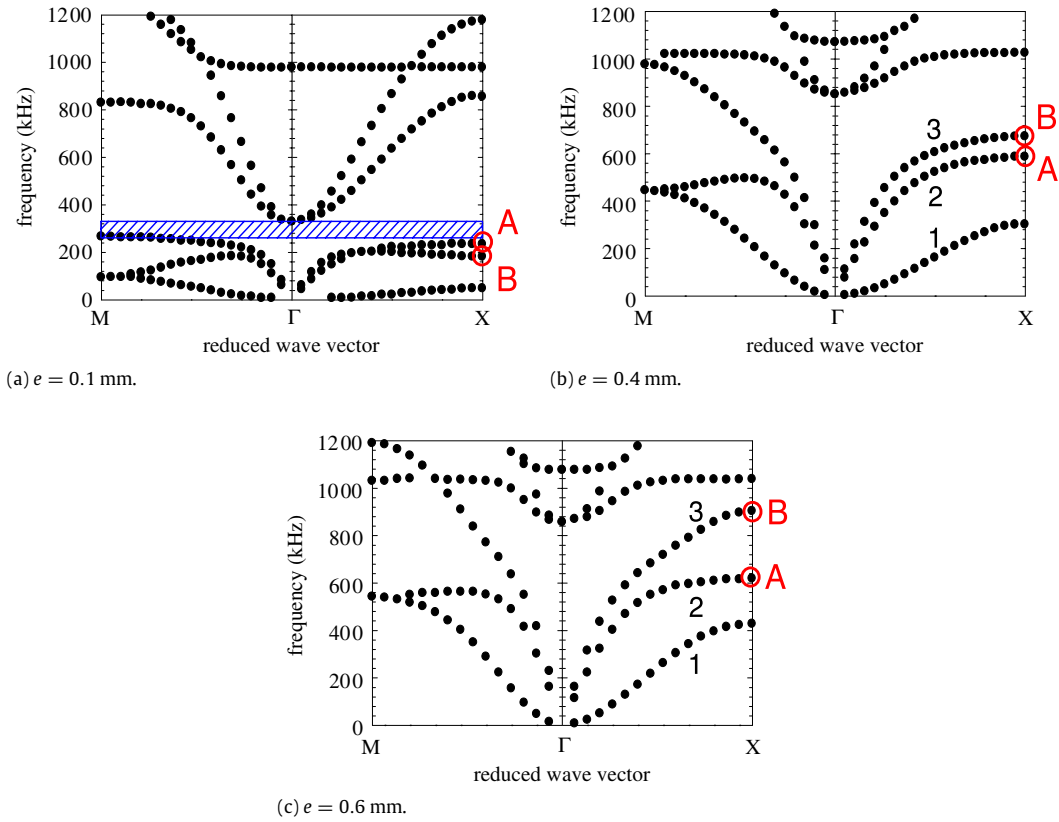
(b) $e = 0.4$ mm.

(c) $e = 0.6$ mm.

Fig. 61. (Color online) Evolution of the band structure as a function of the thickness of the plate keeping constant the height of the dots ($h = 0.6$ mm) and the filling factor ($\beta = 0.564$). (a) $e = 0.1$ mm, (b) $e = 0.4$ mm and (c) $e = 0.6$ mm.

(a) $a = 1.0$ mm, $\beta = 56.4\%$.
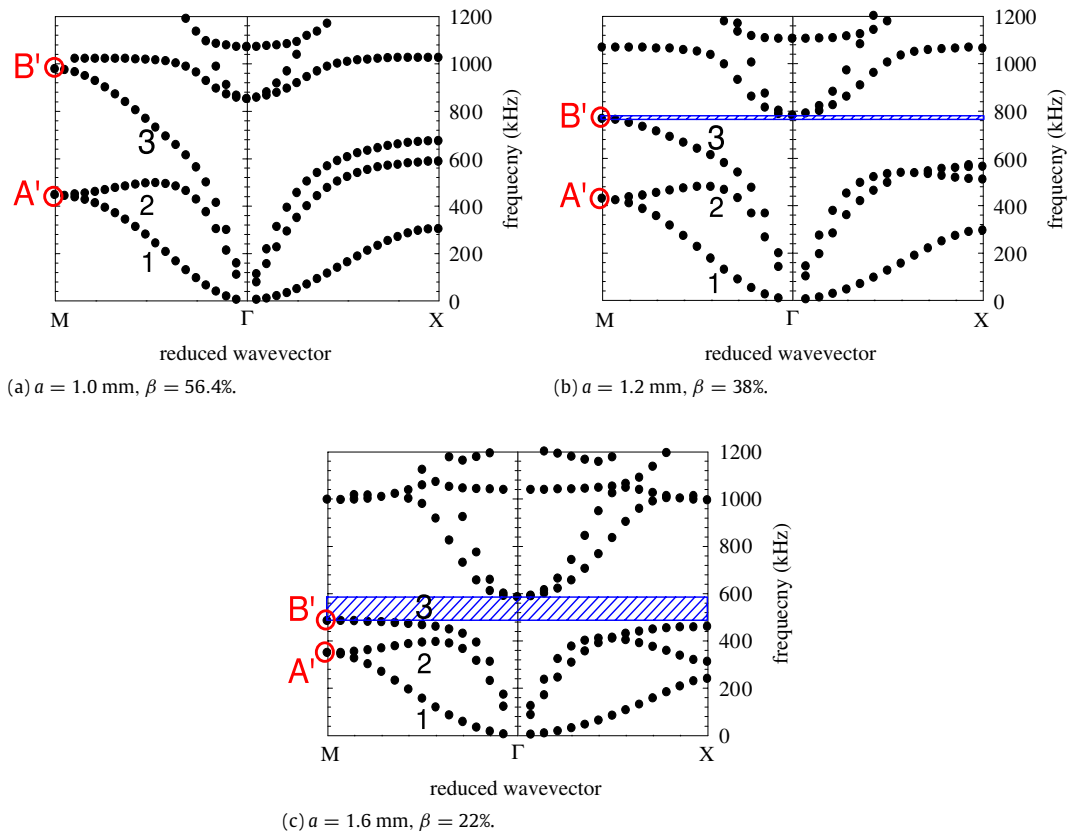
(b) $a = 1.2$ mm, $\beta = 38\%$.

(c) $a = 1.6$ mm, $\beta = 22\%$.

Fig. 62. (Color online) Evolution of the band structure as a function of the filling factor keeping constant the height of the dots ($h = 0.6$ mm), the thickness of the plate ($e = 0.4$ mm) and the radius of the cylinders ($r = 0.42$ mm). (a) $a = 1$ mm ($\beta = 0.564$), (b) $a = 1.2$ mm ($\beta = 0.38$) and (c) $a = 1.6$ mm ($\beta = 0.22$). Points A' and B' correspond respectively to the extremities of branches 2 and 3 at the M point of the Brillouin zone.

(a) Mode (A) branch #2 $f_A = 233.0$ kHz. (b) Mode (B) branch #3 $f_A = 180.6$ kHz.
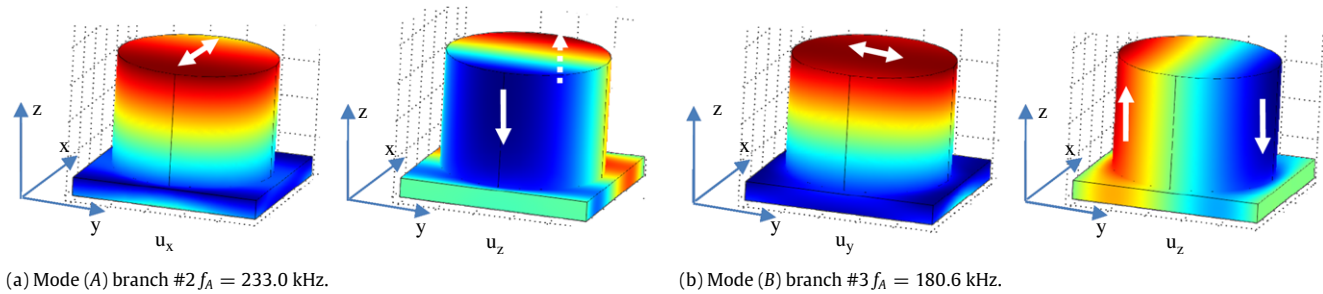
Fig. 63. Displacement fields of the modes A and B in Fig. 59(b). The dashed lines correspond to the rest position of the structure.

frequency range [765.1–778.9 kHz], Fig. 62(b). This result comes from a faster downward shift of point B', situated at the boundary M of the Brillouin zone on branch 3, with respect to the other branch boundaries as seen in the ΓM direction of Fig. 62(c).

To summarize the above trends, the low frequency gap is generated from the bending of both shear horizontal (branch 2) and symmetric Lamb mode (branch 3) of the plate. Since the extremities A and B of these branches move differently (although in the same direction) with the geometric parameters e/a and h/a, the opening of the gap requires an appropriate choice of these parameters. In all cases, the opening of the gap is closely linked to the shift and bending of branch 3 and, for small h, Fig. 60(a), to the shift and bending of branch 2. In comparison with the other band extremities, the evolution of point B is most importantly related to the thickness of the plate and the lattice parameter rather than to the height of the dots. The central frequency of the gap depends upon all the geometrical parameters e, h and a. It decreases either by increasing h, decreasing e or increasing a.

We have investigated the spatial distribution of the eigenmodes inside the unit cell for the modes A and B situated at the extremities of branches 2 and 3 in Fig. 59(b) whose bending is at the origin of the gap. The parameters are $h = 0.6$ mm, $e = 0.1$ mm and $\beta = 0.564$. The initial excitation of the mode is made in the ΓX direction. The results for mode A [wave vector $K_A = (\pi/a, 0, 0)$ and frequency $f_A = 233.0$ kHz] and mode B [($K_B = (\pi/a, 0, 0)$ and frequency $f_B = 180.6$ kHz)] are plotted in Fig. 63(a) and (b) using a cut along the (x, z) or (x, y) plane. In Fig. 63(a), the mode A is clearly associated to an oscillation of the dot in the x direction together with a weak bending of the plate. In Fig. 63(b), the vibration of the mode B involves, in the z direction, an oscillation of the dot correlated to a strong bending of the slab. In both cases, the displacement fields are distributed in the dot as well as in the plate, in agreement with the dependence of the points A and B of the dispersion curves with all the geometrical parameters h, e and a. Moreover, the stronger dependence of mode B with the thickness of the plate (seen in Fig. 61) can be related to a stronger deformation in the plate than in the dot.

We have also investigated the persistence of this gap upon different combinations of the materials constituting the dot and the plate among a set of five materials (tungsten, steel, silicon, aluminum and epoxy). Table 4 reports the densities and velocities of the constituent materials. In Fig. 64(a), we show the limits of the gap by changing the material of the plate when the dots are made of steel. Similarly, Fig. 64(b) displays the gap limits for various materials in the dots and the plate being made of silicon. One can notice the persistence of this gap even if the constituent materials are identical. This supports the origin of the gap as being related to the geometrical rather than physical parameters of the structure. On the other hand, the central frequency of the gap is very dependent upon the choice of the materials and happens at lower frequencies when we combine a high density material (steel) in the cylinders with a low density material (epoxy) in the plate.

For such a system (steel dots on an epoxy plate), the gap extends from 43 to 63 kHz. It is worthwhile to notice that one can obtain a gap in the audible frequency range, around 2 kHz, for a period of $a = 20$ mm and the other parameters being scaled accordingly. Such solid systems could then easily be used as a vibrationless environment for high precision mechanical systems.

In general phononic crystal studies, the band gaps may originate from the Bragg reflections resulting from the periodicity of the structure. We note that the low frequency gap reported here occurs at a frequency such that the wavelength in all constituent materials is at least one order of magnitude larger than the geometrical sizes of the structure. Thus, it shows some similarity with the behavior obtained in locally resonant sonic materials [136–141]. Still, from the spatial distribution of the displacement field, we cannot attribute a totally localized character to the modes in this frequency range. Instead, the competitive motions of branches 2 and 3 by varying the geometrical parameters should allow the opening of the gap.

4.2.1.3. Behavior of the higher gaps. The behavior of the higher gap observed in the band structure of Fig. 59(a) has been studied as a function of the geometrical parameters h, e and β, along the high symmetry axes ΓX and ΓM of the irreducible Brillouin zone (Fig. 65). We choose to refer to the thickness $e = 0.2$ mm to avoid a thin discretization of the space thus decreasing the time of calculation. In Fig. 65, we fix the values of the filling fraction $\beta = 0.564$ and the thickness of the plate ($e = 0.2$ mm) while increasing the height of the dots from $h = 0.6$ mm to $h = 2.7$ mm. For $h = 0.6$ mm, Fig. 65(a), we note the existence of three gaps. The lowest one [519.3–571.7 kHz], discussed in Section 5.2.1, closes for $h > 1.0$ mm. Besides, the band structure exhibits two higher gaps respectively in the frequency ranges [1560–1887 kHz] and [2092–2328 kHz]. When increasing h to 1.5 mm, Fig. 65(b) and then to 2.7 mm, Fig. 65(c), the central frequencies of these gaps move downwards together with the dispersion curves, whereas new absolute band gaps appear at higher frequencies. It is interesting to remark that, up to a certain frequency range, the opening of the gaps results from the crossing of the normal acoustic branches with almost flat bands, which is similar to the case of locally resonant materials.

We have also studied the evolution of the gaps with the thickness of the plate e, keeping constant $h = 2.7$ mm and $\beta = 0.564$, Fig. 66(a). Increasing e from 0.1 mm to 1.0 mm, we observe a slow variation of the central frequency of the gap. In addition, most of the gaps close for $e > 1$ mm, due to many new dispersion branches moving downwards. The evolution of the gaps with the filling factor has also been investigated. When increasing a from 1.0 mm, Fig. 65(c), to 1.4 mm, Fig. 66(b), with the same h and e, several branches move downwards from the high frequency region and progressively fill the higher gaps; at the same time, the lowest remaining gaps keep their central frequencies almost preserved.

(a) Steel cylinders on various plates.   (b) Various cylinders on Si plate.
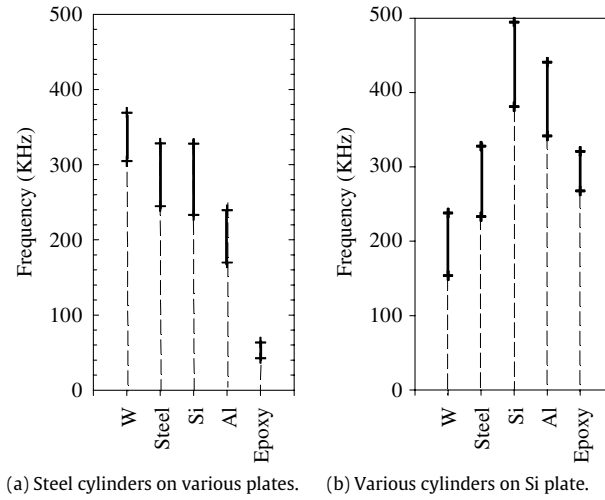
Fig. 64. Evolution of the lowest frequency gap limits for different combinations of constituent materials. (a) Steel dots on a plate of different materials. (b) Various dots on a silicon plate. The geometrical parameters are $e = 0.1$ mm, $h = 0.6$ mm and $\beta = 0.564$.

(a) $h = 0.6$ mm.   (b) $h = 1.5$ mm.   (c) $h = 2.7$ mm.
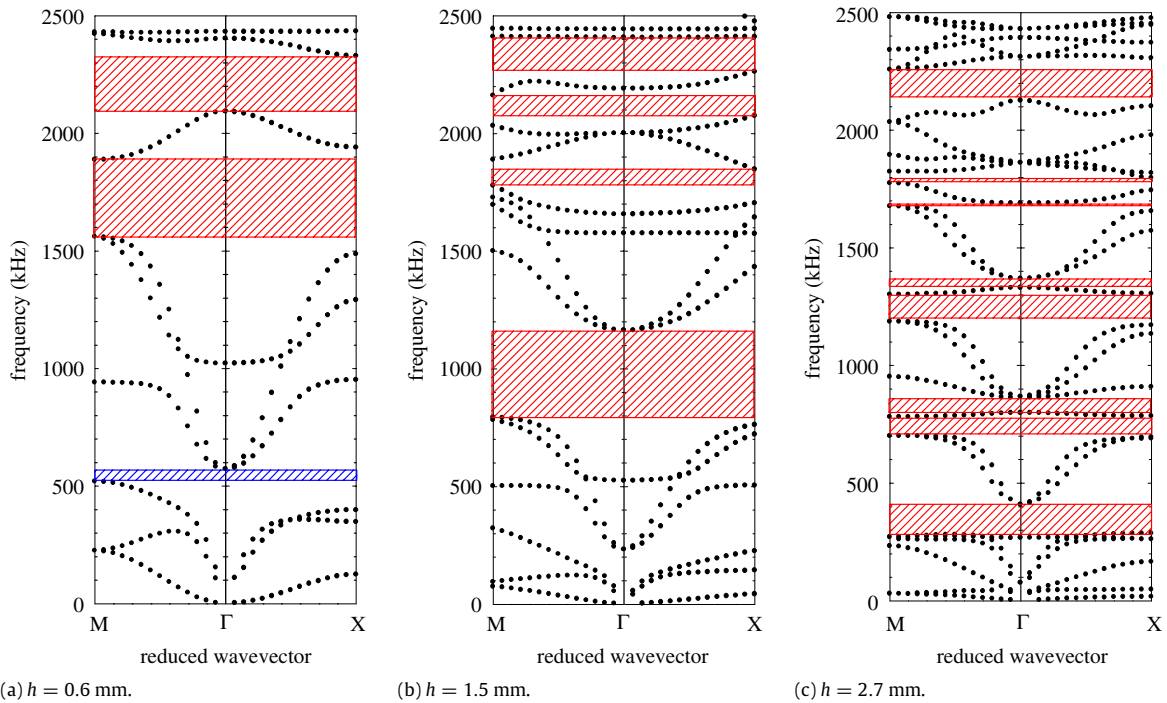
Fig. 65. (Color online) Evolution of the band structure for different values of the height of the dots: (a) $h = 0.6$ mm, (b) $h = 1.5$ mm and (c) $h = 2.7$ mm. The other geometrical parameters are $e = 0.2$ mm and $\beta = 0.564$.

4.2.1.4. Propagation of guiding waves in the slab. We study now the possibility of propagating a confined mode in a rectilinear waveguide created inside the phononic crystal. The geometrical parameters are the same as in Fig. 59, i.e. $\beta = 0.564$, $h = 0.6$ mm and $e = 0.1$ mm that ensures the existence of the largest forbidden gaps. The finite difference time domain calculation is performed by using a supercell containing five unit cells in the y direction. The guide is created by removing one row of dots in the third unit cell, thus constituting a linear waveguide in the x direction. The width of the waveguide, δ, has been chosen as a variable parameter to investigate the existence and number of localized modes in the band gap [81]. Fig. 67(a) shows the band structure in the ΓX direction for the waveguide structure with $\delta = 0.55a$. The dispersion curve exhibits three additional branches inside the higher gap (1287–2106 kHz) while no supplementary branches

appear inside the lowest gap. Increasing the width of the waveguide leads to the lowering of the frequencies of the waveguide modes. Fig. 67(b) shows the band structure for a waveguide with $\delta = 1.05a$ which presents one new mode in the lowest forbidden band (265.2–327.9 kHz). To show the confinement of such modes inside the waveguide, we focus on the points C and D of the dispersion curves. The maps of the displacement fields associated with both modes are respectively sketched in Fig. 67(c) and (d). In both cases, the acoustic field is essentially confined in the area of the waveguide and does not leak out into the rest of the structure.

4.2.2. Second model and wave guiding study [142]

4.2.2.1. Introduction. From the calculation of both transmission coefficients and dispersion relations, the purpose of this subsection

(a) Gap map as a function of e.   (b) $a = 1.4$ mm.
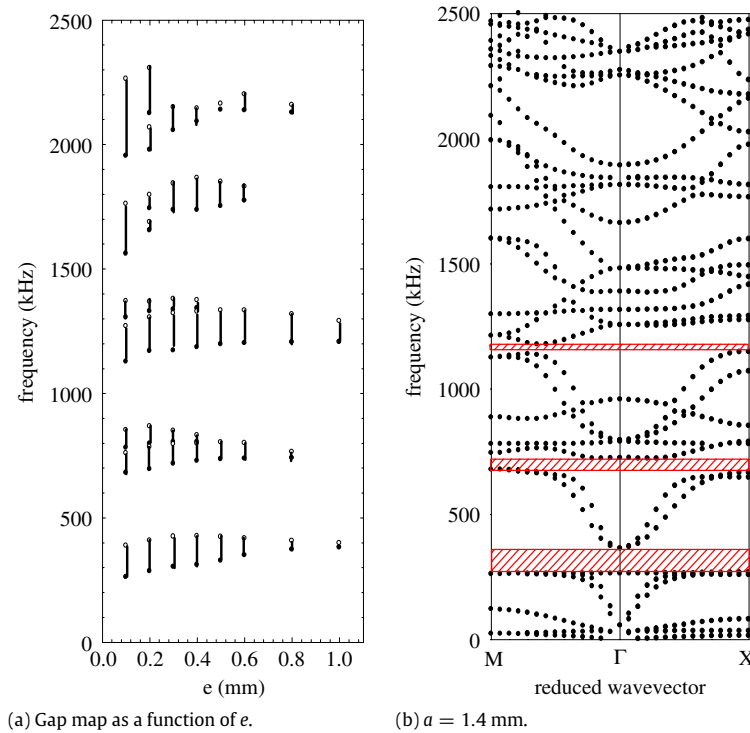
Fig. 66. (Color online) (a) Evolution of the gaps of Fig. 59(a) as a function of the thickness of the plate, keeping constant the other geometrical parameters ($h = 2.7$ mm and $\beta = 0.564$). (b) Dispersion curves for a low filling fraction $\beta = 0.38$ (lattice parameter $a = 1.4$ mm) and the geometrical parameters $h = 2.7$ mm and $e = 0.2$ mm.

is to study in detail the wave guiding effects through different types of linear defects in this novel phononic crystal, made up of cylindrical dots on a thin homogeneous plate. Such waveguides are obtained either by removing a row of dots or by replacing in a row the materials or geometrical parameters of the dots. In each case, we present a detailed study of the confined modes, the transmitting and non-transmitting characters of the corresponding bands, and the possibility of polarization conversion, which could frequently occur. The flexibility of tailoring the acoustic properties of phononic crystals, especially those utilized for waveguide design, makes them particularly suitable for a wide range of applications from transducer technology to filtering and guidance of acoustic waves. Moreover, it should also be pointed out that a knowledge and engineering of phononic band structures is also a necessary step to investigate heat transport in heterogeneous nanostructured materials [143–145] since the existence of gaps and/or flat bands prohibits the propagation of phonons in certain frequency ranges.

Fig. 68(a) is a scheme of the phononic crystal which is studied in this subsection, namely a heterostructure made up of a square array of steel cylindrical dots of radius r and height h, deposited on a thin homogeneous plate of silicon. The z axis is assumed to be perpendicular to the plate and parallel to the cylinders. We define the lattice parameter a of the periodic array as equal to 1 m and the filling factor β, given by $\beta = \pi r^2/a^2$, equal to 0.564. The thickness of the plate is denoted by e and takes the value $e = 0.2$ μm. The materials composing the dots and plate are assumed to be of cubic symmetry with their crystallographic axes oriented along the coordinate axes x, y and z. The elastic constants and mass densities of the materials involved in the calculations were given in Table 4. The dispersion curves were calculated with the help of the finite difference time domain method (see Section 5.2.1.1).

The transmission spectra through perfect or defect-containing phononic structures were computed using a three-dimensional finite difference time domain code. Our calculation is performed in a three-dimensional box with the propagation along the y axis.

The box is finite along y and composed of a phononic crystal containing seven or ten cylinders, sandwiched between an ingoing and an outgoing media, which are two homogeneous plates of thickness e. Perfect matching layer conditions are applied at the boundaries of the box along the y direction. Along the x direction, the structure is periodic, which means that it contains one unit cell when dealing with a perfect phononic crystal. However, the waveguide is studied with a supercell of five periods to avoid the interaction between neighboring guides. Along z, a thin layer of vacuum is added on both sides of the phononic structure in order to decouple the interaction between repeating periodical cells. A broad band wave packet is initiated from the homogeneous plate in front of the phononic crystal. This wave is a longitudinal pulse, with a polarization and Gaussian profile along the y axis, but uniform in the x and z directions. The transmitted signal is recorded at the end of the phononic crystal, and integrated in the (x, z) plane for each component u_x, u_y and u_z of the displacement field. The throughput signal of the waveguide is integrated only over the cross section of the waveguide instead of the whole period in the x direction as was the case for the perfect phononic crystals. We note that, with this procedure, the maximum value of the transmission can exceed unity. In practice, the u_x component vanishes, so that the transmission spectra will be obtained only for the u_y and u_z components. Finally, the signal, recorded as a function of time, is Fourier transformed and normalized by an equivalent signal propagating through a single homogeneous silicon slab to yield the transmission coefficient.

The band structure is presented in Fig. 68(b) in the frequency range [0–2.5 GHz] along the high symmetry axes ΓX and ΓM of the first Brillouin zone. The choice of the geometrical parameters ensures the existence of two absolute band gaps extending respectively from 0.613 to 0.668 GHz and from 1.615 to 2.139 GHz. It should be noticed that the lowest band gap happens in a frequency range where the smallest wavelength in the constituent material is ten times larger than the period of the phononic crystal. The higher gap appears in the Bragg frequency regime, where the
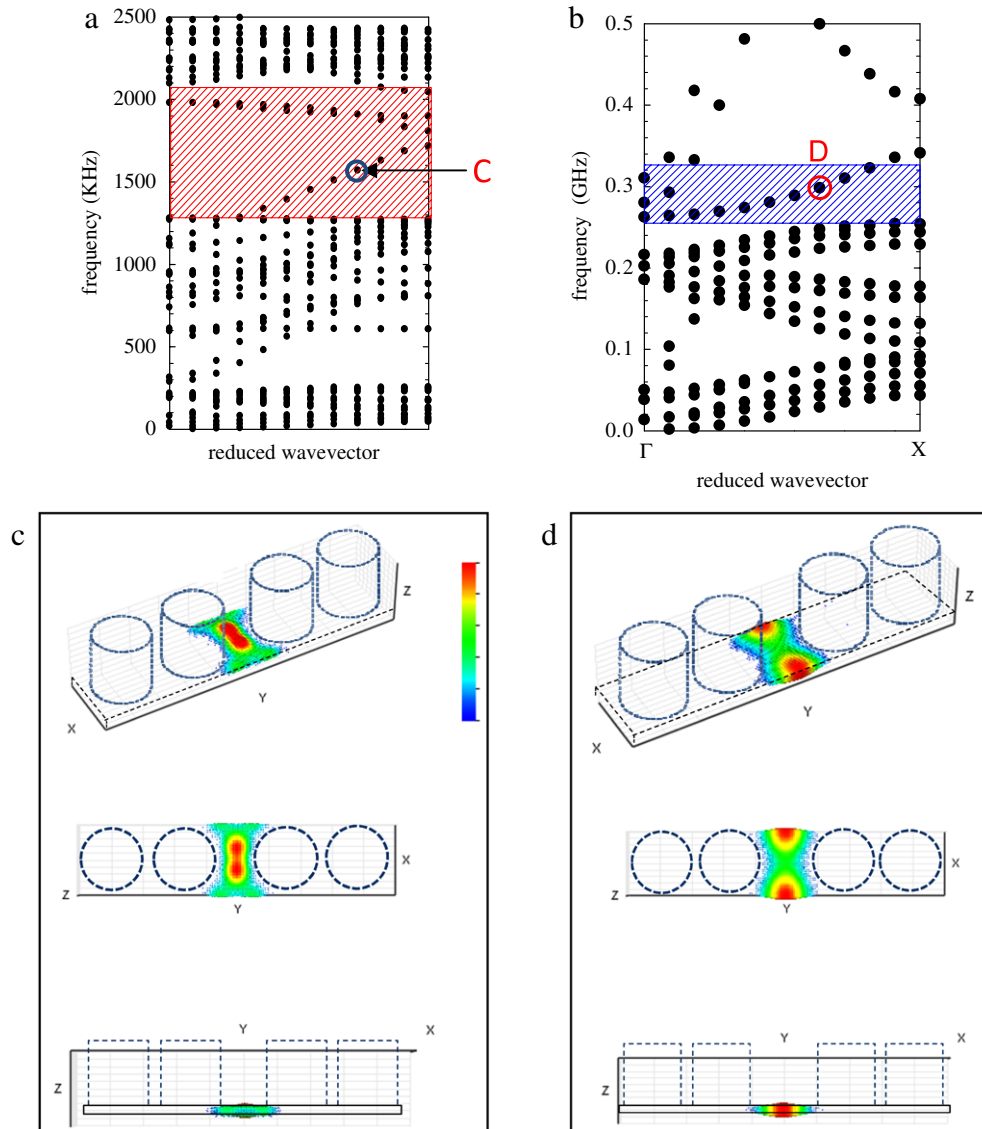
Fig. 67. (Color online) (a, b) Band structures along the ΓX direction for a phononic crystal containing a waveguide of width δ obtained by removing one row of dots. The calculation is performed with a supercell containing 1×5 unit cells and the dots are removed in the third unit cell. The blue and red hatched areas indicate the location of the absolute band gaps of the perfect structure. (a, b) display respectively the dispersion curves for a waveguide width of $\delta = 0.55a$ and $\delta = 1.05a$. (c, d) Maps of the modulus of the elastic displacement fields for the modes labeled C and D, represented in three-quarter, top, and lateral views. The red and blue colors respectively correspond to the maximum and minimum of the displacement.

wavelength is almost of the same order of magnitude as the lattice parameter. The origin and behavior of these gaps as a function of the geometrical and physical parameters of the whole structure have been already studied here above, see sections 5.2.1.2 and 5.2.1.3. The new results, shown in the diagrams of Fig. 68(b), are the computing transmission spectra in the directions ΓX and ΓM of the Brillouin zone, which are displayed on each side of the central band diagram. In the transmission spectra, we differentiate the polarization u_y (black solid lines) and u_z (red dashed lines) of the detected signal. We can notice a good agreement between the transmission and dispersion curves and, in particular, the positions of the gaps. The number of Fabry–Perot oscillations appearing in the transmission spectra below 1.5 GHz is in accordance with the number of unit cells in the phononic crystal along the y direction. At frequencies above 2.1 GHz, we can observe an isolated branch with a negative slope [146] which contributes to a transmission only for the polarization u_z normal to the plate while the detected signal for the component u_y is negligible. We made the calculation of one eigenmode along the negative branch, at the

point A defined by the reduced wavenumber $Ka/\pi = 0.474$ and frequency $f = 2.312$ GHz. This eigenmode, sketched in Fig. 68(c), presents a localization of the acoustic energy in the corners of the unit cell for the normal component u_z. In accordance with the polarization of the negative branch, the incident longitudinal mode has been partially converted into a normal polarized signal. This effect shows that an incident longitudinal symmetric pulse which is initiated inside the plate of thickness e, can be partially converted into a transmitted signal perpendicular to the plate. Such a property can be useful for the observation of the transmitted field with a laser interferometric technique, which is sensitive to the component of the displacement field normal to the plate.

4.2.2.2. Conventional line-defect waveguide. The traditional way of creating a linear defect is to remove a row of dots. In our calculation, the length of the waveguide is assumed to be ten periods of the phononic crystal and the width of the waveguide w_g has been considered as a variable, Fig. 69(a). Fig. 69(b) gives the transmission spectra for both components u_y and u_z of the displacement field through the waveguide with $w_g = 1.2 \ \mu$m. As a
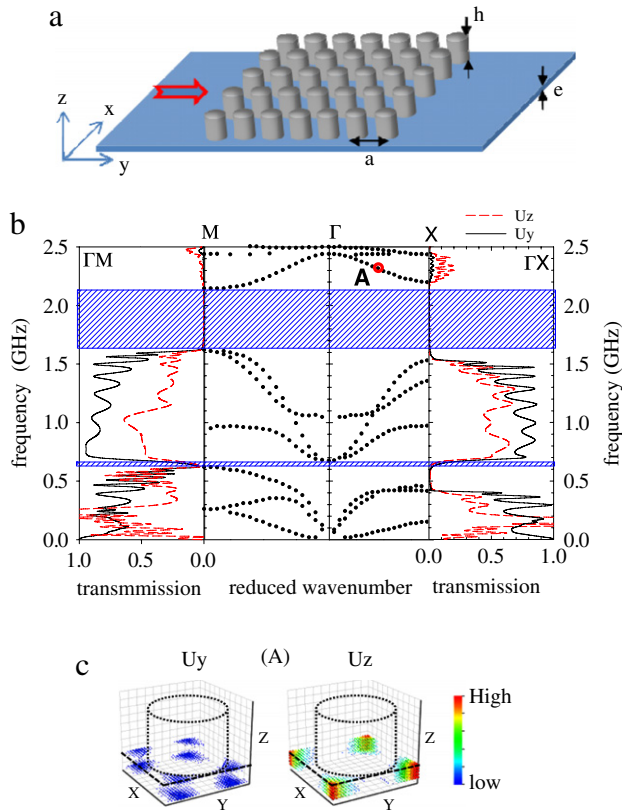
Fig. 68. (Color online) (a) Phononic crystal made of a square lattice of steel finite cylinders deposited on a homogeneous silicon plate. The geometrical parameters are $a = 1$ μm, $h = 0.6$ μm and $e = 0.2$ μm. The red arrow symbolizes the incident longitudinal pulse. (b) Middle: band structure calculated along the high symmetry axis ΓX and ΓM of the Brillouin zone. From each side of the band diagram: transmitted curves of the longitudinal incident wave for the polarization u_y (black solid line) and for the polarization u_z (red dashed lines). The red (blue) area corresponds to the position of the low (high) absolute band gap. (c) Eigenmode calculation at the point A, defined by the coordinates ($Ka/\pi = 0.474$, $f = 2.312$ GHz). The blue (red) color corresponds to the lower (higher) value of the displacement field modulus.

comparison, we also give the transmission coefficient through the perfect crystal as red dashed lines. The shaded red and blue areas, respectively, represent the two band gaps. Increasing w_g from 0 to 1.2 μm leads to the emergence of transmitted signals in the gaps, the case of $w_g = 1.2$ μm being presented in Fig. 69(b). Beyond this value, the number of confined modes in the band gaps increases too much, which is not most suitable for filtering or multiplexing applications. Looking at Fig. 69(b), we observe a full transmission of the acoustic waves within the higher gap [1.615–2.139 GHz] for the u_y component while the u_z component remains weak. For the low frequency gap [0.613–0.668 GHz], the opposite situation occurs, i.e. the transmitted signal has mainly an u_z component. The transmission coefficients in the pass band between the two gaps are also strongly perturbed by the presence of the waveguide.

To highlight the waveguiding properties through the gaps, the finite difference time domain computation was used to simulate a monochromatic source, first at the frequency $f = 1.751$ GHz in the higher gap and then at the frequency $f = 0.6284$ GHz in the lower gap, Fig. 69(c). We display the computed displacements in the (x, y) plane for a section in the middle of the plate ($z = e/2$). It is clearly seen that in both cases the incident wave propagates without attenuation and with a strong confinement inside the waveguide. Only a slight amount of energy leaks out of the waveguide.

The dispersion of the waveguide structure with $w_g = 1.2$ μm is shown in Fig. 70(a). In this diagram, the red dots represent the band structure of the perfect phononic crystal for a supercell

of five periods, and the black dots the band structure with the linear waveguide. In this latter case, we can observe several modes inside both the low and high frequency gaps, which correspond to the existence of defect modes confined in the waveguide. Nevertheless, when comparing with the transmission spectrum, it seems that many of these branches do not contribute to the transmission of the incident longitudinal waves. We made a complete analysis of the eigenmodes for different branches and found that, in the higher gap, only one branch has the appropriate longitudinal polarization in order to efficiently contribute to the transmission. The displacement field of this mode was calculated for a reduced wave number $Ka/\pi = 0.26$ and frequency $f = 1.778$ GHz (point B in Fig. 70(a)), and is presented in Fig. 70(b). The wave is well localized within the waveguide and essentially exhibits a longitudinal displacement u_y whereas the normal component u_z is almost equal to zero. For the low frequency gap, there are two localized branches existing at low and high wave vectors, respectively. For the branch at low wave vector, the polarization is mainly u_x and does not contribute to the transmission. Fig. 70(c) displays the displacement field for the second branch associated with the mode at the point C ($Ka/\pi = 0.737$; $f = 0.6426$ GHz). We can see that the mode is mainly polarized along z with a weak contribution of the polarization u_y. From this analysis, we can understand that the branch at higher wave vectors contributes to a transmission perpendicular to the plate. These conclusions are in accordance with the transmission spectra shown in Fig. 69.

As a summary, the transmission of a longitudinal incident pulse through a conventional waveguide gives rise to a mainly longitudinal wave in the range of the high frequency gap, while a conversion to a wave with a normal component to the plate occurs in the low frequency gap.

4.2.2.3. Linear waveguide made up of dots of different heights. In this paragraph, we study a waveguide structure obtained by changing the height of the dots along one row. We study, more specifically, the case where the height h_g, Fig. 71(a), is smaller than that in the perfect crystal, and is in a scale ranging from 0.6 to 0.1 μm. The band structure analysis reveals that, when $h_g \leq 0.4$ μm, new localized modes appear inside the gaps. Those defect branches shift towards the higher frequencies as far as the height of the dots decreases.

Fig. 71(b) displays the dispersion curves magnified in the frequency range [1.2–2.5 GHz]. In this figure, the black dots represent the band structure of the linear waveguide ($h = 0.2$ μm) compared with the band structure of the perfect phononic crystal ($h = 0.6$ μm) represented by the red dots. We can observe three guided modes inside the high frequency gap; among them we especially focus on the branch which crosses the whole frequency range of the gap. Fig. 71(c) presents the eigenmode corresponding to the point D ($Ka/\pi = 0.58$; $f = 1.885$ GHz) on this branch. We can observe that both components u_y and u_z of the displacement field are represented and strongly localized within the dot constituting the waveguide. In Fig. 72(a), we present, for the incident longitudinal pulse, the transmission coefficients for the components u_y and u_z of the displacement field and observe a similar magnitude of both components in the transmitted waves. To complete the study, the propagation and confinement of the acoustic waves are represented using a displacement field representation for the components u_y and u_z at the incident monochromatic frequency $f = 1.698$ GHz, Fig. 72(b).

Fig. 73(a) displays the dispersion curves and the corresponding transmission spectra in the low frequency range [0.3–0.8 GHz] for $h_g = 0.3$ μm. The value of h_g is chosen in such a way so that we obtain guided modes in the low frequency gap extending from 0.4147 to 0.668 GHz along the ΓX direction. Nevertheless,
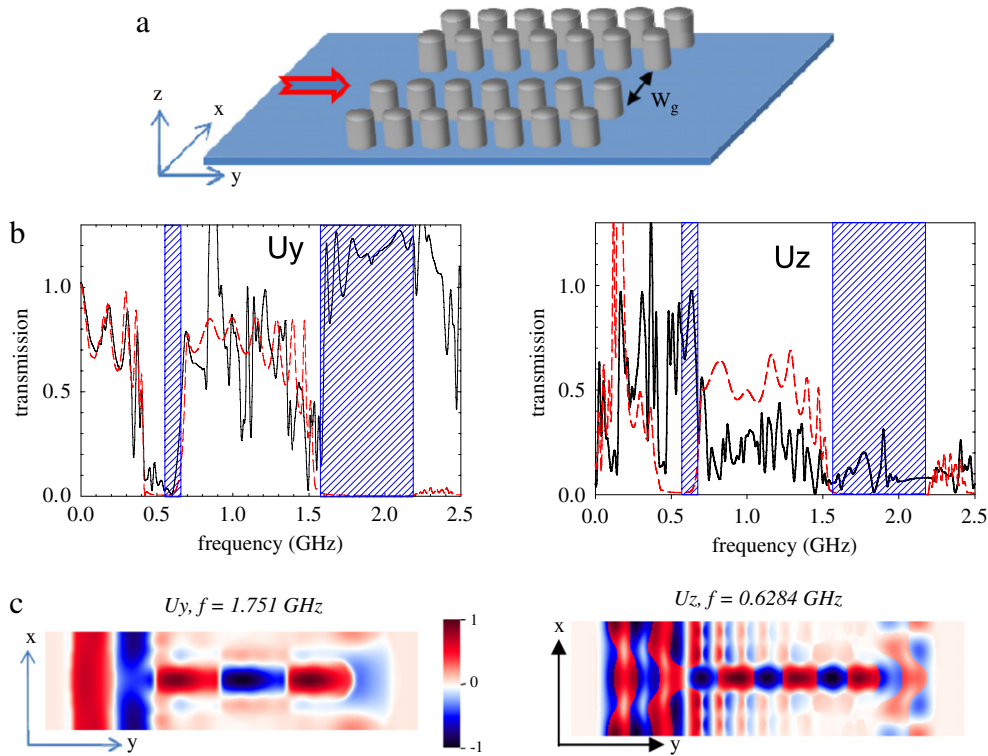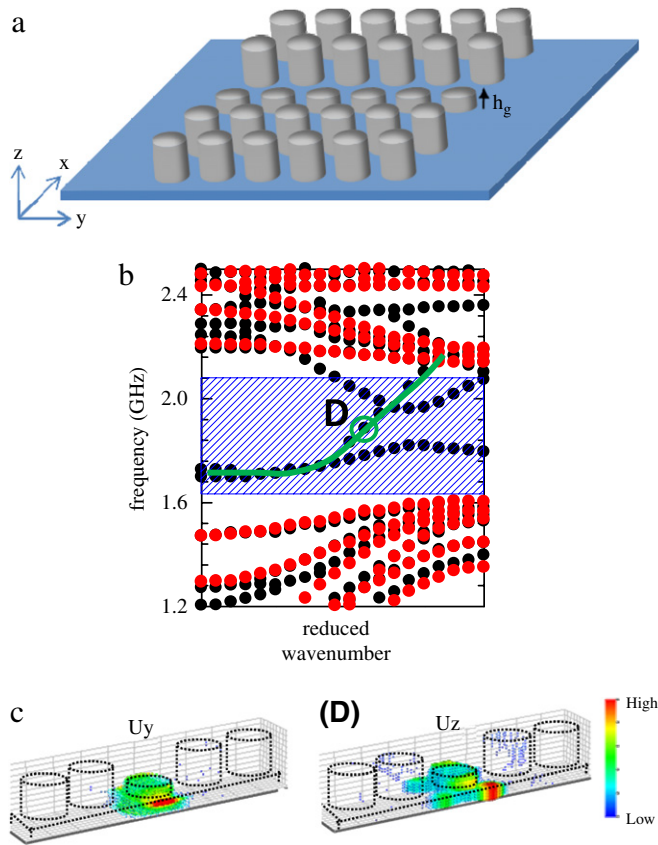
Fig. 69. (Color online) (a) Schematic view of a conventional line-defect waveguide; w_g corresponds to the adjustable waveguide width. (b) Black solid lines: transmission coefficient recorded at the exit of the waveguide for the polarizations u_y and u_z. Red dashed lines: transmission through the perfect phononic crystal structure. (c) Left: planar sections at the thickness $z = e/2$ of the displacement field distribution for the u_y polarization at the monochromatic frequency $f = 1.751$ GHz. Right: same as previously for the polarization u_z and the monochromatic frequency $f = 0.6284$ GHz. The red (blue) color represents the positive (negative) contribution of the wave.
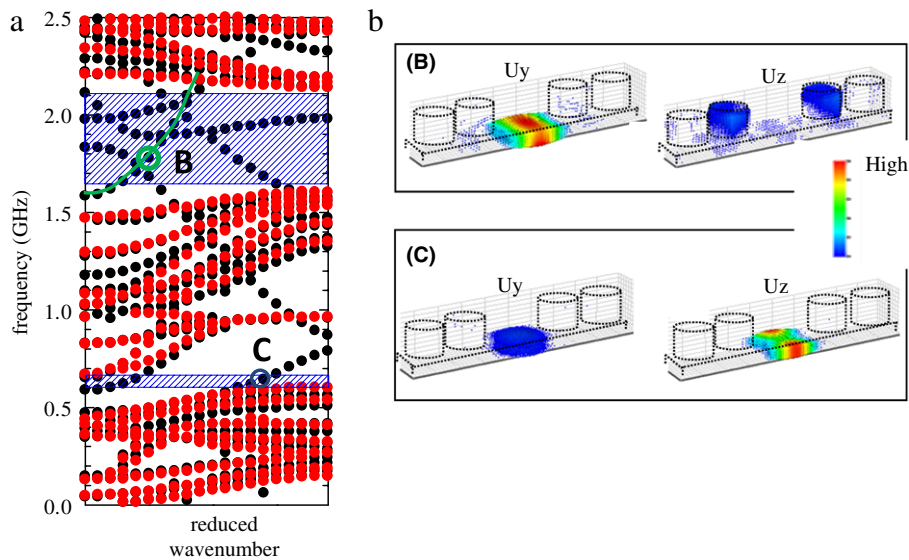
Fig. 70. (a) Dispersion curves of the perfect phononic crystal (red dots) and for the line-defect waveguide structure for a five lattice parameter unit cell in the ΓX direction of the Brillouin zone (black dots). (b) Three-dimensional eigenmode representation at the points B ($Ka/\pi = 0.26$, $f = 1.778$ GHz) and C ($ka/\pi = 0.737$, $f = 0.6426$ GHz) for the two polarizations, parallel (u_y) and perpendicular (u_z) to the plate. The blue (red) color corresponds to the lower (higher) value of the displacement field modulus while the white color corresponds to a displacement equal to zero but does not appear in the color bar.

we notice that this gap is much wider than the absolute band gap because the lower limit of the band gap along the ΓM direction is 0.613 GHz. This effect explains the existence of several peaks of transmission inside the ΓX partial band gap [0.4147–0.613 GHz], which correspond to acoustic waves leaking out of the waveguide towards the ΓM direction. Therefore, this frequency region is not very useful for the guiding of confined modes. In the frequency range of the absolute band gap (red shaded area), there is a

transmitted signal around the frequency 0.6277 GHz for both u_y and u_z, with a higher transmission coefficient for the longitudinal polarization. The corresponding band diagram shows two confined branches. The branch, which crosses the whole gap, has an u_x polarization and does not contribute to the transmission. For the other branch, the eigenmode at point E ($Ka/\pi = 0.16$, $f = 0.6277$ GHz) is sketched in Fig. 73(b). This mode is mainly polarized along y, but is again with a non-negligible component along z. The

Fig. 71. (Color online) (a) Schematic view of a linear waveguide made of dots of different heights h_g. (b) Black dots: dispersion curves for a waveguide structure of height $h_g = 0.2$ μm in the high frequency range. (c) Eigenmode representation at the point D ($ka/\pi = 0.58, f = 1.885$ GHz) for u_y and u_z. The blue (red) color corresponds to the lower (higher) value of the displacement field modulus while the white color corresponds to a displacement equal to zero but does not appear in the color bar.

first of these components is strongly localized inside the guiding dots while the latter is less confined and penetrates over the dots in the neighborhood of the waveguide. Therefore, a good correspondence between the band diagram and transmitted curve is obtained.

To summarize this paragraph, the waveguide created by decreasing the height of the cylinders can transmit confined modes inside both the high and low frequency band gaps. In the former case, the incident longitudinal wave gives rise to transmitted waves with components both parallel and perpendicular to the plates. In the latter case, the transmitted wave has a main longitudinal component but also a smaller normal component with a weaker confinement inside the waveguide. A similar study can be performed if the height of the cylinders is increased with respect to the one in the perfect crystal.

4.2.2.4. Linear waveguide made up of dots of different materials. In this paragraph, we assume that the waveguide is formed from a row of dots made up of a different material than those in the perfect crystal, Fig. 74(a). We chose cylinders made up of Si and Al in the waveguide to obtain propagation in the higher and lower gaps, respectively.

In Fig. 74(b), we show, in the frequency range [1.4–2.5 GHz], both dispersion curves and transmission of u_y and u_z components of the displacement field when the dots in the waveguide are made up of Si. We can observe that the transmitted waves contain both components. This result is in accordance with the eigenvector of the modes in the corresponding branch, as shown in Fig. 74(c) for

the mode situated at wave number $Ka/\pi = 0.37$ and frequency $f = 1.777$ GHz (point F). In addition, this figure shows that the z component of the displacement field is mainly confined in the dots while the y component is essentially localized within the homogeneous plate. We notice that the other two dispersive branches, involved inside the gap, possess an u_x polarization and should not contribute to the transmission.

Similarly, we report, in Fig. 75, the case of a waveguide made up of aluminum dots, which is well adapted for the propagating signal in the low frequency gap. Here, the interesting point is to have only one localized mode appearing in the gap, Fig. 75(a), giving rise to a monomode waveguide. The transmitted waves contain u_y and u_z components of the displacement field. This conclusion is supported by the map of the propagating confined field in the waveguide (Fig. 75(b)) at the frequency $f = 0.6311$ GHz. It is worth remembering that, here, the wavelength of the wave transmitted through the guide is more than ten times larger than the lattice parameter of the phononic crystal. As a result, a waveguide whose length is ten unit cells of the phononic crystal contains less than one period of the confined mode.

4.3. Summary

We introduce in this section a supercell plane wave expansion method to calculate the elastic band structures of perfect and defected two-dimensional phononic crystal plates. Compared with previous works on waves propagating in two-dimensional phononic crystals with free surfaces, our method does not require writing explicitly the boundary conditions on the free surfaces. This alleviates some numerical difficulties such as the computation of pseudo-modes without physical meaning [102, 103,120]. We establish the range of validity of this method with respect to the contrast in material properties and phononic crystal plate geometry. We demonstrate for solid/solid phononic crystals with low contrast materials that the method converges with a reasonably small number of reciprocal space vectors in all directions. High contrast solid/solid phononic crystal plates have been shown to lead to convergence difficulties for most of the plane wave expansion-based methods introduced to date. The supercell plane wave expansion method suffers the same problem. We propose a low impedance medium to serve as a decoupling medium between periodically repeated plates. We also show that the low impedance medium can be used effectively as an inclusion medium to model two-dimensional phononic crystal plates composed of air inclusions and solid matrices. We establish that this approach leads to fast convergence for a wide range of values of solid physical properties. We show the existence of band gaps in air/steel and air/silicon two-dimensional phononic crystal plates composed of square arrays of holes. We also observe wider band gaps for a graphite lattice of air holes in silicon plates. We characterize the effect of the thickness of the plate on the location and the width of the absolute band gaps and find optimum conditions for achieving the widest absolute band gap. We apply the supercell plane wave expansion method with low impedance medium inclusions to a study of air/silicon phononic crystal plates containing a guide of variable width. The defected system is composed of two phononic crystal plates separated by a homogeneous solid plate made of silicon. We demonstrate the existence of waveguide modes inside the absolute forbidden bands. The number of waveguide modes decreases with the decreasing width of the guide. Characterization of the displacement fields associated with the waveguide modes demonstrates, in some cases, their localization inside this structural defect. These defect modes could then be used to realize acoustic devices such as waveguides, specific frequency filters or wavelength multiplexers. In particular,
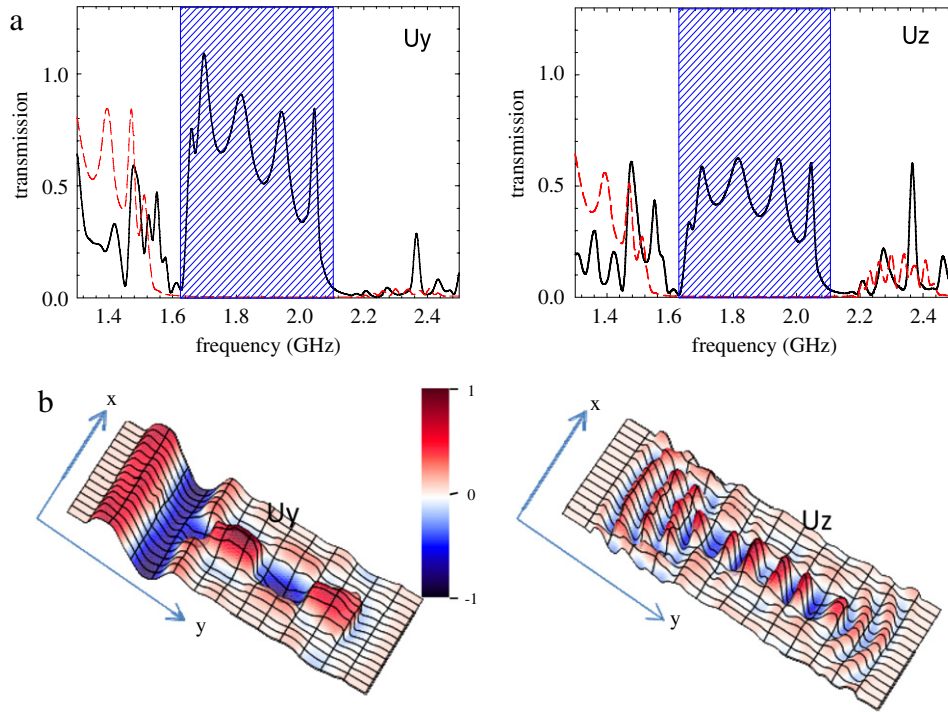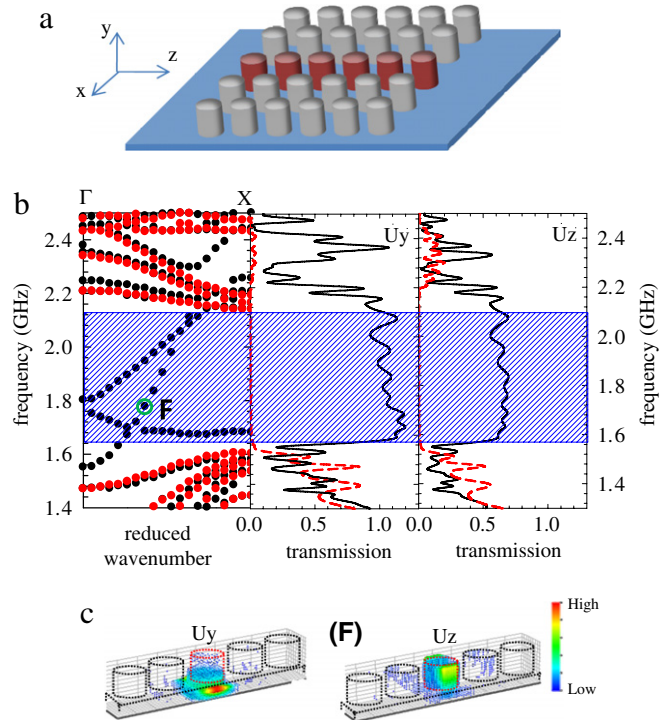
Fig. 72. (Color online) (a) Transmission spectrum for the waveguide structure of Fig. 71(a) for $h_g = 0.2$ μm according to the u_y and u_z polarizations. (b) Displacement field distributions in the (x, y) plane at the thickness $z = e/2$ for the u_y and u_z polarization at the monochromatic frequency $f = 1.698$ GHz. The red (blue) color represents the positive (negative) contribution of the wave.
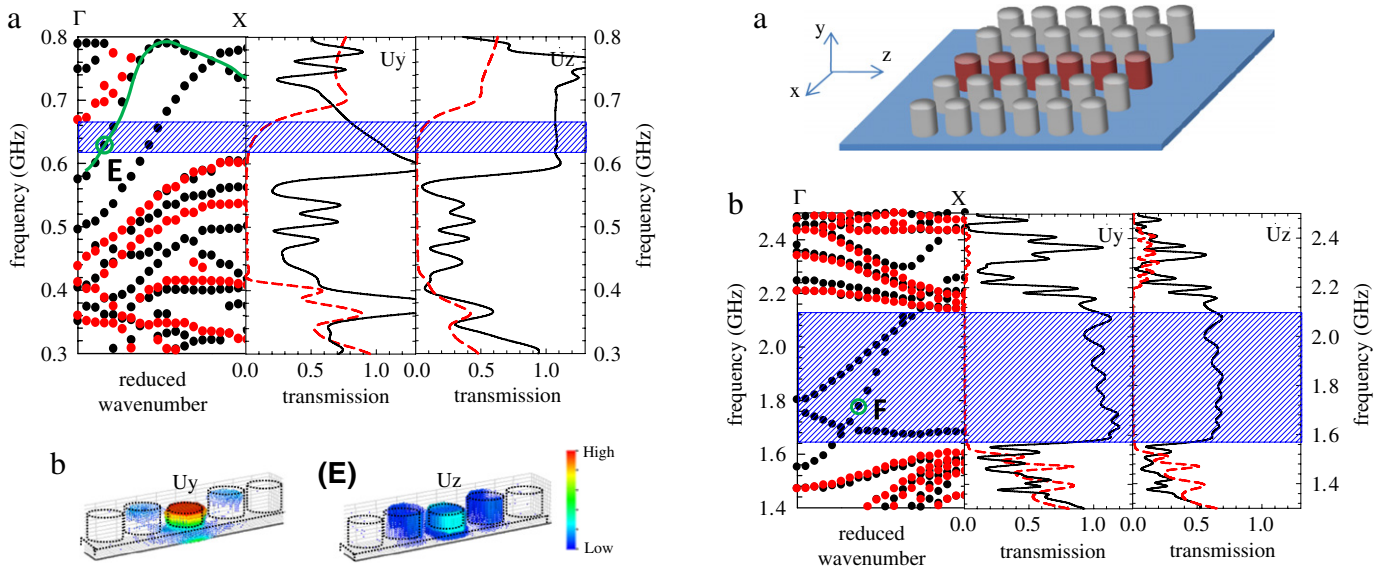
Fig. 73. (Color online) (a) Left dispersion curves in the low frequency range for the waveguide structure of Fig. 71(a) with a height $h_g = 0.3$ μm (black dots). Right: corresponding transmission spectra for the u_y and u_z components. (b) Eigenmode analysis at the point E ($ka/\pi = 0.16$, $f = 0.6277$ GHz) for (u_y) and (u_z). The blue (red) color corresponds to the lower (higher) value of the displacement field modulus.

Fig. 74. (Color online) (a) Schematic view of a linear waveguide made of different material dots symbolized in red. (b) Left: dispersion curves in the high frequency regime for silicon inserted dots forming the waveguide. Middle and right: corresponding transmission spectrum for both components u_y and u_z. (c) u_y and u_z eigenmode calculation at the point F ($Ka/\pi = 0.37$, $f = 1.777$ GHz). The blue (red) color corresponds to the lower (higher) value of the displacement field modulus.

these functionalities are of interest in radio-frequency devices for telecommunication applications [147].

We also investigated, using the finite difference time domain method, the dispersion of the elastic waves in a periodic array of dots deposited on a plate. We showed the possibility of a low frequency gap and its existence conditions as a function of the geometrical parameters in the structure and the physical parameters of the constituent materials. This gap is generated by the bending of the two plate modes, i.e. the shear horizontal

(SH) and the symmetric Lamb mode (S_0). The central frequency of the gap depends on all geometrical parameters (thickness of the plate, the height of the dots and the filling factor). The gap can
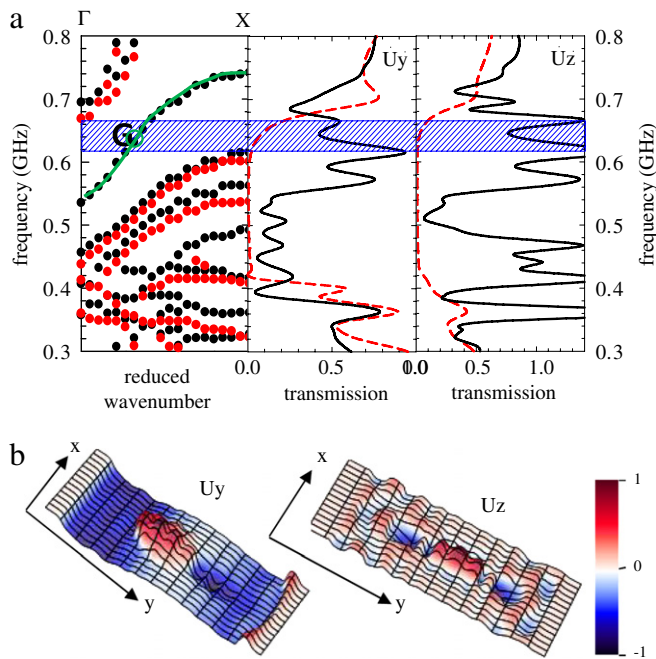
Fig. 75. (Color online) (a) Left: dispersion curves in the low frequency regime for aluminum dots forming the waveguide. Middle and right: corresponding transmission spectrum for both components u_y and u_z. (b) Displacement field distribution in the (x, y) plane at the thickness $z = e/2$ for the u_y and u_z polarizations at the monochromatic frequency $f = 0.6311\,$GHz. The red (blue) color represents the positive (negative) contribution of the wave.

exist for very different combinations of the constituent materials, supporting the origin of the gap as being due to the geometry of the structure. However, the central frequency and the width of the gap are dependent upon the material properties. More particularly, in view of acoustic isolation, it would be suitable to choose a high density material for the cylinders and a low density one for the plate. We also showed the existence of higher gaps, especially by increasing the height h of the cylinders. Those gaps can also appear at low frequency for much larger values of h. We showed that plate modes can be guided inside a linear defect created by removing one row of dots. With an appropriate choice of the physical and geometrical parameters, existence of two absolute band gaps is ensured. The first is in a frequency range where all wavelengths in the constituting materials are at least ten times larger than the period of the phononic crystal. The second falls in the Bragg frequency regime. We showed that there is a good correspondence between the transmission spectrum and dispersion curves. Using both transmission and dispersion phonon calculations, we studied propagation of the symmetric longitudinal Lamb wave S_0 through linear waveguides obtained either by removing a row of dots or changing the nature or the geometrical parameters of the dots in a row. In the first case, the polarization of the transmitted wave remains mainly longitudinal in the higher band gap while a conversion to the normal polarization occurs in the lower band gaps. When the waveguide is obtained by changing the height of the dots in a row, the transmitted wave contains both components of the displacement field in the frequency range of the higher as well as the lower gap. However, in the second, confinement is better ensured for the longitudinal component. Finally, transmission can also be achieved through a waveguide where the material constituting the dots is different from the one in the perfect phononic crystal. The transmitted waves travel with a good confinement in the guide, and contain both components of the displacement field. The advantage of this case is to limit the number of defect modes inside each band gap, which could be

more suitable for filtering applications. Results presented in this section could be applied to the innovative design of new acoustic-wave devices for wireless applications.

5. Sonic insulators

In the field of sound isolation, the main interest consists of finding structures that attenuate the propagation of sound over a sample whose thickness remains smaller than, or of the order of, the wavelength in air. A first attempt to find giant acoustic stop bands at low frequencies has been made by considering phononic crystals composed of air inclusions of cylindrical [148] or spherical [149] shapes in water. In these structures, the first band remains very narrow due to the low value of the sound velocity in the inclusions together with the large contrast between the acoustic properties of both constituents, while the next few higher bands are just flat bands associated with the internal resonances of the air inclusions. It has been shown [137] that these useful sound attenuation properties remain valid when the air cylinders are protected from water by surrounding them with a soft solid rubber material, for instance giving rise to a large attenuation between 1 and 10 kHz with the whole sample thickness not exceeding 70 mm. However, most of the recent studies have been directed towards a new class of phononic crystals, the so-called locally resonant materials [136,150,151,138,152,153,139, 154–156], first introduced by Sheng and co-workers [136]. These structures essentially consist [136,150,138,152,153,139,154–156] of a hard core, such as a metal, surrounded by a soft coating (silicone rubber) and immersed in a polymer such as epoxy. Due to the local resonances associated with the soft coating material, drastic dips can appear in the transmission coefficient at very low frequencies situated about two orders of magnitudes below the Bragg frequency. Such behaviors have been obtained in both three [136,150,151] and two-dimensional [138,152,153,139,154, 155,157,158] locally resonant phononic crystals. The dips in the transmission spectrum display an asymmetric line shape typical of Fano resonances [151]. Nevertheless, the width of the attenuation peaks is in general rather small and, in order to obtain a broad band attenuation, it is necessary to combine different locally resonant materials to overlap the dips resulting from several resonant frequencies.

In most of the preceding studies about locally resonant phononic crystals, the structure is made only by solid constituents. One object of this section is to investigate similar structures when the matrix is made by a fluid such as water whereas the embedded core remains a cylindrical solid. Indeed, it will be shown that the transmission properties and band structure can be significantly affected by the solid or fluid nature of the matrix as well as the nature of the coating material which is in contact with the matrix. The other main object of the section is to generalize, for two-dimensional phononic crystals, the most studied case of a coated core inclusion to the case of a multilayer cylindrical core composed of two or several coaxial shells surrounding the internal hard core. The resonant nature of the scatter is obtained by alternating shells of a soft polymer and a hard material such as steel. This new geometry of the scatter yields several dips in the transmission coefficient in a given frequency range. Moreover, we show that by combining two or more phononic crystals of different parameters, it is also possible to overlap some dips and obtain a widening of the frequency gaps. The organization of this section is as follows. The geometry of the structure is presented in the next subsection. In the next one, we discuss the behavior of the transmission coefficient as a function of the number and the order of the materials composing the shells, in particular the uttermost materials respectively in the internal core and in contact with the water matrix. The conclusions are given in the last subsection.

Table 5
Structural parameters of the constituents in the phononic crystal: mass density (ρ), longitudinal (c_L) and transverse (c_T) velocities of sound.

Material	Water	Steel	Butyl rubber	Silicone rubber
ρ (kg/m^3)	1000	7780	933	1300
c_L (m/s)	1490	5825	55	24
c_T (m/s)	0	3226	19	6

Fig. 76. Representation of the basic unit structure made of a hard cylinder core covered by a multilayer of rubber and steel. N is the number of shells in the coating ($N = 6$ in this figure).

5.1. Geometrical and simulation parameters

The structural unit used to build the phononic crystal consists of an infinitely long cylinder, composed of multi-coaxial shells, embedded in a water matrix. The inner (core) cylinder is made of steel. This core is coated by alternate shells composed respectively of a thin layer of an elastically soft material and a thin layer of a hard material (steel). In this way, we obtain an alternation of hard and soft materials (Fig. 76). We call N the number of shells coating the core and, depending on whether N is even or odd, the uttermost shell in contact with water will be steel or the polymer. In most of our calculation, the soft polymer is chosen to be butyl rubber (poly-isobutene-co-isoprene) which has very small elastic constants and consequently very low velocities of sound [159]. The structural parameters and the sound velocities of the materials used are reported in Table 5. In our calculations, we fix the outer radius of the cylinder to be equal to 8.4 mm and the thickness of each layer in the coating equal to 1.6 mm. The filling fraction of the whole cylinder, taken to be $f = 0.55$, will be kept constant throughout the paper. Finally, the sonic crystal is composed of six rows of elementary units arranged on a square lattice, with a lattice parameter of $a = 20$ mm. The whole size of the sonic crystal is therefore 12 cm.

Numerical calculations of dispersion curves, transmission co-efficients and maps of elastic displacement fields are based on a two-dimensional finite difference time domain scheme already described in the previous sections of this review paper. Space is discretized in both x and y directions using a mesh interval equal to $\Delta x = \Delta y = a/100$ where a is the lattice parameter of the crystal. This value insures a minimum of 8 intervals of the discretized mesh inside the smallest shell we studied. The equations of motion are solved with a time integration step $\Delta t = \Delta x/(4c_l)$ where c_l is the highest longitudinal velocity involved in the structure and a number of time steps equal to 2^{22} which is the necessary test time for a good convergence of the numerical calculation. More details about the calculation are given in Ref. [137].

5.2. Results and discussion

This subsection is divided into two parts dealing respectively with odd and even values of the number N of coating layers. This means the shell in contact with the water matrix will be respectively the polymer or steel. Our emphasis will be put on the latter case where, for the purpose of practical realization, the polymer will be protected from water. Nevertheless, for the sake of comparison and to show a totally different behavior, we also briefly describe the case where the polymer is in contact with water.

#### 5.2.1. Odd number of shells

Let us first consider the case where the solid core made of steel is coated only by one layer of elastically soft polymer (butyl rubber) (see the inset in Fig. 77(a)). In Fig. 77(a) and (b), we present the complete dispersion curves of the composite crystal and the transmission spectrum along the main directions of the reduced Brillouin zone, i.e. ΓX and ΓM (see the inset of Fig. 77(a)). The first band extends up to 1.7 kHz where it bends in the vicinity of the Brillouin zone. In the long wavelength limit, the average velocity of sound is about 80 m/s which is much smaller than the velocity in water due to the presence of the soft polymer shell. Above the absolute band gap, which extends from 1.7 to 1.85 kHz, most of the dispersion curves are rather flat. The transmission coefficient in the first band displays a set of peaks corresponding to Fabry–Perot oscillations of the whole phononic crystal. A few oscillations are also visible in the next bands but the transmission drops to negligible values when going to higher frequencies, probably due to the flatness of the dispersion curves.

The addition of supplementary shells, keeping always N as an odd number (see Fig. 77(c)), does not change the above general trends. The effect of increasing N is essentially a broadening of the lowest band gap, which extends, for the ΓX direction, from 1.35 to 2.0 kHz in the example of Fig. 77(c). The main conclusion is the possibility of opening an absolute band gap in the low frequency range when the polymer is in contact with the water matrix, while the effect is not related to the existence of a local resonance that cuts a band of propagating modes.

5.2.2. Even number of shells

5.2.2.1. $N = 2$.
First, we assume that the inner core is coated with only one double layer, made of the soft polymer and steel respectively, see the inset in Fig. 78(a). With a filling fraction $f = 0.55$, the diameter of the inner core is 5.2 mm and the thickness of each layer has been chosen to be 1.6 mm. Fig. 78(a) shows the transmission curve of the corresponding phononic crystal along ΓX. For the sake of comparison we also present in Fig. 78(b) the transmission coefficient of the conventional crystal without coating layers. It can be seen that in both cases, the first Bragg gap appears around a frequency of 35 kHz, i.e. $f = \nu/2a$ where ν is the velocity of sound in water and a the period. Due to the coating layers, there are two main differences occurring in the transmission curve of Fig. 78(a) with respect to that of Fig. 78(b): (i) several dips in the first pass band that extends up to 30 kHz, and (ii) a new pass band inside the Bragg gap that is also an effect of the coating (see also Ref. [137]). The occurrence of low frequency dips, about one to two orders of magnitude lower than the Bragg gap, is a characteristic feature of the locally resonant sonic materials constituted by solid media [136,150,151, 138,152,153,139,154–156], as first obtained by Liu et al. in a three-dimensional phononic crystal [136].

The first two dips appearing at 1.45 and 6.65 kHz in the transmission coefficient for both ΓX and ΓM directions of the Brillouin zone, Fig. 78(d), can also be seen in the dispersion curves, Fig. 78(c). The linear dispersion curve of the propagating modes is cut by two flat dispersion curves, giving rise to the opening of small low frequency gaps. Thus, such a phononic crystal leads to absolute acoustic stop bands in the sonic range. In the following, we discuss the behavior of the displacement fields associated with the first two dips at 1.45 kHz, Fig. 79 and 6.65 kHz, Fig. 80, assuming that the propagation is along the y direction. At 1.45 kHz, we represent the displacement components u_y, Fig. 79(a), and u_x, Fig. 79(b), both with a three dimensional map and along a cross section in the x direction. We note that the hard (steel) materials, both in the inner core and in the outside shell, move as rigid bodies essentially parallel to the y direction (see also Fig. 79(c)), whereas the soft
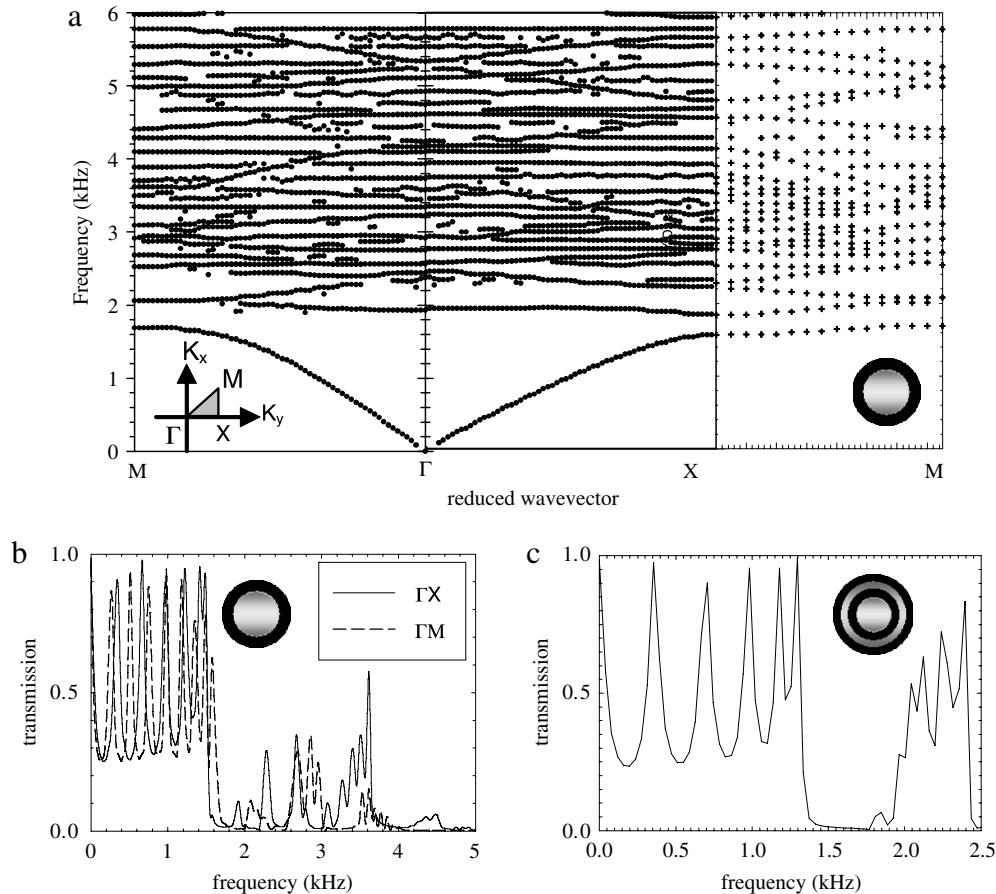
Fig. 77. Dispersion curves (a) and transmission coefficient along ΓX and ΓM (b) for a phononic crystal ($f = 0.55$ for the whole cylinder) in which the rigid core is coated with a polymer. (c) Transmission coefficient when the core is coated by three shells.

rubber undergoes an elastic deformation with both components of the displacement field. Thus, this first low frequency resonance (1.45 kHz) can be understood as an oscillation in which the core and the shell move along the direction of propagation in opposite phase with respect to each other, whereas the polymer acts as a spring linking the two hard materials. This scheme is displayed in Fig. 79(c) where O and O' are respectively the centers of the core and the shell. Finally, we can see the presence of a displacement field outside the cylinders in the water matrix, for both x and y directions. In particular, the displacement along x implies an interaction between cylinders in neighboring cells, as will be discussed below.

Fig. 80 present the displacement field associated with the second dip in Fig. 78(a) occurring at 6.65 kHz. It can be observed that the displacement is now totally localized inside the polymer shell, whereas the hard materials as well the matrix are at rest. Therefore, this dip originates from a localized mode of the polymer shell sandwiched between two hard materials. This mode is comparable to the one described with an epoxy matrix [136].

We now discuss the evolution of the dip frequencies, especially the lowest one, as a function of different geometrical and physical parameters of the multi-coaxial cylinders. Indeed, these frequencies can be changed with the thickness of the coating layers, the nature of the polymer material and the separation between the neighboring cylinders. In Fig. 81(a) we decrease the radius of the inner hard core and increase by the same amount the thickness of the polymer layer, the other parameters being kept fixed. This produces a downward shift of the dip frequencies which mainly results from the increase in the amount of soft material. The effect is weak for the first dip, while it becomes

more significant for the second dip for which the displacement field is localized inside the polymer. In Fig. 81(b), the parameters of the cylindrical inclusions are kept constant, while we change the period a of the crystal and therefore the separation between cylinders. The change in the frequency of the dip indicates that the interaction between neighboring cylinders is not negligible for a relatively high filling fraction. This result differs from the case of locally resonant phononic crystals with only solid constituents. In Fig. 81(c), we decrease the thickness of the outside steel shell and increase by the same amount the radius of the inner core. The decrease in the thickness of the steel shell increases the interaction between the polymer and the incoming wave from water and results in a broadening of the dip. This may be useful for the realization of a broadband sonic shield. In Fig. 81(d), we keep constant the geometrical parameters and change the nature of the polymer in the coatings, namely butyl rubber is replaced by silicone rubber (see Table 5 and Ref. [136]) which has lower velocities of sound. This results in a downward shift of the dip frequency, from 1.45 to 0.7 kHz.

Finally, to widen the phononic band gap, we make a combination of two phononic crystals in which we have respectively an outer shell thickness of 0.4 mm (0.6 mm) and a core radius of 3.6 mm (4.0 mm) (Fig. 82). These phononic crystals (A and B) display attenuation dips centered at frequencies of 1.0 and 1.06 kHz respectively. The association in tandem of both phononic crystals leads to a wider gap resulting from the overlap of the two initial dips. In Fig. 81(f), we observe the same behavior for the ΓM direction that confirms the absolute character of the acoustic stop band.

5.2.2.2. $N \geq 4$. We consider now the case of multi-coaxial cylindrical inclusions containing an even number of shells. Fig. 83(a)
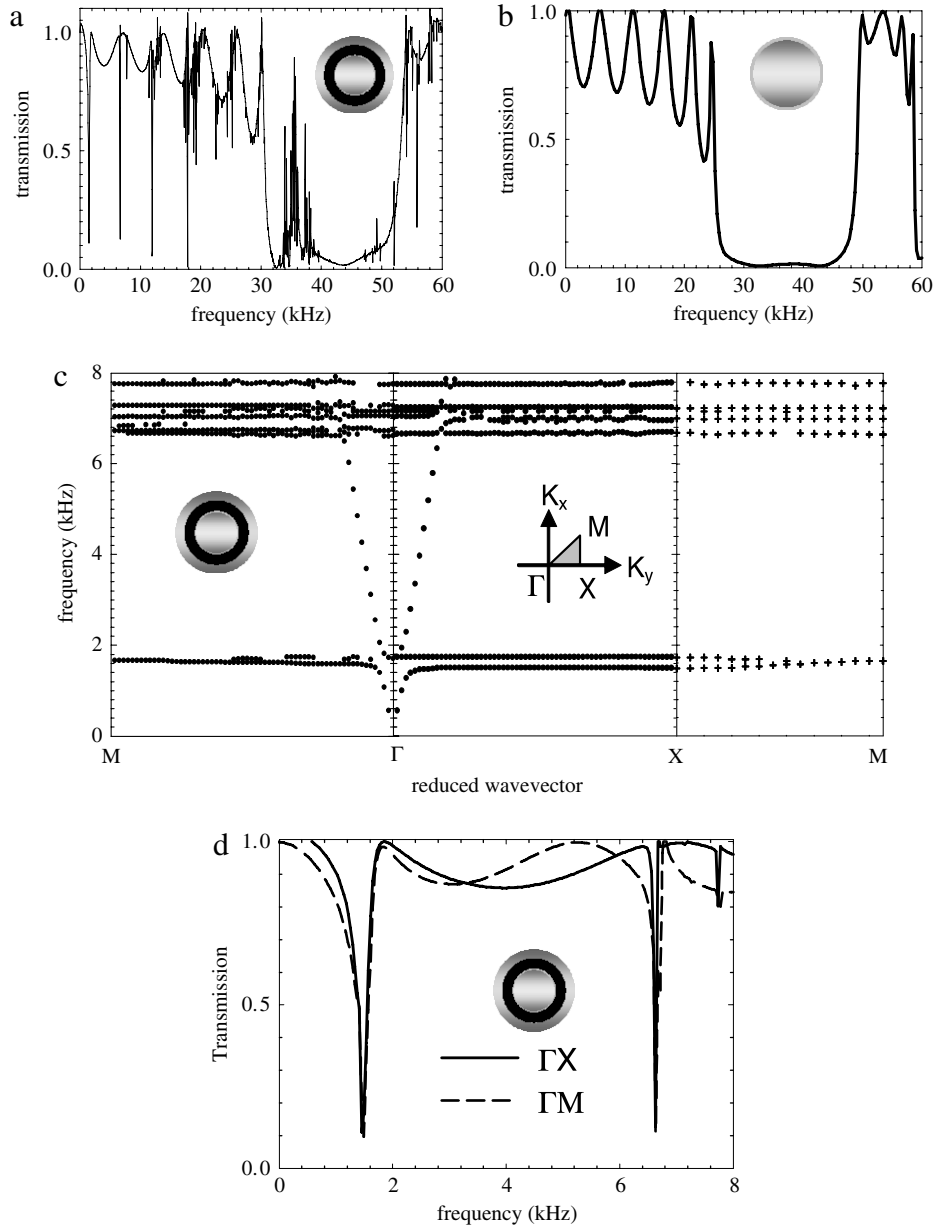
Fig. 78. (a) Transmission spectrum of the phononic crystal ($f = 0.55$ for the whole cylinder) where the rigid cores are coated with a double shell of polymer and steel. (b) Same as (a) for a conventional crystal without coating of the cores. (c) Band structure of the phononic crystal of Fig. 78(a). (d) Magnification of the transmission coefficient for both ΓX and ΓM directions.

presents the low frequency transmission curves for $N = 2$, 4 and 6. The number of dips evolves in relation with N, namely in comparison to the case $N = 2$ discussed above, each dip is divided into two (respectively three) dips when N becomes equal to 4 (respectively 6). As a matter of comparison, we also give in Fig. 83(b) the transmission coefficient for a phononic crystal in which the matrix is a stiff solid such as epoxy and the number of shells is 1, 3 or 5. Again, the number of dips increases according to the number of shells. The main difference with the former case is a stronger asymmetry in the line shape of the dips. Fig. 83(c) shows, in the case of a water matrix, the transmission behavior obtained in the ΓM direction. The acoustic stop bands overlap perfectly the dips obtained in the ΓX direction, showing that the band gaps should be absolute. Coming back to the water matrix and choosing $N = 6$, we illustrate in Fig. 83 the displacement fields of the first three resonance modes. For each frequency, we give the component u_y of the displacement along the direction of propagation, as well as a schematic view of the vibrations in the (x, y) plane. The common feature to all

these three modes is the fact that the hard parts of the inclusion, namely the inner core and the three steel cylindrical shells, vibrate as rigid bodies linked together through the polymer shells that act as springs. In the lowest mode, occurring at $f = 1.61$ kHz, the inner core and the two following steel shells vibrate in phase along the propagation direction (i.e. y), while the outer steel shell moves with the opposite phase (see Fig. 84a). This behavior is somewhat similar to the one obtained in Fig. 79 with $N = 2$ if we assume that the core is now constituted by the inner core plus the two following steel shells. The displacement fields of the second ($f = 3.0$ kHz) and third ($f = 3.77$ kHz) resonant modes are represented in Fig. 84(b) and (c). They correspond to other vibrational states of four rigid bodies linked together through the polymer shells. These modes seem to be more localized inside the inclusion than the first resonant mode since the outer steel shell remains almost at rest.

In Fig. 85(a), we give the transmission coefficient of the phononic crystal at higher frequencies (between 6 and 10 kHz) showing the occurrence of the next set of three dips. The
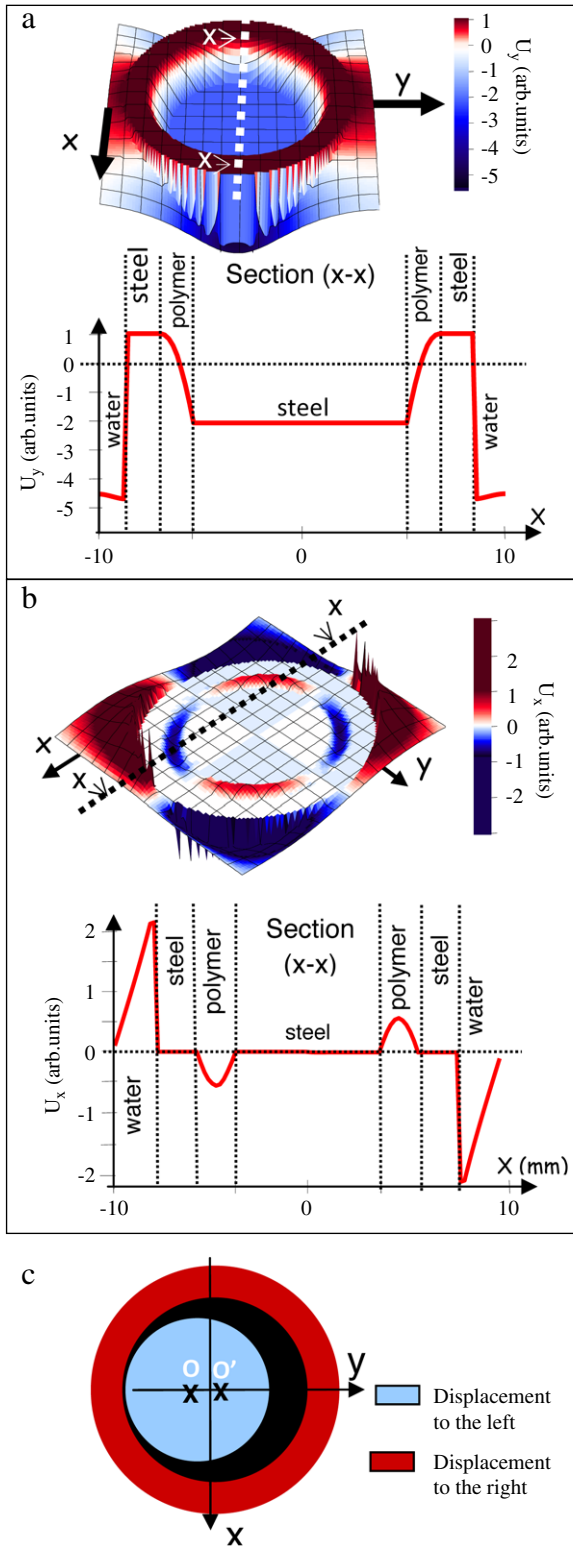
Fig. 79. (Color online) (a) and (b) Components u_y (parallel to the propagation direction) and u_x (perpendicular to the propagation direction) of the displacement vector for a frequency of 1.45 kHz associated to the first dip in Fig. 78(a). (c) Another representation of the displacement field showing that the hard materials constituting the inner core and the outside shell move as rigid bodies in opposite phase with respect to each other.

displacement fields associated with these dips are sketched in Fig. 85(b$_1$–b$_3$). The common feature to all these modes is their localization in the polymer shells while the hard materials and the matrix remain almost at rest.
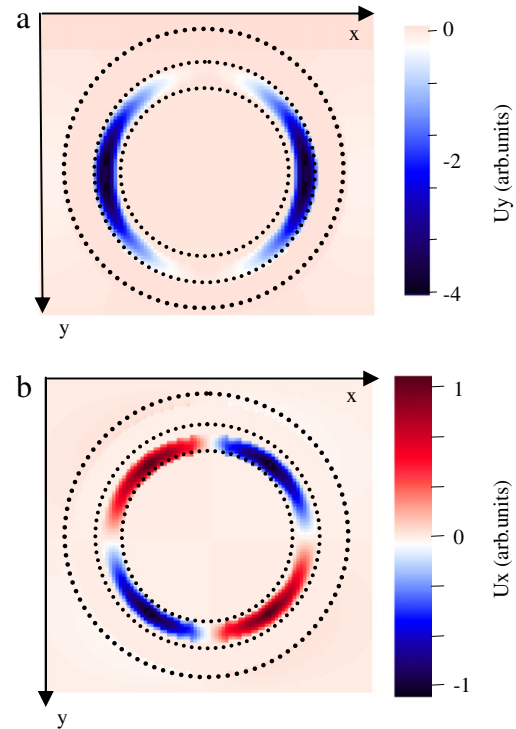

Fig. 80. (Color online) Displacement vector for the frequency associated to the second dip in Fig. 78(a) at 6.65 kHz. The dotted lines represent the position of the core and the shells. The displacement is localized inside the polymer shell.

Finally, we illustrate in Fig. 86 the transmission through a structure composed of a combination of three different phononic crystals (labeled *A*, *B* and *C*), embedded in a water matrix. The crystals differ from each other by the radius of the inner core which affects differently each resonance mode. We choose the values 2.6, 3.0 and 3.4 mm for the crystals *A*, *B* and *C* respectively. The thicknesses of the steel shells surrounding the core have been chosen identical in the three crystals: the outer shell has a thickness of 0.4 mm to ensure the width of the lowest frequency attenuation peak, as illustrated in Fig. 82(c); the two other shells have a thickness of 0.6 mm. Finally, the thicknesses of the polymer shells have been adjusted in each crystal in such a way as to keep constant the whole radius of the cylinder inclusions (namely 8.4 mm). Fig. 86 presents the transmission through the associated structure compared to the transmissions of the individual crystals. For the lowest gap, since the frequencies and widths of the initial gaps are almost identical, we find a similar behavior for the combined structure. However, the second gap results from the overlap of three close attenuation peaks in the individual crystals. Therefore, these dips can overlap together and form a larger forbidden frequency gap. The next three frequency gaps result from the superposition of the individual dips coming from each phononic crystal involved in the structure. Since the attenuation peaks associated to each component are rather separated from each other, one can observe an increase in the number of dips in the transmission spectrum without a widening. As a conclusion, the association of several phononic crystals that differ from each other by their geometrical parameters leads to the superposition of the individual gaps and could modify the transmission spectrum in three different ways, namely keeping a dip in size and position, widening a gap, and increasing the number of dips.

5.3. Summary

In this section we studied the transmission coefficient and dispersion curves of phononic crystals in which the matrix is a
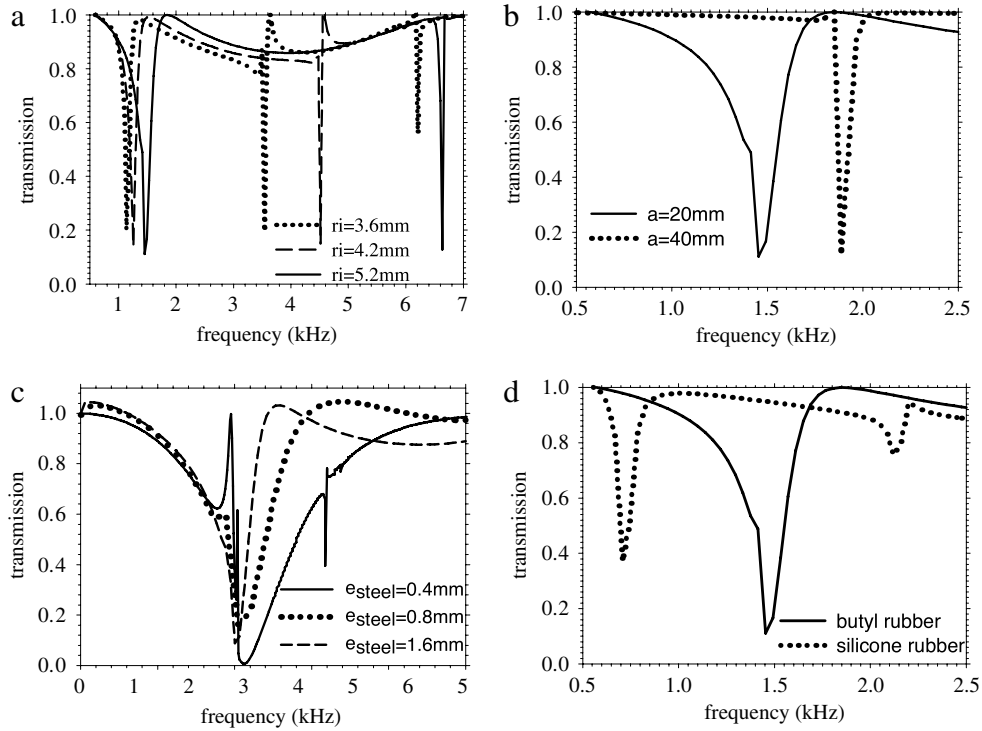
Fig. 81. Transmission coefficient through a sonic crystal with double-shell coating as a function of various geometrical and physical parameters (see text for details). (a) The radius of the inner core is decreased while the thickness of the polymer is increased by the same amount. (b) The period of the phononic crystal is twice as big. (c) The thickness of the outer steel shell is decreased while the radius of the inner core is increased by the same amount. (d) The polymer is changed from butyl rubber to silicone rubber.
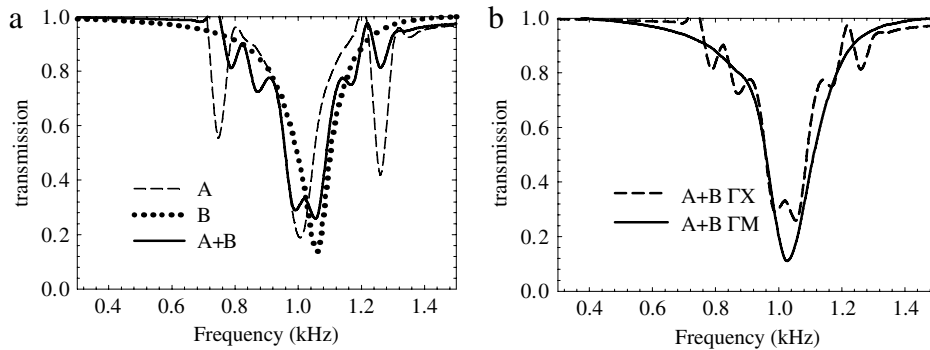

Fig. 82. (a) Transmission spectrum in the ΓX direction for two phononic crystals A and B and for the associated phononic crystal ($A + B$). The phononic crystals A and B, are composed respectively of an outer shell thickness of 0.4 mm (0.6 mm) and a core radius of 3.6 mm (4.0 mm). (b) Transmission spectrum for the ($A + B$) phononic crystal for the two directions ΓX and ΓM.

fluid such as water and the inclusions are composed of multi-coaxial cylindrical shells. Each inclusion is composed of a hard (steel) core coated with alternate shells of a soft polymer and steel. Totally different behaviors are obtained depending on whether the outer shell in contact with water is the soft polymer (odd number of shells) or steel (even number of shells). In the first case, low frequency gaps can appear as a result of the very low average velocity of sound in the phononic crystal. In the second case, several dips appear in the transmission coefficient, inside the pass band of the crystal below the first Bragg gap. These dips correspond to the interaction of flat bands with the linear dispersion curve of the propagating modes and result from the existence of quasi-local resonances in the unit cell of the phononic crystal. This result is similar to the one obtained in locally resonant sonic materials with solid constituents. However, in the structures with a fluid matrix, the interaction between neighboring unit cells is not totally negligible and the positions of the dip frequencies

are dependent upon the filling fraction, i.e. the separation between neighboring cylinders. By increasing the number of shells in the coating, the number of dips is increased, for example they are multiplied by 2 (or 3) when N is changed from 2 to 4 (or 6). We have discussed the displacement field of the resonant modes and generalized the behaviors obtained in the case of a single shell coating. Finally, we have analyzed the evolution of the lowest dips with the relevant geometrical and physical parameters of the phononic crystal. Values of the dip frequencies can be tuned using various parameters of the crystal such as the inner core radius, the shell thicknesses, or the period or the nature of the soft rubber. By associating several phononic crystals that differ from each other by their geometrical or physical parameters, one can keep unchanged or enlarge a phononic band gap or increase the number of dips, depending on the degrees of overlap between the single dips.
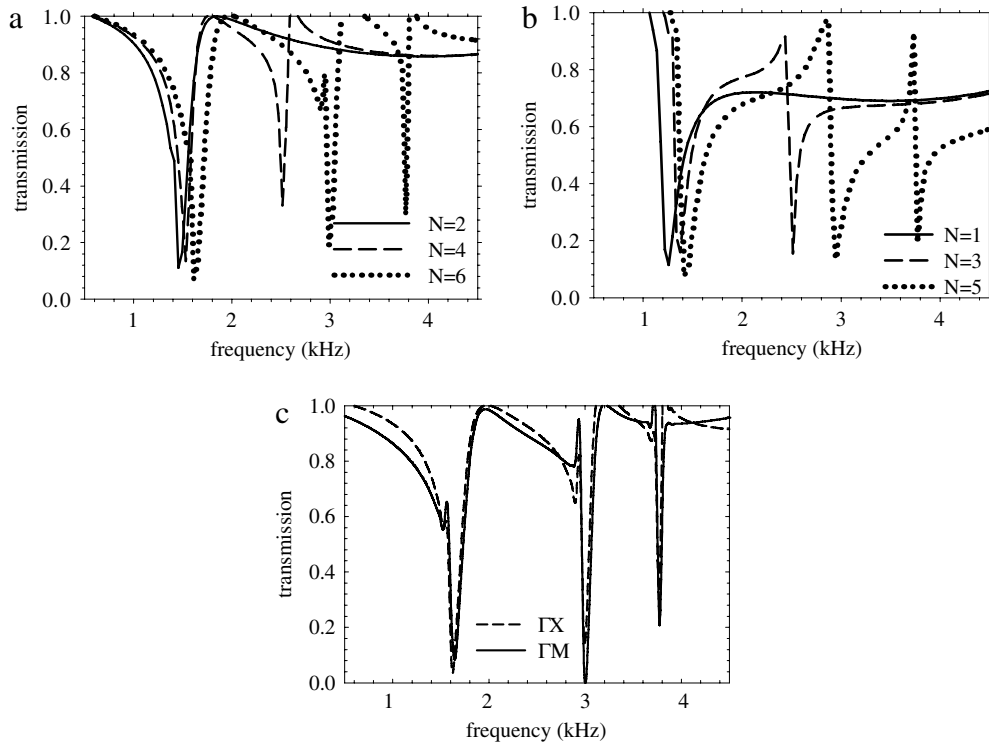
Fig. 83. Transmission curves through a phononic crystal where the coating contains N shells of polymer and steel, embedded in (a) water and (b) epoxy. (c) Transmission spectrum for $N = 6$ shells of polymer and steel, embedded in water, for the ΓM direction compared to the ΓX direction.
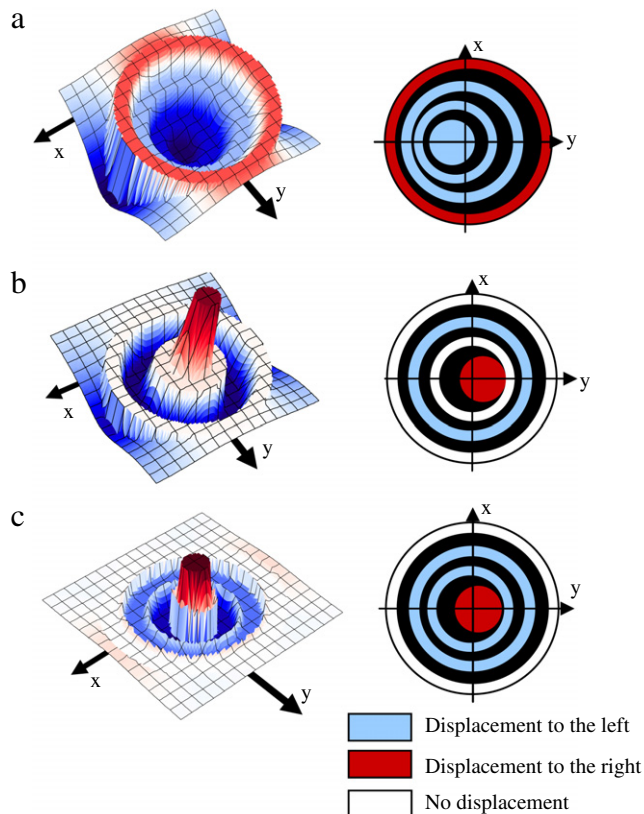
Fig. 84. (Color online) Map of the displacement component u_y (parallel to the propagation direction) and schematic view of the motion in the (x, y) plane for the first three dip frequencies when the coating contains $N = 6$ shells. (a) $f = 1.61$ kHz, (b) $f = 3.0$ kHz and (c) $f = 3.77$ kHz.

6. Prospectives

This review paper focused on two-dimensional phononic crystals and more particularly on the properties related to the existence of band gaps. Indeed, such crystals prohibit the propagation of sound for frequencies within the band gaps and allow the control and manipulation of the acoustic wave propagation. Several examples of phononic crystals were presented and some possible applications such as filtering, multiplexing and sound isolation were discussed. Special attention has been devoted to crystal plates, where the thickness of the phononic crystal is finite, and their potentialities. They open exciting new ways in integrated technological circuits to control sound. Theoretical works are dealing currently with the functionalities of phononic plates, analyzing the effect of point and linear defects introduced in the crystal. From the experimental point of view, new works devoted to submicron and nanometer scale structures represent a challenge in technological realizations and experimental characterizations at GHz frequency range [160]. Similar applications are expected based on structures where the phononic crystal is supported by a semi-infinite substrate [161,162]. The design of the phononic crystal on the surface is studied to control and manipulate the surface acoustic waves. Beyond the study on the existence and behavior of absolute band gaps, one topic of interest is about the engineering of the dispersion curves in the band structure that opens the way to new applications. The architecture of the dispersions curves can be modified by the size or the nature of the inclusions embedded in the host matrix. For instance, a phononic crystal made up of holes in a solid matrix can be infiltrated with different liquid, polymers or gas. This produces drastic modifications of the dispersion curves, in particular creating flat bands or new bending of the acoustic branches. Such behaviors of the acoustic properties in infiltrated phononic crystals can be used as biochemical sensors [163]. Moreover, external physical stimuli such as electric or magnetic field, tensile deformation, variations of temperature or phase transformation [164,165] open the way to a new topic based on tunable and reversible phononic crystals. During the past few years,
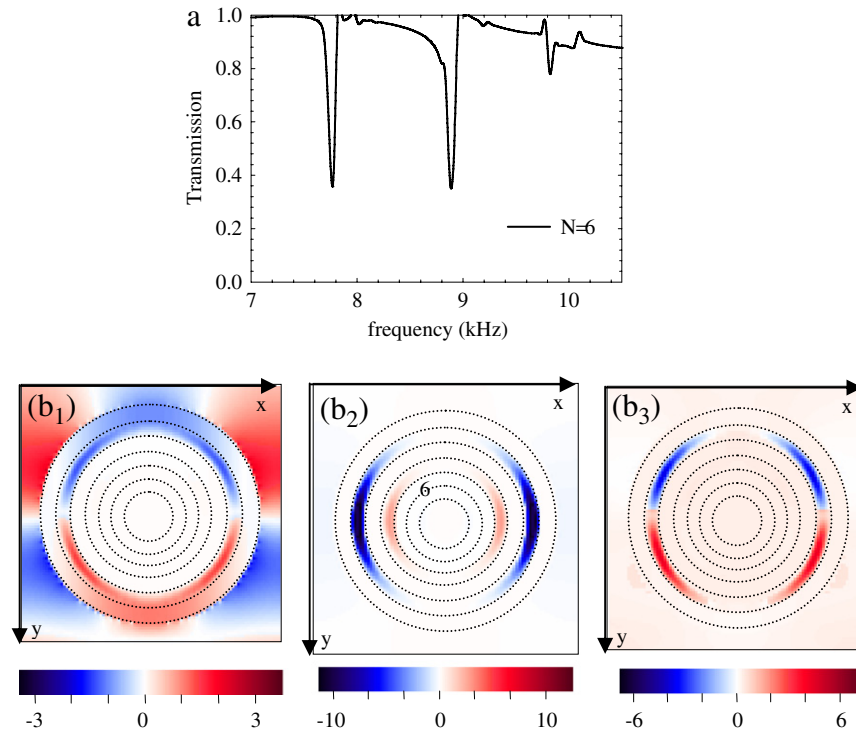
Fig. 85. (Color online) Transmission coefficient (a) and displacement component u_y (parallel to the propagation direction) when $N = 6$ for the dip frequencies (b_1) $f = 7.8$ kHz (b_2) $f = 8.9$ kHz and (b_3) $f = 9.8$ kHz.

many efforts have been devoted to technological fabrications of the phononic structure in two or three dimensions. Until recently, most of the experimental studies have been conducted in the sub-millimeter range, at ultrasonic frequencies, in particular interest in medical environments. Several papers are dealing with the applications of negative refraction phenomena in this range. More interesting for the telecommunication applications, phononic crystals of submicron and nanometer sizes, operating at GHz frequencies, have been realized recently. Additionally, such structures allow the confinement and control of both elastic and optical waves in the same structure. Such materials exhibiting dual phononic–photonic band gaps [166,167] also called phoXonic crystals, may find useful applications for enhancing the phonon–photon interaction. By merging both fields (nanophotonics and nanophononics) within the same platform, novel unprecedented control of light and sound in very small regions will be achieved. This would be interesting for the purpose of designing new compact acousto-optic and sensing devices, but also as a source of high frequency phonons. In this review, we have shown that the local resonances can lead to low frequency gaps one or two orders of magnitude below the Bragg gap. Such sub-wavelength phononic crystals can present forbidden frequencies in the audible range. Beyond the application of such materials as noise-damping and shielding materials, their underlying microstructures offer new opportunities in material science. Acoustic metamaterials, as a counterpart to electromagnetic metamaterials, have begun to emerge as a new field [168]. The main purpose of acoustic metamaterials is to provide an effective medium description of the structure, such as acoustic impedance or index. Acoustic metamaterials present negative refraction properties at specific frequencies. Such a property could be used to focus the acoustic field and define negative index lenses which present the property to break the diffraction limit. Thermal transport in non-metallic nanostructured materials can be strongly affected by the specific phonon dispersions as well as different scattering mechanisms. Phononic crystals represent a novel way to develop new materials and technologies for improving thermal transport and
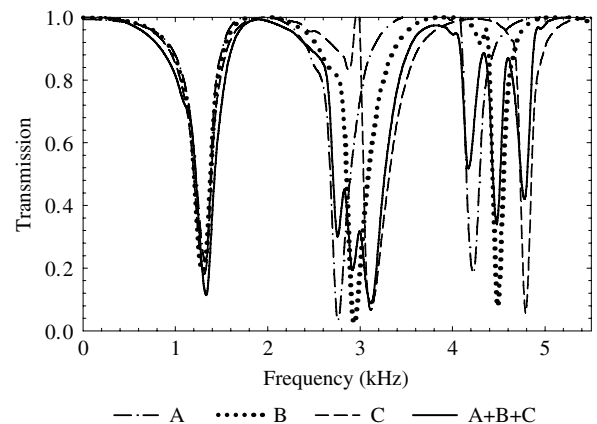
Fig. 86. Calculated transmission spectrum through a structure resulting from the combination of three different phononic crystals *A*, *B* and *C* which differ from each other by their inner core radius (2.6 mm, 3.0 mm and 3.4 mm respectively). In the associated structure ($A + B + C$), the resulting gaps correspond to the superposition of each individual gap.

reducing interface resistances in nanodevices [169]. Therefore, the knowledge and engineering of phononic band structure is a necessary step for the purpose of heat management. In particular, the existence of band gaps and/or the lowering of group velocities due to the bending of the dispersion curves are detrimental for phonon transmission and hence contribute to decrease the thermal conductivity. This may find useful applications for thermoelectric devices.

This is not however a complete survey of all the numerous works devoted to two-dimensional phononic crystals [18] and we hope that the authors of not cited or badly cited papers will be kind and excuse us.

Acknowledgements

References

[1] See for example, A. Yariv, P. Yeh, Optical Waves in Crystals, Wiley, New York, 1984.
[2] See for example, J.M. Bendickson, J.P. Dowling, M. Scalora, Phys. Rev. E 53 (1996) 4107.
[3] J.O. Vasseur, B. Djafari-Rouhani, L. Dobrzyński, A. Akjouj, J. Zemmouri, Phys. Rev. B 59 (1999) 13446.
[4] See for a review, J.O. Vasseur, A. Akjouj, L. Dobrzyński, B. Djafari-Rouhani, E.H. El Boudouti, Surf. Sci. Rep. 54 (2004) 1.
[5] See for example, J.D. Joannopoulos, R.D. Meade, J.N. Winn, Photonic Crystals, Princeton University Press, Princeton, 1995.
[6] See for example, C.M. Soukoulis (Ed.), Photonic Band Gaps and Localization, Plenum, New York, 1993.
[7] See for example, C.M. Soukoulis (Ed.), Photonic Band Gap Materials, Kluwer, Dordrecht, 1996.
[8] See for example, C.M. Soukoulis (Ed.), Photonic Crystals and Light Localization in the 21st Century, in: NATO Sciences Series, Kluwer, Dordrecht, 2001.
[9] M.S. Kushwaha, P. Halevi, L. Dobrzyński, B. Djafari-Rouhani, Phys. Rev. Lett. 71 (1993) 2022.
[10] J.D. Achenbach, M. Kitahara, J. Acoust. Soc. Am. 81 (1987) 595.
[11] See the review paper, M.S. Kushwaha, Internat. J. Modern Phys. B 10 (1996) 977.
[12] For a review, see M.S. Kushwaha, Recent Res. Dev. Appl. Phys. 2 (1999) 743.
[13] See the review paper, M. Sigalas, M.S. Kushwaha, E.N. Economou, M. Kafesaki, I.E. Psarobas, W. Steurer, Z. Kristallogr. 220 (2005) 765.
[14] Suxia Yang, J.H. Page, Zhengyou Liu, M.L. Cowan, C.T. Chan, Ping Sheng, Phys. Rev. Lett. 93 (2004) 024301.
[15] See the review paper, Ping Sheng, Che Ting Chan, Zeit. Kristal. 220 (2005) 757.
[16] See the review paper, T. Miyashita, Meas. Sci. Technol. 16 (2005) R47.
[17] See the review paper, W. Steurer, D. Sutter-Widmer, J. Phys. D: Appl. Phys. 40 (2007) R229.
[18] See the bibliographic compilation online at http://www.univ-lehavre.fr/recherche/lomc/phonon/PhononicDatabase1.html.
[19] R.E. Camley, B. Djafari-Rouhani, L. Dobrzyński, A.A. Maradudin, Phys. Rev. B 27 (1983) 7318.
[20] B. Djafari-Rouhani, L. Dobrzyński, O. Hardouin-Duparc, R.E. Camley, A.A. Maradudin, Phys. Rev. B 28 (1983) 1711.
[21] L. Dobrzyński, B. Djafari-Rouhani, O. Hardouin-Duparc, Phys. Rev. B 29 (1984) 3138.
[22] R. Esquivel-Sirvent, G.H. Cocoletzi, J. Acoust. Soc. Am. 95 (1994) 86.
[23] J.P. Dowling, J. Acoust. Soc. Am. 91 (1992) 2539.
[24] See the review paper, J. Sapriel, B. Djafari-Rouhani, Surf. Sci. Rep. 10 (1989) 189.
[25] See the review paper, E.H. El Boudouti, B. Djafari-Rouhani, A. Akjouj, L. Dobrzyński, Surf. Sci. Rep. 64 (2009) 471.
[26] M.M. Sigalas, E.N. Economou, Solid State Commun. 86 (1993) 141.
[27] M.S. Kushwaha, P. Halevi, G. Martinez-Montes, L. Dobrzyński, B. Djafari-Rouhani, Phys. Rev. B 49 (1994) 2313.
[28] M.M. Sigalas, E.N. Economou, J. Appl. Phys. 75 (1993) 2845.
[29] M.S. Kushwaha, P. Halevi, Appl. Phys. Lett. 64 (1994) 1085.
[30] M.S. Kushwaha, P. Halevi, Appl. Phys. Lett. 69 (1996) 31.
[31] J.O. Vasseur, B. Djafari-Rouhani, L. Dobrzyński, M.S. Kushwaha, P. Halevi, J. Phys.: Condens. Matter 6 (1994) 8759.
[32] J.O. Vasseur, P.A. Deymier, G. Frantziskonis, G. Hong, B. Djafari Rouhani, L. Dobrzyński, J. Phys.: Condens. Matter 10 (1998) 6051.
[33] F.R. Montero de Espinosa, E. Jimenez, M. Torres, Phys. Rev. Lett. 80 (1998) 1208.
[34] M. Kafesaki, M.M. Sigalas, E.N. Economou, Solid State Commun. 96 (1995) 285.
[35] M.S. Kushwaha, B. Djafari-Rouhani, J. Appl. Phys. 80 (1996) 3191.
[36] M. Kafesaki, M.M. Sigalas, E.N. Economou, in: C.M. Soukoulis (Ed.), Photonic Band Gaps Materials, in: NATO ASI Series, Kluwer Academic Publishers, Dordrecht, 1996, p. 143.
[37] J.O. Vasseur, B. Djafari-Rouhani, L. Dobrzyński, P.A. Deymier, J. Phys.: Condens. Matter 9 (1997) 7327.
[38] Z. Liu, C.T. Chan, Ping Sheng, A.L. Goertzen, J.H. Page, Phys. Rev. B 62 (2000) 2446.
[39] J.H. Page, A.L. Goertzen, S. Yang, Z. Liu, C.T. Chan, Ping Sheng, in: C.M. Soukoulis (Ed.), Photonic Crystals and Light Localization in the 21st Century, Kluwer, Dordrecht, 2001, p. 59.
[40] R. Martinez-Sala, J. Sancho, J.V. Sanchez, V. Gomez, J. Llinares, F. Meseguer, Nature 378 (1995) 241.
[41] M.M. Sigalas, E.N. Economou, Europhys. Lett. 36 (1996) 241.
[42] M.S. Kushwaha, Appl. Phys. Lett. 70 (1997) 3218.
[43] W.M. Robertson, J.F. Rudy III, J. Acoust. Soc. Am. 104 (1998) 694.
[44] D. Caballero, J. Sanchez-Dehesa, C. Rubio, R. Martinez-Sala, J.V. Sanchez-Perez, F. Meseguer, J. Llinares, Phys. Rev. E 60 (1999) R6316.
[45] M.S. Kushwaha, B. Djafari-Rouhani, L. Dobrzyński, J.O. Vasseur, Eur. Phys. J. B 3 (1998) 155.
[46] M. Sigalas, E.N. Economou, in: C.M. Soukoulis (Ed.), Localization and Propagation of Classical Waves in Random and Periodic Structures, Plenum Press, New York, 1993.
[47] J.V. Sanchez-Pérez, D. Caballero, R. Mártinez-Sala, C. Rubio, J. Sánchez-Dehesa, F. Meseguer, J. Llinares, F. Gálvez, Phys. Rev. Lett. 80 (1998) 5325.
[48] J.O. Vasseur, P.A. Deymier, A. Khelif, P. Lambin, B. Djafari-Rouhani, L. Dobrzyński, A. Akjouj, N. Fettouhi, J. Zemmouri, Phys. Rev. E 65 (2002) 56608.
[49] M.M. Sigalas, N. Garcia, J. Appl. Phys. 87 (2000) 3122.
[50] D. Garcia-Pablos, F.R. Montero de Espinosa, M. Torres, M. Kafesaki, N. Garcia, Phys. Rev. Lett. 84 (2000) 4349.
[51] A. Taflove, The Finite Difference Time Domain Method, Artech, Boston, 1998.
[52] C.T. Chan, Q.L. Yu, K.M. Ho, Phys. Rev. B 51 (1995) 16635.
[53] Shanhui Fan, P.R. Villeneuve, J.D. Joannopoulos, Phys. Rev. B 54 (1996) 11245.
[54] M. Kafesaki, E.N. Economou, Phys. Rev. B 60 (1999) 11993.
[55] E.N. Economou, M.M. Sigalas, in: C.M. Soukoulis (Ed.), Photonic Band-Gaps and Localization, Plenum Press, New York, 1993, p. 317.
[56] M.M. Sigalas, E.N. Economou, J. Sound Vibration 158 (1992) 377.
[57] E.N. Economou, M.M. Sigalas, Phys. Rev. B 48 (1993) 13434.
[58] D. Gay, Matriaux Composites, Herms, 1991.
[59] American Institute of Physics Handbook, 3rd ed., A.I.P., New York, 1972.
[60] J.O. Vasseur, P.A. Deymier, B. Chenni, B. Djafari-Rouhani, L. Dobrzyński, D. Prevost, Phys. Rev. Lett. 86 (2001) 3012.
[61] D. Cassagne, C. Jouanin, D. Bertho, Phys. Rev. B 52 (1995) R2217.
[62] D. Cassagne, C. Jouanin, D. Bertho, Phys. Rev. B 53 (1996) 7134.
[63] Y. Tanaka, Y. Tomoyasu, S. Tamura, Phys. Rev. B 62 (2000) 7387.
[64] D. Garcia-Pablos, M. Sigalas, F.R. Montero de Espinosa, M. Torres, M. Kafesaki, N. Garcia, Phys. Rev. Lett. 84 (2000) 4349.
[65] R.M. Hornreich, M. Kugler, S. Shtrikman, C. Sommers, J. Phys. I France 7 (1997) 509.
[66] A. Mekis, S. Fan, J.D. Joannopoulos, Phys. Rev. B 58 (1998) 4809.
[67] J.V. Hryniewicz, P.P. Absil, B.E. Little, R.A. Wilson, P.T. Ho, IEEE Photon. Techn. Lett. 10 (2000) 320.
[68] P.P. Absil, J.V. Hryniewicz, B.E. Little, R.A. Wilson, L.G. Joneckis, P.T. Ho, IEEE Photon. Techn. Lett. 12 (2000) 398.
[69] J. Moosburger, M. Kamp, A. Forchel, S. Olivier, H. Benisty, C. Weisbuch, U. Oesterle, Appl. Phys. Lett. 79 (2001) 3579.
[70] S. Olivier, H. Benisty, M. Rattier, C. Weisbuch, M. Qiu, A. Karlson, C.J.M. Smith, R. Houdré, U. Oesterle, Appl. Phys. Lett. 79 (2001) 2514.
[71] C.J.M. Smith, R.M. De La Rue, M. Rattier, S. Olivier, H. Benisty, C. Weisbuch, T. Krauss, R. Houdré, U. Oesterle, Appl. Phys. Lett. 78 (2001) 1487.
[72] M.M. Sigalas, C.A. Flory, Phys. Rev. B 65 (2002) 125909.
[73] Shanhui Fan, Appl. Phys. Lett. 80 (2002) 908.
[74] M.S. Kushwaha, A. Akjouj, B. Djafari-Rouhani, L. Dobrzyński, J.O. Vasseur, Solid State Commun. 106 (1998) 659.
[75] B. Djafari-Rouhani, J.O. Vasseur, A. Akjouj, L. Dobrzyński, M.S. Kushwaha, P.A. Deymier, J. Zemmouri, Prog. Surf. Sci. 59 (1998) 255 and references therein.
[76] A. Khelif, B. Djafari-Rouhani, J.O. Vasseur, P.A. Deymier, Phys. Rev. B 68 (2003) 024302.
[77] M. Kafesaki, M.M. Sigalas, N. Garcia, Physica B 296 (2001) 190.
[78] A. Khelif, B. Djafari-Rouhani, J.O. Vasseur, P.A. Deymier, Ph. Lambin, L. Dobrzyński, Phys. Rev. B 65 (2002) 174308.
[79] M. Kafesaki, M.M. Sigalas, N. Garcia, Phys. Rev. Lett. 85 (2000) 4044.
[80] T. Miyashita, C. Inoue, Jpn. J. Appl. Phys. 40 (2001) 3488.
[81] A. Khelif, B. Djafari-Rouhani, J.O. Vasseur, P.A. Deymier, Phys. Rev. B 68 (2003) 024302.
[82] H. Chandra, P.A. Deymier, J.O. Vasseur, Phys. Rev. B 70 (2004) 054302.
[83] M. Torres, F.R. Montero de Espinosa, D. Garcia-Pablos, N. Garcia, Phys. Rev. Lett. 82 (1999) 3054.
[84] F.R. Montero de Espinosa, E. Jimenez, M. Torres, Phys. Rev. Lett. 80 (1998) 1208.
[85] T. Miyashita, C. Inoue, K. Sakata, Poster session on Numerical methods in acoustics, in: 17th International Congress on Acoustics, Rome, September 2–7, 2001.
[86] A. Khelif, A. Choujaa, S. Benchabane, B. Djafari-Rouhani, V. Laude, Appl. Phys. Lett. 84 (2004) 4400.
[87] J.O. Vasseur, P. Deymier, M. Beaugeois, Y. Pennec, B. Djafari-Rouhani, D. Prevost, Z. Kristallogr. 220 (2005) 829.
[88] A. Khelif, A. Choujaa, S. Benchabane, B. Djafari-Rouhani, V. Laude, Z. Kristallogr. 220 (2005) 836.
[89] W.M. Robertson, G. Arjavalingam, R.D. Meade, K.D. Brommer, A.M. Rappe, J.D. Joannopoulos, Phys. Rev. Lett. 68 (1992) 2023.
[90] T.F. Krauss, R.M. de la Rue, S. Brand, Nature (London) 383 (1996) 699.
[91] V. Karathanos, J. Modern Opt. 45 (1998) 1751.
[92] I.E. Psarobas, A. Modinos, R. Sainidou, N. Stefanou, Phys. Rev. B 65 (2002) 064307.
[93] D. Royer, E. Dieulesaint, Ondes élastiques dans les solides, Vol. 1, Masson, Paris, 1996, p. 280.
[94] G. Mur, IEEE Trans. Electromagn. Compat. 23 (1981) 377.
[95] Y. Pennec, B. Djafari-Rouhani, J.O. Vasseur, A. Khelif, P.A. Deymier, Phys. Rev. E 69 (2004) 046608.

[96] Y. Pennec, B. Djafari-Rouhani, J.O. Vasseur, H. Larabi, A. Khelif, A. Choujaa, S. Benchabane, V. Laude, Appl. Phys. Lett. 87 (2005) 261912.
[97] S. Fan, P.R. Villeneuve, J.D. Joannopoulos, H.A. Haus, Phys. Rev. Lett. 80 (1998) 960.
[98] S. Fan, P.R. Villeneuve, J.D. Joannopoulos, M.J. Khan, C. Manolatou, H.A. Haus, Phys. Rev. B 59 (1999) 15882.
[99] S. Fasquel, X. Melique, D. Lippens, O. Vanbésien, Opt. Commun. 233 (2004) 305.
[100] A. Khelif, A. Choujaa, B. Dajafari-Rouhani, M. Wilm, S. Ballandras, V. Laude, Phys. Rev. B 68 (2003) 0214301.
[101] I. Sliwa, M. Krawczyk, Acta Phys. Polon. A 108 (2005) 943.
[102] Y. Tanaka, S. Tamura, Phys. Rev. B 58 (1998) 7958.
[103] Y. Tanaka, S. Tamura, Phys. Rev. B 60 (1999) 13294.
[104] T.T. Wu, Z.G. Huang, S. Lin, Phys. Rev. B 69 (2004) 094301.
[105] V. Laude, M. Wilm, S. Benchabane, A. Khelif, Phys. Rev. E 71 (2005) 036607.
[106] R. Sainidou, B. Djafari-Rouhani, J.O. Vasseur, Phys. Rev. B 77 (2008) 094304.
[107] J.J. Chen, K.W. Zhang, J. Gao, J.C. Cheng, Phys. Rev. B 73 (2006) 094307.
[108] J.J. Chen, H.L.W. Chan, J.C. Cheng, Phys. Lett. A 366 (2007) 493.
[109] J. Gao, X.Y. Zou, J.C. Cheng, B.W. Li, Appl. Phys. Lett. 92 (2008) 023510.
[110] J.O. Vasseur, P.A. Deymier, B. Djafari-Rouhani, Y. Pennec, in: Proceedings of IMECE 2006, ASME International Mechanical Engineering Congress and Exposition, Chicago, IL, USA, November 5–10, 2006.
[111] J.C. Hsu, T.T. Wu, Phys. Rev. B 74 (2006) 144303.
[112] A. Khelif, B. Aoubiza, S. Mohammadi, A. Adibi, V. Laude, Phys. Rev. E 74 (2006) 046610.
[113] J.O. Vasseur, A.C. Hladdky-Hennion, B. Djafari-Rouhani, P. Duval, B. Dubus, Y. Pennec, J. Appl. Phys. 101 (2007) 114904.
[114] J.C. Hsu, T.T. Wu, Appl. Phys. Lett. 90 (2007) 201904.
[115] J.O. Vasseur, P.A. Deymier, B. Djafari-Rouhani, Y. Pennec, A.C. Hladky-Hennion, Phys. Rev. B 77 (2008) 085415.
[116] Y. Pennec, B. Djafari-Rouhani, H. Larabi, J.O. Vasseur, A.C. Hladky-Hennion, Phys. Rev. B 78 (2008) 104105.
[117] J.F. Robillard, A. Devos, I. Roch-Jeune, Phys. Rev. B 76 (2007) 092301.
[118] C. Giannetti, B. Revaz, F. Banfi, M. Montagnese, G. Ferrini, F. Cilento, S. Maccalli, P. Vavassori, G. Oliviero, E. Bontempi, L.E. Depero, V. Metlushko, F. Parmigiani, Phys. Rev. B 76 (2007) 125413.
[119] J.J. Chen, B. Qin, J.C. Cheng, Chin. Phys. Lett. 22 (2005) 1706.
[120] C. Charles, B. Bonello, F. Ganot, Ultrasonics 44 (2006) 1209(E).
[121] B. Manzanares-Martinez, F. Ramos-Mendieta, Phys. Rev. B 68 (2003) 134303.
[122] R. Sainidou, N. Stefanou, Phys. Rev. B 73 (2006) 184301.
[123] T.T. Wu, Z.G. Huang, S.Y. Liu, Z. Kristallogr. 220 (2005) 841.
[124] T.T. Wu, L.C. Wu, Z.G. Huang, J. Appl. Phys. 97 (2005) 094916.
[125] S. Benchabane, A. Khelif, J.-Y. Rauch, L. Robert, V. Laude, Phys. Rev. E 73 (2006) 065601.
[126] X. Zhang, T. Jackson, E. Lafond, P. Deymier, J.O. Vasseur, Appl. Phys. Lett. 88 (2006) 041911.
[127] C. Goffaux, J.P. Vigneron, Phys. Rev. B 64 (2001) 075118.
[128] Ph. Langlet, Ph.D. Thesis, Université de Valenciennes et du Hainaut-Cambrésis, 1993.
[129] Ph. Langlet, A.-C. Hladky-Hennion, J.-N. Decarpigny, J. Acoust. Soc. Am. 98 (1995) 2792.
[130] T. Gorishnyy, C.K. Ullal, M. Maldovan, G. Fytas, E.L. Thomas, Phys. Rev. Lett. 94 (2005) 115501.
[131] M. Maldovan, E.L. Thomas, Appl. Phys. B 83 (2006) 595.
[132] T. Miyashita, C. Inoue, Jpn. J. Appl. Phys. 40 (2001) 3488.
[133] J.-H. Sun, T.T. Wu, Phys. Rev. B 74 (2006) 174305.
[134] J.-H. Sun, T.T. Wu, Phys. Rev. B 76 (2007) 104304.
[135] J. Chen, B. Bonello, Z. Hou, Phys. Rev. E 78 (2008) 036609.
[136] Z. Liu, X. Zhang, Y. Mao, Y.Y. Zhu, Z. Yang, C.T. Chan, P. Sheng, Science 289 (2000) 1734.
[137] Ph. Lambin, A. Khelif, J.O. Vasseur, L. Dobrzyński, B. Djafari-Rouhani, Phys. Rev. E 63 (2001) 066605.
[138] C. Goffaux, J. Sanchez-Dehesa, A. Levy Yeyati, Ph. Lambin, A. Khelif, J.O. Vasseur, B. Djafari-Rouhani, Phys. Rev. Lett. 88 (2002) 22.
[139] M. Hirsekorn, Appl. Phys. Lett. 84 (2004) 3364.
[140] Y.A. Kosevich, C. Goffaux, J. Sanchez-Dehesa, Phys. Rev. B 74 (2006) 012301.
[141] H. Larabi, Y. Pennec, B. Djafari-Rouhani, J.O. Vasseur, Phys. Rev. E 75 (2007) 066601.
[142] Y. Pennec, B. Djafari-Rouhani, H. Larabi, A. Akjouj, J.N. Gillet, J.O. Vasseur, G. Thabet, Phys. Rev. B 80 (2009) 144302.
[143] R. Chen, A.I. Hochbaum, P. Murphy, J. Moore, P. Yang, A. Majumdar, Phys. Rev. Lett. 101 (2008) 105501.
[144] J.N. Gillet, Y. Chalopin, S. Volz, J. Heat Transfer 131 (2009) 043206.
[145] Y. Chalopin, J.N. Gillet, S. Volz, Phys. Rev. B 77 (2008) 233309.
[146] A.C. Hladky-Hennion, J. Vasseur, B. Dubus, B. Djafari-Rouhani, D. Ekeom, B. Morvan, J. Appl. Phys. 104 (2008) 064906.
[147] C. Campbell, Surface Acoustic Wave Devices for Mobiles and Wireless Communications, Academic Press, San Diego, 1985.
[148] M.S. Kushwaha, B. Djafari-Rouhani, J. Appl. Phys. 84 (1998) 4677.
[149] M.S. Kushwaha, B. Djafari-Rouhani, L. Dobrzyński, Phys. Lett. A 248 (1998) 252.
[150] Z. Liu, C.T. Chan, P. Sheng, Phys. Rev. B 65 (2002) 165116.
[151] Z. Liu, C.T. Chan, P. Sheng, Phys. Rev. B 71 (2005) 014103.
[152] C. Goffaux, J. Sanchez-Dehesa, Phys. Rev. B 67 (2003) 144301.
[153] C. Goffaux, J. Sanchez-Dehesa, Ph. Lambin, Phys. Rev. B 70 (2004) 184302.
[154] M. Hirsekorn, P.P. Delsanto, N.K. Batra, P. Matic, Ultrasonic 42 (2004) 231.
[155] Q. Bo, C. Jiu-Jiu, C. Jian-Chun, Chin. Phys. 14 (2005) 2522-07.
[156] G. Wang, D. Yu, J. Wen, Y. Liu, X. Wen, Phys. Lett. A 327 (2004) 512.
[157] G. Wang, X. Wen, J. Wen, L. Shao, Y. Liu, Phys. Rev. Lett. (2004) 93.
[158] G. Wang, L. Shao, Y. Liu, J. Wen, Chin. Phys. 15 (2006).
[159] Encyclopedia of Polymer Science and Engineering, 2nd ed., Wiley-Interscience, 1987.
[160] S. Mohammadi, A.A. Eftekhar, W.D. Hunt, A. Adibi, Appl. Phys. Lett. 94 (2009) 051906.
[161] A. Khelif, Y. Achaoui, S. Benchabane, V. Laude, B. Aoubiza, Phys. Rev. B 81 (2010) 214303.
[162] J.O. Vasseur, A.C. Hladky-Hennion, B. Djafari-Rouhani, F. Duval, B. Dubus, Y. Pennec, P.A. Deymier, J. Appl. Phys. 101 (2007) 114904.
[163] R. Lucklum, J. Li, Meas. Sci. Technol. 20 (2009) 124014.
[164] A. Sato, Y. Pennec, N. Shingne, T. Thurn-Albecht, W. Knoll, M. Steinhart, B. Djafari-Rouhani, G. Fytas, ACS Nano 4 (6) (2010) 3471.
[165] J.-F. Robillard, O. Bou Matar, J.O. Vasseur, P.A. Deymier, M. Stippinger, A.-C. Hladky-Hennion, Y. Pennec, B. Djafari-Rouhani, Appl. Phys. Lett. 95 (2009) 124104.
[166] Y. Pennec, B. Djafari-Rouhani, E.H. El Boudouti, C. Li, Y. El Hassouani, J.O. Vasseur, N. Papanikolaou, S. Benchabane, V. Laude, A. Martinez, Opt. Express 18 (2010) 14301.
[167] S. Mohammadi, A.A. Eftekhar, A. Khelif, A. Adibi, Opt. Express 18 (2010) 9164.
[168] L. Fok, M. Ambati, Z. Xiang, Acoustic metamaterials, MRS Bull. 33 (2008) 931.
[169] K.L. Jim, C.W. Leung, S.T. Lau, S.H. Choy, H.L.W. Chan, Appl. Phys. Lett. 94 (2009) 193501.